MIMO Radar Processing Methods for Anticipating and Preventing Real World Imperfections

Mathieu Cattenoz

UNIVERSITÉ PARIS-SUD

DOCTORAL SCHOOL 422:
SCIENCES ET TECHNOLOGIES DE L'INFORMATION, DES TÉLÉCOMMUNICATIONS ET DES SYSTÈMES

ONERA — The French Aerospace Lab
L2S — *Laboratoire des Signaux et Systèmes* (CentraleSupélec–CNRS–Univ. Paris-Sud)

PHD THESIS

COMPUTER ENGINEERING, AUTOMATIC CONTROL AND SIGNAL PROCESSING

by

Mathieu CATTENOZ

MIMO Radar Processing Methods for Anticipating and Compensating Real World Imperfections

Defense date: May 27th, 2015

Thesis committee:

Reviewers:	Philippe FORSTER	Professor (Univ. Paris-Ouest and SATIE, ENS Cachan)
	Xavier NEYT	Professor (Royal Military Academy, Bruxelles)
Examiners:	François LE CHEVALIER	Professor (Delft University of Technology and Thales)
	Josef WORMS	Mathematician (FHR, Fraunhofer-Gesellschaft)
	Pascal CHEVALIER	Professor and Expert (CNAM and Thales-Communications-Security)
	Sylvie MARCOS	Thesis director, Director of Research (L2S)
	Laurent SAVY	Thesis supervisor, Engineer (ONERA)
Guest members:	Chin Yuan CHONG	Senior Member of Technical Staff (DSO National Laboratories, Singapore)
	Erwan COMTE	Head of Radar Engineering (Direction Générale de l'Armement)
	Philippe BROUARD	Thesis supervisor, Engineer (ONERA)
	Laurent CONSTANCIAS	Thesis supervisor, Engineer (ONERA)

"I hope you don't mean, Captain, that you expect to come out of the war alive?"

Gavoille was not joking. He was sincerely shocked. We knew perfectly well that there was nothing for us but to go on flinging ourselves into the forest fire. Even though it serves no purpose. Fifty crews for the whole of France. The whole strategy of the French army rested upon our shoulders. An immense forest fire raging, and a hope that it might be put out by the sacrifice of a few glassfuls of water. They would be sacrificed. [...] The major is out of sorts because the orders are absurd. We know that they are absurd; but the Staff knows that as well as we do. It gives orders because orders have to be given. Given order is its trade, in time of war. [...] Everybody struggles as hard as he can to make war looks like war. Piously respects the rules of the game. So that war may perhaps be good enough to agree to look like war. Orders are given for the sacrifice of the air arm because war must be made to look like war. And nobody admits meanwhile that this war looks like nothing at all. That no part of it makes sense. That not a single blueprint fits the circumstances. That the puppets have been cut free of the strings which continue to be pulled. [...] There was a reason for the miracle. It used to happen occasionally that the beautiful administrative machine would break down and everybody would agree that it could not be repaired. For want of better, men would be substituted for the machine. And men would save France.

— Antoine de Saint-Exupéry, *Flight to Arras* (1942)

Contents

Acknowledgements

First of all, I would like to warmly thank the reviewers and the examiners of my thesis committee for having accepted the invitation and haven given me all these feedbacks.

For the following acknowledgments, since it addresses French-speaking people, I will write in this language.

Donc qui dit remerciements, dit aussi bilan. Ces remerciements sont longs, mais il faut bien cela pour résumer trois ans de vie sans oublier trop de monde.

Pour commencer, je remercie tout spécialement ma directrice de thèse, Sylvie Marcos du L2S, ainsi que mes encadrants de l'ONERA, Laurent Savy, Philippe Brouard et Laurent Constancias, pour avoir accepté de me prendre sous leur aile et pour avoir toujours été là pour répondre à mes questions.

Je salue également le reste de l'équipe et collègues de l'ONERA : Arnaud Brun tout particulièrement, mais également Jean-Marc Boutry, Sylvain Azarian, Jack Peyret, René Guern, Olivier Rabaste. Remercions également SONDRA et l'ONERA pour le financement de ma thèse et des participations aux congrès, ainsi que le L2S pour l'accueil dans ses locaux et le financement de l'école d'été.

Un remerciement particulier à tous les doctorants, postdocs et apprentis qui ont gravité autour de moi, que ce soit à l'ONERA (Jean-François, Nicolas, Etienne, Thibaut, Corinna, Damien, Rata, Aurélien, Stéphane) ou au L2S (Elsa, Najett, Jean-François, Pierre, François, Benjamin, Olivier, Achal, Chengfang, Stéphanie, Anna, Panagiotis). On remarquera le double remerciement pour Jean-François, qui a été en quelque sorte mon "mentor" pour m'avoir ouvert la voie à l'ONERA, au L2S et même à Gentilly.

Une pensée également à Jessica, Baptiste et Etienne pour l'équipe qu'on a formée pour

l'organisation des Journées des Doctorants à l'ONERA. Je tiens également à remercier Meryem, Najett, Elsa, Pierre, Daniel, Maud sans qui il n'aurait pas été possible de mettre en place et faire vivre l'association des doctorants de Supélec. Merci également à Julien, Clément, Hossein, Zineb, Kathleen (et tous les autres) pour avoir contribué ensemble à mettre en place cette incroyable aventure qu'est Start in Saclay !
Une pensée également à toutes les personnes rencontrées au cours de ces trois années : Doctoriales (Samah), Ecole d'été, conférences (Alexis, Jérôme), plongée avec l'ASCO ONERA (Eric, Raphaël, Vanina, ...), etc.
Je remercie également toutes les personnes qui m'ont aidé à un moment ou à un autre : Nabil El Korso de l'ENS Cachan (et ancien L2S) pour mes premiers TP donnés à l'ENS, ainsi qu'Alexandre Renaux pour mes TD donnés à Polytech Paris-Sud, mais aussi Elisabeth Bertheau et Françoise Ricci de l'ONERA, Odette Leroux du L2S, Anne-Hélène Picot de SONDRA. Et je tiens à remercier très sincèrement Aline Bouchard de l'ONERA qui m'a soutenu et conseillé au cours de mes "démarches" administratives.

En dehors du boulot, je remercie tout ceux qui ont été présents sur la durée : Jim (un peu à cause de lui que j'ai commencé cette thèse, et un peu grâce à lui que je la termine), Manu (pour la musculation intellectuelle et physique), Sébastien L, Jérôme, Solène et Francis (pour m'avoir donné du boulot en dehors de ma thèse). Citons également les personnes qui ont été là à un moment ou à un autre, même si beaucoup ne liront probablement pas ces lignes : mes parents, ma soeur, Sébastien V, Maxime, Kai, Patrick, Rémi, Valentina, Sébastien G, Hélène, Mathieu, Caroline, Anne-Lise, Dimitri, Karina, Jérémy, Clément, Alexis, Eléonore, Bénédicte, Stéphanie, David, Josefin, Ruth, Geoffrey, Damien et Filipe.

Abstract

The MIMO radar concept promises numerous advantages compared to today's radar architectures: flexibility for the transmitting beampattern design – including wide scene illumination and fine resolution after processing – and system complexity reduction, through the use of less antennas and the possibility to transfer system control and calibration to the digital domain. However, the MIMO radar is still at the stage of theoretical concept, with insufficient consideration for the impacts of waveforms' lack of orthogonality and system hardware imperfections.

The ambition of this thesis is to contribute to paving the way to the operational MIMO radar. In this perspective, this thesis work consists in anticipating and compensating the imperfections of the real world with processing techniques. The first part deals with MIMO waveform design and we show that phase code waveforms are optimal in terms of spatial resolution. We also exhibit their limits in terms of sidelobes appearance at matched filter output. The second part consists in taking on the waveform intrinsic imperfections and proposing data-dependent processing schemes for the rejection of the induced residual sidelobes. We develop an extension for the Orthogonal Matching Pursuit (OMP) that satisfies operational requirements, especially localization error robustness, low computation complexity, and nonnecessity of training data. The third part deals with processing robustness to signal model mismatch, especially how it can be prevented or anticipated to avoid performance degradation. In particular, we propose a digital method of transmitter phase calibration. The last part consists in carrying out experiments in real conditions with the Hycam MIMO radar testbed. We exhibit that some unanticipated encountered distortions, even when limited at the matched filter output, can greatly impact the performance in detection of the data-dependent processing methods.

Keywords: MIMO radar, MIMO waveform, sidelobe mitigation, data-dependent processing, OMP, IAA, model mismatch, MIMO experiment.

Résumé

Le concept du radar MIMO est prometteur en raison des nombreux avantages qu'il apporte par rapport aux architectures radars actuelles : flexibilité pour la formation de faisceau à l'émission — large illumination de la scène et résolution fine après traitement — et allègement de la complexité des systèmes, via la réduction du nombre d'antennes et la possibilité de transférer des fonctions de contrôle et d'étalonnage du système dans le domaine numérique. Cependant, le radar MIMO reste au stade du concept théorique, avec une prise en compte insuffisante des impacts du manque d'orthogonalité des formes d'onde et des défauts matériels.

Ce travail de thèse, dans son ambition de contribuer à ouvrir la voie vers le radar MIMO opérationnel, consiste à anticiper et compenser les défauts du monde réel par des traitements numériques. La première partie traite de l'élaboration des formes d'onde MIMO. Nous montrons que les codes de phase sont optimaux en termes de résolution spatiale. Nous présentons également leurs limites en termes d'apparition de lobes secondaires en sortie de filtre adapté. La seconde partie consiste à accepter les défauts intrinsèques des formes d'onde et proposer des traitements adaptés au modèle de signal permettant d'éliminer les lobes secondaires résiduels induits. Nous développons une extension de l'Orthogonal Matching Pursuit (OMP) qui satisfait les conditions opérationnelles, notamment par sa robustesse aux erreurs de localisation, sa faible complexité calculatoire et la non nécessité de données d'apprentissage. La troisième partie traite de la robustesse des traitements vis-à-vis des écarts au modèle de signal, et particulièrement la prévention et l'anticipation de ces phénomènes afin d'éviter des dégradations de performance. En particulier, nous proposons une méthode numérique d'étalonnage des phases des émetteurs. La dernière partie consiste à mener des expérimentations en conditions réelles avec la plateforme radar MIMO Hycam. Nous montrons que certaines distorsions subies non anticipées, même limitées en sortie de filtre adapté, peuvent impacter fortement les performances en détection des traitements dépendant du modèle de signal.

Mots-clefs : radar MIMO, forme d'onde MIMO, réduction des lobes secondaires, traitement dépendant du modèle de signal, OMP, IAA, écart au modèle, expérimentation MIMO.

List of Acronyms

ADC	Analog-to-Digital Converter
AWG	Arbitrary Waveform Generator
CDMA	Code Division Multiple Access
CLRB	Cramér-Rao Lower Bound
CS	Compressed Sensing
DBF	Digital Beam Forming
DDMA	Doppler Division Multiple Access
FDMA	Frequency Division Multiple Access
GUI	Graphic User Interface
HPA	High-Power Amplifier
IAA	Iterative Adaptive Approach
ISLR	Integrated Side Lobe Ratio
LNA	Low-Noise Amplifier
MF	Matched Filter
MIMO	Multiple-Input Multiple-Output
OMP	Orthogonal Matching Pursuit
PRF	Pulse Repetition Frequency
PSLR	Pointed Side Lobe Ratio
RAID	Redundant Array of Independent Disks
Rx	Receiver
SIMO	Single-Input Multiple-Output
SNR	Signal-to-Noise Ratio
TDMA	Time Division Multiple Access
Tx	Transmitter

1 Context and Outline of the Thesis Work

1.1 Basic Review of Radar

The objective of this section is not to go deeply in the radar description but to give key elements for the basic understanding of radar systems. For more details, the interested reader is invited to refer to general literature on radar systems like [1], [2] and [3].

1.1.1 Introduction

Radar is an electronic device for the detection and location of objects. It operates by transmitting a particular type of waveform, and detects the echo signal. Radar can be designed to see through conditions impervious to normal human vision, such as darkness, haze, fog, rain, snow. In addition, radar has the advantage of being able to measure target parameters like range and velocity.

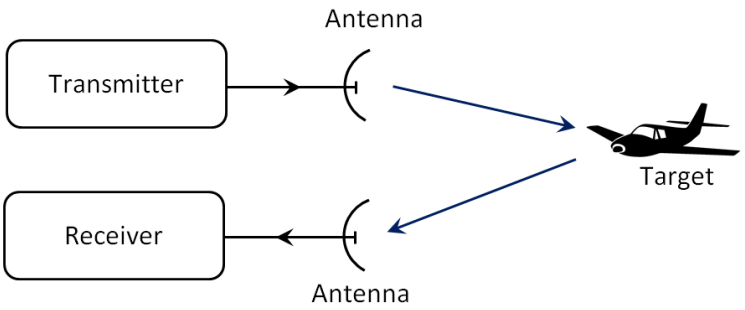

Figure 1.1: Block diagram of an elementary form of radar.

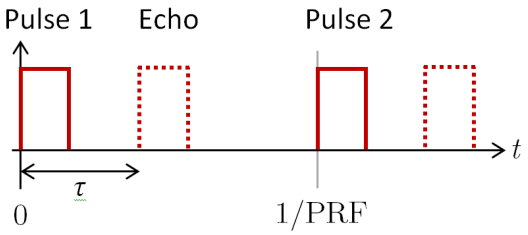

Figure 1.2: Illustration of a radar pulse transmission.

Radar is employed for a large range of civilian, military and scientific applications like air surveillance, surface search, tracking and guidance, weather radar, Earth observation.

An elementary form of radar, shown on fig. 1.1, consists of a transmitting antenna emitting electromagnetic radiation, a receiving antenna, and processing and detecting devices. A portion of the transmitted signal is intercepted by a target and is reradiated in all directions. The receiving antenna collects the returned energy and delivers it to a receiver, where it is processed to detect the presence of the target and to extract some of its parameters.

Even if there are many suitable modulations, most radars transmit a pulse-modulated waveform to fulfill the functions of target detection and location.

1.1.2 Information Content in Radar Signals

Range

As illustrated in fig. 1.2, the distance r, or range, to the target is measured as a function of the time τ taken by the signal to travel to the target and return:

$$r = c \cdot \frac{\tau}{2} \tag{1.1}$$

The signal propagation speed c typically corresponds to the velocity of light $c = 3 \cdot 10^8$ m/s. The maximum unambiguous range of coverage R_{unamb} is limited by the pulse repetition frequency PRF:

$$R_{\text{unamb}} = \frac{c}{2 \cdot \text{PRF}} \tag{1.2}$$

The range resolution $R_{\min}$, *i.e.* the minimum distinguishable range between two targets, is inversely proportional to the bandwidth B: $R_{\min} > \frac{c}{2B}$

Velocity

The radial velocity v_r of the target produces a phase shift of the received signal, known as Doppler effect, leading to a signal frequency shift by $\nu = -\frac{2v_r f_c}{c}$, with f_c the carrier frequency.

Direction (Azimuth or Elevation)

Antennas usually form a specific radiation diagram in order to focus the transmitted power to one specific direction at each moment. The orientation of the beam gives therefore information on the angle of the target. This angle can be the azimuth (angle in the horizontal plane) and/or the elevation (angle with the horizontal plane).

Polarization

Some types of radar – called polarimetric radar – have the capacity to estimate the polarization (horizontal, vertical, circular, etc.) of the received signals. It offers for instance the possibility to determine and/or differentiate different types of structures in an environment (vegetation, constructions, etc). Indeed the signal polarization is affected differently depending on the material and the geometry of the illuminated object.

1.1.3 The SIMO Radar

An array antenna for transmission consists of a number of individual radiating elements suitably spaced with respect to one another, typically $\lambda/2$ with λ the carrier wavelength. The relative amplitude and phase of the signals applied to each of the elements are controlled to obtain the desired radiation pattern (*e.g.* pencil beam, wide beam) from the combined action of all the elements. Scanning of the beam formed by an array can be accomplished by mechanically moving the entire array-antenna structure. However, the beam can also be electronically steered by varying the relative phase shift between the elements of the array, and so forming a diagram focused in specific directions.

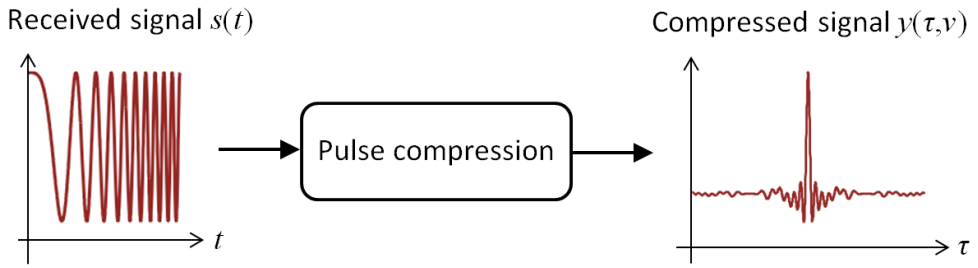

Figure 1.3: Illustration of the pulse compression.

In the conventional phased array radar, the system can only transmit scaled versions of a single waveform. Since only a single waveform is used – even if there are multiple radiating elements –, the phase array radar is also called SIMO (single-input multiple-output) radar.

In the case of an array antenna in reception, the directivity of this antenna is recovered through digital beamforming (DBF) on receive, which consists in digitally forming multiple simultaneous focused beams.

1.1.4 Detection

A typical radar used for the detection of conventional aircrafts might employ a pulse width of several µs, and a pulse repetition frequency of several hundred pulses per second. The modulated RF pulse generated by the transmitter travels along the transmission line to the antenna, where it is radiated into space. A portion of the radiated power is reflected by the target back to the radar and captured by the receiver antenna. The received signal is then pre-processed in the front-end. As main stages of a typical radar front-end, we can cite low-noise amplification and filtering, frequency down-conversion, analog-to-digital conversion (sampling and quantization).

Then, to detect the target, it is necessary to distinguish the signal reflected from the target, from the signal containing only noise. This is the purpose of the stage of pulse compression which is usually the application of a matched filter (MF) which matches to the transmitted pulse. It corresponds to the correlation of the received signal $s(t)$ with the transmitted pulse $u(t)$, as illustrated in fig. 1.3. The MF output

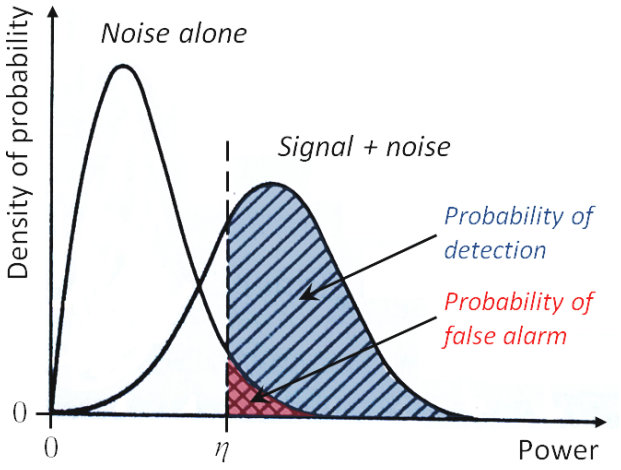

Figure 1.4: Probability-density functions for noise alone and for signal-plus-noise.

can be expressed as:

$$y(\tau,\nu) = \int s(t)\, u^*(t-\tau)\, e^{-j2\pi\nu t}\, dt \tag{1.3}$$

The target range can be estimated directly from the received echo after a pulse transmission (“fast time"). The target velocity is generally estimated from the received signal phase evolution from pulse to pulse (“slow time"). The target direction can be estimated through the direction of the antenna, with a precision depending on its directivity.

Note that the radar front-end is subject to noise due to unwanted electromagnetic energy which interferes with the ability of the receiver to detect the wanted signal. It may originate within the receiver itself, or it may enter via the receiving antenna along with the desired signal.

To determine whether there is a target or not, a threshold is set on the MF output. If the estimated power crosses a predetermined threshold η, then a target detection is considered to have occurred. When setting the threshold η, there is a trade-off between false-alarm rate (*i.e.* the probability that the noise alone crosses this threshold) and detection rate (*i.e.* the probability that the power crosses this threshold when the target is present) [4]. A small threshold value improves the detection rate but also increases the false alarm rate, and *vice versa*, as illustrated in fig. 1.4.

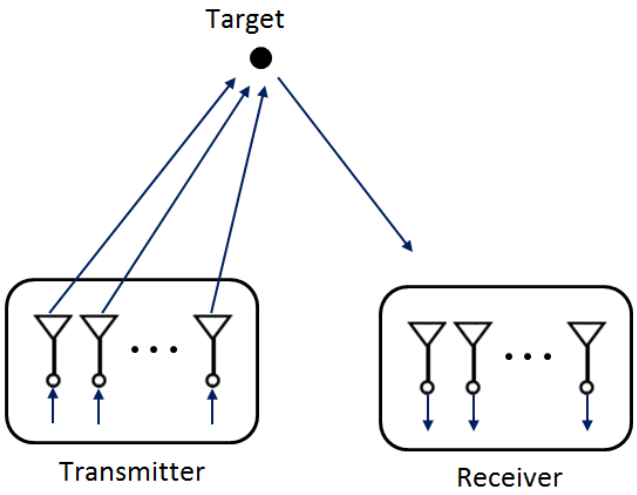

(a) SIMO radar (phased array).

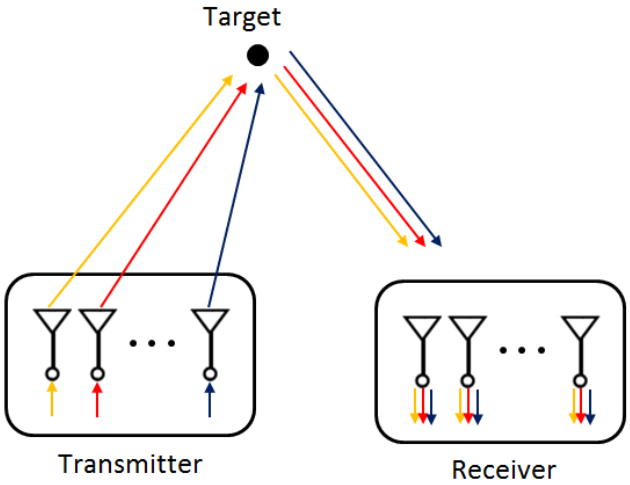

(b) MIMO radar.

Figure 1.5: Schematic comparison between the SIMO and the MIMO radars.

1.2 General Review of MIMO Radar

1.2.1 Origins of MIMO Architectures

MIMO stands for multiple-input multiple-output. The notion of MIMO radar simply refers to multiple radiating and receiving sites. Beside the multiple-inputs multiple-outputs architecture, the idea of MIMO starts from *diversity* [5]. According to *diversity*, receiving antenna elements should receive different information and then improve the global performance of the system: quality of the link (in communication), detection

probability or localization accuracy in radar.

From the processing point of view, the MIMO radar allows to form the transmission diagram “after the fact" through DBF on receive. In a way, in continuity with the earlier coming up of the Tx phased array, the MIMO concept achieves the outcome of the “digitization" of the radar (*i.e.* software controlled).

The MIMO is not a new concept, and has been developed for communication applications (*e.g.* WiFi), offering a lot of advantages to mitigate propagation effects because of multipath and fading environments. The use of MIMO in the radar context is more recent. The first introduction of a MIMO radar architecture, even if not called MIMO then, is probably the RIAS invented in ONERA at the end of the 80's [6]. A demonstrator made of two concentric circular arrays was also built to demonstrate the MIMO capacity. Research works have followed, for example the RIAS of Thomson-CSF (now Thales) [7], and a similar radar in China, used for early warning surveillance and tracking [8].

1.2.2 Description of the MIMO Concept

Contrary to the SIMO radar, the MIMO radar allows the transmission of different waveforms on each antenna element, simultaneously, resulting in a antenna diagram which is not focused in one unique direction. It consists thus of space-time coding on transmit for each individual transmitter. Figure 1.5 illustrates the differences between SIMO and MIMO configurations. Once captured in the receiver, these waveforms can be extracted by a set of MF, each one adapted to a specific waveform. Each of the extracted components contains the information of an individual transmitting path. The collected information is then processed together. It allows to recover the angular directivity of the whole Tx antenna.

There are two basic regimes of operation according to the literature:

- **Statistical MIMO radar:** the transmit array elements (and receive array elements) are broadly spaced, providing independent scattering responses for each antenna pairing. The diversity provided by the multiplicity in transmit and receive angles can be exploited to improve the detection performance. Benefits of spatial diversity enabled by using MIMO radar are discussed in [9] and [10].
- **Coherent MIMO radar:** the transmit array elements (and receive array ele-

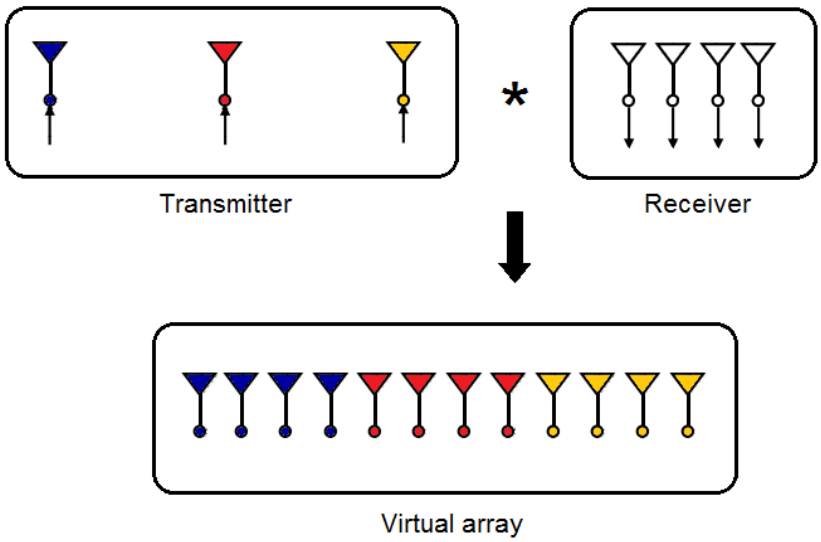

Figure 1.6: Illustration of the MIMO virtual array which is the convolution of the positions of the transmitting antenna elements (sparse array here) with the receiving antenna elements.

ments) are closely spaced so that the target is in the far field of the transmit (and receive) array. Here, it is assumed that the target's scattering response is the same for each antenna pair, up to some small delay. The estimation performance improvement can be dramatic when optimized sparse arrays are used. In some sense, the performance of the MIMO systems can be characterized by a virtual array constructed by the convolution of the locations of the transmit and receive antenna locations, as illustrated on fig. 1.6. Consequently, a filled virtual array can be constructed by using sparse constituent arrays. In principle, with the same number of antenna elements, this virtual array can be much larger than the array of an equivalent traditional system. Thus, with comparison with the equivalent physical array, the MIMO system will have much better intrinsic spatial resolution at a small cost [11] [12].

An extended description of the MIMO radar concept can be found in [13]. In this thesis, we will focus on the second configuration.

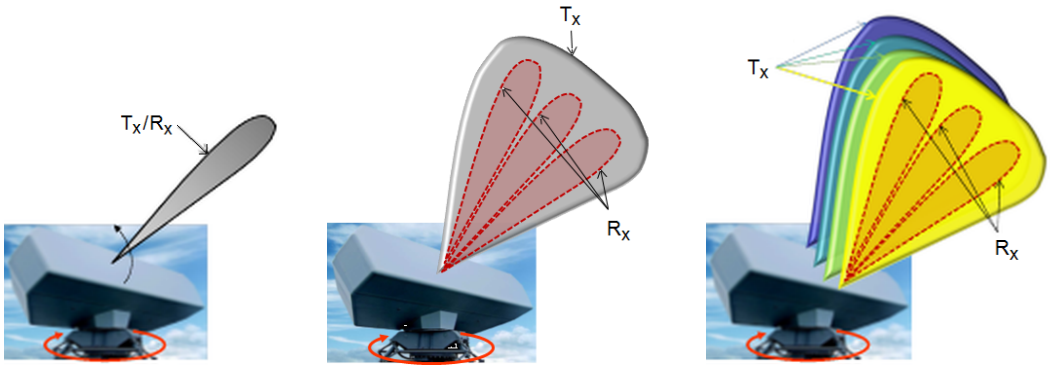

(a) Scanning pencil beams. (b) Wide beam on transmit. (c) Coded multiple simultaneous beams on transmit.

Figure 1.7: Radar transmit (Tx) and receive (Rx) beam strategies.

1.2.3 Performance Enhancements

It has been shown that the co-located MIMO radar systems have many advantages such as excellent clutter interference rejection capability [14] [15], improved parameter identifiability [16], and enhanced flexibility for transmitting beampattern design [17] [18]. These advantages lead to improved target detection performance and improved angle estimation accuracy. As an illustration, we propose to give a performance comparison between 3 transmission configurations [12]:

- **SIMO radar – pencil beam on Tx** (fig. 1.7a): electronic scanning of a focused beam to successively explore the directions of interest. This beam pattern is typically obtained by a linear law for the transmitter phases. The digital reception pattern is focused in the same direction as the instant Tx beam.
  - *Angular resolution*: optimal, since the Tx beam is narrow.
  - *Space covering*: limited, since only a small portion of the space is illuminated at once. It could be of strong issue in case of critical scenario, *e.g.* the presence of numerous targets to track.
  - *SNR*: optimal, since the transmitted energy is concentrated to a limited sector of the space.
- **SIMO radar – wide beam on Tx** (fig. 1.7b): broadened beam in elevation on transmit. This beam pattern can be obtained by a quadratic law for the transmitter phases. Digital pencil patterns for the reception can be set in parallel in

different directions of the instrumented sector.

  - *Angular resolution*: degraded, since the Tx beam is wider than the previous configuration.
  - *Space covering*: enhanced, since the broad beam allows longer illumination time. It also induces a longer time on target and thus an enhanced Doppler resolution.
  - *SNR*: degraded, in comparison with the previous configuration, since the energy is transmitted in a large angular sector. Moreover, the sensitivity to interferences from other directions is increased.

- **MIMO radar** (fig. 1.7c): from a radar functional point of view, everything appears as if all directions were explored simultaneously by coded focused beams.
  - *Angular resolution*: optimal, since we recover the Tx directivity of the SIMO focused beam through DBF on receive. It is also possible to take benefit of the MIMO flexibility by forming specific beams, simultaneously, according to different radar functions (surveillance, target tracking and characterization, jamming mitigation). This is the ubiquity ability of the MIMO radar.
  - *Space covering*: optimal, since a wide angle domain is illuminated during the pulse transmission (isotropical radiation).
  - *SNR*: degraded, in comparison with the SIMO focused beam, since the energy is transmitted in a large angular sector.

Eventually, the coherent co-located MIMO is the only mean for a radar to obtain both an ultra-wide angular beam on transmit (more than the classical factor 3 or 4 compared to the focused beamwidth) and good mainlobe and sidelobe properties (beamwidth, ripple, sidelobe level). A wide beam is of crucial interest for instance for transitory targets (helicopter pop-up, periscope), or slow small-moving targets in competition with clutter where longer illumination times are needed for Doppler separation.

As examples of possible applications for MIMO radar systems, we can cite works on radar imaging taking advantage of the better spatial resolution, like through-the-wall detection [19] and 2D imaging of an environmental ground scene [20]. The MIMO enhanced flexibility for transmitting beampattern design is illustrated in [21] through

a demonstration of ultrasound hyperthermia treatment of breast cancer that enables to focus the transmitted energy on a specific region of the flesh. In the context of ground surveillance from an aircraft, we can cite the extension of STAP (Space Time Adaptive Processing) to MIMO-STAP that provides an increased antenna directivity without the use of a full dense antenna [5]. In the context of maritime over-the-horizon surveillance, MIMO configurations in High Frequency Surface Waves Radars (HFSWR) can overcome the limited directivity in azimuth and limited bandwidth of the conventional radars [22].

1.3 MIMO Waveform Considerations

1.3.1 The MIMO Ambiguity Function

The ambiguity function represents the equivalent spread energy in range/Doppler/angle domains and so captures some of the inherent resolution properties of a radar system. Early work on radar ambiguity has been done in the 60's [23]. The MIMO ambiguity function has been extensively defined and studied in [24]. We introduce here the general model of [25].

We consider a transmitting array of M elements (antennas or sub-arrays) and a receiving array of N antennas. The position of the m^{th} element of the transmitting array is denoted by the vector $\mathbf{x}_{\text{Tx},m}$, while the position of the n^{th} element of the receiving array is denoted by the vector $\mathbf{x}_{\text{Rx},n}$. We assume that the transmitting and receiving arrays are co-located.

Denoting by $s_m(t)$ the waveform assigned to the m^{th} antenna, the signal transmitted by the array is:

$$s(t,\theta) = \sum_{m=1}^{M} g_{\text{Tx},m}(\theta)\, e^{j\mathbf{x}_{\text{Tx},m}^T \mathbf{k}(\theta)}\, s_m(t) \tag{1.4}$$

where θ is the considered direction, $\mathbf{k}(\theta)$ the wave vector, $g_{\text{Tx},m}(\theta)$ the gain of transmitting element m in direction θ. The notation $(\cdot)^T$ represents the matrix transpose.

For a target in direction θ_t with delay τ_t and Doppler ν_t, the signal received on the n^{th}

antenna is:

$$s_n^r(t) = g_{\mathrm{Rx},n}(\theta_t)\, e^{j\mathbf{x}_{\mathrm{Rx},n}^T \mathbf{k}(\theta_t)} \sum_{m=1}^{M} g_{\mathrm{Tx},m}(\theta_t)\, e^{j\mathbf{x}_{\mathrm{Tx},m}^T \mathbf{k}(\theta_t)} s_m(t-\tau_t)\, e^{j2\pi\nu_t t} \tag{1.5}$$

where $g_{\mathrm{Rx},n}(\theta)$ is the gain of receiving element n in direction θ.

The optimal coherent MIMO processing on receive, where we have skipped the antenna gains for simplicity, is given by (with $(\cdot)^*$ denoting the conjugate):

$$\begin{aligned} A_r(\tau,\nu,\theta) = & \overbrace{\left(\sum_{n=1}^{N} e^{-j\mathbf{x}_{\mathrm{Rx},n}^T \mathbf{k}(\theta)} \right)}^{\text{Beamforming on receive}} \times \overbrace{\left(\sum_{m=1}^{M} e^{-j\mathbf{x}_{\mathrm{Tx},m}^T \mathbf{k}(\theta)} \right.}^{\text{Beamforming on transmit}} \\ & \times \underbrace{\left. \int s_n^r(t)\, s_m^*(t+\tau)\, e^{-j2\pi\nu t}\, dt \right)}_{\text{Transmitter separation + range compression + Doppler processing}} \end{aligned} \tag{1.6}$$

Clearly, this optimal processing can be decomposed into three steps:

1. At each reception antenna, application of a MF to each transmitted waveforms (*i.e.* M matched filters applied to N received data, producing MN output data streams). The MF is known to maximize the output signal-to-noise ratio [1].

2. A transmission processing that permits to retrieve the transmission directivity.

3. A reception processing that corresponds to the usual beamforming step.

Inserting the expression of $s_n^r(t)$ in (1.6) and replacing $\nu - \nu_t$ by ν and $\tau - \tau_t$ by τ provides the so-called MIMO ambiguity function:

$$\begin{aligned} A(\tau,\nu,\theta,\theta_t) = & \left(\sum_{n=1}^{N} e^{j\mathbf{x}_{\mathrm{Rx},n}^T (\mathbf{k}(\theta_t) - \mathbf{k}(\theta))} \right) \times \\ & \sum_{m=1}^{M} \sum_{m'=1}^{M} e^{j\mathbf{x}_{\mathrm{Tx},m'}^T \mathbf{k}(\theta_t) - j\mathbf{x}_{\mathrm{Tx},m}^T \mathbf{k}(\theta)} \int s_{m'}(t)\, s_m^*(t+\tau)\, e^{-j2\pi\nu t}\, dt \end{aligned} \tag{1.7}$$

which is a function of four parameters (delay, Doppler, target angle, reception angle) if only one angle direction (azimuth of elevation) is considered. If two directions are considered, it becomes a function of six parameters.

Note that the waveform orthogonality is achieved when:

$$\int s_m(t)\, s_k^*(t+\tau)\, dt = \delta_{mk}(\tau) \tag{1.8}$$

with $\delta_{mk}(\tau) = \begin{cases} \delta(\tau) & \text{if } m = k \\ 0 & \text{otherwise} \end{cases}$

Note that $\delta(\tau)$ is the Dirac delta function.

We will now introduce a vectorial notation for the expressions. Concatenating signal $s_n^r(t)$ from all receiving antennas in a single vector $\mathbf{s}^r(t) = \left[s_1^r(t), s_2^r(t), \cdots, s_N^r(t)\right]^T$, and transmitted waveforms $s_m(t)$ in a single vector $\mathbf{s}(t) = [s_1(t), s_2(t), \cdots, s_M(t)]^T$, we get:

$$\mathbf{s}^r(t) = \mathbf{s}_{\mathrm{Rx}}(\theta_t)\left(\mathbf{s}_{\mathrm{Tx}}(\theta_t)^T\, \mathbf{s}(t-\tau_t)\, e^{j2\pi\nu_t t}\right) \tag{1.9}$$

where $\mathbf{s}_{\mathrm{Tx}}(\theta)$ and $\mathbf{s}_{\mathrm{Rx}}(\theta)$ are the steering vectors for transmission and reception, respectively, whose m^{th} and n^{th} elements, respectively, are given by:

$$\left(\mathbf{s}_{\mathrm{Tx}}(\theta)\right)_m = g_{\mathrm{Tx},m}(\theta)\, e^{j\mathbf{x}_{\mathrm{Tx},m}^T\mathbf{k}(\theta)} \quad \text{and} \quad \left(\mathbf{s}_{\mathrm{Rx}}(\theta)\right)_n = g_{\mathrm{Rx},n}(\theta)\, e^{j\mathbf{x}_{\mathrm{Rx},n}^T\mathbf{k}(\theta)} \tag{1.10}$$

The ambiguity function can be rewritten the following way (with $(\cdot)^H$ denoting the conjugate transpose):

$$\begin{aligned} A(\tau,\nu,\theta,\theta_t) = &\left(\mathbf{s}_{\mathrm{Rx}}^H(\theta)\,\mathbf{s}_{\mathrm{Rx}}(\theta_t)\right)\times \\ &\mathbf{s}_{\mathrm{Tx}}^T(\theta)\int \mathbf{s}(t)\,\mathbf{s}^H(t+\tau)\, e^{-j2\pi\nu t}\, dt\, \mathbf{s}_{\mathrm{Tx}}^*(\theta_t) \end{aligned} \tag{1.11}$$

Since the reception processing is completely decoupled in (1.11), we can avoid to consider the digital beamforming on receive. Besides, for applications where the Doppler effect is negligible within the pulse duration, it can be decoupled in (1.11) too. This is the case for instance for the detection of slow moving targets. Thus, the expression can be simplified further to:

$$A_t(\tau,\theta,\theta_t) = \mathbf{s}_{\mathrm{Tx}}^T(\theta)\int \mathbf{s}(t)\,\mathbf{s}^H(t+\tau)\, dt\, \mathbf{s}_{\mathrm{Tx}}^*(\theta_t) \tag{1.12}$$

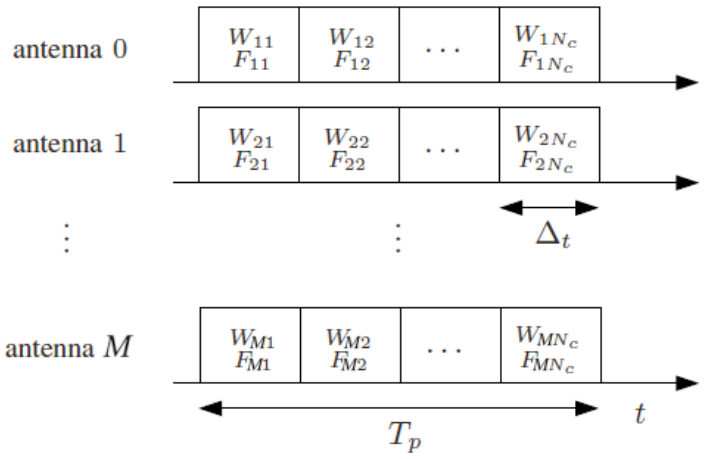

Figure 1.8: General intrapulse coding scheme.

1.3.2 Intrapulse Coding Formalism

We present here the general formalism for intrapulse coding of MIMO waveforms of [25]. We consider that the MIMO radar transmits a pulse train. Each antenna transmits its specific waveform during one pulse, and we assume here that this waveform is identical from pulse to pulse. Therefore, the orthogonality between the different waveform arises only from the intrapulse coding.

Each pulse can be decomposed into N_c times slots or “chips". To each time slot and each antenna can be assigned specific phases and frequencies. We therefore propose the general model for intrapulse coding:

$$s_m(t) = \sum_{p=1}^{N_c} W_{mp} e^{j2\pi F_{mp} t} u\left(t - p\Delta_t\right) \tag{1.13}$$

where W_{mp} represents the phase offset and F_{mp} represents the frequency associated to the signal transmitted by antenna m during the time slot p. The parameter Δ_t represents the duration of one chip, and $u(t)$ represents the elementary waveform, that can be for instance a simple rectangular pulse or a linear frequency modulated signal – called “chirp" in the following. The duration of the waveform (actually the pulse length) is $T_p = N_c\Delta_t$. The general expression (1.13) permits to design at the same time waveforms with phase and/or frequency coding. The general scheme of such a code is represented in fig. 1.8. Note that the number of chips N_c can be set as desired depending on the signal to transmit. For instance, if the transmitted pulse is a

chirp, we can set $N_c = 1$ and use a chirp as elementary pulse $u(t)$.

Using the vector notation, the transmitted signal can be expressed as:

$$\mathbf{s}(t) = (\mathbf{W} \odot \mathbf{F}(t))\,\mathbf{u}(t) \tag{1.14}$$

where $\odot$ denotes the Hadamard product, $\mathbf{W}$ and $\mathbf{F}(t)$ are matrices of size $M \times N_c$ whose elements are provided by W_{mp} and $e^{j2\pi F_{mp} t}$, respectively, and

$$\mathbf{u}(t) = [u(t),\quad u(t-\Delta_t),\quad \cdots,\quad u(t-(N_c-1)\,\Delta_t)]^T \tag{1.15}$$

1.3.3 MIMO Waveform Design

For the implementation of practical MIMO radar systems, the choice of a proper waveform family is of crucial importance. In addition to the general requirements for radar waveforms like good range resolution, low sidelobes, etc., MIMO radar waveforms should also present good orthogonality properties. Nonetheless, in practice, it is not possible to find a waveform family that perfectly satisfies these properties.

Many works of the literature have proposed quasi-orthogonal waveform for MIMO radar applications. Nevertheless, only a very few number of works, *e.g.* [26], gives a comprehensive evaluation and comparison of all types of MIMO radar waveforms. In this section, we give a brief overview of MIMO radar waveforms based on the latterly-mentioned publication and extended in [27], while still using the formalism of [25].

TDMA

An intuitive and simple way to operate orthogonality through Time Division Multiple Access (TDMA) is the alternative transmitting where the transmit antennas are switched alternatively from pulse to pulse. Nevertheless, with this approach the transmission capabilities of the antennas are not fully utilized and it induces significant loss of transmit power.

The circulating MIMO waveform is a more efficient scheme. In this configuration, the waveform transmitted by each antenna is a time-circulating copy of the same signal, where the circulating time step should be equal to $1/B$ – where B is the signal bandwidth – to satisfy the orthogonality requirement. We take the circulating chirp as

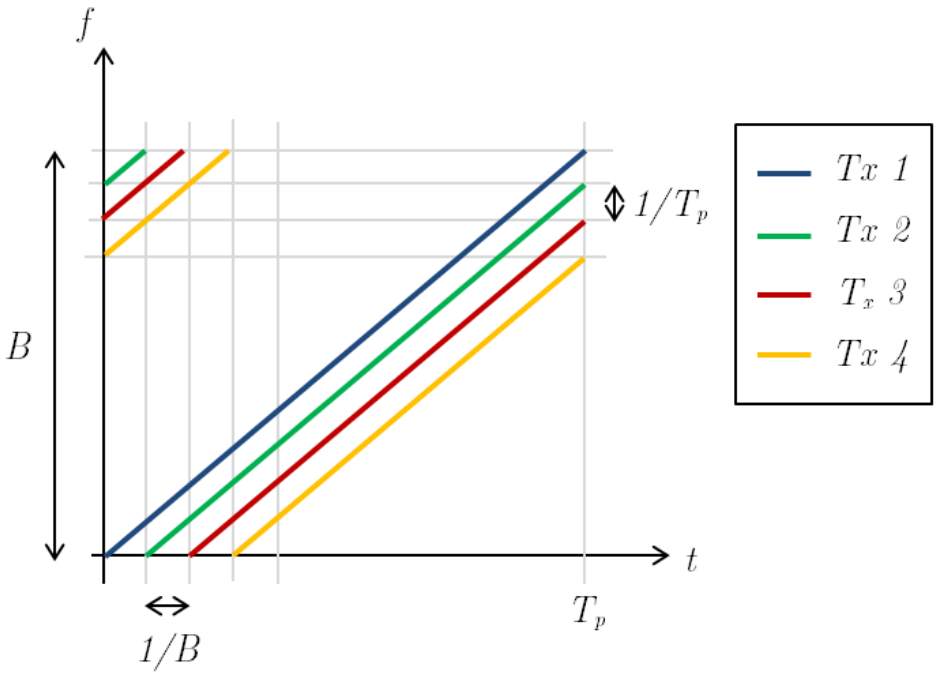

(a) Illustration of the waveform family.

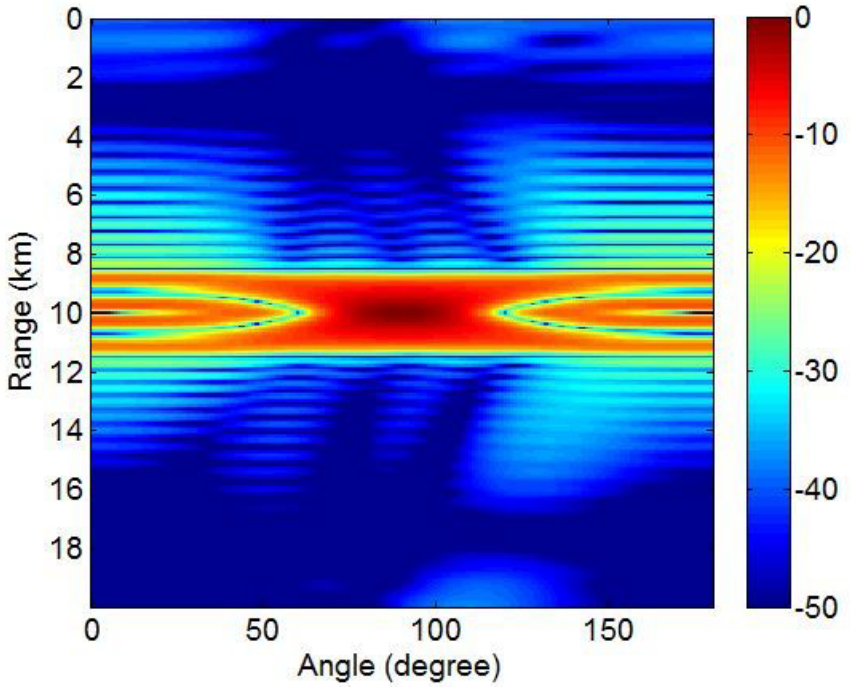

(b) Range-angle ambiguity function.

Figure 1.9: TDMA waveform (circulating chirp).

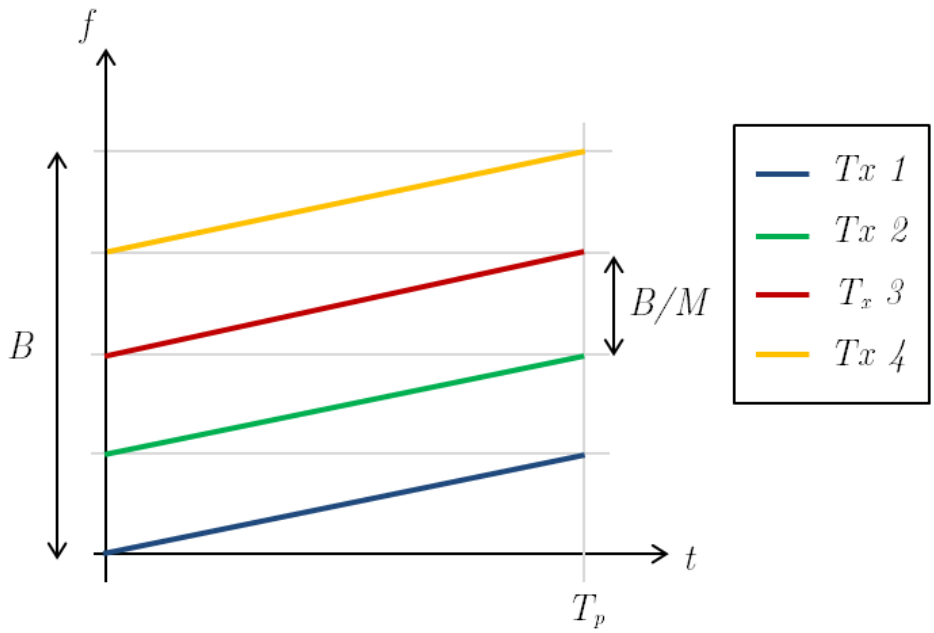

(a) Illustration of the waveform family.

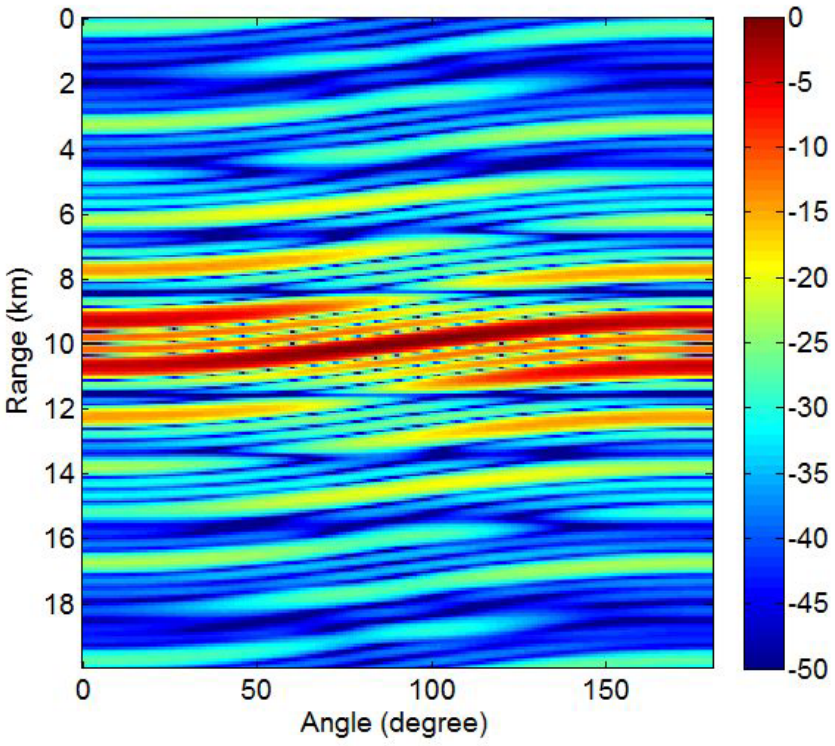

(b) Range-angle ambiguity function.

Figure 1.10: FDMA waveform (chirp transmission on each frequency sub-band).

an example, which is illustrated in 1.9a. This scheme can be expressed through:

$$\mathbf{W} = \mathbf{1}_{M \times N_c} \quad \text{and} \quad \mathbf{F}(t) = \mathbf{C}(\mathbf{s}_F(t)) \tag{1.16}$$

where $\mathbf{C}(\mathbf{s}_F(t))$ is the circulant matrix (*i.e.* each line is the previous line shifted by one element) built from vector

$$\mathbf{s}_F(t) = \left[1, \quad e^{j2\pi \frac{B}{N_c} t}, \quad \cdots, \quad e^{j2\pi\left(\frac{B}{N_c}-1\right)t}\right] \tag{1.17}$$

and $u(t)$ is a chirp with a frequency span of B/N_c.

Figure 1.9b extracted from [27] exhibits the simulated range-angle ambiguity function of the circulating chirp waveform family for $M = 4$ antennas (with half-wavelength inter-element spacing), with a total bandwidth $B = 400$kHz, and with a target at 10 km and 90 degrees. Let us notice that for that specific code, the transmission directivity and the very low range sidelobes have been obtained at the price of a loss in the range resolution.

Note that different signals can be chosen as circulating waveform. As an example, another possibility is to use a phase code signal. The corresponding expression is:

$$\mathbf{W} = \mathbf{C}(\mathbf{s}_W) \quad \text{and} \quad \mathbf{F}(t) = \mathbf{1}_{M \times N_c} \tag{1.18}$$

where $\mathbf{s}_W$ is a signal code of N_c chips.

FDMA

This strategy corresponds to Frequency Division Multiple Accesss (FDMA) in digital communications and it corresponds to the case where all antennas transmit signals at different frequencies. The corresponding expression is:

$$N_c = 1, \quad \mathbf{W} = \mathbf{1}_{M \times 1} \quad \text{and} \quad \mathbf{F}(t) = \left[1, \quad e^{j2\pi\Delta_f t}, \quad \cdots, \quad e^{j2\pi(M-1)\Delta_f t}\right]^T \tag{1.19}$$

where Δ_f is a frequency interval larger or equal to the signal bandwidth, *i.e.* $\Delta_f \geq B_u = B/M$, with B_u the bandwidth of $u(t)$, as illustrated in fig. 1.10a with the transmission of chirp on each individual frequency band. Clearly, the transmitted signals are orthogonal since they do not share the same frequency domains. But this is not sufficient to get perfect delay/angle decoupling. Indeed, if the initial phases are the

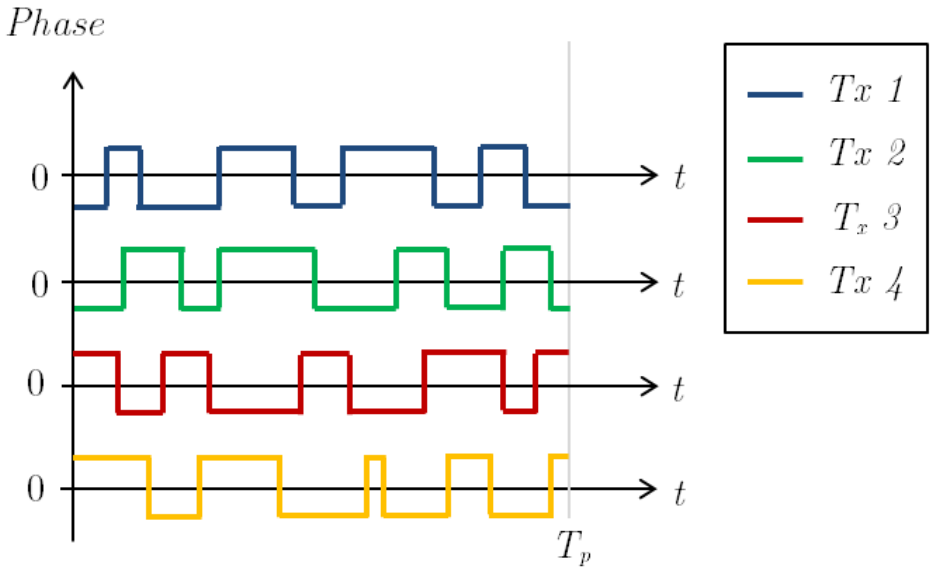

(a) Illustration of the waveform family.

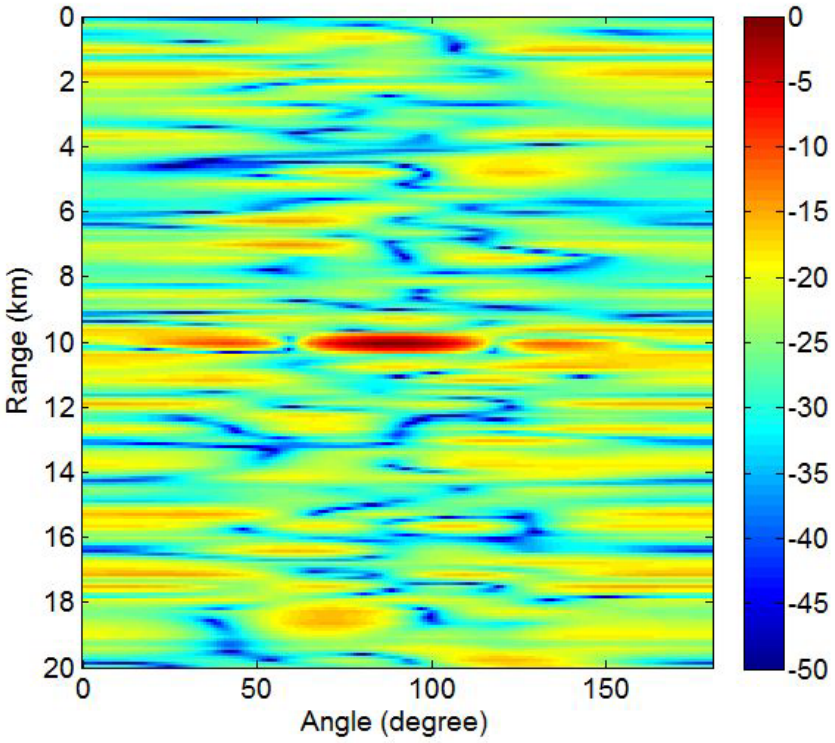

(b) Range-angle ambiguity function.

Figure 1.11: CDMA waveform.

same for the different signals, then the signal transmitted by the array at a given time instant t is the vector

$$\left[1, \quad e^{j2\pi\Delta_f t}, \quad \cdots, \quad e^{j2\pi(M-1)\Delta_f t}\right]^T \tag{1.20}$$

which corresponds to a direction $\theta = \text{asin}\left(2\Delta_f t\right)$ when considering a linear array with half-wavelength element spacing. Therefore, this coding scheme resorts to a fast sweeping of the different angular directions during the pulse, thus leading to a range-angle coupling along the line $\tau = 1/\left(2\Delta_f\right)\sin(\theta)$. This coupling can be easily seen in fig. 1.10b extracted from [27] that presents the MIMO ambiguity function for the FDMA coding scheme and same parameters as the previous section.

CDMA

For Code Division Multiple Access (CDMA) schemes, the perfect orthogonality cannot be obtained but it is possible to consider code families that present features close to this orthogonality. For phase codes, the number of chips N_c is set so to provide a given desired bandwidth. The frequency matrix is simply set to $\mathbf{F}(t) = \mathbf{1}_{M\times N_c}$ while the phase matrix $\mathbf{W}$ is provided by the considered phase codes. An illustration with binary-phase codes is given in fig. 1.11a.

The good range and angle resolutions are at the price of high range sidelobes, depending on the cross-correlation property of the code sequence. The latter effect can be easily seen in fig. 1.11b extracted from [27] that presents the MIMO ambiguity functions for a CDMA coding scheme and same parameters as the previous sections.

Many different phase codes have been defined. As examples, we can cite three sequences schemes designed in digital communications that can be often encountered in the literature:

- Barker sequences [28], which are sequences of binary values $+1$ and -1 (or binary phases 0 and π), and their autocorrelation sidelobes levels are at most 1.
- Hadamard (also called Walsh) sequences [29], which are easy to generate and are frequently used in wireless communications.
- Gold sequences [30], which exhibit very good auto- and cross-correlation properties (for periodic correlations though).

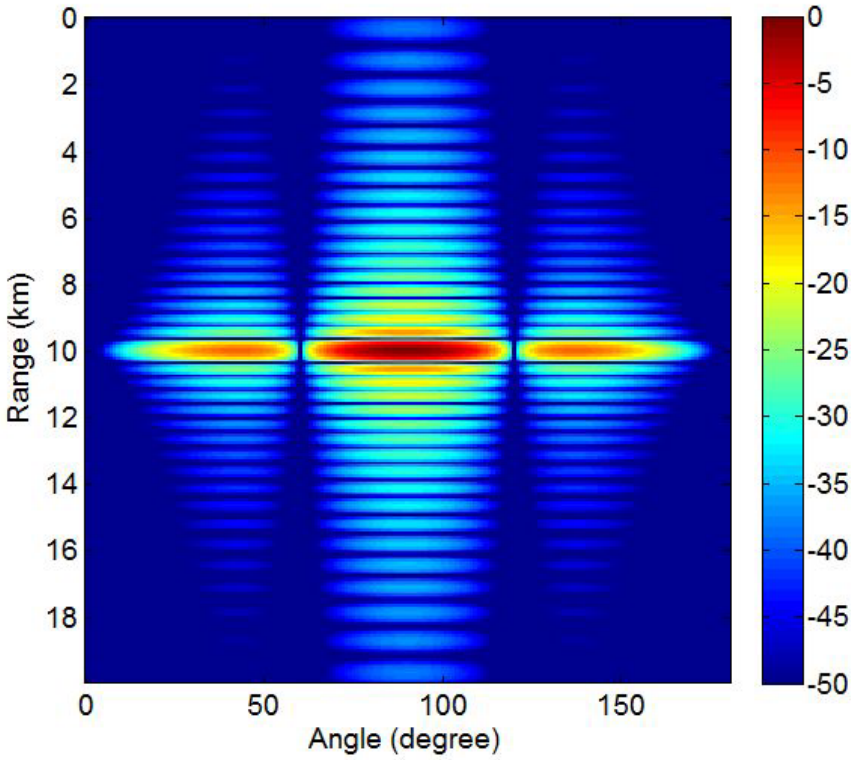

Figure 1.12: DDMA waveform: range-angle ambiguity function.

DDMA

In contrast to the waveforms presented above, Doppler Division Multiple Access (DDMA) is an inter-pulse coding scheme (“slow-time" coding). In this configuration, the signal spectrum of each transmitter is shifted slightly, so that the waveforms can be separated in Doppler domain. The resulting ambiguity function with a chirp waveform and same parameters as the previous section is given in fig. 1.12 extracted from [27]. The DDMA waveform can achieve very good performance, but the requirement on the PRF is particularly constraining, since it must be larger than $2M$ times the maximum Doppler frequency of the targets, were M is the number of transmitters.

1.4 Outline of the Thesis

1.4.1 Problem Statement

As previously developed, MIMO radar architectures are of specific interest for various applications since the theory about MIMO radar shows promising performance improvement possibilities (higher spatial resolution, improved parameter identifiability, etc.). Nevertheless, most of the cited works of section 1.2 (*e.g.* [9] and [18]) were based on the assumption of ideal orthogonal waveforms. In most cases, this assumption was implicit. In other cases, studies explicitly mentioned that in order to be able to separate the waveforms on reception side, the MIMO radar theory imposes that they have to be so defined that they are orthogonal with each other.

But in reality, the ideal orthogonal MIMO waveform does not exist. Most of the cited works of section 1.3 (*e.g.* [26] and [25]) underlined the fact that the model of perfect orthogonality is too conservative and that the effects of the practical non-ideal orthogonal waveforms were not addressed in the previously-mentioned literature. These works pointed out that the choice of a proper waveform family is therefore of crucial importance for the implementation of practical MIMO radar systems. For this purpose, some of these works identified and compared MIMO waveforms that can be suitable for practical implementation, as it was summarized in section 1.3.3. They addressed the advantages of each types of waveform, but also their limits that come in return, like a lack of orthogonality and/or parameters coupling.

These papers usually considered that “there is no free lunch" [27] and that the choice of the waveform has to be adapted to the application. In return, trade-offs have to be conceded in order to preserve specific performances. Consequently, loss on other performances (transmit power, range sidelobes, etc.) is not avoided which may result in degraded capacities, like a worse ability to detect targets, or less spatial resolution on target. Finally, this situation may not be satisfying in practice, especially for critical operational contexts where performances are expected to reach high levels on every front.

Therefore, the global problematic of this thesis can be formulated the following way: **how to overcome the MIMO waveform intrinsic imperfections so as to be able to implement MIMO radar architectures in practice with enhanced performance and acceptable operational constraints?**

1.4.2 Existing Work Addressing The Problem

Waveform Optimization

Some works of the literature propose to design the MIMO waveform so to approach the ideal orthogonality property or specific performance. In [31], [32] and [33], time series are designed for good waveform auto- and cross-correlation properties and range estimation characteristics using simulated annealing and genetic algorithms. In [34], Doppler characteristics are also considered. Waveform optimization in terms of maximizing the mutual information is discussed in [35], given knowledge of the wide-sense-stationary target response covariance structure. Discussions on optimization of inter-transmitter waveform correlation are given in [36] and [37].

Finally, the cited techniques usually enhance the performance on one front only, or with consequent trade-offs on other fronts. Note that the degrees of freedom, even if greater than for the SIMO radar, are not sufficient to allow ideal performance for each set of range-angle-Doppler hypothesis. Besides, for the case of the phased codes, the proposed design algorithms allow a performance gain which is limited (*e.g.* 3 dB gain on cross-correlation peak for the CAN sequence proposed in [32] compared to Hadamard sequences).

Adaptive Processing

In classical processing, the pulse compression is based on MF which is defined so to optimize the signal-to-noise ratio (SNR) only, without consideration of other properties (sidelobes suppression, etc).

Some works of the literature propose adaptive target estimation techniques which aims at improving the performance of the MF. We can cite high-resolution techniques like Capon (*e.g.* estimation of direction of arrival in [21]) or MUSIC (*e.g.* mitigation of clutter return in [11]), both based on ℓ_2-norm minimization. For the implementation of such techniques, some attention must be paid to the efficiency of the covariance matrix which needs to be estimated on a sufficient number of training data, and in many situation, this condition is not fulfilled. To the contrary, the Adaptive Iterative Approach (IAA) gives results equivalent to Capon method with only a very small number of training data [38], but at the price of consequent computation complexity, making it difficult to implement in practical operation. Other techniques are based on

ℓ_1-norm minimization, like the compressed sensing detectors designed in [39]. It can give interesting performance but the algorithm is complex and difficult to implement. Besides, note that these adaptive techniques are likely to present more sensitivity than the MF to unexpected signal distortions.

We can also cite some other works which focus on optimal filter computation (*e.g.* mismatched filter optimization for phase codes in [40]). Similar to the limitations of waveform optimization approaches, they can present specific enhanced performances but usually restricted to a limited domain.

1.4.3 Objectives of the Thesis Work

The thesis work is based on the consideration that the waveform design has reached its limits and that the efforts have to be put on the processing, even with “imperfect" MIMO waveforms. In this way, the thesis work will consist in proposing and validating processing schemes for MIMO radar signals that can overcome the MIMO waveform intrinsic imperfections in practical implementations. The objective is to go beyond the initial performance of the MF, not only in theory but also in the real world. With “real world", we mean that these processing schemes should be implementable in realistic operational contexts, in particular by taking into account the processing computational complexity, the needed number of training data and the sensitivity to signal distortions. The work will also consist in confronting the proposed processing schemes to the radar hardware imperfections through experiments in real conditions.

In **CHAPTER 2**, the work will consist in studying and comparing the intrinsic performance of each type of waveform in order to select one whose drawbacks are expected to be compensated with a specific processing at reception. This first study will be based on the estimated Cramér-Rao bounds and factors of merit applied on the ambiguity functions of each waveform family.

In **CHAPTER 3**, the work will consist in defining processing methods adapted to the selected waveform for the compensation of the waveform imperfections impact on performance. These methods will have to satisfy operational conditions related to computational complexity and greed on training data. The proposed techniques will be compared to existing approaches – like IAA – that have complexity limitations but provide quasi-optimal performance in target detection.

In **CHAPTER 4**, the work will first consist in evaluating the impact on performance of signal distortions possibly issued from hardware imperfections. Then, based on the observation that MIMO radar architectures offer interesting flexibility for calibration and system monitoring, a *a posteriori* digital calibration will be proposed.

In **CHAPTER 5**, the work will consist in defining and setting up experiments with a MIMO radar capable platform in order to evaluate the performance of the proposed processing schemes in real conditions. We will depict how the signals are processed from the raw data to the final detection information, and also where the encountered signal distortions originate from in order to explain the obtained results.

It is worth mentioning that in the thesis work, the study will relates to the co-located MIMO radar. The practical implementations will concern especially ground-based radars for air target detection – even if extension to other kinds of radar is possible. This type of radar typically transmits in the S band (2-4 GHz), based on considerations like the size of the antenna, the possible range, and the target localization precision. Besides, the S-band surface radar testbed used in this work will be extensively described in chapter 3.

2 The Phase Codes as MIMO Waveforms: Motivation and Challenge

2.1 Introduction

The central objective of this chapter is to focus on phase codes as MIMO waveforms in order to show that they are good candidates for improved MIMO radar performance, or more precisely, that they can provide optimal performance in target detection once their drawbacks are mitigated. First, we will qualify precisely their merits but also their limitations in term of target detection, and we will make the comparison with other types of waveform. We will base on characteristics of the different types of waveform provided by the literature but also on factors of merit we will specially propose here. The main factors of interest are the spatial resolution (range and angle) and the ability to reject interferences. Secondly, we will introduce the signal model considered for this thesis work, and based on that, we will depict the origin of the high level of undesired sidelobes, which is the main reluctance for the use of phased codes in MIMO radar applications. We will then exhibit the impact of these sidelobes on target detection and describe how it leads to performance degradation.

Note that we consider the different phase codes as a whole, since they have similar properties, especially the inevitable lack of orthogonality which is the source of sidelobes in the range/angle plane. The design – optimized, or not – of the code sequences does only change the magnitude of these sidelobes. Here, we take the Gold codes as representative MIMO waveforms of the CDMA waveform type.

Table 2.1: Comparison of general performance of MIMO waveforms.

	Merits	**Limitations**	**Possible applications**
TDMA – Alternative transmitting	Good orthogonality, low range/Doppler sidelobes, simple to implement	Loss of transmit power, artefacts in angle-Doppler domain	Low-power radar for short-range detection
TDMA – Circulating chirp	Good orthogonality, Ultra low range/Doppler sidelobes	Loss of range resolution, artefacts in angle-Doppler domain	All, if M-times larger bandwidth can be transmitted
FDMA	Good orthogonality, simple to implement	Raised sidelobes in the range-Doppler plane	Ground-based radar with many transmitters
CDMA	Approximate orthogonality, low Doppler sidelobes	High range sidelobes	All, if high range sidelobes can be accepted
DDMA	Good orthogonality, low range/Doppler sidelobes	Doppler ambiguities	Low-frequency radar

2.2 The Spatial Resolution as Motivation

2.2.1 Waveform Comparison From the Literature

Comparison on General Performance

An overview of MIMO radar waveform has been given in section 1.3.3. We refer here to the comparison between waveforms from [27] (itself partially based on [26]). The merits (“what we get"), the limitations (“what we paid for") and the possible applications of each type of waveform are listed in table 2.1.

Based on this information, it can be pointed out that many types of waveform do not seem to be suitable for practical implementation. We can cite for instance TDMA with alternative transmitting that could suffer from limited range-detection with some radar applications, or DDMA whose Doppler ambiguities can avoid compatibility with high frequencies. Nevertheless, when we focus on CDMA waveforms, it comes out

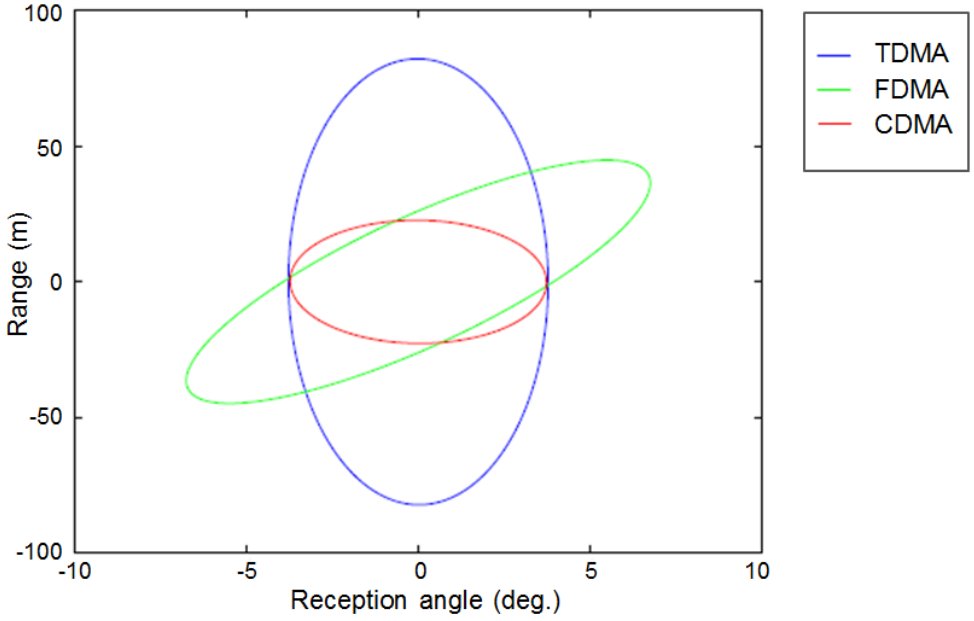

Figure 2.1: CLRB ellipses in range and reception angle for the TDMA, FDMA and CDMA waveforms.

that they are likely to be used for all applications as long as the high range sidelobes can be accepted, or even better, mitigated. If this can be done, this type of waveform will theoretically give quasi-optimal performance for target detection with respect to the provided resources (bandwidth, number of transmitters, etc.).

Comparison on Cramér-Rao Lower Bound

The coupling between parameters can be highlighted through the determination of the Cramér-Rao Lower Bound (CRLB) [4] which corresponds to the minimal possible bound that can be achieved for any estimator. Therefore, it can provide insight on the range/angle coupling and intrinsic spatial resolution for a given coding scheme. The CRLB is given by the inverse of the Fisher information matrix **J**, and in radar, each term J_{kl} of the matrix can be computed from the ambiguity function by [4]:

$$J_{kl} = -\mathrm{SNR}\frac{\partial^2 |A_e(\tau,\theta,\theta_t)|^2}{\partial\gamma_k\partial\gamma_l} \tag{2.1}$$

where γ_k is one of the parameters τ, θ, θ_t, and SNR is the signal-to-noise ratio at the output of the MIMO processing. The CRLB is computed in [25] for TDMA (circulating waveform), FDMA and CDMA (Gold codes), and presented in fig. 2.1. Clearly, the

shapes of the ellipses differ between the waveform types. Here again, one can notice the range/angle coupling for FDMA, and loss in range resolution for TDMA. Among these three waveforms, the CDMA is the one that produces the CRLB ellipse with the smallest surface, thus allowing the best estimate for single target estimation.

2.2.2 Waveform Comparison Based on Figures of Merit

Definition of Factors of Merit for Performance Analysis

The comparison based on general performance from the literature was principally made “qualitatively", *i.e.* based on visual considerations of the ambiguity function (width of the main lobe, level of sidelobes, etc.). We propose here to use factors of merit for the fine qualification of the performance of different waveforms. It should be possible to apply these factors on the ambiguity function since its characteristics are directly related to the operational performances of the radar. Here are some reasons for the introduction of these factors of merit:

- The display context makes that it could be difficult to extract the information: 3-dimension complex data cube, restricted visualization window, color discrimination ability, etc.
- It is sometimes difficult to visually make the comparison between specific characteristics, *e.g.* concerning the global energy of the sidelobes.
- We need tools to finely measure the performance evolution when small discrepancies occur. For instance, it is one of the objectives of this thesis to quantify the degradation of performance due to hardware imperfections which are likely to be impossible to notice to the naked eye.

Therefore, we would like to have to disposal analytic tools for a finer qualification of the waveform performance. These tools should be focused on the capacities of the waveform in target estimation resolution and rejection of interference signals.

Reference [41] proposes basic tools for performance analysis of space-time coding for active antenna systems (including co-located coherent MIMO systems). In particular, they define factors of merit for performance qualification that can be extracted directly from the ambiguity functions $|A_e(\tau,\theta,\theta_t)|^2$ (note that with the notation of this paper,

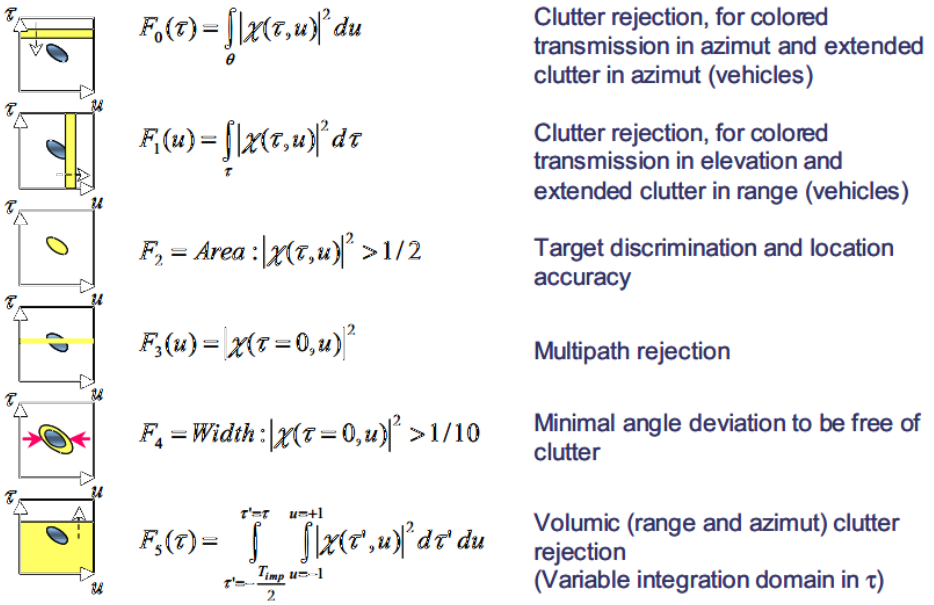

Figure 2.2: Definitions and objectives of the factors of merit defined in [41]. The ambiguity function is denoted by $\chi(\tau,u)$, the propagation time by τ, and the angle parameter by $u = \sin\theta$.

it is written $|\chi(\tau,u)|^2$ with u the angle parameter). The definition and the objective of each proposed factor of merit is given in fig. 2.2.

Clearly, these factors of merit are of interest, nevertheless, some limitations have been identified with respect to the context of the thesis, for instance:

- With the cumulative integrals (F_0, F_1, F_5), it is difficult to extract insight since it provides a plot which still needs interpretation, instead of a figure which can be directly compared with others.
- The information of the area of the main lobe (F_2) is an integration on both range and angle parameters. It could be more relevant to consider these parameters independently and therefore calculate range and angle resolution separately (note that angle resolution is taken into consideration in F_4 though).

In order to define precise factors of merit that can be directly applicable on the ambiguity function for computing comparative figures of merit, we have decided to focus on four main properties: range accuracy and angle accuracy (target discrimination

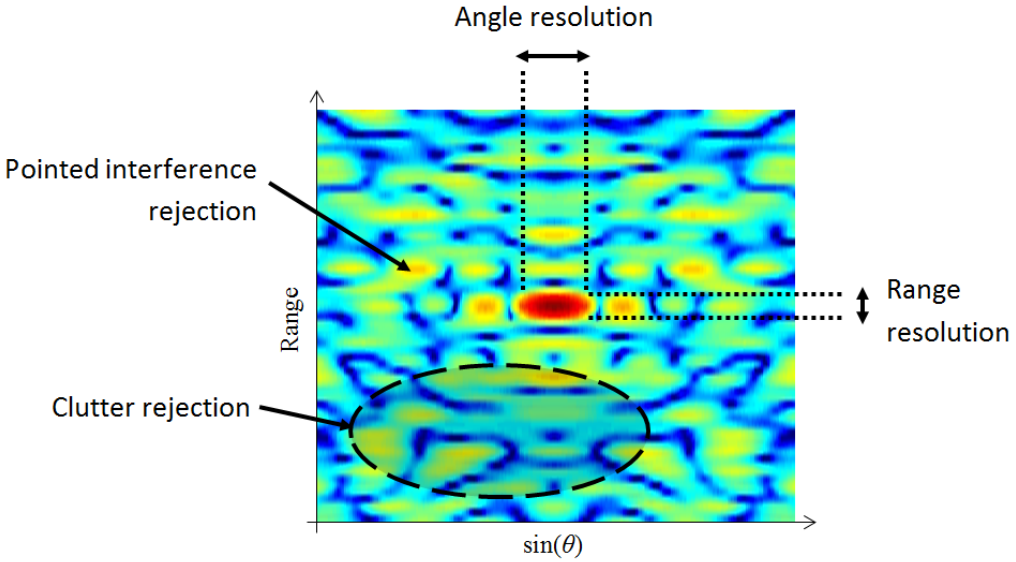

Figure 2.3: Illustrative representation of the four proposed factors of merit.

capacity), sensitivity to diffuse clutter, sensitivity to one isolated interference. An illustration which exhibits on what each factor of merit focuses is given in fig. 2.3. We give the analytic expressions of the factors of merit in the following:

- **Range Accuracy:**

  This factor represents the ability (or resolution) for target localization on range axis. It is defined as the range width at 3 dB of the rectangular frame that borders the main lobe, normalized by $c/(2B)$ (*i.e.* the range lower bound):

$$f_1 = \frac{\max\left\{r \;\middle|\; |A_e(r,\theta)|^2 > 1/2\right\} \;-\; \min\left\{r \;\middle|\; |A_e(r,\theta)|^2 > 1/2\right\}}{c/(2B)} \tag{2.2}$$

  When the figure computed by this factor is equal to 1, it means that the available resource (the allocated bandwidth here) is optimally used.

- **Angle Accuracy:**

  This factor represents the ability (or resolution) for target localization on angle axis. It is defined as the angle width at 3 dB of the rectangular frame that borders

the main lobe, normalized by $2/M$ (*i.e.* the angle lower bound):

$$f_2 = \frac{\max\left\{\sin\theta \;\middle|\; |A_e(r,\theta)|^2 > 1/2\right\} \;-\; \min\left\{\sin\theta \;\middle|\; |A_e(r,\theta)|^2 > 1/2\right\}}{2/M} \tag{2.3}$$

When the figure computed by this factor is equal to 1, it means that the available resource (the number and position of transmitters here) is optimally used.

- **Clutter rejection:**

  This factor of merit and the following one are inspired from metrics commonly used for SAR (Synthetic Aperture Radar) techniques [42]. This factor represents the sensitivity to a diffuse clutter. It corresponds to the Integrated Side Lobe Ratio (ISLR) and is defined as the ratio of the energy of a homogeneous clutter to the energy of the target. For a target of Radar Cross Section (RCS) of σ^2, we consider a constant diffuse clutter of energy equal to σ^2 per unitary surface S (equivalent to $S = 1$ m/s):

$$f_3 = \frac{\int \frac{\sigma^2}{S} |A_e(r,\theta)|^2 \; r dr d\theta}{\sigma^2 |A_e(r_t,\theta_t)|^2} \equiv \frac{\int |A_e(r,\theta)|^2 \; \frac{rdr}{S} d\theta}{|A_e(r_t,\theta_t)|^2} \tag{2.4}$$

- **Pointed interference rejection:**

  This factor represents the sensitivity to an isolated interference, *e.g.* another target. It corresponds to the Peak Side Lobe Ratio (PSLR) and is defined as the ratio of the peak value of the sidelobes to the peak value of the main lobe:

$$f_4 = \frac{\max\left\{|A_e(r,\theta)|^2 \;\middle|\; (r,\theta) \text{ outside the main lobe}\right\}}{|A_e(r_t,\theta_t)|^2} \tag{2.5}$$

Besides, it is worth noting that these four factors of merit are so defined that the lower the resulting figures of merit, the better the performance in detection.

Computation of the Figures of Merit and Comparison

For the application of the factors of merit, we have generated three types of waveform already mentioned:

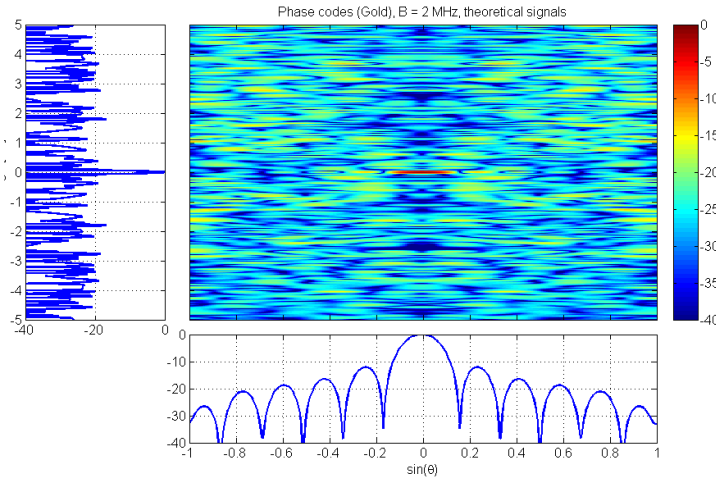

(a) Phase codes (Gold sequences).

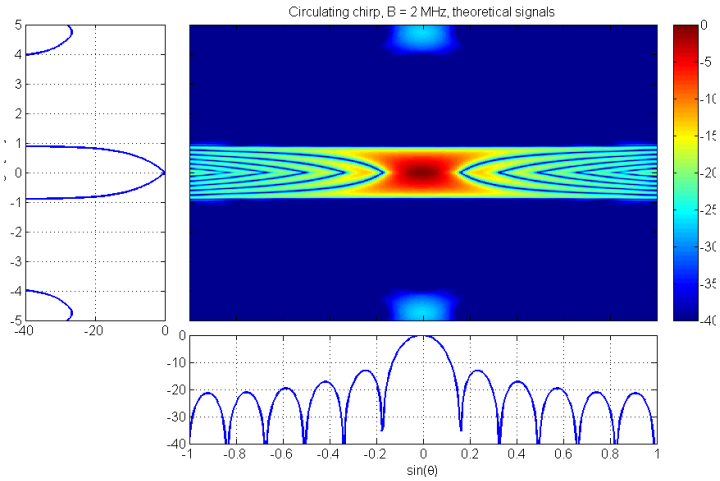

(b) Circulating chirp.

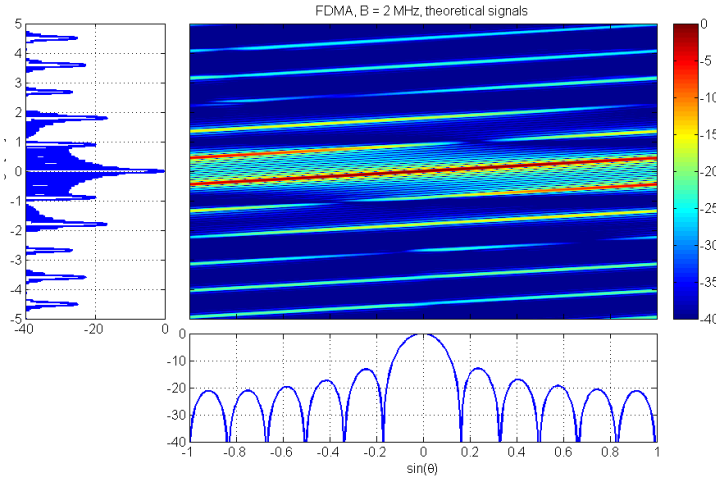

(c) FDMA.

Figure 2.4: Ambiguity functions (MF output) for different waveform families.

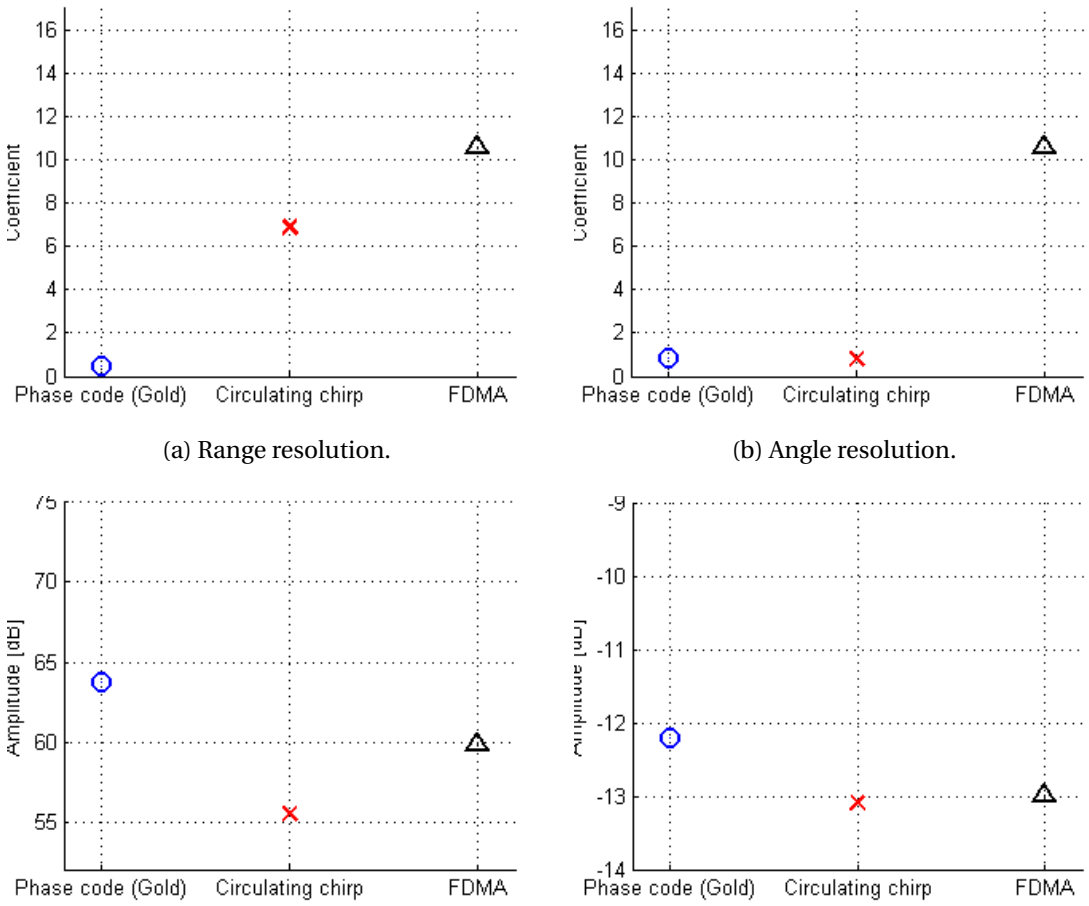

(a) Range resolution.

(b) Angle resolution.

(c) ISLR.

(d) PSLR.

Figure 2.5: Computed figures of merit for the four defined factors of merit qualifying the performances of the CDMA, TDMA and FDMA waveforms. Note that higher values mean worse performances.

- Circulating chirp (TDMA): a unique chirp with a $1/B$ incremental delay between one transmitter to the next one.
- FDMA: to each transmitter is allocated a section B/M of the entire bandwidth for the transmission of a chirp.
- Phase codes (CDMA): binary phase codes based on Gold sequences of $N_c = 127$ chips.

with the following values for the common parameters:

- Number of transmitters (ULA array): $M = 12$

- Total bandwidth: $B = 2$ MHz
- Target range: $r_t = 0$
- Target angle: $\theta_t = 0$

The resulting ambiguity functions are exhibited in fig. 2.4.

Based on these ambiguity functions, we have computed the four factors of merits. The resulting computed figures of merit are represented in fig. 2.5, making it possible to compare the performance of the different waveform families. We can now extract some information from these figures. Regarding the target localization accuracy (fig. 2.5a and 2.5b), the phase codes family has optimal range and azimuth resolutions ($c/(2B)$ and $2/M$, respectively). It is explained by the fact that the main lobe is similar to what can be obtained with a conventional radar in the same conditions (same bandwidth, same number of transmitters, etc.). As comparison considering the range resolution (fig. 2.5a), the circulating chirp and the FDMA families give around 7 and 11 times worse resolution, respectively, due to the spread of the main lobe on the range axis. Concerning the angle resolution (fig. 2.5b), the FDMA gives no angle accuracy due to the strong range/angle coupling (whereas the circulating chirp gives the same resolution as phase codes). With the MF only, the localization performances of the phase codes family are counterbalanced by worse performance for interference rejection due to its numerous sidelobes all around the main lobe. That explains why we get an ISLR (fig. 2.5c) around 4 dB worse than with the FDMA, and up to 9 dB worse than with the circulating chirp. Concerning the PSLR of -12 dB (fig. 2.5d), it can be deduced that the CDMA is subject to residual lobes above the sidelobes from the antenna geometry (antenna diagram that gives a sinc function with a second maxima at -13 dB).

Note that all this information matches (and extends) the already-mentioned analysis of performance.

2.3 The Residual Sidelobes as Challenge

We have exhibited the advantages of the phase codes waveforms over FDMA and TDMA waveforms. Nevertheless, we have also mentioned the main drawback of phase codes which is their imperfect orthogonality leading to numerous sidelobes all around

the main lobe. Here, we will explore more deeply the origins of these sidelobes. For that, we will first give the signal formalism we have considered, and on this base, we will exhibit where the lack of orthogonality comes from.

2.3.1 Signal Formalism

The signal formalism for the following thesis work is based on the general model of [25] presented in section 1.3.1. For our situation, it is chosen to represent the temporal signals as vectors instead of scalars depending on t. The motivation behind this choice principally comes from a wish to represent the operation of shifting in time a signal by τ (due to time of travel for example) as a multiplication (in the spectral domain) with a vector containing this parameter τ. Therefore, it will be similar to the angle dimension where the steering vectors $\mathbf{s}_{\mathrm{Tx}}(\theta)$ and $\mathbf{s}_{\mathrm{Rx}}(\theta)$ aims at focusing the beam pattern in direction θ. Besides, since it is not convenient to represent signal correlation with vectors, we will often prefer the multiplication in the Fourier domain and therefore often represent the signals in spectral domain. Note that the notations which are not introduced in the following are those already introduced in section 1.3.1.

Here again, we consider that the MIMO radar transmits a pulse train, with each antenna transmitting its specific intrapulse code during one pulse, and we assume that this code is identical from pulse to pulse. The signal during the pulse is assumed discrete, and K is the number of samples. The vector $\mathbf{s}_m$ of size $K \times 1$ denotes the waveform, in time domain, assigned to the m^{th} antenna. Thus, the signal of size $K \times 1$ transmitted by the array is :

$$\mathbf{s}(\theta) = \sum_{m=1}^{M} g_{\mathrm{Tx},m}(\theta)\, e^{j\mathbf{x}_m^T \mathbf{k}(\theta)} \mathbf{s}_m \tag{2.6}$$

Concatenating all transmitted waveforms $\mathbf{s}_m$ in a single matrix $\mathbf{S} = [\mathbf{s}_1 \cdots \mathbf{s}_M]$ of size $K \times M$, we get:

$$\mathbf{s}(\theta) = \mathbf{S}\mathbf{s}_{\mathrm{Tx}}(\theta) \tag{2.7}$$

We will now write the expression in the spectrum domain, by considering $\tilde{\mathbf{v}}$ the spec-

trum of any time vector $\mathbf{v}$, and $\tilde{\mathbf{S}} = [\tilde{\mathbf{s}}_1 \cdots \tilde{\mathbf{s}}_M]$:

$$\tilde{\mathbf{s}}(\theta) = \tilde{\mathbf{S}}\mathbf{s}_{\mathrm{Tx}}(\theta) \tag{2.8}$$

For the sake of simplicity, we will make two considerations in the following:

- One single antenna on receive. Indeed, it has been demonstrated that for MIMO radar, transmission and reception processing schemes are completely decoupled, as already mentioned in section 1.3.1.
- No consideration of the Doppler dimension, in order to work in the range/angle domain only. As an illustration, it corresponds to a situation of detection of slow moving targets only. Note that the Doppler dimension is already optimal for CDMA since phases codes present low Doppler sidelobes and no Doppler ambiguity, as already mentioned in section 2.2.1.

If a target of unit amplitude is present in direction θ_t and at range r_t, then the signal $\tilde{\mathbf{s}}^r$ of size $K \times 1$ received on the antenna is:

$$\tilde{\mathbf{s}}^r = \tilde{\mathbf{S}}\mathbf{s}_{\mathrm{Tx}}(\theta_t) \odot \tilde{\mathbf{s}}_f(r_t) \tag{2.9}$$

where the vector $\tilde{\mathbf{s}}_f(r)$ of size $K \times 1$ is the range-“steering" vector whose components are given by:

$$\left(\tilde{\mathbf{s}}_f(r)\right)_k = e^{i2\pi k \frac{2r}{c}\Delta f} \tag{2.10}$$

with Δf the frequency sampling interval and $(\cdot)_k$ denoting the k^{th} element of a vector. In other words, the effect of $\tilde{\mathbf{s}}_f(r)$ in time domain is time-shifting the waveforms by r.

The first step of the optimal coherent MIMO processing is the transmitter separation, which is the correlation of the received signal with the transmitted waveforms, one by one. In spectral domain, this operation consists in multiplying the received signal spectrum with each waveform spectrum. Let us explicit the expression $\mathbf{a}^m(r_t,\theta_t)$ of the signal of size $K \times 1$ after correlation with waveform m, in the spectral domain:

$$\tilde{\mathbf{a}}_m(r_t,\theta_t) = \tilde{\mathbf{S}}\mathbf{s}_{Tx}(\theta_t) \odot \tilde{\mathbf{s}}_f(r_t) \odot \tilde{\mathbf{s}}_m^* \tag{2.11}$$

Finally, the expression of vector $\tilde{\mathbf{a}}(r_t,\theta_t)$ of the received data after pulse compression

(whose size is $KM \times 1$) is written:

$$\tilde{\mathbf{a}}(r_t,\theta_t) = \begin{bmatrix} \tilde{\mathbf{a}}_1(r_t,\theta_t) \\ \vdots \\ \tilde{\mathbf{a}}_M(r_t,\theta_t) \end{bmatrix} \tag{2.12}$$

Considering now α_t the complex amplitude of a target at range r_t and at angle θ_t, and $\mathbf{n}$ the additive noise, the received vector after pulse compression $\tilde{\mathbf{z}}$, expressed in the spectral domain, is written:

$$\tilde{\mathbf{z}} = \alpha_t \tilde{\mathbf{a}}(r_t,\theta_t) + \tilde{\mathbf{n}} \tag{2.13}$$

Then, estimating the target echoes of the scene through MF corresponds to estimating α_t, *i.e.* the target amplitude for all (r,θ) hypothesis:

$$\hat{\alpha}(r,\theta) = \frac{\tilde{\mathbf{a}}^H(r,\theta)\,\tilde{\mathbf{z}}}{\tilde{\mathbf{a}}^H(r,\theta)\,\tilde{\mathbf{a}}(r,\theta)} \tag{2.14}$$

Note that this expression actually corresponds to (1.12) with the normalization, r instead of τ, $\alpha_t = 1$ and $\tilde{\mathbf{n}} = 0$.

2.3.2 The Residual Sidelobes Issue

Origin of Residual Sidelobes

In order to exhibit the effects of the imperfect orthogonality of the phase codes on the ambiguity function, we first make the comparison between hypothetical perfectly orthogonal waveforms and realistic non-perfectly orthogonal waveforms. First, we propose to rewrite (2.11) the following way:

$$\tilde{\mathbf{a}}_m(r_t,\theta_t) = \sum_{n=1}^{N} (\mathbf{s}_{\mathrm{Tx}}(\theta_t))_n \cdot \mathbf{s}_f(r_t) \odot \tilde{\mathbf{s}}_n \odot \tilde{\mathbf{s}}_m^* \tag{2.15}$$

It it worth noting that:

- $\tilde{\mathbf{s}}_m \odot \tilde{\mathbf{s}}_m^*$ is the autocorrelation of waveform m in the spectral domain. In the case of hypothetical perfectly orthogonal waveforms, it is a constant complex

exponential vector (*i.e.* a Dirac function in the time domain).

- $\tilde{\mathbf{s}}_n \odot \tilde{\mathbf{s}}_m^*$ with $n \neq m$ is the cross-correlation function of waveform n with waveform m in the spectral domain. In the case of hypothetical perfectly orthogonal waveforms, it is a zero-value vector.

In the case of a hypothetical family of perfectly orthogonal waveforms, the expression of $\tilde{\mathbf{a}}(r_t, \theta_t)$ becomes (with $\otimes$ denoting the Kronecker product):

$$\tilde{\mathbf{a}}_{\text{th}}(r_t, \theta_t) = \begin{bmatrix} (\mathbf{s}_{\text{Tx}}(\theta_t))_1 \, \mathbf{s}_f(r_t) \\ \vdots \\ (\mathbf{s}_{\text{Tx}}(\theta_t))_M \, \mathbf{s}_f(r_t) \end{bmatrix} = \mathbf{s}_f(r_t) \otimes \mathbf{s}_{\text{Tx}}(\theta_t) \tag{2.16}$$

In the realistic situation of non-perfectly orthogonal waveforms, the auto- and cross-correlation functions induce residues in the ambiguity function which are at the root of the grating sidelobes all around the mainlobe of the target. We will call them “residual sidelobes" in the following.

It is worth precising that the sidelobes coming directly from the “interference figure" (sinc profile usually) due to the sum of vector components (actually $\tilde{\mathbf{a}}_{\text{th}}^H(r, \theta)\, \tilde{\mathbf{a}}_{\text{th}}(r_t, \theta_t)$) are not seen as “residual sidelobes". Consequently, in the situation of perfect waveform orthogonality, it comes out of (2.16) that no residual sidelobes appears.

Impact of Residual Sidelobes

We have mentioned that the residual sidelobes may be above the noise level. Consequently, these sidelobes are likely to induce a higher probability of false alarm or a lower probability of target detection, since secondary targets may be buried in the residual sidelobes of targets of higher power.

In order to exhibit the coming out of residual sidelobes in the case of non-perfectly orthogonal waveforms and make the comparison with the ideal orthogonal case, we process a simulation of phase codes with the same parameters as in section 2.2.2, with addition of noise. For the comparison, we also provide the MF output in case of perfectly orthogonal waveforms, based on (2.16). We precise here the extra parameters:

- Output (*i.e.* after processing) SNR: 30 dB
- Noise distribution: white Gaussian

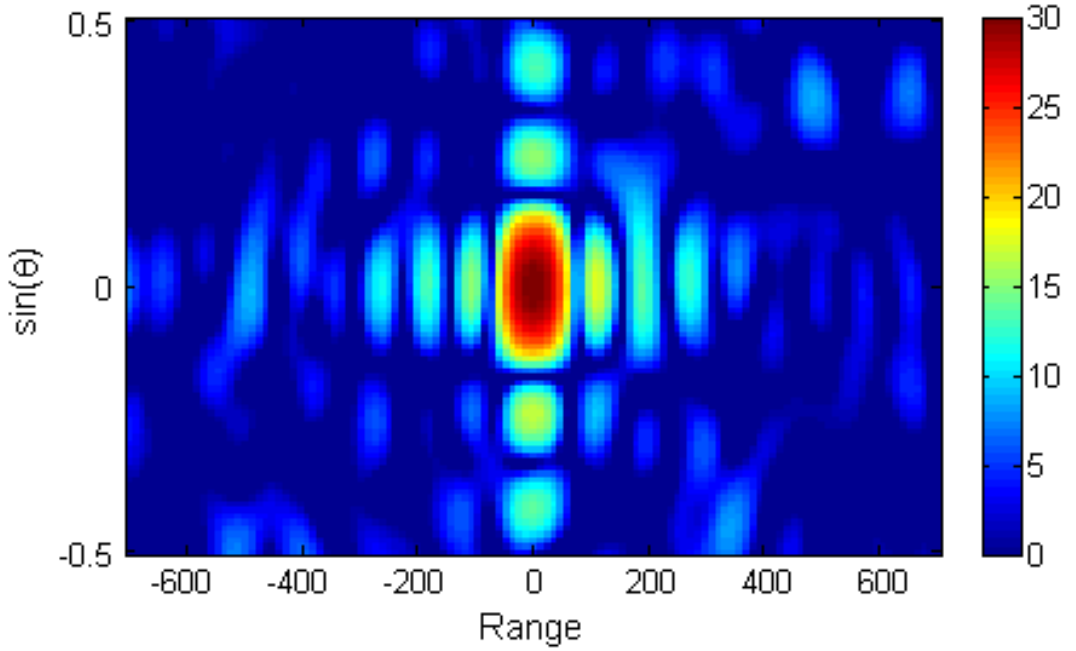

(a) Simulation of a family of perfectly orthogonal waveforms (range in m).

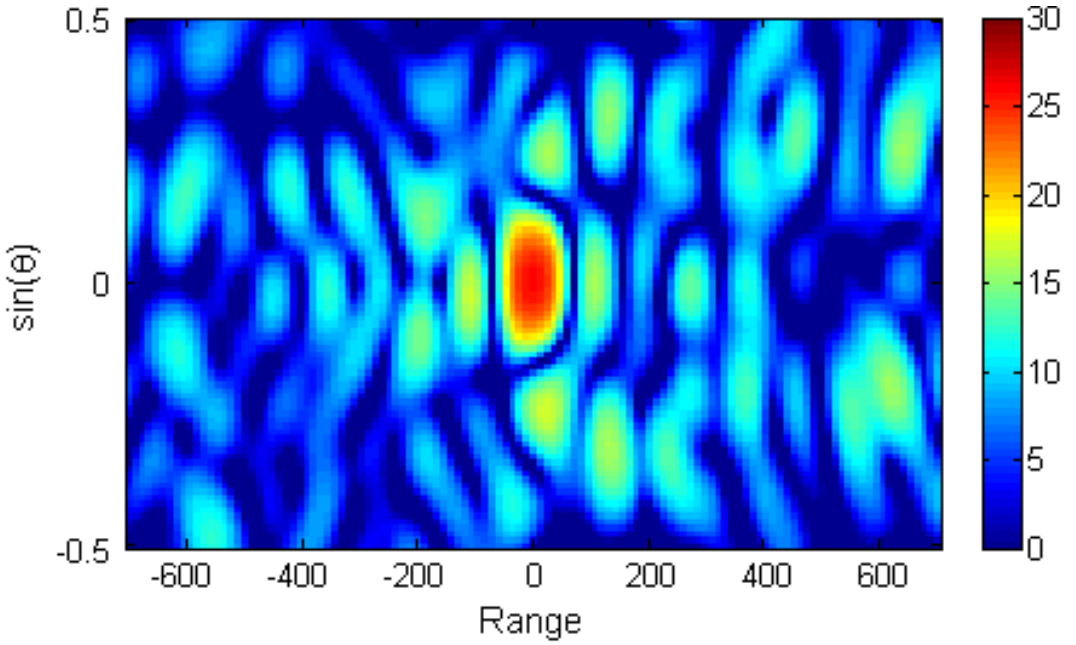

(b) Simulation of a family of Gold codes

Figure 2.6: Range-angle estimation based on MF for one point target (range in m).

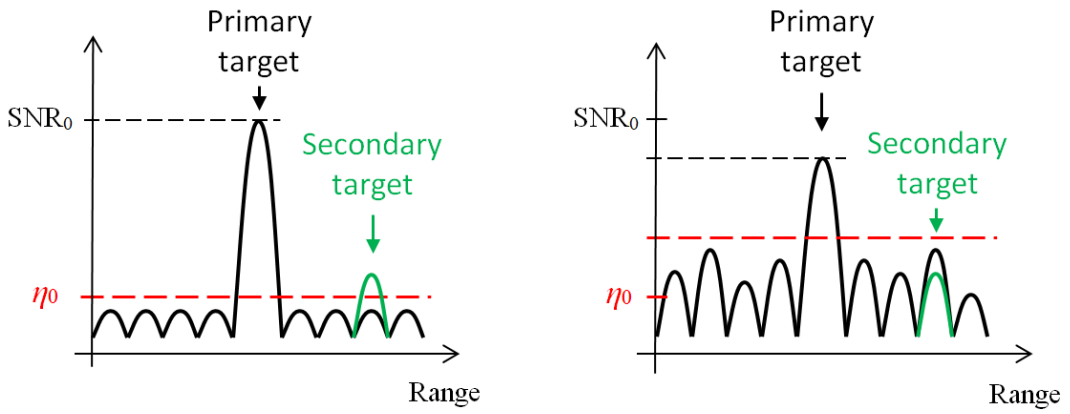

(a) Ideal waveforms (perfect orthogonality).

(b) Phase codes waveforms (imperfect orthogonality).

Figure 2.7: Schema of the impact of residual sidelobe level on target detection performance (detection threshold and peak value).

The parameters are set such a way (through noise power normalization) to give, after processing, a target peak value similar to the expected output SNR, and a noise level around 0 dB.

The corresponding results for the ideal ambiguity function are displayed on fig. 2.6a. We clearly notice the intersection of the range and angle sinc profiles originating from the point target (*i.e.* the “interfering figure"). The main lobe is centered and close to the expected value of 30 dB, *i.e.* the SNR value. All around appears the noise “floor" at around 0 dB. This figure has to be compared with the results of target amplitude estimation based on the simulated realistic signals displayed on fig. 2.6b. For this ambiguity function, the main lobe is also centered and close to 30 dB (around 5 dB below though). To the difference with the previous situation, one can clearly notice the presence of a “floor" of residual sidelobes distributed in all range and angle positions, sometimes with a power up to 10 dB below the peak value.

Therefore, the comparison of the two figures clearly shows that the residual sidelobes are indeed due to the lack of orthogonality of the waveforms which induces residues when the waveform auto and cross-correlations are added. It can be noticed that the average sidelobes level is around 20 dB under the target peak value, which corresponds to what can be expected from phase codes of 127 chips. Besides, the range extension of the positions affected by the sidelobes is of order of magnitude of the pulse length (around 10 km in the current situation).

Finally, the direct consequences of the residual sidelobes are listed below:

- **Desensitization to secondary targets**: in this situation, even if the noise level is at 0 dB, any secondary target giving a peak power more than 10 dB below the primary target is virtually impossible to detect, since the target detection threshold should be set above the residual sidelobes which reach 20 dB here. It results in performance degradation on target detection capacities.
- **Loss of target peak value**: the loss of 5 dB of the target mainlobe is due to the fact that more energy is spread in the residual sidelobes. A lower mainlobe actually corresponds to a lower SNR, which also has an impact on performance degradation on target detection capacities.
- **Increased sensitivity to clutter**: because of the extensive “floor" of sidelobes, the scatterers of a clutter (vegetation, human facilities, etc.) will return their contribution within a large domain (range and angle) around their location, so it may impact the detection of targets which are relatively distant.

The two first effects are illustrated with the schema of fig. 2.7. In the first case (perfect orthogonality), the peak of the secondary target is above the detection threshold and thus the target can be detected. In the second case (residual sidelobes due to imperfect orthogonality), the peak of the secondary target is below the threshold and thus the target remains undetected. Note also that the peak of the primary target is lower than in the first case, thus resulting in a lower “margin" to detect this target.

2.4 Conclusion

In this chapter, we have qualified and compared the intrinsic merits of the different types of waveforms thanks to the Cramér-Rao lower bounds and figures of merit computed on simulated signals. We have exhibited the optimal performances of the CDMA waveforms in terms of spatial resolution (range and angle) and shown that on this criteria, they clearly outperform the TDMA and FDMA waveforms.

Nevertheless, the phase codes suffer from non-ideal auto- and cross-correlations. Therefore, they provide a high sidelobe level, spread over an extensive domain of the ambiguity function. We have shown the harmful impact it can have on target detection performance. Possible solutions to reduce the residual sidelobe level are to use longer

code sequences (for better correlation properties) through larger bandwidth or longer pulses, when possible, or consider waveform design optimization (mentioned in chapter 1.4.2). Nevertheless, these techniques have reached their limits in terms of sidelobe reduction. It is worth noticing that these sidelobes stay proportional to the target peak value, making thus the SNR irrelevant since the residual sidelobes may be above noise level. At this stage, this situation prevents the use of such waveforms in strong clutter situations or for weak target detection.

Finally, it can be concluded that the phase code waveforms are optimal with respect to the intrinsic spatial resolution and can thus be of particular interest for MIMO radar applications once the residual sidelobes issue is solved. For this latter challenge, defining enhanced processing methods on receive may be investigated.

3 Development of Processing Methods for Residual Sidelobe Rejection

3.1 Introduction

We have seen that the residual sidelobes in case of the use of phase codes as MIMO radar waveforms are a strong limitation in terms of target detection performance. Actually, the pulse compression in conventional radar processing is based on MF: this method optimizes the SNR without consideration of other properties. The challenge lies in going beyond the MF performance in terms of sidelobe reduction. Therefore, the objective of this chapter is to propose enhanced processing techniques on receive which could offer both sidelobe reduction performance and operational feasibility. More precisely, the proposed techniques should provide accurate target localization estimation and residual sidelobe elimination, while still satisfying operational constraints, in terms of computation time and greed on training data, especially.

The residual sidelobes directly come from the response pattern of each target in the ambiguity function. Since the signal model is known, this pattern can be determined *a priori*, depending on the target localization, making it possible to refer to the inverse problem theory. From this perspective, we will first investigate possible data-dependent techniques for the estimation of the target parameters, and exhibit the merits and limitations of each of these techniques with respect to the context of operational MIMO radar for target detection. We will give our motivations for selecting the OMP (Orthogonal Matching Pursuit) as a suitable technique to solve the problem. Second, we will depict the biased target localization issue inherent to this latter technique, coming for example from the parameter grid ganularity or neighbor target influence. We will also exhibit to which extent it can damage the target detection performance. Then, we will propose an extension for the OMP algorithm in

order to improve the robustness with respect to this issue. Finally, we will illustrate the performance improvement in terms of residual sidelobe rejection and robustness to localization error on realistic scenarios.

3.2 Adaptation of Data-Dependent Methods to MIMO radar

3.2.1 Adaptive Processing Based on ℓ_2-Norm

An Overview of the Capon Estimator

It is mentioned in [21] that MIMO radars are good candidates for adaptive localization and detection techniques. Such methods are known to have much better resolution and much better interference rejection capability than their data-independant counterparts. Different adaptive techniques – Capon, APES, etc. – for the estimation of direction of arrival (*i.e.* the angle parameter only) were investigated in [21]. They all lie on the use of a covariance matrix of size $N_0 \times N_0$, with N_0 the number of "data channels", in this case the number of receivers. This covariance matrix should be estimated on a sufficient number of data samples – also called realizations, or snapshots – in order to have full rank. As an illustration, we present the Capon estimator [43], which aims at minimizing the variance of the weighted sum of $\mathbf{z}_0$ under constraint, $\mathbf{z}_0$ being for instance a signal received on the different antennas of a phased array. The minimization problem under constraint can be formulated the following way:

$$\begin{aligned} &\min_{\mathbf{w}} \left\| \mathbf{w}^H \mathbf{z}_0 \right\|_2^2 \\ &\text{subject to} \quad \mathbf{w}^H \mathbf{a}_0(\theta) = 1 \end{aligned} \tag{3.1}$$

where $\mathbf{a}_0(\theta)$ is the steering vector in direction θ, and $\mathbf{w}$ is the weight vector used to reject all what is not matching the desired signal (noise, interference, etc.) while keeping the desired signal undistorted. Finally, the resulting estimation for the directions of arrival (DOA) is the maxima of the Capon output:

$$\hat{\alpha}_0(\theta) = \frac{\mathbf{a}_0^H(\theta)\,\Gamma_0^{-1}\mathbf{z}_0}{\mathbf{a}_0^H(\theta)\,\Gamma_0^{-1}\mathbf{a}_0(\theta)} \tag{3.2}$$

The target amplitude estimation is based on the covariance matrix Γ_0 of the received signal $\mathbf{z}_0$. The covariance matrix can be estimated on a set of realizations $\left(\mathbf{z}_{0,k}\right)_{k=1..K_0}$

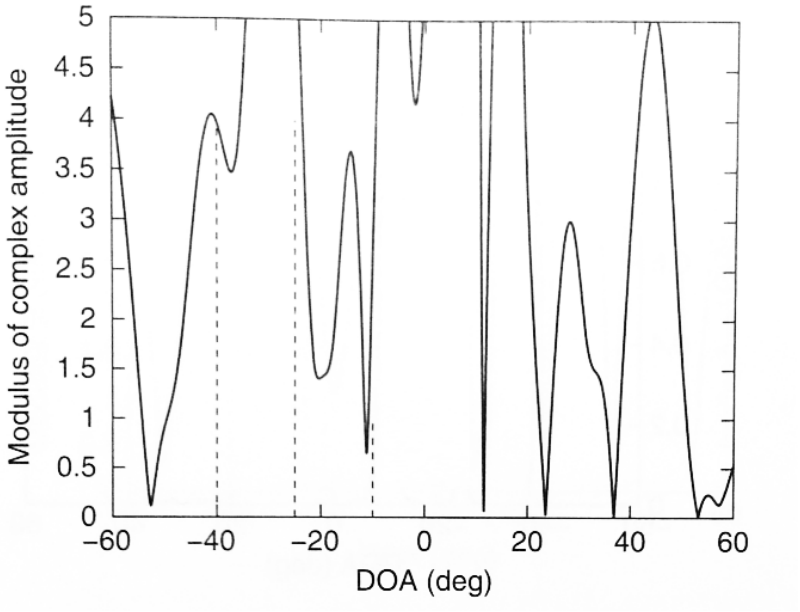

(a) MF.

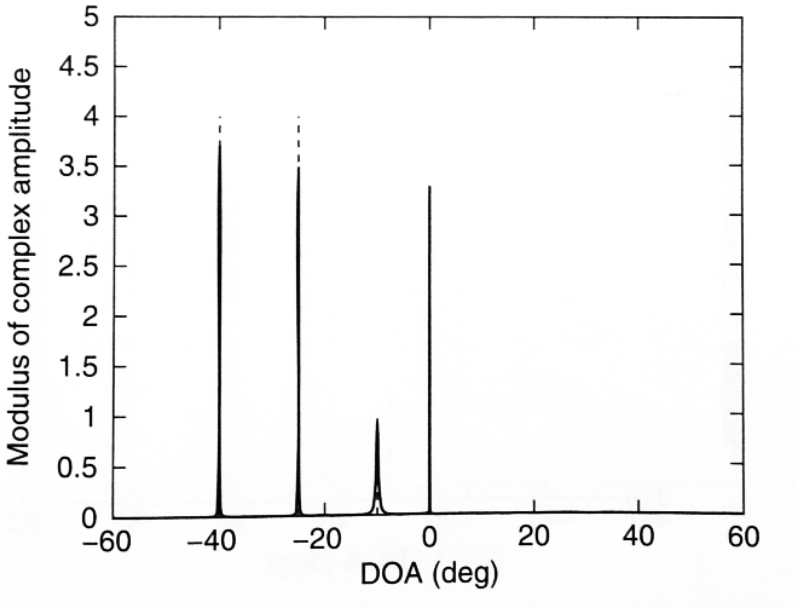

(b) Capon.

Figure 3.1: Spatial spectral estimates with Capon method for targets located at -40°, -25° and -10°.

of the observed data $\mathbf{z}_0$:

$$\hat{\Gamma}_0 = \frac{1}{K_0} \sum_{k=1}^{K_0} \mathbf{z}_{0,k} \mathbf{z}_{0,k}^H \tag{3.3}$$

A simulation is proposed in [21] for the estimation of direction of arrival with a uniform linear array composed of 10 antennas (half-wavelength spacing) for both transmitting and receiving antennas, 3 targets located at -40°, -25° and -10°, with complex amplitudes 4, 4 and 1, respectively, and a strong jammer at 0° with amplitude 1000. The calculation of the covariance matrix for the Capon estimation is based on 256 data samples. Clearly, the MF method suffers from high sidelobes, visible in 3.1a. On the contrary, as seen on fig. 3.1b, Capon possesses great interference and jamming suppression capabilities. Note also that the jammer at 0°, even if still present, has been strongly mitigated.

Capon Estimation of Two Parameters in MIMO Radar Context

The interest of methods like Capon for our problematic is the constraint imposed on the output energy, which is expected to lead to the mitigation of the sidelobes caused by the lack of orthogonality of the waveforms – and also increase the main lobe amplitude in the same time.

In our context, two (at least) spatial parameters have to be estimated: range, angle (and Doppler possibly). This problem is somehow similar to Space-Time Adaptive Processing (STAP) where the filtering is done over multiple dimensions [44]. A typical use of STAP is clutter rejection for airborne radar, while keeping the desired signal return. The main difference with our context is that STAP is often used for angle-Doppler estimation the range data are used as snapshots for the computation of the covariance matrix, while we expect to process angle-range estimation and use the pulses as snapshots. We will see here why it is actually a consequent limitation in our context.

The application of the Capon estimator to the considered signals provides the following expression, adapted from (3.2):

$$\hat{\alpha}(r,\theta) = \frac{\tilde{\mathbf{a}}^H(r,\theta)\,\Gamma^{-1}\tilde{\mathbf{z}}}{\tilde{\mathbf{a}}^H(r,\theta)\,\Gamma^{-1}\tilde{\mathbf{a}}(r,\theta)} \tag{3.4}$$

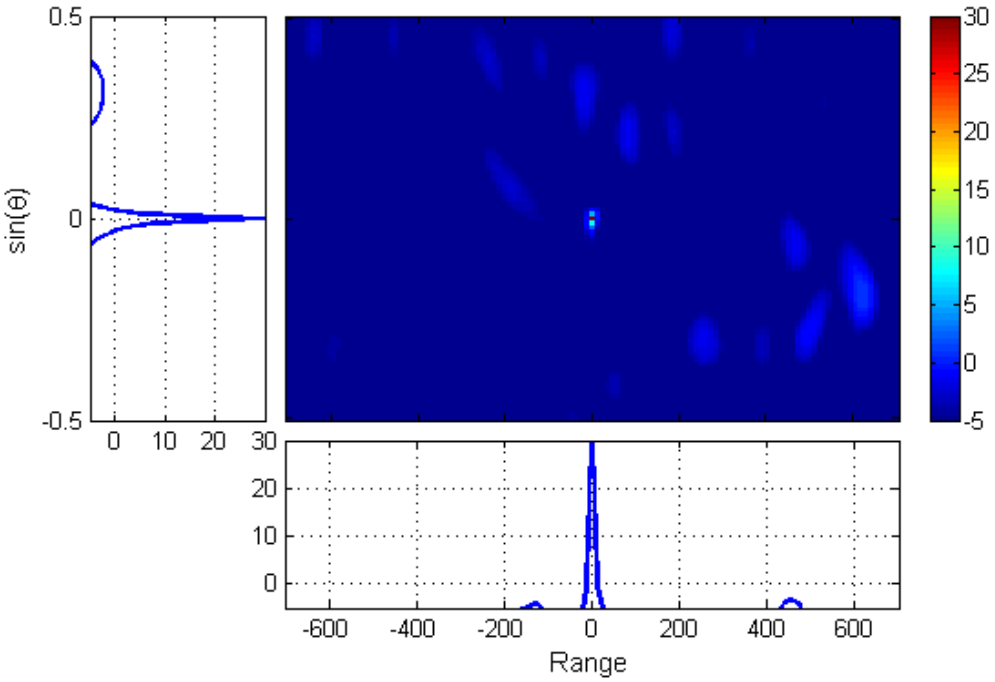

Figure 3.2: Capon estimation on range-angle domain for a well-estimated covariance matrix from simulated MIMO waveforms (Gold phase codes) plus noise transmitted to one point target. Cuts at target range and angle are plotted on each side.

with $\tilde{\mathbf{z}}$ the vector of the received signals defined in chap. 2.3.1 and Γ the covariance matrix of $\tilde{\mathbf{z}}$.

As an illustration of the Capon estimator for two parameters, we first consider that it is possible to correctly estimate the covariance matrix Γ, which would be the case when the number of independent snapshots is much larger than the dimension of $\tilde{\mathbf{z}}$.

Then, the Capon estimation is expected to give the correct target amplitudes, even in case of lack of orthogonality between waveforms. The expression of the so-called power spectral density is then:

$$|\alpha(r,\theta)|^2 = \frac{1}{\tilde{\mathbf{a}}^H(r,\theta)\,\Gamma^{-1}\tilde{\mathbf{a}}(r,\theta)} \tag{3.5}$$

Note that for one target at range r_t and angle θ_t and white noise, the expression of the covariance matrix is:

$$\Gamma = \alpha_t^2 \tilde{\mathbf{a}}(r_t,\theta_t)\,\tilde{\mathbf{a}}^H(r_t,\theta_t) + \sigma^2\mathbf{I} \tag{3.6}$$

To exhibit these ideal results in case of perfect estimation of the covariance matrix, we process a simulation of range-angle estimation with one point target and Gold sequences as phase code waveforms. We generate a large number of synthetic pulses in order to provide an accurate estimation of the covariance matrix. The parameters for the simulation are given here:

- Number of transmitters: $M = 12$
- Total bandwidth: $B = 2$ MHz
- Number of chips: $N_c = 127$
- Number of pulses: $N_p = 10^4$
- Target range: $r_t = 0$
- Target angle: $\theta_t = 0$
- Output (*i.e.* after processing) SNR: 30 dB
- Noise distribution: white Gaussian

The results obtained with this simulation are displayed on fig. 3.2. As expected, all sidelobes have been reduced to values below the noise level of 0 dB. All the undesired contributions, which were actually not matching the signal model, have been filtered. Note also that the target peak reaches the expected value of 30 dB, when we got 5 dB loss with the MF only (Cf. fig 2.6b).

Finally, this estimation method has been shown of to be efficient for target estimation and sidelobes mitigation, on condition that the covariance matrix could be estimated. In the current situation of range and angle estimation, many more than $M \times N_c$ snapshots are needed to expect a correct estimation of the covariance matrix. Nevertheless, in most radar situations in practice, this large number of pulses is not available. As an example, in the typical use of the MIMO radar at ONERA, it has been estimated that the possible number of available pulses (where the signal keeps its properties in terms of stationarity) is of the order of magnitude of several tens, making it impossible to estimate the covariance matrix. Indeed, according to radar experts of ONERA, it has been stated that several hundreds of targets can be expected in critical scenes.

More generally, other methods based on ℓ_2-norm minimization where a covariance matrix has to be estimated will be subject to the same limitation. In the best case, the number of snapshots has to be twice the number of point targets (*e.g.* for low-rank methods), which is still limiting for our situation though.

Capon Estimation of One Parameter in MIMO Radar Context

In the same context as before, another idea is to perform a Capon estimation on one dimension only, and to use another technique for the estimation on the other spatial dimension. In section 1.4.2, we have presented works that aim at defining enhanced processing methods on receive. More specifically, [40] proposes a mismatched filter optimization for phase codes which can perform sidelobe reduction on the whole range axis but in a restricted angle sector only. Therefore, if we can combine such technique with another efficient technique on the angle axis, it will be possible to reject all residual sidelobes. Therefore, we propose here to apply a Capon estimation on the angle dimension only, and to use the samples of the range dimension – *i.e.* the spectral bins – as snapshots to compute the covariance matrix. To estimate the potential of this technique, we will only use a MF for the range estimation, so to investigate if we can provide sidelobe reduction on the angle axis.

In this configuration, we consider $\mathbf{s}_{T_x}(\theta)$ instead of $\tilde{\mathbf{a}}(r,\theta)$, and we introduce the matrix $\tilde{\mathbf{Z}}$ for the observed signal, which is actually the matrix of size $M \times K$ built from the vector $\tilde{\mathbf{z}}$ of size $MK \times 1$ defined in (2.13). We remind that K is the number of frequency bins (corresponding to the number of snapshots for the Capon estimation) and M the number of transmitters. Thus, this construction allows us to perform MF and Capon estimation on each "side" of the matrix $\tilde{\mathbf{Z}}$, respectively. The expression of the matrix of the received signal for one target at range r_t, angle θ_t, and complex amplitude α_t is:

$$\tilde{\mathbf{Z}} = \alpha_t \begin{bmatrix} \tilde{\mathbf{a}}_1^T(r_t,\theta_t) \\ \vdots \\ \tilde{\mathbf{a}}_M^T(r_t,\theta_t) \end{bmatrix} + \tilde{\mathbf{N}} \tag{3.7}$$

with $\tilde{\mathbf{N}}$ the additive noise matrix.

The deduced expression for the estimation of the target amplitude with this hybrid method is:

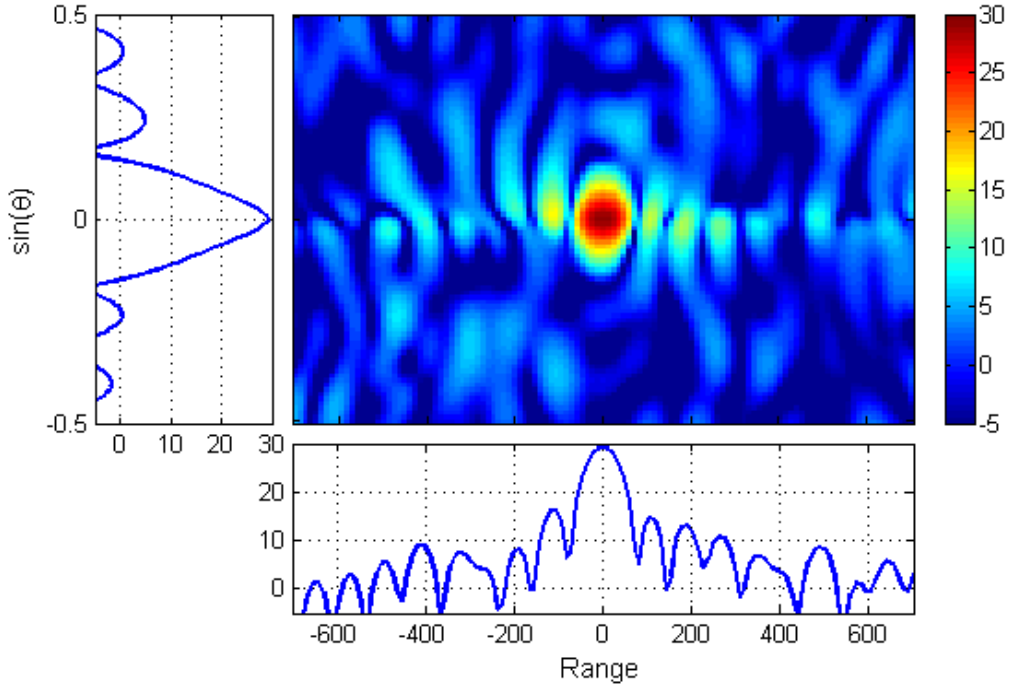

(a) Ideal perfectly-orthogonal waveforms.

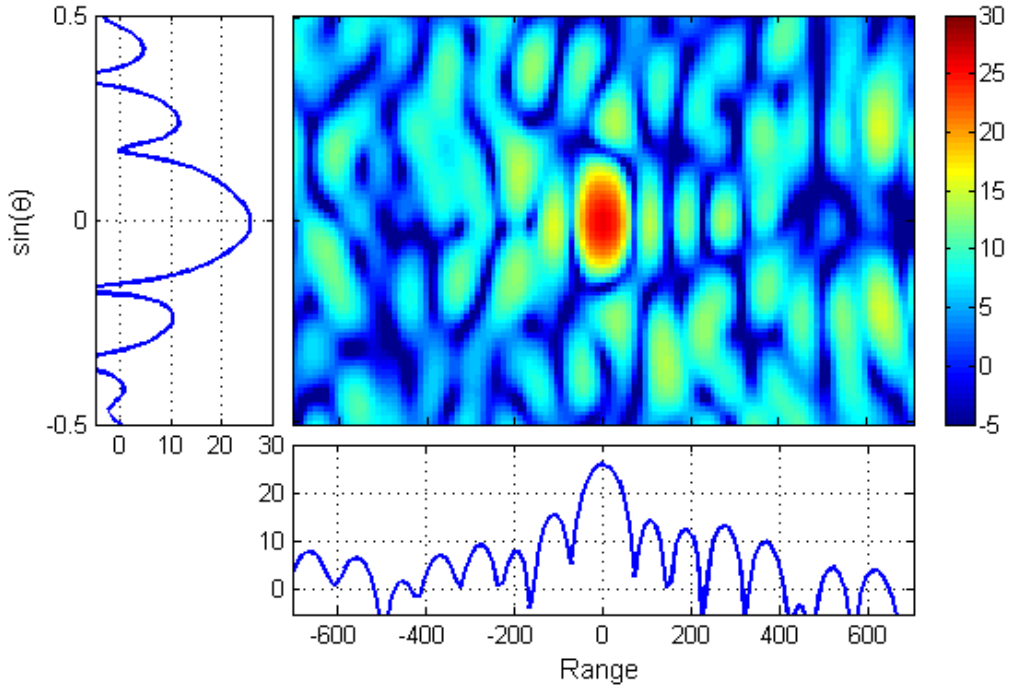

(b) Simulated Gold phase codes.

Figure 3.3: Capon estimation on angle domain and MF on range domain from signal composed of point target echo plus noise. Cuts at target range and angle are plotted on each side.

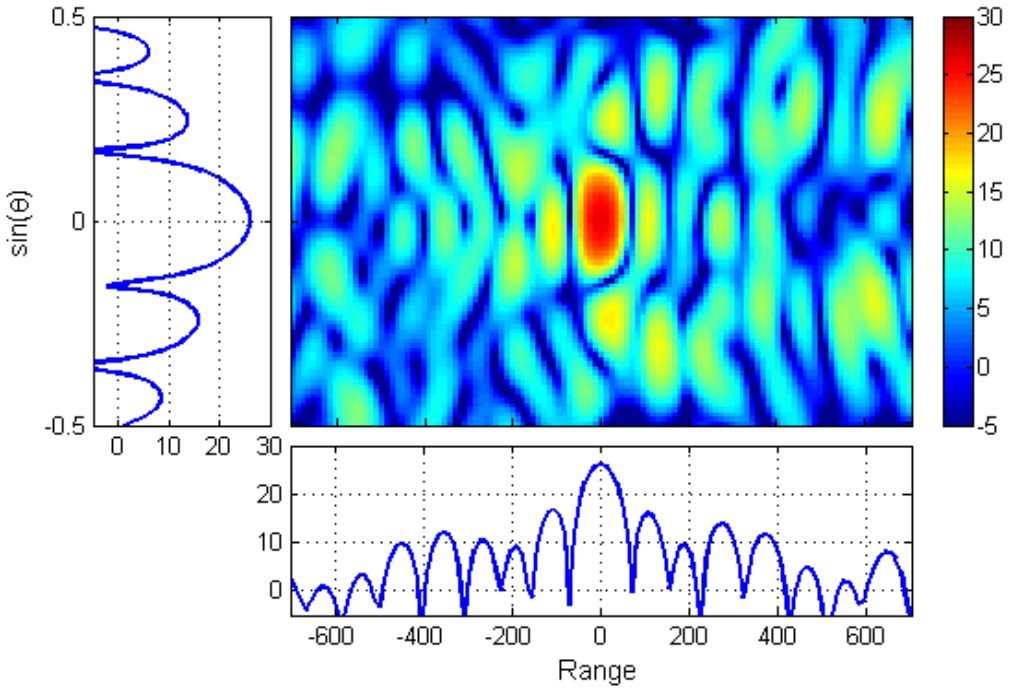

Figure 3.4: For the comparison: MF estimation on range and angle domains from signal composed of point target echo (Gold phase codes) plus noise.

$$\hat{\alpha}(r,\theta) = \frac{\mathbf{s}_{T_x}^H(\theta)\,\Gamma^{-1}\tilde{\mathbf{Z}}\,\mathbf{s}_f^*(r)}{\left(\mathbf{s}_{T_x}^H(\theta)\,\Gamma^{-1}\mathbf{s}_{T_x}(\theta)\right)\cdot\left(\mathbf{s}_f^H(r)\,\mathbf{s}_f(r)\right)} \tag{3.8}$$

and the covariance matrix Γ of the transmitter channels (of size $M \times M$) is estimated with the data in the range domain the following way:

$$\hat{\Gamma} = \frac{1}{K}\tilde{\mathbf{Z}}\tilde{\mathbf{Z}}^H \tag{3.9}$$

Then, we make the same simulation as previously, to the difference we consider only one pulse. We also generate signals corresponding to – hypothetical – perfectly orthogonal waveforms based on (2.16). We apply the proposed method on both signals. The results are displayed in fig. 3.3a for ideal perfectly-orthogonal waveforms, and in fig. 3.3b for the phase code waveforms. With the ideal waveforms, we clearly distinguish the effect of Capon optimization on angle dimension. The main lobe has been vertically “shrinked", as well as the sidelobes that have been reduced to noise level everywhere, except for the specific angle of the target where the sidelobes

are intact. Indeed, the Capon estimation has been applied on angle dimension only. Nevertheless, with the phase code waveforms, the results are much different. Actually, they are very close to those obtained with the MF on both dimensions, as exhibited for comparison in fig. 3.4. Here again, we get a high level of sidelobes above noise all around the mainlobe. Note however that the main lobe has been slightly “shrinked" and that the sidelobe level is a little bit lower (no more than 2 dB though). Here again, the main lobe is several dB lower than the 30 dB of the main lobe of fig. 3.3a, since more energy is spread in the sidelobes.

The reduced impact of the current method can be *a priori* explained by the fact that the covariance matrix has a small degree of freedom (so has the filtering vector $\mathbf{w}$ of (3.1)) in comparison with all the frequency bins that have to be “filtered". Indeed, the joint Capon estimation on both range and angle presented MK degrees of freedom, when it here presents only M degrees of freedom, for the same amount of sidelobes to reject all around the main lobe. Therefore, it is deduced that the degree of freedom provided here cannot prevent a “random" combination of waveform cross-correlations.

Finally, we can conclude that this hybrid method has only given a marginal performance enhancement with comparison to the performance obtained with the MF only. Even if it seemed promising at first, it has shown to be not satisfying enough in the current context.

3.2.2 Compressed Sensing (CS)

Unlike the previously-mentioned techniques, the CS relies on the ℓ_1-norm minimization for the reconstruction of the target scene [45]. In its general principle, the CS exploits the sparsity of a signal to reduce the sampling rate and the amount of data generated, while keeping the resolution fixed. In the radar domain, this condition is usually fulfilled since the number of targets is typically much smaller than the number of resolution cells of the scene.

Consider the general problem of the recovering of a sparse vector $\mathbf{x_0}$ from measurements $\mathbf{y}$:

$$\mathbf{y} = \mathbf{A}\mathbf{x_0} + \mathbf{n} \tag{3.10}$$

where $\mathbf{A}$ is the sensing matrix and $\mathbf{n}$ is independent identically distributed (i.i.d.)

complex Gaussian noise. In the radar context, it can be considered that $\mathbf{x_0}$ is the sparse vector containing non-zero entries for target locations, $\mathbf{A}$ incorporates the spatial geometry and the transmitted waveforms, and $\mathbf{y}$ is the received signal.

One of the most successful recovery algorithm is the LASSO or Basis Pursuit Denoising [46], given by

$$\hat{\mathbf{x}}(\lambda) = \arg\min_{\mathbf{x}} \frac{1}{2} \left\| \mathbf{y} - \mathbf{A}\mathbf{x} \right\|_2^2 + \lambda \left\| \mathbf{x} \right\|_1 \tag{3.11}$$

where λ is called the regularization parameter.

Reference [39] claims that the standard approaches for solving this problem are computationally expensive and therefore proposes an iterative algorithm for CS recovery called Complex Approximate Message Passing (CAMP). According to the authors, this algorithm has appealing properties for radar applications. More specifically, situations of better detection performance than the MF are exhibited.

Nevertheless, the proposed method still suffers from possible computational complexity. In the cited work, the following function is introduced:

$$\eta(\mathbf{u}; \lambda) = (|\mathbf{u}| - \lambda)\, e^{i \arg(\mathbf{u})} \mathbf{1}(|\mathbf{u}| > \lambda) \tag{3.12}$$

where $\mathbf{1}$ is the indicator function, and $\eta(\cdot; \lambda)$ is called the complex soft thresholding function, applied component-wise to the input vector $\mathbf{u}$. In the proposed CAMP algorithm, the partial derivatives of the function η with respect to the input have to be computed. It turns out that this operation applied on vectors of size MK (or much more if Doppler is considered) presents a computational complexity which is scarcely compatible with the operational conditions. Besides, it has also been experienced that the tuning of the regularization parameter is particularly delicate. For these reasons, it has been chosen not to select the CS as a candidate for target parameter estimation in a situation of residual sidelobes.

3.2.3 Iterative Adaptive Approach (IAA)

An Overview of the IAA

The IAA is based on a weighted least squares approach proposed in [38] for passive sensing, channel estimation, and single-antenna radar applications. One interest of

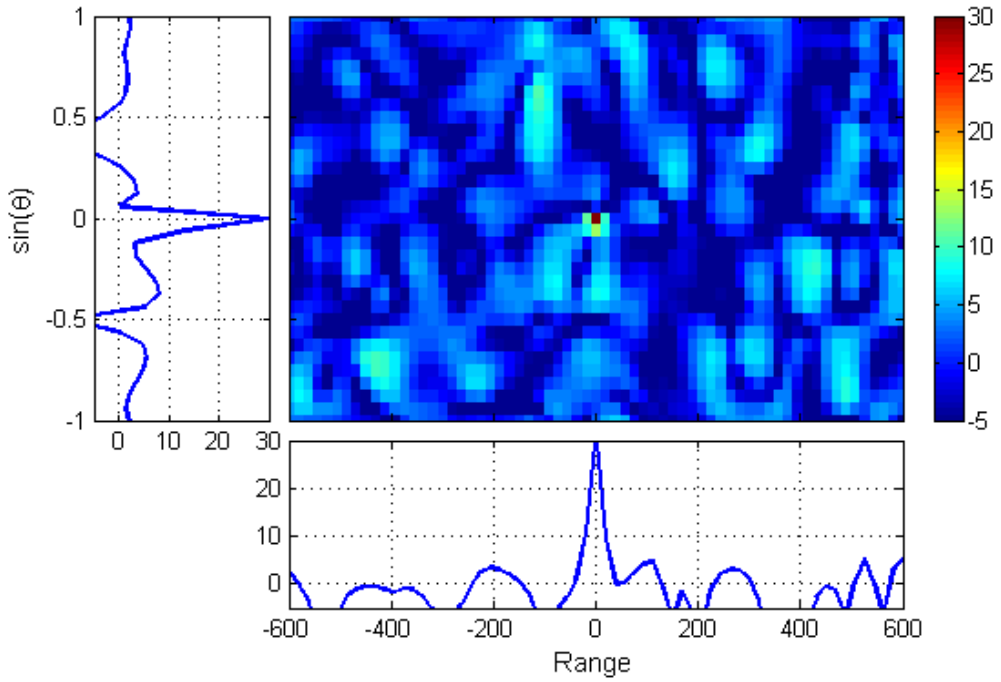

Figure 3.5: IAA estimation (iteration 7) on range-angle domain from simulated MIMO waveforms (Gold phase codes) plus noise transmitted to one point target. Cuts at target range and angle are plotted on each side.

this approach in the context of MIMO radar is that, similarly to the already-presented adaptive processing schemes, it allows accurate high-resolution estimates, but with a small number of data snapshots instead – up to one unique snapshot, possibly.

We express here the iterative estimation process at step n ($n \geq 1$):

$$\hat{\alpha}_n\left(r_i,\theta_j\right) = \frac{\tilde{\mathbf{a}}^H\left(r_i,\theta_j\right)\Gamma_{n-1}^{-1}\tilde{\mathbf{z}}}{\tilde{\mathbf{a}}^H\left(r_i,\theta_j\right)\Gamma_{n-1}^{-1}\tilde{\mathbf{a}}\left(r_i,\theta_j\right)} \tag{3.13}$$

$$\Gamma_n = \sum_{i,j}\left|\hat{\alpha}_n\left(r_i,\theta_j\right)\right|^2\tilde{\mathbf{a}}\left(r_i,\theta_j\right)\tilde{\mathbf{a}}^H\left(r_i,\theta_j\right) \tag{3.14}$$

with Γ_0 initialized to the identity matrix $\mathbf{I}$, and $\left(r_i,\theta_j\right)$ taking all the (r,θ) values of the parameter grid.

This approach can be interpreted as a Capon estimation where the covariance matrix is actually estimated on one (or a few) snapshot(s). In the process, the covariance matrix is built iteratively: it is computed from an approximated output (started with the MF output) which is progressively “sharpened" at each new iteration.

The IAA in MIMO Radar Context

The IAA is expected to give accurate estimations of the target parameters while dramatically mitigating the sidelobes, even with a very small number of snapshots. As an illustration, we have applied the IAA on the signal obtained from the simulation with the phase codes described previously in this section. Only one realization (*i.e.* one single pulse) has been considered for $\tilde{\mathbf{z}}$. Note that even if not mentioned in the literature, we make a “diagonal loading" of the covariance matrice with the expected value of the noise power, in order to make it have full rank. The results after 7 iterations of the algorithm are displayed in fig. 3.5. Clearly, the mainlobe has become much narrower than with MF – and still at 30 dB – while the sidelobes have been mitigated to the expected level of 0 dB, *i.e.* to noise level.

The significant drawback of this method is its high computational complexity (also mentioned in [38]). The impact can be dramatic in terms of computation time in the situation of MIMO radar where a covariance matrix of size $MK \times MK$ (or much more if Doppler is considered) has to be inverted. As an illustration, it has been experienced in the specific context of the simulations exposed here that the IAA could be 10^3 times slower to compute than classical techniques like the MF.

Finally, due to its merits in terms of estimation accuracy and training data frugality, it has been decided to consider the IAA as a “reference technique" for the comparison of detection performance with the next proposed techniques.

3.2.4 Orthogonal Matching Pursuit (OMP)

We first focus on the Matching Pursuit (MP) algorithm that decomposes a measured signal into the contributions of several waveforms piked up from a predefined dictionary [47]. This leads to the OMP [48], a similar algorithm that consists in building an approximation of the multitarget MF. It permits to successively detect and reject each contribution – and the associated sidelobes thus – of the strong targets. Initialized with $\tilde{\mathbf{z}}_1 = \tilde{\mathbf{z}}$, the proposed algorithm follows an iterative procedure, that we display here at k^{th} iteration ($k \geq 1$):

Detection step: find $\left(\hat{r}_k, \hat{\theta}_k\right) = \underset{r,\theta}{\arg\max} \dfrac{\left|\tilde{\mathbf{a}}(r,\theta)^H \tilde{\mathbf{z}}_k\right|^2}{\tilde{\mathbf{a}}(r,\theta)^H \tilde{\mathbf{a}}(r,\theta)}$

Rejection step: $\tilde{\mathbf{z}}_{k+1} = \left(\mathbf{I} - \tilde{\mathbf{A}}_k \left(\tilde{\mathbf{A}}_k^H \tilde{\mathbf{A}}_k\right)^{-1} \tilde{\mathbf{A}}_k^H\right) \tilde{\mathbf{z}}$

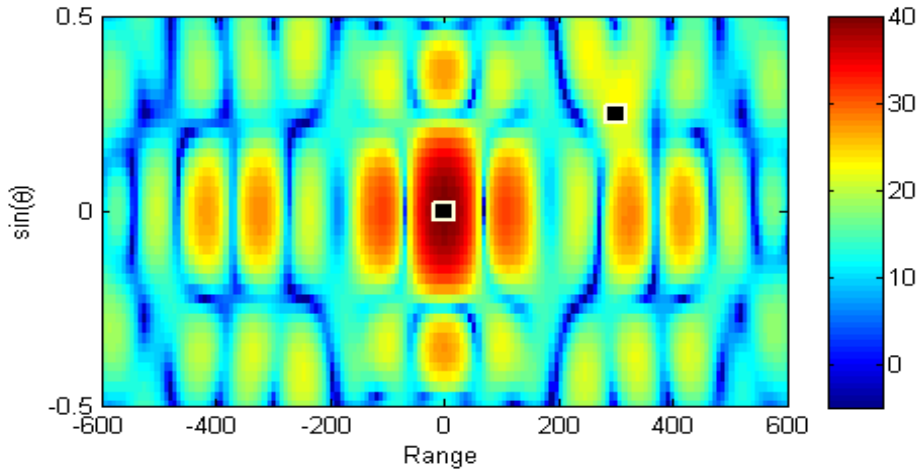

(a) Initialization (MF estimation). Target localizations are represented by the black marks.

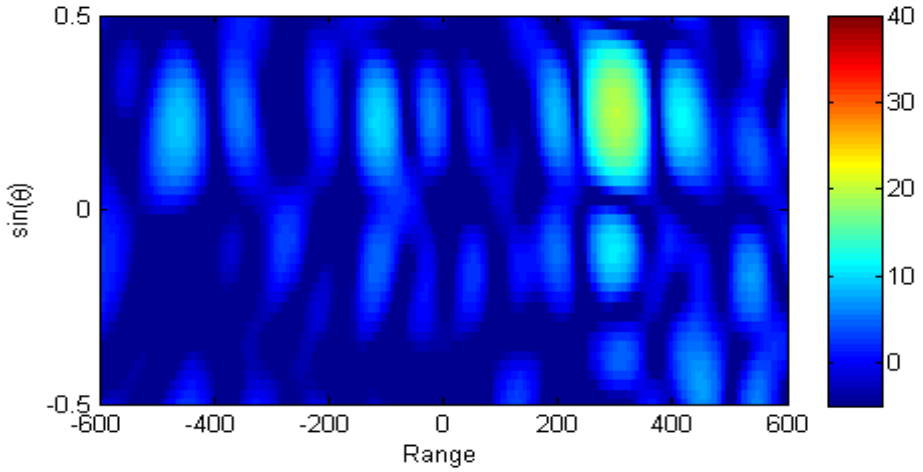

(b) After first rejection.

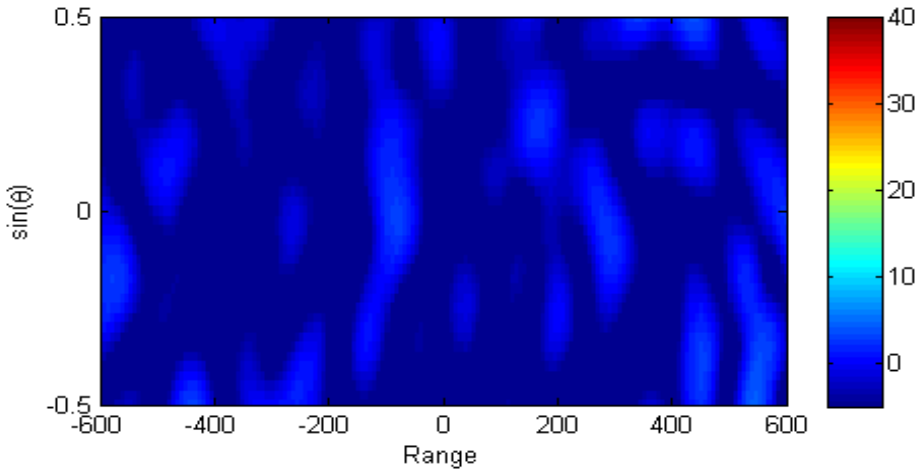

(c) After second rejection.

Figure 3.6: Successive steps of OMP estimation on range-angle domain from simulated MIMO waveforms (Gold phase codes) transmitted to two point targets, plus noise.

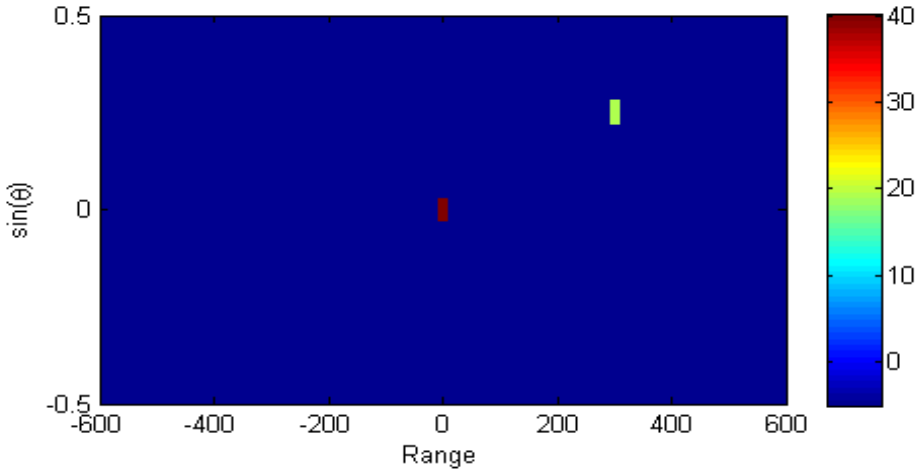

(d) Final output (detection).

Figure 3.6: *Continued.*

$$\text{with } \tilde{\mathbf{A}}_k = \begin{cases} \tilde{\mathbf{a}}\left(\hat{r}_1, \hat{\theta}_1\right) & \text{if } k = 1 \\ \left[\tilde{\mathbf{A}}_{k-1},\, \tilde{\mathbf{a}}\left(\hat{r}_k, \hat{\theta}_k\right)\right] = \left[\tilde{\mathbf{a}}\left(\hat{r}_1, \hat{\theta}_1\right), \cdots, \tilde{\mathbf{a}}\left(\hat{r}_k, \hat{\theta}_k\right)\right] & \text{otherwise} \end{cases}$$

In other words, at each iteration k, the algorithm detects the predominant value of the MF output and attributes the corresponding localization $\left(\hat{r}_k, \hat{\theta}_k\right)$ to the newly detected target. Then, the algorithm “filters out" this localization from the target parameter space. It results in removing all contributions of the detected target in the output of the MF, and it makes it possible then to detect the targets of lower power which were possibly “buried" in the sidelobes of the original predominant targets. The iterations are usually stopped when a certain stopping criteria is satisfied. For example, a detection threshold can be set to insure a specific false alarm rate. In the following, we will consider a stopping threshold at 10 dB (after processing) over noise level, which corresponds for MF in Gaussian noise to a probability of false alarm of 4.5×10^{-5}.

To illustrate how the OMP algorithm operates, we make here a simulation with the parameters introduced above, plus a second target:

- Target 1: $\text{SNR}_1 = 40\text{dB}$, $r_1 = 0\text{m}$, $\sin\theta_1 = 0$
- Target 2: $\text{SNR}_2 = 20\text{dB}$, $r_2 = 300\text{m}$, $\sin\theta_2 = 0.25$

In this situation, the peak power of the second target is 20 dB below the peak power of the first target, *i.e.* below the strongest residual sidelobes induces by the first target.

With the MF only, this second target cannot be detected, as illustrated in fig. 3.6a. With the OMP algorithm, one clearly notices in fig. 3.6b the effect of the detection and rejection of the first target: the associated pattern has been removed from the ambiguity function, so that it is now possible to distinguish the second target pattern. The next step of detection and rejection of the second target allows to reach the noise level at around 0 dB, as visible in fig. 3.6c. The algorithm cannot detect anymore targets above the threshold and then stops. The final target detections are displayed in fig. 3.6d.

Concerning the computation complexity, we can make the following considerations:

- Number of iterations: limited to the total number of targets detected.
- Matrix inversion: the matrix $\tilde{\mathbf{A}}_k$ to be inverted at iteration k (*i.e.* for the detection of the k^{th} target) is of size $k \times k$.

The other operations are of negligible complexity with respect to the two listed above. Therefore, it has been exhibited that the OMP algorithm has at first order a complexity related to the number of targets detected, and little sensitivity to the scene parameters (number of resolution cells, etc.). This is an advantageous point of the OMP for radar applications, since the number of targets is typically much smaller than the number of resolution cells of the scene. As an example, it has been experienced from the simulations processed that the computation time for OMP was greater but still of the same order of magnitude as the MF.

Finally, due to its merit in terms of fast computing and training data frugality, the OMP has been exhibited to be a convenient processing scheme candidate to go beyond the MF detection performance in radar operational conditions. We will now focus on the qualification of its main limitations and study possible compensation strategies.

3.3 OMP Robustification to Localization Error

3.3.1 The Target Localization Issue

The target detection is processed over the target scanning grid, which is a discretization of the target parameter space, (r,θ) in our case. Each node on the grid corresponds to a different parameter hypothesis. The OMP detection step is therefore likely to

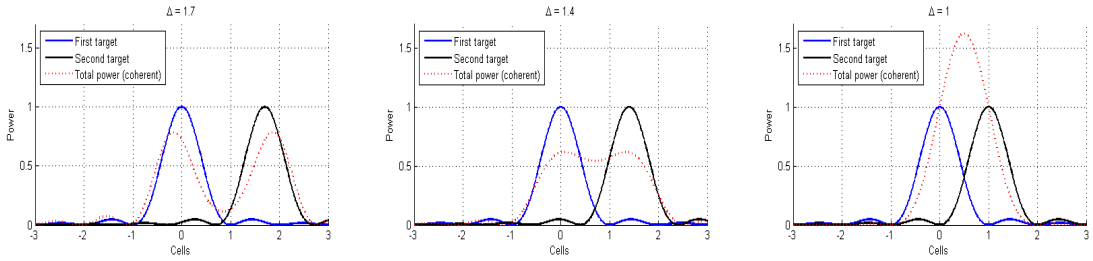

(a) 1.7 cell width distance. (b) 1.4 cell width distance. (c) 1.0 cell width distance.

Figure 3.7: Effect on target localization of two coherent targets of same amplitude and phase (worst case) at different distances.

attribute a biased localization for the target to detect. Two different causes can be identified:

Granularity of the grid: it is unlikely that a node of the scanning grid corresponds exactly to the arguments of the real maximum of the ambiguity function. Therefore, the algorithm will attribute a nearby node for the estimated localization of the detected target. A possible solution to this issue is to increase the density of the grid, but it consequently increases the computational complexity in the same time.

Close targets: since the MF is optimal for one single target only, the detection of a target may be biased by the presence of another close target. Indeed, the algorithm finds the maximum of the output of the MF, and in some cases, the powers from two close targets add up so to create a single maximum between these two targets. In this situation, increasing the grid density is useless. Nevertheless, it is possible to determine the “minimum resolvable distance" (similar to Rayleigh criterion in optics). In the worst case, this distance is around the width of the resolution cell. This effect is illustrated on fig. 3.7 for two sinc functions at different distances.

In classical OMP, it is therefore crucial to accurately estimate the localization of each target – especially the ones of strong power –, because an error on localization is likely to lead to residues and therefore induce possible additional detection of “ghost" targets.

3.3.2 Robustification Through Extension of the Rejection Area

A possible improvement to localization error issues has been proposed in [49]: it consists in estimating jointly at each iteration the target states in the maximum

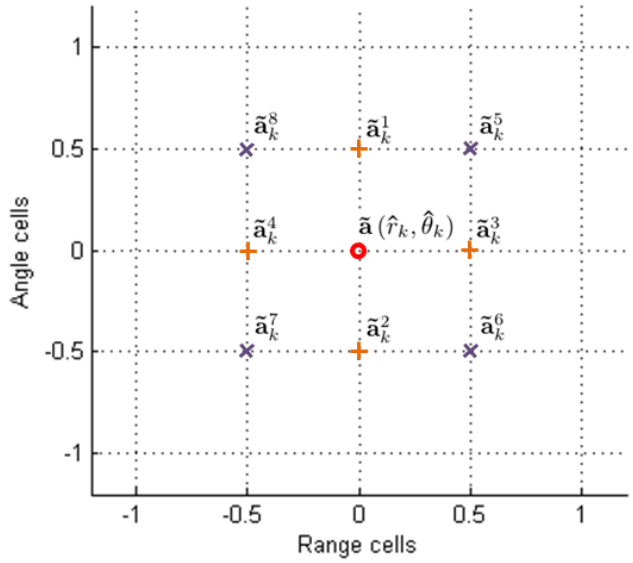

Figure 3.8: Neighbor localizations (in target space) to consider for the extended rejection at step k, relatively to the estimated localization (r_k,θ_k) of the predominant target.

likelihood sense. This copes with the problem of grid granularity but it will still be sensitive to the pernicious influence of neighbor targets. We propose here to take into consideration the localization uncertainty due to both scanning grid granularity and neighbor targets influence. Instead of removing the estimated – and possibly biased – position of the target only, we try to remove all possible positions of the target. Considering the two identified causes of biased localization, one can deduce that the uncertainty on localization is smaller than the resolution cell width (for each parameter to estimate). Of course, we consider that there is at least one node in each resolution cell. Besides, the cell width corresponds to the precision bound on localization, so the impact of the extension of rejection area on this precision will be limited if we filter targets with a granularity of the cell size.

To augment the robustness of the classical OMP with respect to localization error, we propose, at each rejection step, to concatenate into $\tilde{\mathbf{A}}_k$ the estimated target contribution $\tilde{\mathbf{a}}\left(\hat{r}_k,\hat{\theta}_k\right)$ and also those of close neighbor targets. We focus on the extension for the rejection step that considers the localization $\left(\hat{r}_k,\hat{\theta}_k\right)$ and its eight neighbors represented in fig. 3.8:

$$\tilde{\mathbf{A}}_k = \left[\tilde{\mathbf{A}}_{k-1}, \tilde{\mathbf{a}}\left(\hat{r}_k,\hat{\theta}_k\right), \tilde{\mathbf{a}}_k^1, \tilde{\mathbf{a}}_k^2, \tilde{\mathbf{a}}_k^3, \tilde{\mathbf{a}}_k^4, \tilde{\mathbf{a}}_k^5, \tilde{\mathbf{a}}_k^6, \tilde{\mathbf{a}}_k^7, \tilde{\mathbf{a}}_k^8\right] \tag{3.15}$$

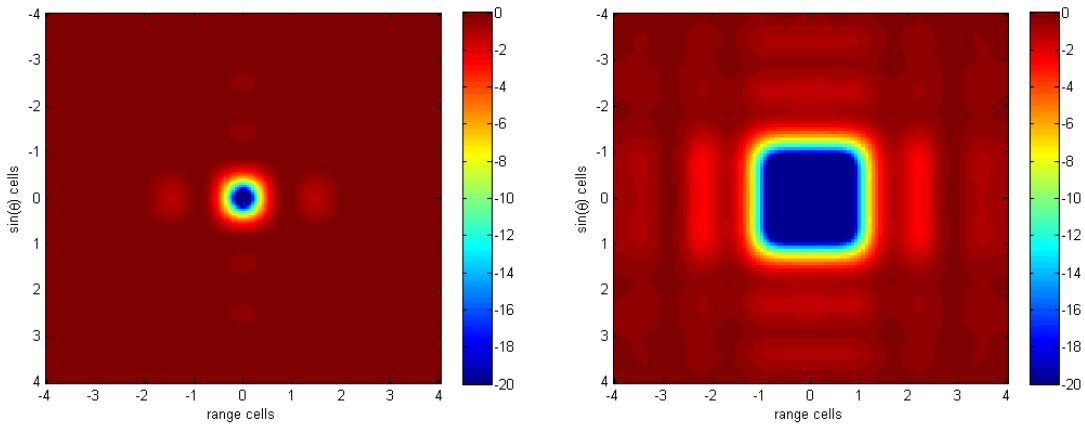

(a) Classical OMP rejection.

(b) Extended OMP rejection.

Figure 3.9: Power gain in target parameter space after one rejection.

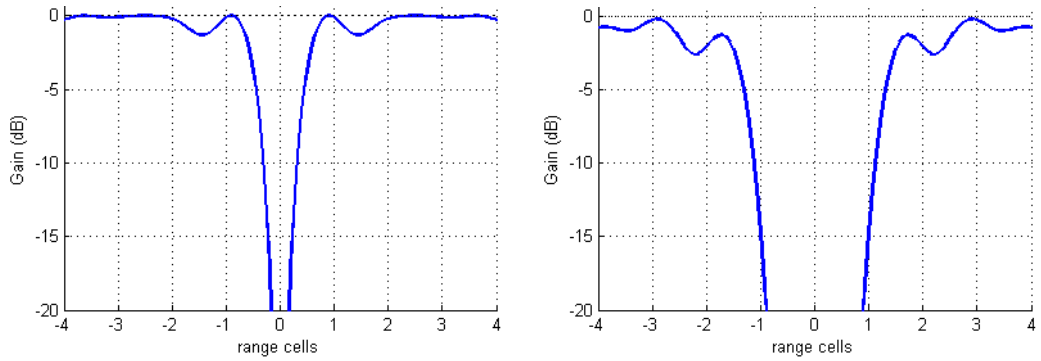

(a) Classical OMP rejection.

(b) Extended OMP rejection.

Figure 3.10: Range cut of power gain in target parameter space after one rejection.

In formal words, for the extension of rejection step k, we concatenate $\tilde{\mathbf{A}}_{k-1}$ with the nine following vectors into $\tilde{\mathbf{A}}_k$:

$$\left\{ \tilde{\mathbf{a}}\left(\hat{r}_k + \epsilon_r \frac{\Delta r}{2},\, \hat{\theta}_k + \epsilon_\theta \frac{\Delta\theta}{2}\right) \,\middle|\, \epsilon_r \in \{-1,0,1\},\, \epsilon_\theta \in \{-1,0,1\} \right\} \tag{3.16}$$

with Δr and $\Delta\theta$ the resolution cell widths for range and angle, respectively. Typically, $\Delta r = \frac{c}{2B}$ and $\Delta\theta = \arcsin\left(\frac{\lambda}{L}\right)$, with λ the transmission wavelength and L the whole radar Tx antenna length.

The effects of the classical rejection and the extended rejection on the power gain of the rejection step in target parameter space are displayed in fig. 3.9. It can be noticed that the extended rejection mitigates the complete cell, when the classical rejection

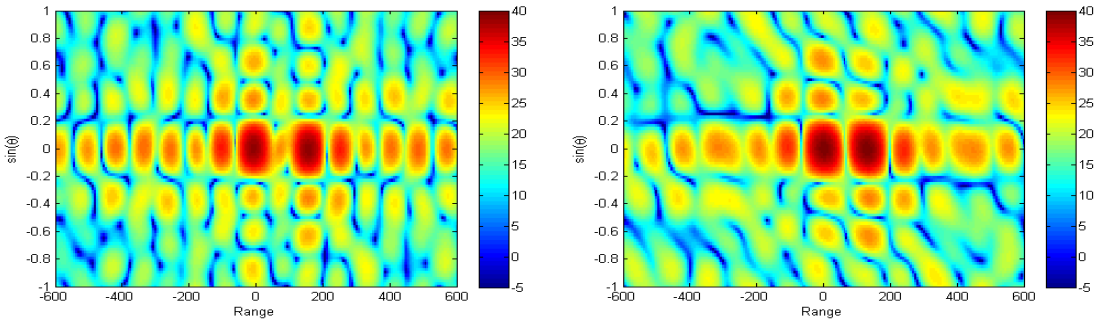

(a) $d = 2.00$.

(b) $d = 1.75$.

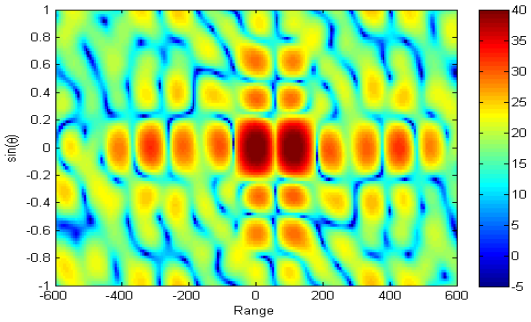

(c) $d = 1.50$.

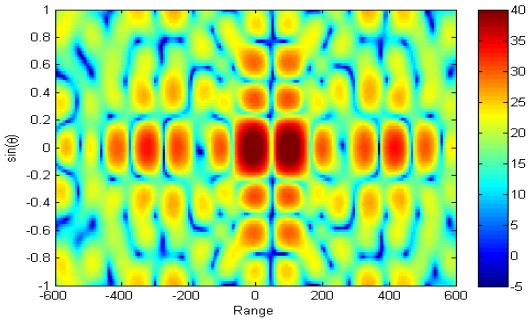

(d) $d = 1.25$.

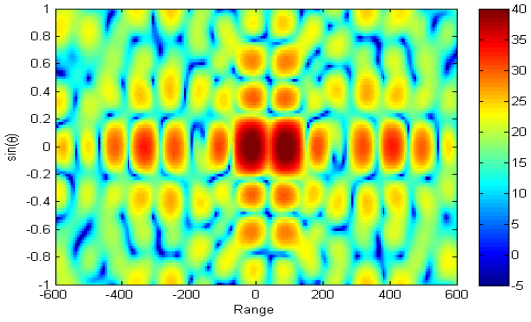

(e) $d = 1.00$.

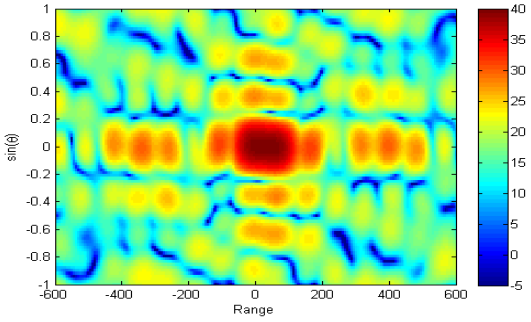

(f) $d = 0.75$.

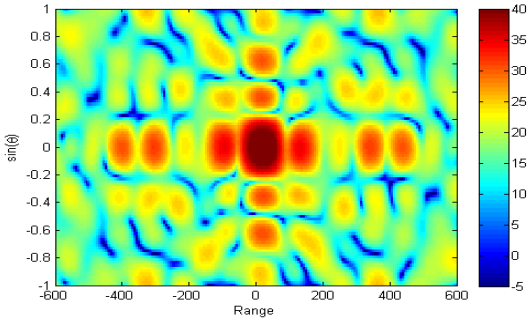

(g) $d = 0.50$.

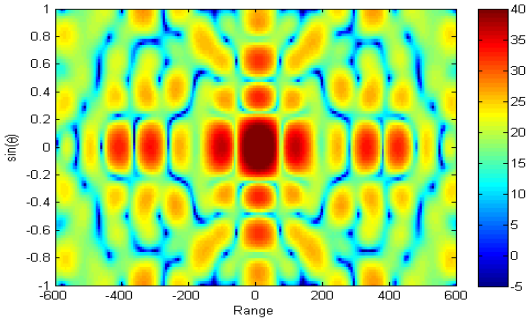

(h) $d = 0.25$.

Figure 3.11: Output of MF for two targets at 40 dB of SNR for different distances d (in number of range cell widths). Range resolution cell width = 75 m, $\sin\theta$ resolution cell width = 0.25.

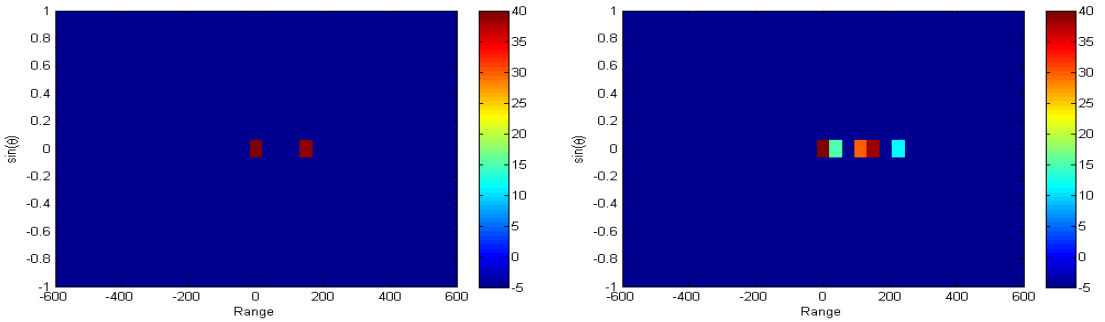

(a) $d = 2.00$.

(b) $d = 1.75$.

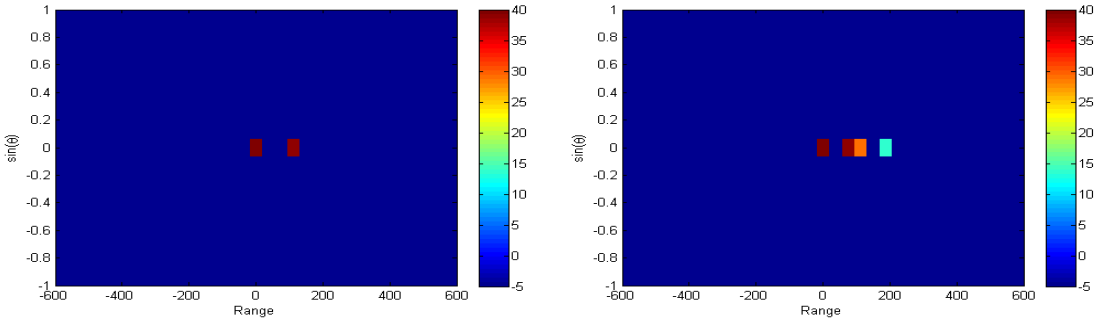

(c) $d = 1.50$.

(d) $d = 1.25$.

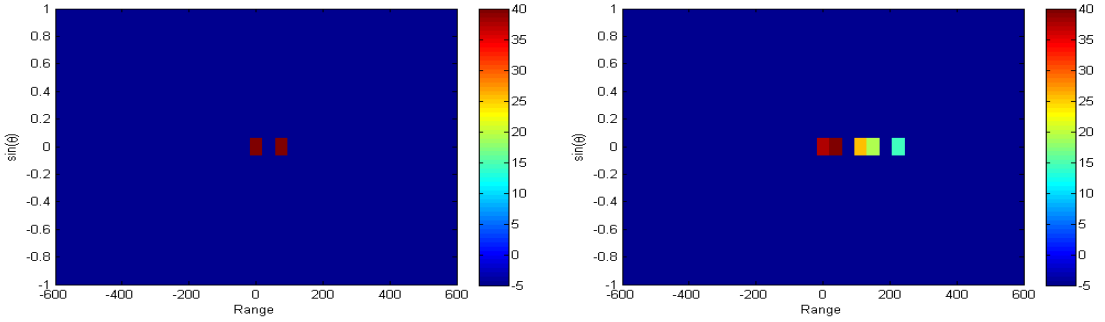

(e) $d = 1.00$.

(f) $d = 0.75$.

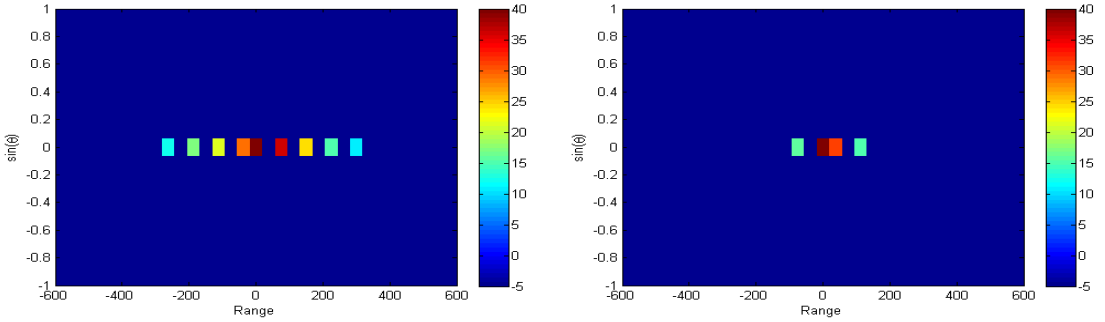

(g) $d = 0.50$.

(h) $d = 0.25$.

Figure 3.12: Output of classical OMP for two targets at 40 dB of SNR for different distances d (in number of range cell widths). Range resolution cell width = 75 m, $\sin\theta$ resolution cell width = 0.25.

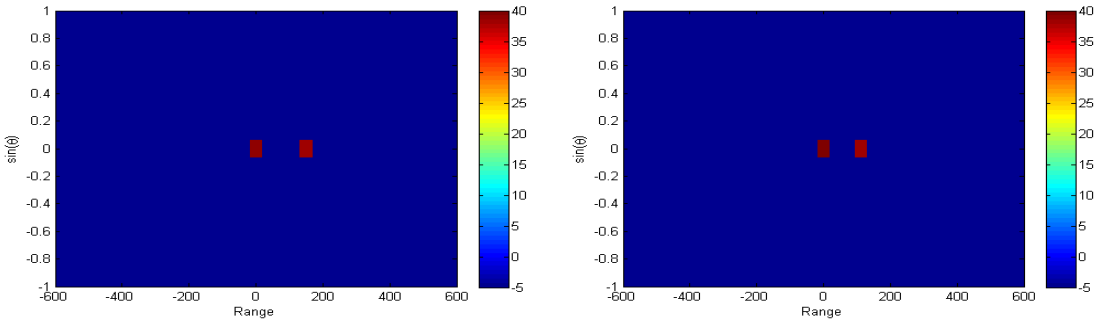

(a) $d = 2.00$.

(b) $d = 1.75$.

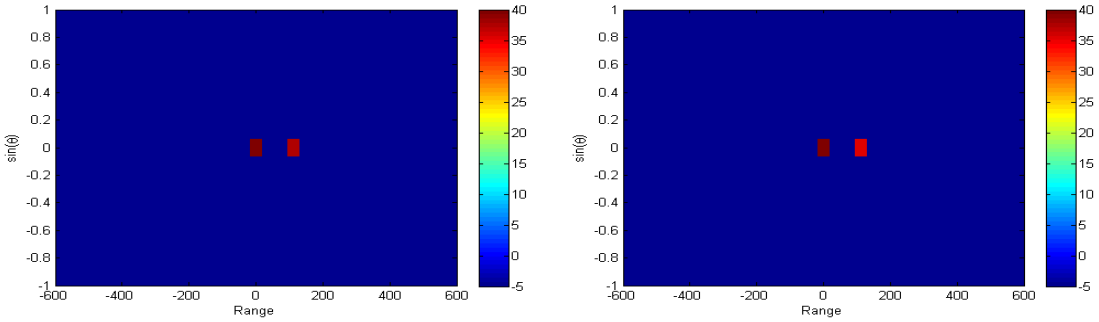

(c) $d = 1.50$.

(d) $d = 1.25$.

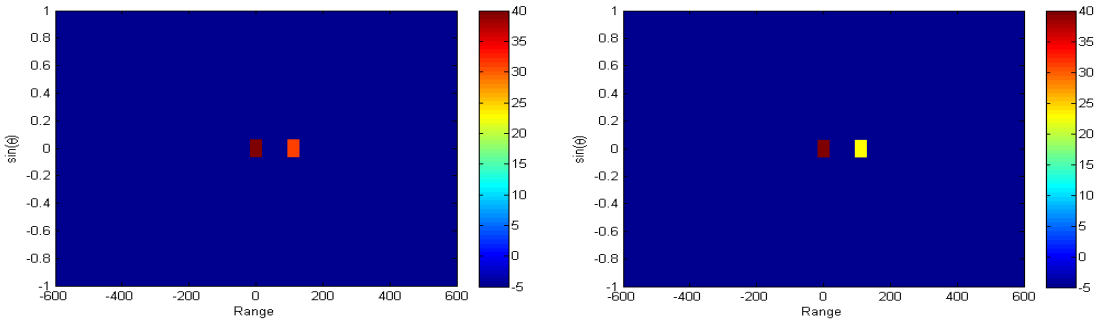

(e) $d = 1.00$.

(f) $d = 0.75$.

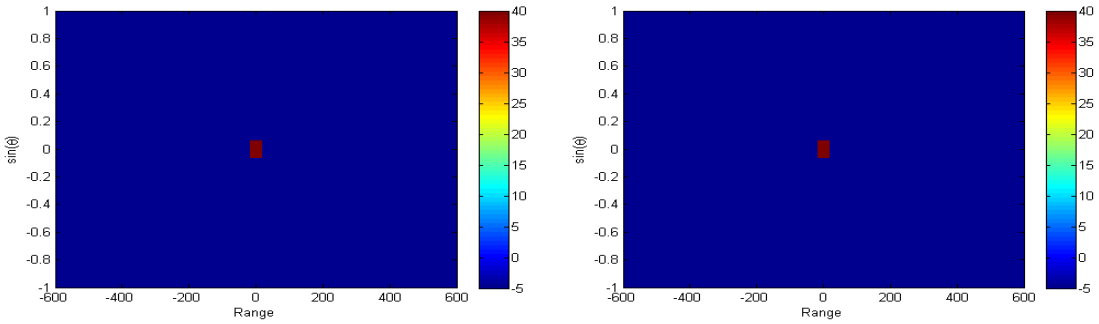

(g) $d = 0.50$.

(h) $d = 0.25$.

Figure 3.13: Output of extended OMP for two targets at 40 dB of SNR for different distances d (in number of range cell widths). Range resolution cell width = 75 m, $\sin\theta$ resolution cell width = 0.25.

mitigates only a reduced area around the considered localization. This effect is even more visible on the comparison of the gain profiles for the range cuts at target angle displayed in fig. 3.10.

Besides, it is worth noticing that this wider filtered area is at the price of power mitigation of the direct adjacent cells (up to 15 dB). This can have an impact on detection capacity on these cells. Nevertheless, the next neighbor cells are subject to no more than a marginal loss.

3.3.3 Exhibition of the Detection Performance Improvement

We will now introduce different scenarios in order to exhibit the improvement of robustness with respect to the localization bias. In this section (as well as all the previous simulations, implicitly), we consider that all simulated signals fulfill signal model assumptions, *i.e.* no signal distortions considered. In other words, we assume that the general form of the received signal does not differ from the expected expression (2.13).

Simulation of Two Targets at Different Close Distances

In order to evaluate the “side effect" of the extended rejection method, *i.e.* how the filter manages two neighbor targets at around one resolution cell width of distance, we define a scenario of two targets (same SNR of 40 dB) with a decreasing distance d from 2 to 0.25 with steps of 0.25 range cell distances. For the OMP detection steps, we consider a target grid made of two nodes per cell dimension. The left-hand target is fixed on a grid node, while the right-hand target has a changing position, localized on a node only when its distance to the left target is a multiple of 0.5 cell width. To make the comparison, we calculate for each scenario the output of the MF, the results after classical OMP and the results after the OMP with extended rejection area. The results are displayed in fig. 3.11, fig. 3.12 and fig. 3.13, respectively. We can deduce the following analysis:

- It is clear from the ambiguity function (MF) that many residual sidelobes are induced in a large area around the two target localizations. Besides, for $d \in \{0.75, 0.5, 0.25\}$, it can be seen that the two close targets induce a unique main lobe, which will give one unique detection at a localization between the two

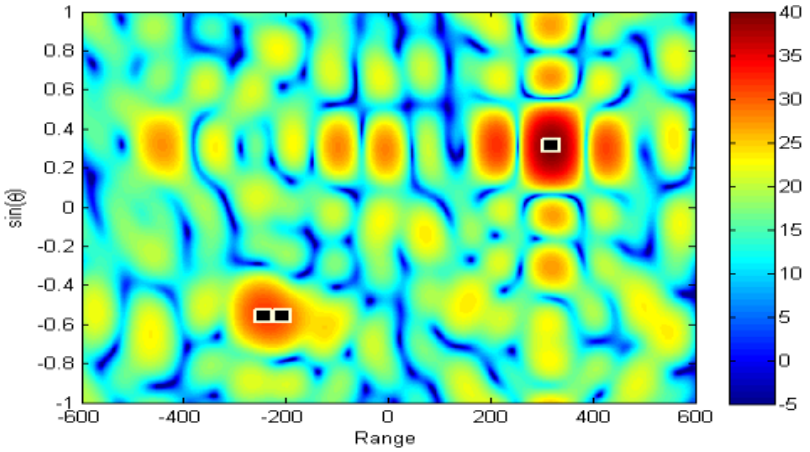

(a) MF output. The targets are localized with the black marks.

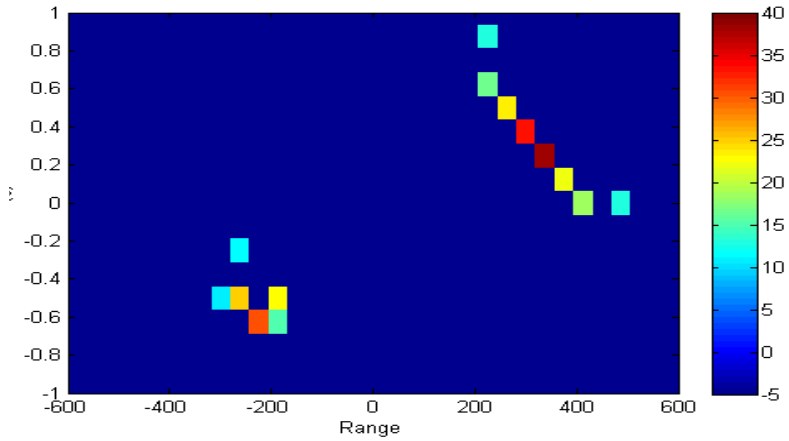

(b) OMP output – classical rejection.

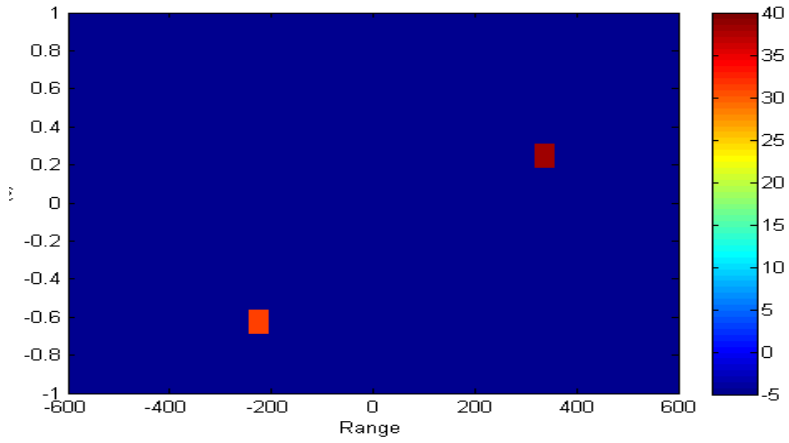

(c) OMP output – extended rejection.

Figure 3.14: Target detection for the proposed “pernicious" scenario, from simulated CDMA waveforms (Gold phase codes). Range resolution cell width = 75 m, $\sin\theta$ resolution cell width = 0.25.

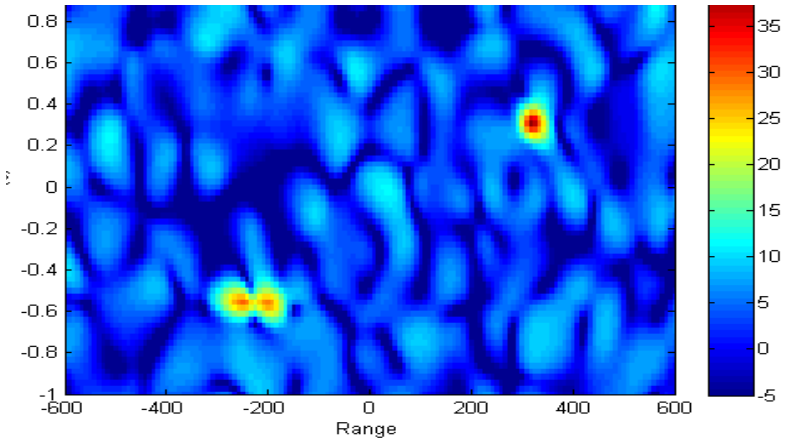

(d) IAA output (iteration 11).

Figure 3.14: *Continued.*

targets.

- For $d \in \{2, 1.5, 1\}$, both targets are on a node of the grid and the mutual influence is still low (nominal case). For both classical and extended OMP rejection methods, we get two detected targets at correct localizations, without any ghost detection, as expected.

- For $d \in \{1.75, 1.25\}$, one of the two targets is situated between two nodes of the grid and therefore its detected localization is biased due to grid granularity. The two targets are localized correctly (relatively to grid resolution) but it induces several ghost targets for classical OMP, whereas none for the extended OMP rejection.

- For $d \in \{0.75, 0.25\}$ where we face both issues, ghost targets are induced for classical OMP but avoided for the extended OMP rejection.

- For $d = 0.5$, where only neighbor target influence occurs, it leads to numerous ghost targets for classical OMP, whereas none for the extended OMP rejection.

- For $d \in \{1.25, 1, 0.75\}$, note that with the extended OMP, the right-hand target is detected with an estimated power lower than the exact one (up to 17 dB loss for $d = 0.75$).

Besides, note that due to the resolution bound, it is not a special issue if two close targets ($d < 1$) are attributed to the same resolution cell.

Eventually, we have shown that for these scenarios, the proposed extension for the OMP rejection step correctly solves the issues of grid granularity and neighbor target influence.

Simulation of a Pernicious Scenario

The idea here is to test the performance of the proposed extension on a more complex scenario. We define here again a “non-dense" grid of two nodes per cell dimension, and a “pernicious" scenario: one target of SNR = 40 dB at the “center" of four nodes of the grid, two close targets of 30 dB of SNR at half-cell distance (and also not located on nodes). The localization of these targets is displayed with the black marks in fig. 3.14a. The resulting MF output is also given in this figure, so to display the initial sidelobes. The outputs for each rejection of the OMP are computed and exhibited. The classical OMP rejection (fig. 3.14b) induces numerous ghost targets, whereas the extended rejection (fig. 3.14c) gives accurate results. Besides, note that there is one unique detection for the two close targets. Actually, one of the two targets has been filtered out during rejection of the other one, since both are located in the same resolution cell (and this is therefore no issue). For the comparison, we have also computed the IAA output from the simulated data. It can be deduced from fig. 3.14d that the three targets are correctly estimated (localization and power) and that the residual sidelobes have been mitigated to noise level.

3.4 Conclusion

In this chapter, we have introduced different processing schemes for inverse problem solving that were expected to accurately estimate the target parameters and eliminate the residual sidelobes caused by the CDMA waveforms. In the literature, many of these techniques have been shown to be performing in their respective context. For our specific situation of ground MIMO radar that should not only be performing but also implementable in real conditions, strict constraints are imposed. We have especially mentioned limitations on computation time and on number of training data.

In this regard, the OMP has been introduced here, and we could exhibit that it satisfies these latter requirements. Indeed, this scheme allows an accurate detection of targets – even those initially buried in residual sidelobes – with substantial complexity limitation and no need for training data. Yet, we have illustrated the sensitivity of

the OMP to the target localization errors and the potential impact in terms of false alarm in detection. We have then proposed an extension for the rejection step of the algorithm and we have shown that this strategy provides satisfying robustness with respect to target localization error. In parallel, we have selected the IAA as a reference scheme for the evaluation of OMP performance. Indeed, its accuracy in detection is well-known, but its computational complexity makes it not suitable for many operational scenarios.

Now, we propose to question about the sensitivity of the processing methods with respect to signal distortions. Indeed, it has been assumed till here that the considered signals always matched the model assumptions. But when it is not the case, adaptive methods are known to be much less tolerant than MF.

4 Model Mismatches: Analysis of Impact and Strategies of Prevention

4.1 Introduction

The adaptive methods (*e.g.* Capon, etc.) usually rely on the detection of the “pattern" of each target in the ambiguity function, and the rejection of all other signals that do not match the expected model. The signal model is built on assumptions concerning the spatial geometry and the transmitted waveforms. Thus, if an echo of interest differs from this expected model, it may be partially detected, or even filtered out. The difference between the expected signal and the one received in reality can induce artifacts in the ambiguity function. Therefore, any distortion of the transmitted signals may have an impact on the detection performance at processing output. Moreover, a processing scheme that presents good performance in ideal conditions can greatly suffer from signal model mismatches in real conditions, according to its specific sensitivity to this issue.

In this chapter, once stated that signal distortion is inevitable in the real world, we will present some examples of discrepancies which are often not taken into account in the ideal – and simplified, thus – signal models, but are likely to be encountered during generation, propagation and reception of MIMO radar signals. We will evaluate to which extent the proposed processing schemes are sensitive to model mismatches, and investigate their possible impact on the ambiguity functions and so on detection performance.

Then, we will address possible strategies for preventing signal distortions to occur. In this context,we will present the MIMO-capable radar testbed conceived at ONERA, with a special focus on the hardware specification and calibration considerations

during the system conception. We will also describe how MIMO radar architectures can bring more flexibility and simplicity for system monitoring and calibration. For the illustration of this concept, we will propose a method of auto-calibration of the transmitter phases after signal reception and exhibit its performance on experimental MIMO signals acquired in real conditions.

4.2 Impact of Signal Model Mismatches

4.2.1 Origins of Signal Model Mismatches

Non-Linearities in the Radar Chain

Hardware components (*e.g.* amplifiers) are likely to partially work out of the linear operating range or even totally in saturation. Besides, some components do not have a linear profile. It also happens that components have different behavior depending on the frequency (*e.g.* when operating at the edge of the bandwidth, or when subject to band-stop filtering). Through measurements, it is usually possible to determine the global behavior of the hardware chain. Nevertheless, some component properties can still change with time depending on the environmental conditions, like aging, temperature or humidity.

Lack of Alignment Between Channels

For MIMO radar systems, different waveforms must be generated simultaneously and transmitted into independent channels to the antennas. Difference of radio electric paths, especially when dealing with wideband signals, is likely to happen. This leads to phase offsets between transmitters, all the more so for high frequencies. This effect can be generally measured and compensated, through radar closed-loop and line length calibration for example. Besides, a phenomenon of jitter can also concern the transmitter phase alignment. It can be induced by the waveform generators that suffer from an imprecise trigger synchronization. Indeed, the rising edge of the synchronization clock has no infinite slope in practice, and for high sampling frequencies, different triggering times can be delivered to the waveform generators. It might result in time delay – and therefore phase offset – between transmitters.

Antenna Mutual Coupling

The electromagnetic interaction between the radiating elements induces additional currents and modifies the impedance of each of them. This phenomenon of antenna coupling originates from direct electromagnetic influence and reflection on metallic parts of the antenna. This effect is therefore determined by the geometry of the array, and is likely to change the phase and amplitude of the current that feds the antennas. With conventional phased arrays, where the same waveform is radiated on each element, the antenna coupling is generally seen as a distortion of the beam pattern that yet stays constant with time (for a specific frequency). On the contrary, the MIMO arrays are subject to more complexity since each channel of transmission is independent and the antennas radiate different waveforms simultaneously. Therefore, the resulting beam pattern on transmit is a “chaotic" shape that changes constantly with time. The received voltage on each element will depend not only on the incident field, but also on the voltages on the other elements [50].

Fast Moving Targets

In section 2.3.1, we have made the hypothesis of slow moving targets. Due to the Doppler effect, the phase of the signal from a target evolves during the pulse. Writing f_d the Doppler frequency of the faster target of the scene ($f_d = 2v/\lambda$, with v the target radial speed and λ the signal wavelength), the phase evolution due to target speed during the pulse can be neglected as long as the hypothesis $T_p f_d < 0.1$ is satisfied [51]. We can deduce the condition on the speed v of the considered target:

$$v < \frac{0.1\lambda}{2T_p} \tag{4.1}$$

For $T_p = 50$ µs and $\lambda = 0.1$ m (S band), the condition corresponds to: $v < 100$ m/s.

Therefore, for any target with a radial speed larger than 100 m/s (*i.e.* more than 360 km/h), the resulting Doppler will induce a model mismatch on the received signal. Then, during the signal processing, it may lead to distortions like loss on the detected power.

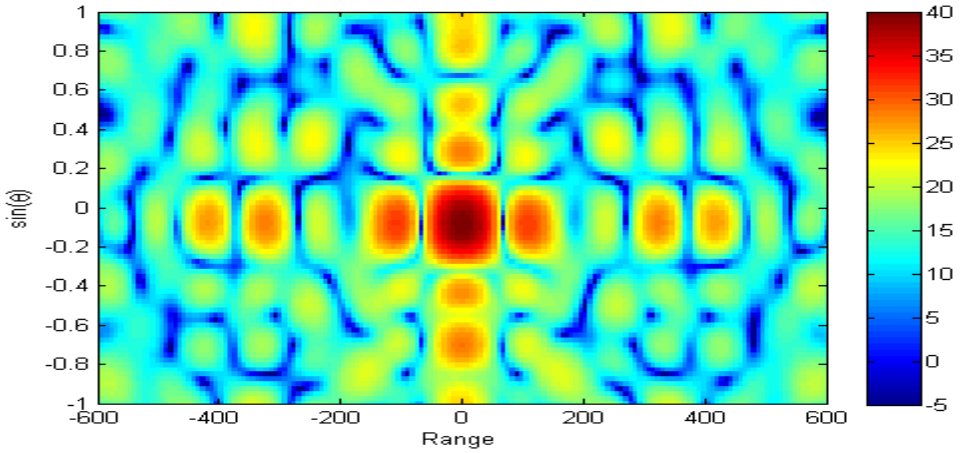

(a) MF.

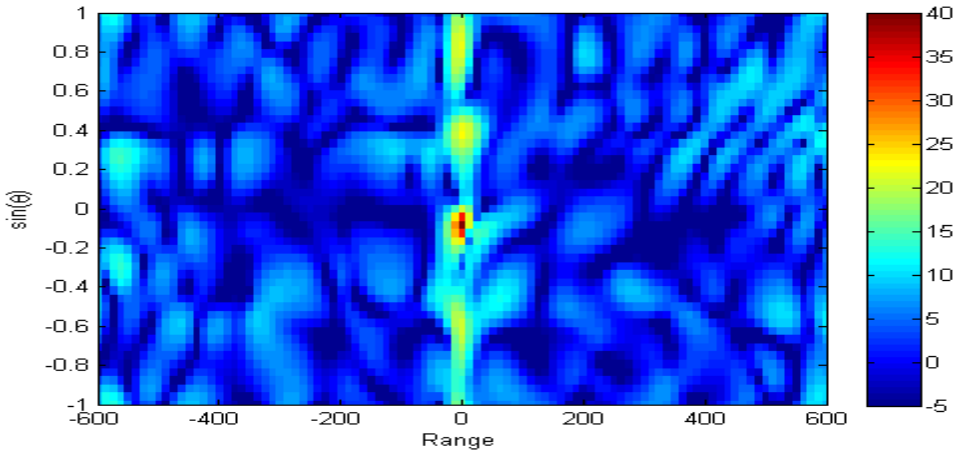

(b) IAA (iteration 10).

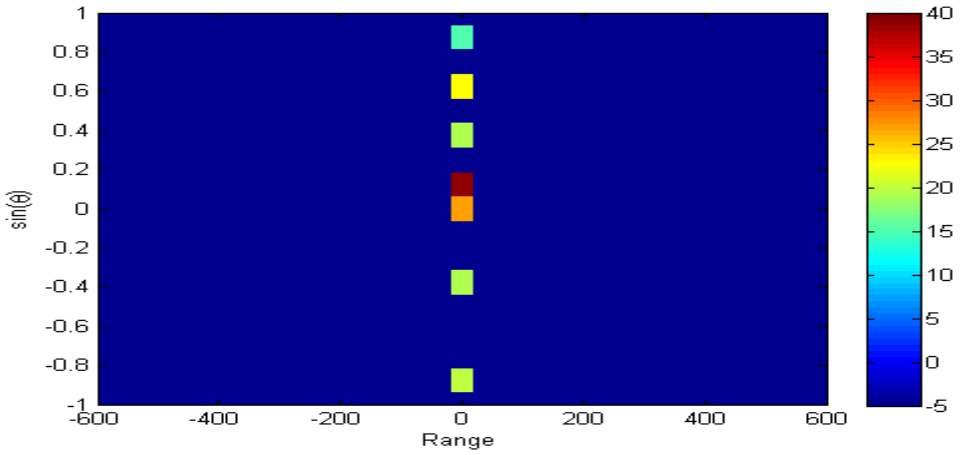

(c) OMP – Classical rejection.

Figure 4.1: Output of different processing schemes from simulated CDMA waveforms with one point target, and phase and modulus errors on transmitters. Range resolution cell width = 75 m, $\sin\theta$ resolution cell width = 0.25.

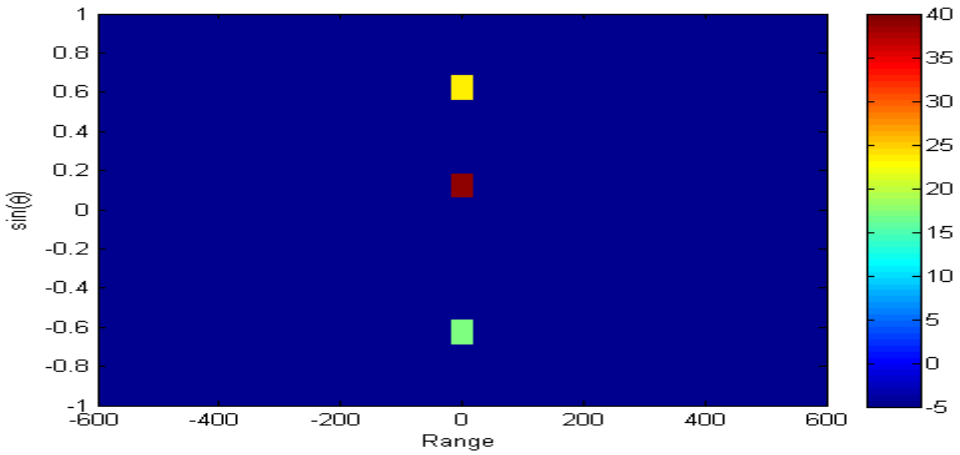

(d) OMP – Extended rejection.

Figure 4.1: *Continued.*

4.2.2 Processing Sensitivity to Model Mismatches

We will now give some elements of discussion on induced detection performance degradation in the case that the received signal differs from the expected expression of (2.13). The idea is to give insight to which extent the introduced processing schemes are robust to representative model mismatches. The objective is not to experiment the effect of each signal mismatches separately, but to illustrate the induced effect globally, and compare the sensitivity of the MF, IAA and OMP schemes to signal distortions.

In this purpose, we will exhibit the impact of random errors on transmitters. More precisely, we set up a simulation of one point target with the same parameters as section 3.2.1, and with random discrepancies (phase and modulus) on each transmission channel, constant with time, with standard deviations of $2\pi/10$ for the phase, and 10% for the modulus. This way, the errors produced are sufficiently general to encompass many different effects (lack of calibration between transmitters, hardware imperfections, etc.). We apply then the different processing schemes on the generated signals. The results for MF are given in fig. 4.1a, where the numerous sidelobes make it difficult to distinguish the impact of model mismatches. Concerning the IAA output exhibited in fig. 4.1b, we can observe a narrow peak of 40 dB corresponding to the point target. There is also a coming up of sidelobes at target range with power up to 22 dB. It can be deduced that these sidelobes are induced by the transmitter errors. Now, when we consider the output of classical OMP in fig. 4.1c, we can notice the detection of the target at correct power, plus six false alarms at target range. Here again, these

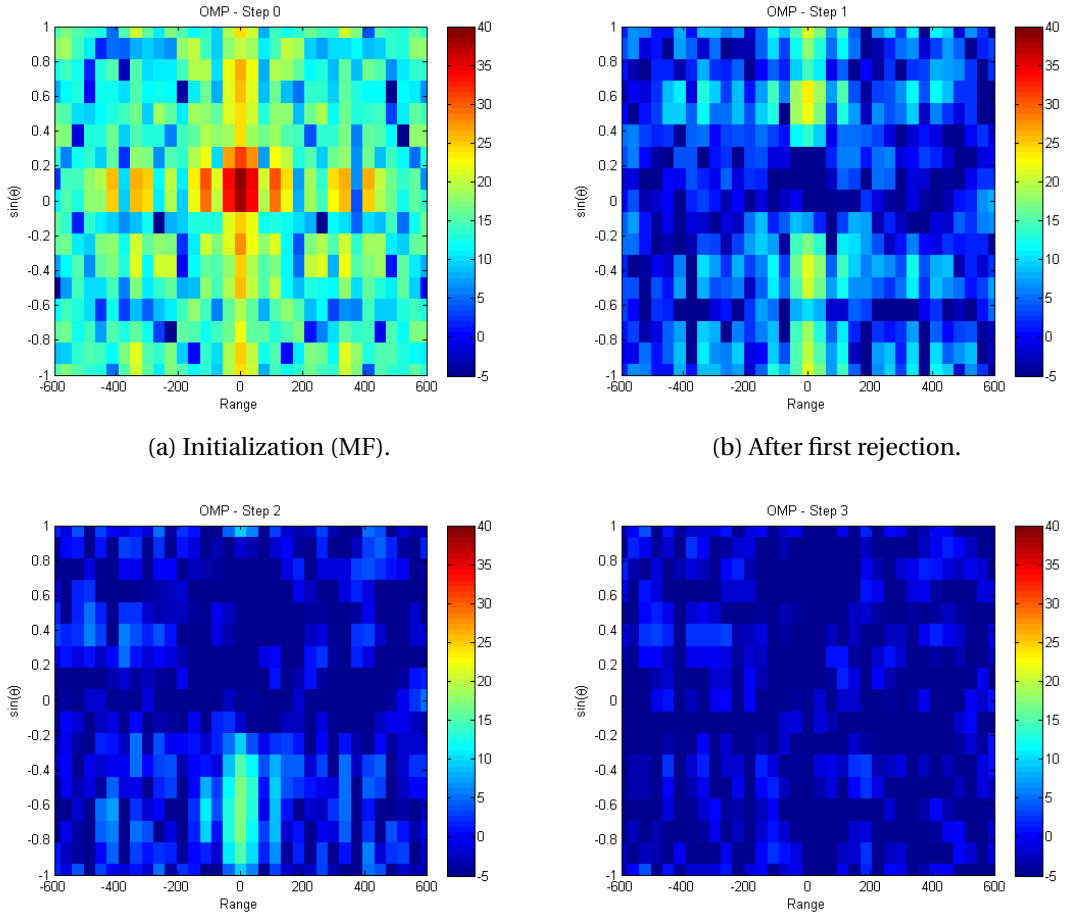

(a) Initialization (MF).

(b) After first rejection.

(c) After second rejection.

(d) After third rejection (last step).

Figure 4.2: Successive steps of the extended OMP algorithm for the simulation of one point target, subject to random phase and modulus discrepancies on Tx channels.

discrepancies are due to the transmitter errors. We also display the results with the extended rejection in fig. 4.1d, where there are fewer false alarms. Moreover, it can be noticed that the two false alarms correspond – in both localization and power – to strong sidelobes of the IAA output. Eventually, we draw two general deductions from these results:

- Both IAA and OMP processing schemes are sensitive to model mismatches. Actually, it could be awaited since they are defined as to reduce the difference between the received signal and a modeled signal.
- The extended rejection of the OMP algorithm has shown to have the capacity to reject more false alarms than the classical rejection. It can be explained by the

fact that the classical OMP is not robust with respect to target localization error, and a distorted signal is more likely to induce a bias on target localization.

To give more insight on how the (extended) OMP operates in case of model mismatches, and so where the false alarms come from, we display in fig. 4.2 the successive steps for getting the results presented latterly. It can be noticed after first rejection that the target has been correctly localized but the inflected ambiguity function – due to signal distortion – induces an incomplete rejection of the target pattern. Therefore, it has induced residues in the ambiguity function that are then mistakenly detected as targets.

4.3 Model Mismatch Prevention Strategies

Some classical methods for radar design and calibration will be briefly presented here but we will especially focus on the MIMO flexibility for digital system control and calibration. We will take benefit of the Hycam MIMO-capable radar testbed at ONERA which is an illustrative example for these concepts since its specification, conception and use have involved a large range of control and calibration methods.

4.3.1 The Hycam Experimental Plateform

In order to study the MIMO radar and other radar concepts in real conditions, a multifunction radar platform was designed and built at ONERA (before the thesis started), thanks to the support of the French Ministry of Defense. This platform, named Hycam, is one configuration of a versatile S-band surface radar testbed taking into account current and future radar architectures [52]. At conception, the focus was put on a reconfigurable architecture combined with transposition of "analog radar parts" to digital. The final design includes a set of arbitrary waveform generators (AWG), frequency down- and up-converters, a rotary joint, a pedestal, 24 high-power amplifiers (HPA) with analog beamforming device, two phased array antennas - one for transmit (Tx) and one for receive (Rx) –, a set of low-noise receivers (LNA) and a system dedicated to signal acquisition, processing and recording. The Tx phased array is made of 12 independent columns, while the receiving antenna integrates 16 columns. In the version of Hycam at the time of the thesis work, up to 3 independent signals could be simultaneously managed (it is possible to associate columns 4 by 4 to make 3 independent sub-arrays though). The antennas can rotate in azimuth and

(a) Hycam multifunction testbed. PhD student for scale.

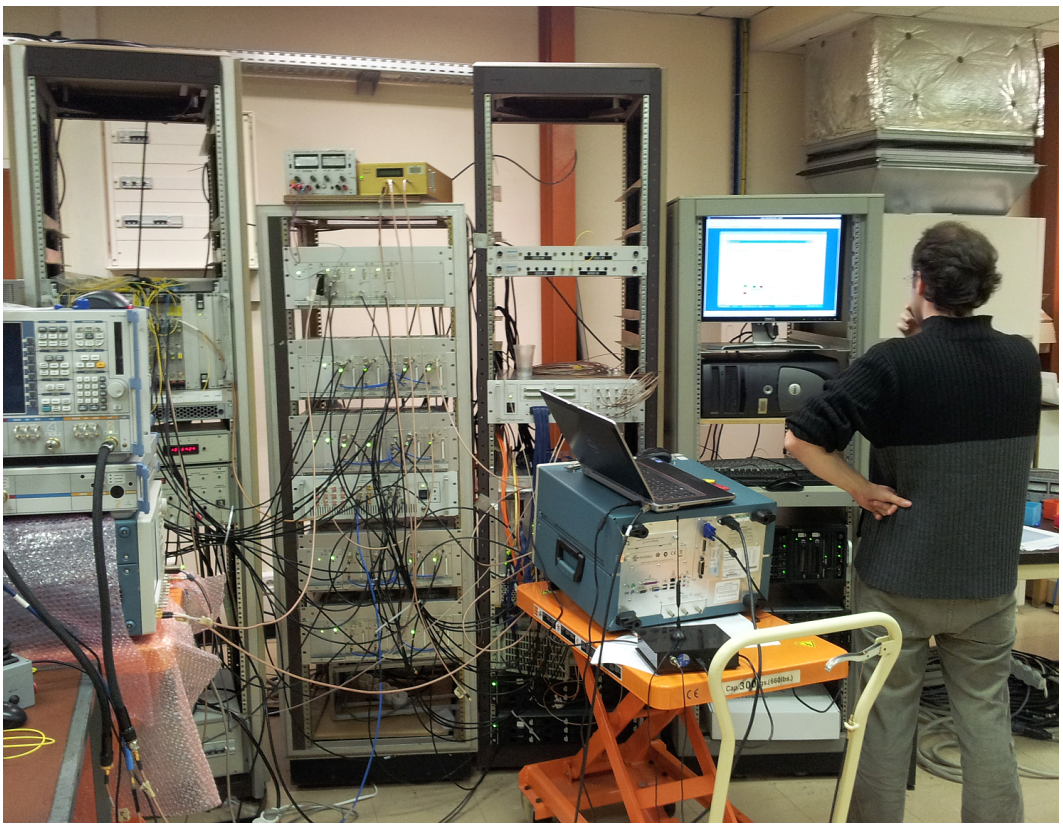

(b) Hycam control system. Focused Arnaud on the right.

Figure 4.3: The Hycam system installed at ONERA (site of Palaiseau).

elevation, whereas their vertical or horizontal positioning is predefined. The Hycam radar with antennas in horizontal position is visible in fig. 4.3a. The digital core is dedicated to “raw" signal acquisition and recording, real-time sequencing and signal processing. After down-conversion and gain control, the channels are digitized at 2 GSamples/s. The signals are finally recorded on hard disks for off line processing. The Hycam control and saving system is exhibited in fig. 4.3b.

Some design choices mentioned in [52] show that prevention of signal distortion was taken into account. We can cite for instance the tilting of 45° of the radiating elements of the antennas so to reduce the mutual coupling, or the stability requirement of 60 dB imposed on the HPA so to guarantee the accuracy of the signal to transmit.

4.3.2 The MIMO Flexibility for Digital System Monitoring and Calibration

The MIMO transmission – through the orthogonality properties of the waveforms – gives the possibility to separate each transmitted waveform in the received signals, and gives therefore the opportunity to operate, *a posteriori*, any digital array processing with the transmitted signals. In a way, long after the emergence of the digital radar on receive (through DBF with the signal received on each element of the antenna), it opens the way to DBF on transmit and therefore to a “full-digital radar".

This consequently provides more flexibility for system monitoring and calibration. From a system point of view, the exploitation of the MIMO configuration of a radar gives the possibility to transfer system control to digital processing on reception side, and to make it easier to keep the system in operational conditions. Calibration issue is one of the key points when dealing with radar system design. Indeed, either for studies of operational modes and systems or target signature analysis, the radar "transfer function" (TF) has to be known and mastered as completely as possible. So, the measurement results, inputs for all the studies dealing with real data, will be uncorrelated – to some extend of course – from the measurement system. Generally speaking, calibration procedures have to be integrated during the system conception phase with:

- Defining sub-system requirements like standing wave ratio (SWR), phase and delay balance, amplitude offset and so on.

- Setting up closed loops and calibration procedures with external devices in the system architecture.

For multi-channel systems like Hycam, closed loops are set up at different radiofrequency (RF) stages: the 12 transmitters TFs, the 16 receiver TFs and all the combinations of one transmitter TF and up to 16 receiver TFs can be measured. External devices – passive and active – to access to the full TF, including antennas, complete the calibration set-up.

This “procedure" fulfills MIMO radar calibration requirements. However, a special task has to be scheduled for calibration and monitoring purposes which is resource consuming. This is far from what a ubiquitous system, like a MIMO radar, can offer. Indeed, if we consider that a MIMO radar can adapt its behavior - mainly task scheduling - to its environment in terms of mission and protection thanks to real time software defined capabilities we can also think about taking advantage of the MIMO radar flexibility to define a digital calibration of the transmitter antennas.

4.3.3 A Posteriori Digital Calibration Method

To demonstrate the possibilities of transfer of transmission system control and calibration to digital processing on the reception side, we propose to focus on Tx phase calibration issues, which are a representative example of a system calibration that can be proceeded “after the fact" with MIMO radars.

The Transmitter Phase Calibration Challenge

Operators of phased-array radars have to calibrate the phase and the magnitude of each Tx channel to prevent altering the desired Tx beam pattern. Loss of signal phase alignment because of undesired phase offsets between radiating elements may cause defocusing of the radar beam pattern, and therefore an unwanted spread of the transmitted energy outside the direction of interest. Tx phase calibration is even more challenging for MIMO radars. To the difference with array antennas all connected to one unique waveform generator, MIMO radar antennas should be fed by independent signal generators. Then, not only the RF lines should be designed so to guarantee a length precision much smaller than the signal carrier wavelength, but the signal generators should be also precisely synchronized. Finally, the channel calibration

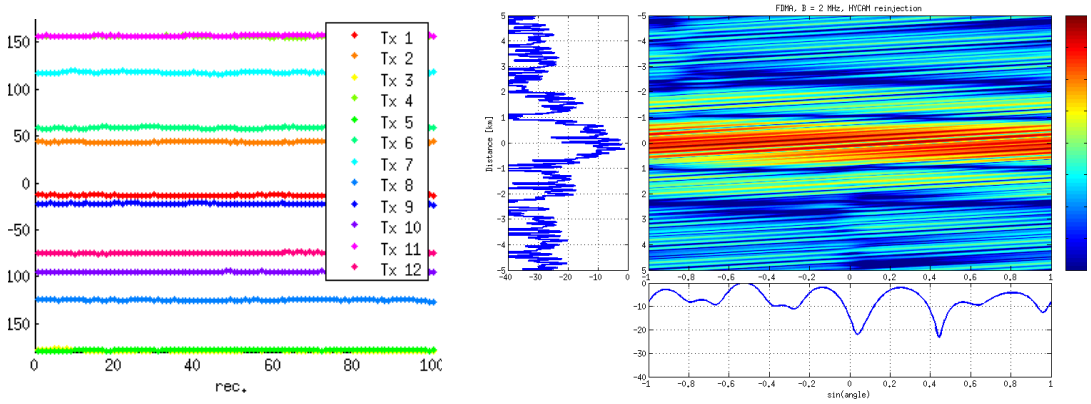

(a) Estimated phase (deg.) of each transmitter for several recurrences.

(b) Resulting ambiguity function (range-angle section).

Figure 4.4: MIMO radar simulation with a family of 12 FDMA waveforms, random constant phase for each transmitter and no phase calibration.

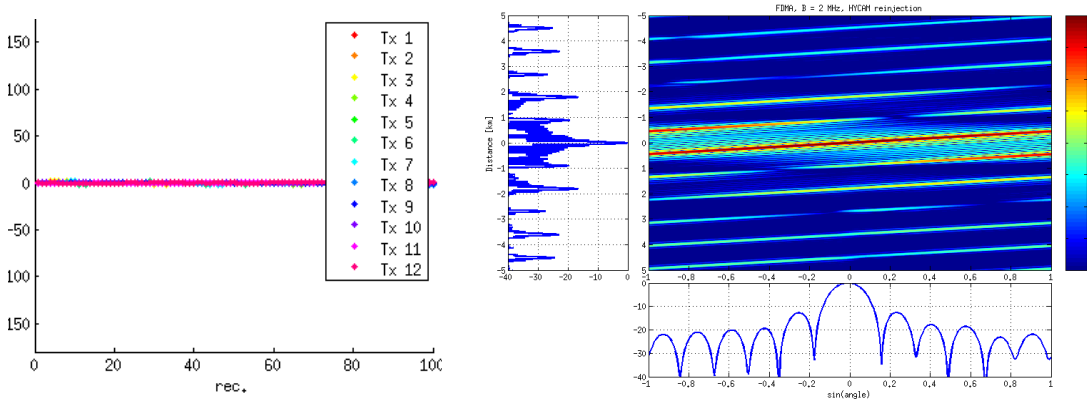

(a) Estimated phase (deg.) of each transmitter for several recurrences.

(b) Resulting ambiguity function (range-angle section).

Figure 4.5: MIMO radar simulation with a family of 12 FDMA waveforms, random constant phase for each transmitter and Tx phase calibration after reception.

complexity is increased and more resources are needed for this task.

To illustrate the impact of the non-calibration of a MIMO Tx antennas on the resulting beampattern after DBF, we simulate a MIMO radar configuration with 12 transmitters and the transmission of FDMA waveforms (presented in section 1.3.3) to one point target at $r = 0$ and $\sin\theta = 0$. We introduce a random phase offset on each transmitter that stays constant from one pulse to the next one, as illustrated in fig. 4.4a. Then, from the signals obtained, we compute the MIMO radar processing up to MF and

DBF. The resulting ambiguity function displayed in fig. 4.4b exhibits a highly-erratic pattern, due to the random combination of the waveforms at DBF stage. For the comparison, we display in fig. 4.5b the perfectly-focused pattern obtained when the transmitters are perfectly calibrated in phase.

Nevertheless, with MIMO radar architectures, it is not required to produce an instant transmit beam pattern that is focused in one specific direction. Indeed, the central point is to illuminate a whole sector during the pulse and recover the Tx beam directivity through digital processing on receive. As an illustration, the instant beam pattern with CDMA waveforms is actually a “chaotic" shape (random phases on each transmitter) that changes at each new code chip. The transmitter calibration is therefore not essential for the instant Tx beamforming – since the energy is spread anyway – but it becomes crucial at the stage of Tx DBF on receive. And as already mentioned, combining transmitted signals with phase errors will make it impossible to form specific beam patterns.

Description of the Calibration Method

Based on this latter observation, we propose an innovative calibration method which consists in carrying out the Tx phase calibration in digital domain, just after the pulse compression on receive. The method allows an automatic alignment of all Tx phases in two steps:

1. Estimation of the phase offsets of each Tx transmitter on the separated signals after pulse compression. The phase estimation can be based on echoes of opportunity, *e.g.* a selection of scatterers of the scene that satisfy specific criteria, and so get rid of the need for external calibration device.

2. Calibration, *i.e.* application of the appropriate phase corrections on each Tx channel.

Thus, the proposed method opens the way to a significant relief of the initial calibration burden. Transferring radar functions to the digital domain after signal reception leads to the fact that much less resources are then needed for the system conception (*e.g.* less constraints on radio path precision) and calibration procedures (*e.g.* no strict phase alignment requirement before transmission).

(a) Hycam radar testbed with antennas in vertical position.

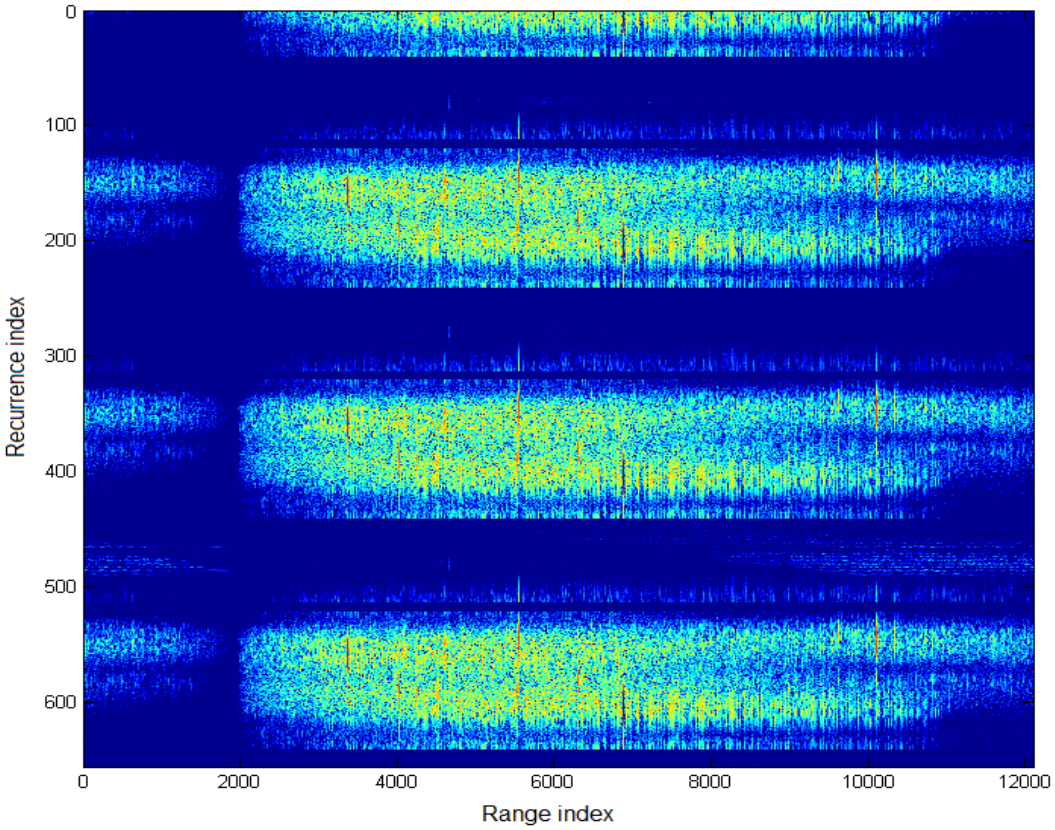

(b) Experimental data after MIMO radar processing (“waterfall") for one receiver.

Figure 4.6: Surrounding clutter acquisition with the Hycam platform.

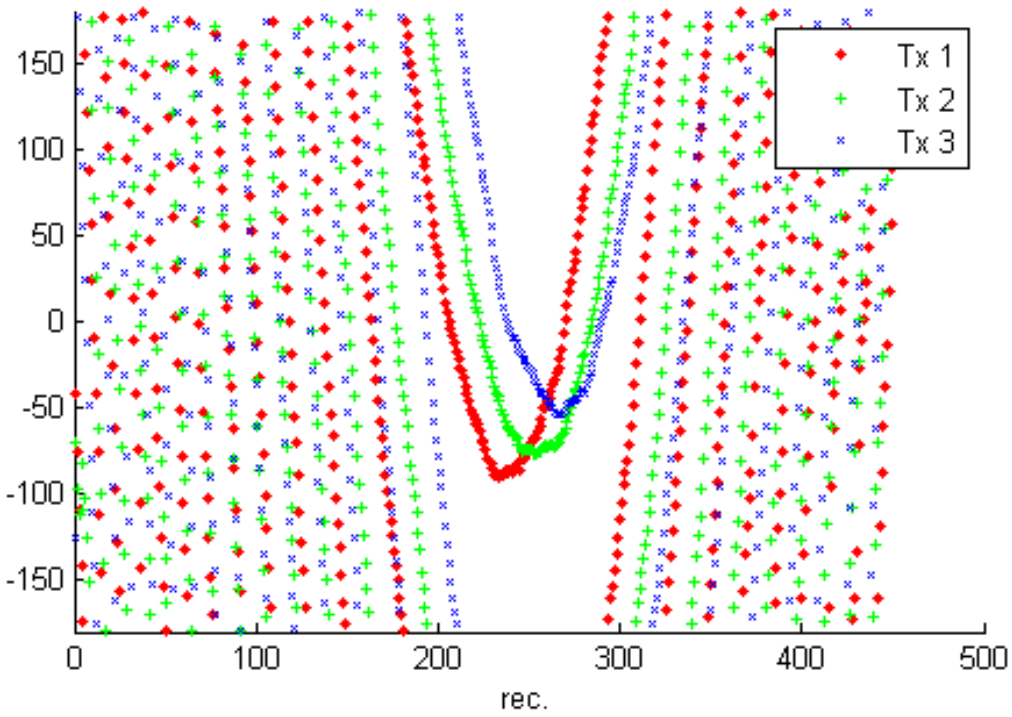

Figure 4.7: Phase evolution (in deg.) with respect to recurrence (*i.e.* radar azimuth) at scatterer range. Each color corresponds to one specific waveform extracted from the received signal.

We cannot go deeper into details about the proposed calibration method as long as a patenting process is underway, but we will now give an overview of the method proceedings on an experimental set of data.

Acquisition of Experimental Data

In order to exhibit the phase calibration process on real MIMO signals, we define an experimental scenario of transmitters subject to a lack of phase calibration. The objective is then to use the Hycam radar testbed for the acquisition of a set of real data that we will use for the application of the proposed calibration method.

The Hycam radar is installed on the roof of our 5-floor building. The Tx antenna is set up in 3 independent subarrays of 4 adjoining antennas each, and antenna arrays are positioned vertically so to allow wide horizontal illumination, as visible in fig. 4.6a. We generate a family of Gold phase codes of 1023 moments as MIMO waveforms, transmitted in S-band on a bandwidth of 20 MHz. No system calibration on Tx antenna phases is carried out, so that the intentional rough trigger synchronization of

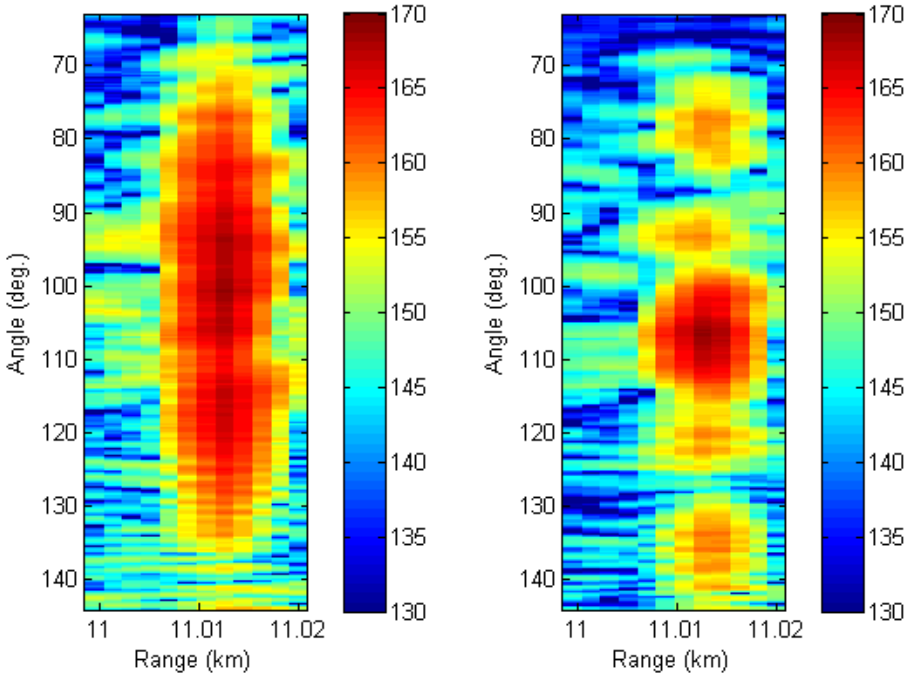

(a) Consideration of one transmitter only.

(b) After phase calibration and Tx beam forming.

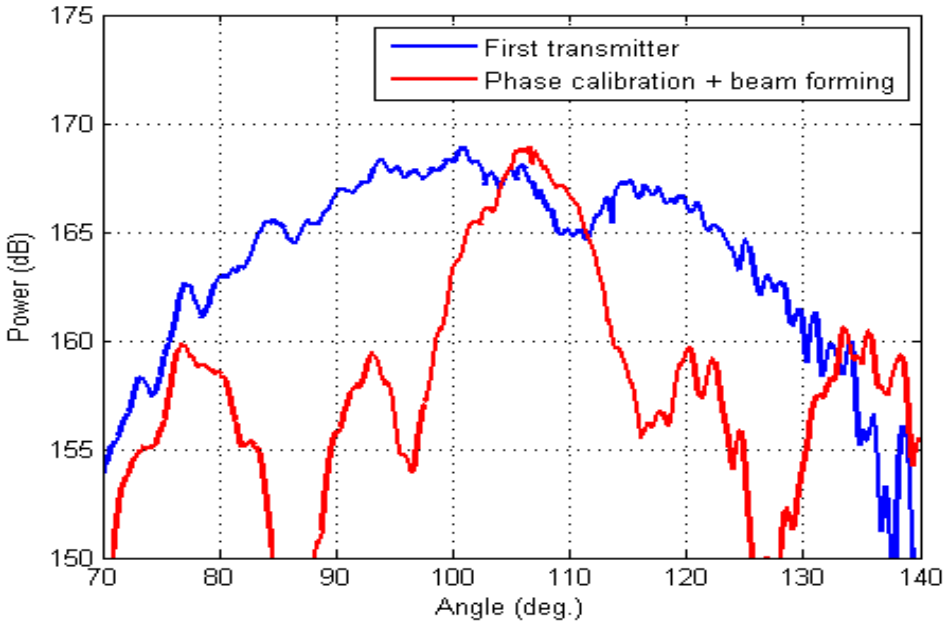

(c) Cut at scatter range. Blue curve: consideration of one transmitter only. Red curve: after phase calibration and Tx beam forming.

Figure 4.8: Contribution of a strong scatterer of the instrumented scene.

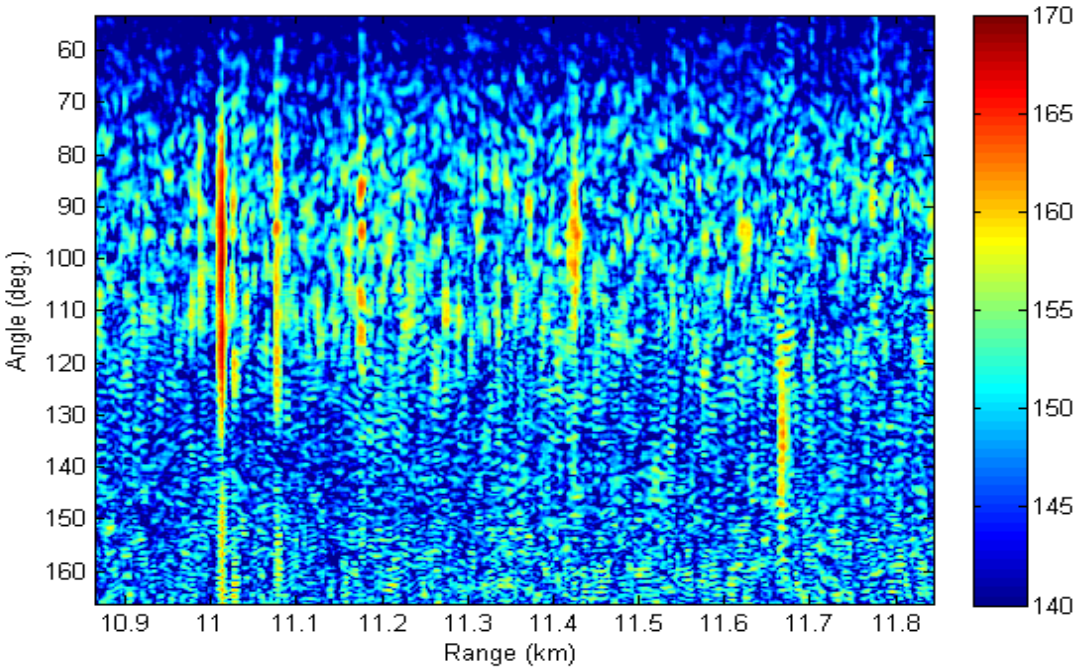

(a) Consideration of one transmitter only.

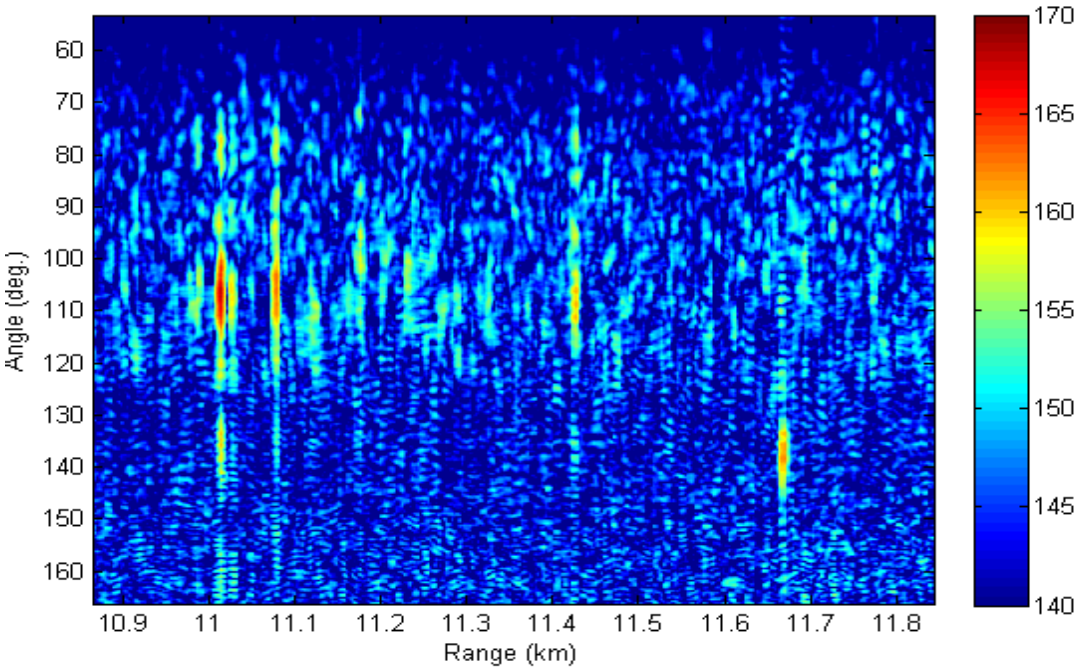

(b) After phase calibration and Tx beam forming.

Figure 4.9: Environmental scene.

the waveform generators causes uncontrolled phase offsets for each of the 3 subarrays. Nevertheless, these phase offsets stay constant with time, *i.e.* from one pulse to the other. The Hycam radar operates in “clutter acquisition" mode where the mobile module of the radar makes several rotations in order to acquire the echoes from the whole scene around the radar. Therefore, we can instrument an area of several kilometers of range in all directions, except in two angular sectors where the transmission is forbidden.

The recorded data are processed offline. The received signal is demodulated, decimated and compressed through MF adapted to each Tx waveform. For the extended description of all proceedings of data acquisition and radar digital processing that have been developed during the thesis, it should be referred to appendix A. We finally obtain the so-called “waterfall" which is the succession of range profiles acquired recurrence to recurrence (*i.e.* between each two pulses) and for each transmitter, as displayed on fig 4.6b. One can distinguish the periodic pattern due to the radar rotation, and the blanked recurrences which corresponds to the “forbidden" angular sectors.

Method Implementation and Results

In order to exhibit the effect of the calibration scheme, we focus on one scatterer of the instrumented scene. First, in case of no calibration, we display in 4.7 the phase evolution with the recurrence – *i.e.* with the angle – of each transmitted signal at scatterer range. The parabolic shapes of the dotted curves are explained by geometric considerations. Then, we apply the proposed calibration scheme on the received signals and we process the Tx DBF of the corrected signals. The resulting effect in the ambiguity function is specially visible when zooming on the scatterer echo in fig. 4.8b and compared to the echo in the signal from one transmitter in fig. 4.8a. The scatterer lobe which is widely spread in angle for one transmitter is then narrower after calibration and DBF. The angle profile at scatterer range for both cases is given in fig. 4.8c. From these figures, it can be deduced that the calibration is efficient since a narrow Tx beam pattern has been formed in the scatterer direction.

Finally, when applying the calibration and DBF for all signals, we can get the “mapping" of the instrumented area. As an illustration, we exhibit on fig. 4.9 a section of this area restricted to an extension of size 1 km in range and 110° in angle. On this mapping, it is possible to distinguish several scatterers of strong power. It can be

concluded that after calibration and DBF, the sidelobes have been clearly reduced and the main lobes have become narrower in angle.

Besides, note that an angle sector of 110° at this range corresponds to a length of around 22 km. This means that the mapping is approximately of size 22km × 1km, and so the angular extension of the scatterers is deduced to be still consequent in comparison to their range extension. We remind that this experiment was done to provide an illustrative “proof of concept" of the proposed calibration method and exhibit its performance. However, the range accuracy of the final mapping can be greatly improved by processing a Rx DBF and so fully benefit from the virtual array capability provided by MIMO radar architectures. Obviously, it is also possible to increase the number of independent antennas on transmit.

4.4 Conclusion

In this chapter, we have addressed the issue of signal model mismatches, which are likely to greatly degrade the performance of a processing scheme that looks optimal in theory. We have first presented different phenomena encountered in radar architectures that might create distortions of the transmitted signal, more specially non-linearities of hardware components and lack of alignment or mutual coupling between channels. In order to exhibit the possible impact of such model mismatches on the detection performance degradation for different processing schemes, we have set up a simulation of MIMO signals transmitted through a radar chain subject to intentional hardware errors. We have then applied the OMP and IAA processing schemes directly on the simulated signals, and we could show that they all present a certain sensitivity to such unexpected signal distortion. More precisely, we could exhibit that OMP and IAA outputs were subject to residual sidelobes, possibly leading to false alarm in the case that the signal distortion reaches a certain magnitude. We could also exhibit from the simulation results that the proposed extension for the OMP presents a better capacity for eliminating false alarms than the classical OMP, and actually similar detection performance than the IAA

Second, we have addressed possible strategies for preventing the signal model mismatches. Through the representative example of the conception of the versatile MIMO-capable testbed radar Hycam, we have expounded conventional strategies like anticipating the performance at design stage through strict specifications, and

calibrating the hardware system before the transmission. Then, we have described how MIMO radar architectures can bring more flexibility and simplicity for system monitoring and calibration, especially through the “digitalization" of the transmission function. In this context, we have proposed a method of *a posteriori* digital auto-calibration of the Tx phases, where these phase offsets are estimated from the echoes of the instrumented scene and the correction is applied after pulse compression. After an experimental signal acquisition with Hycam on surrounding clutter with MIMO waveforms in the context of an initial lack of calibration of Tx phases, we have shown that the proposed method provided an accurate calibration on final signals, so that we could recover the focused Tx beam to map the scene.

Finally, we highlight that the radar testbed Hycam, like any other physical platform, is subject to hardware imperfections. Therefore, it can constitute a particular opportunity for evaluating waveform and processing schemes performance in real conditions.

5 Evaluation of the Processing Schemes on Experimental Signals

5.1 Introduction

In the previous chapter, we presented the Hycam MIMO-capable radar testbed that was installed on site at ONERA. This technical tool actually represents a good opportunity for the acquisition of MIMO signals in real conditions, especially since MIMO experimental results are very rare in the literature (some examples though: [6], [53], [20]). Indeed, this platform is certainly subject to hardware imperfections among those mentioned in the previous chapter, and it will thus allow us to challenge the robustness of the developed techniques with respect to such real conditions.

In this chapter, we will describe the context and the parameters of the two different configurations set up for the experiments with Hycam. Based on the proceedings of the experiments and data acquisition, we will investigate the possible causes of the main signal distortions that could occur during the operations. It will allow us to anticipate or even compensate possible consequent discrepancies with the ideal case. Afterwards, we will compute and display the resulting ambiguity functions for all waveforms and acquisition contexts, and provide a first analysis of the degradation based on visual comparison. It will be followed by more quantitative analysis and comparisons based on the figures of merit related to detection performance. In a last section, we will apply the proposed processing schemes on the experimental signals: firstly, the IAA detection method for the reference, and secondly the OMP method with the classical rejection and then with the extended rejection, in order to exhibit their respective sensitivity to the encountered imperfections of the real world.

Figure 5.1: Installation for the target simulator, localized at 250 m of Hycam

5.2 Definition of the Experiments

In order to exhibit the performance degradation induced by the hardware imperfections in real conditions, we define specific experimental configurations. We generate also different families of MIMO waveforms (described later) in order to investigate how these different waveforms will be affected by the hardware imperfections.

As all hardware implementations, the Hycam radar testbed (presented in section 4.3.1) is subject to imperfections. In our situation, we take it as an opportunity for testing the impact of such imperfections on the performance of the introduced processing techniques. The radar chain is a succession of components that cannot be isolated. Nevertheless, there is a possibility with Hycam to bypass the RF circuit at the input of the antennas: just after the power amplifiers for the Tx antenna, and just after the LNA for the Rx antenna. This was actually designed for system calibration, but it also allows us to feed only a restricted part of the whole radar chain. Finally, two different experimental scenarios are defined and settled up with Hycam:

- **Closed-loop configuration:** It corresponds to a closed – *i.e.* bypassed – circuit configuration of the complete radar chain except the antennas. The signal is captured just before the radiating elements and re-injected directly in the reception channels. The special interest of this configuration is the possibility to isolate the impact of the radar microwave component imperfections.

- **Reflection on a target simulator:** The signal is transmitted toward a target simulator system facing the Hycam platform at about 250 meters. The system is composed of an active radar calibrator, electronic/optical devices and horn antennas, as seen on fig. 5.1. The signal received by this system is then transmitted back with additional delay and Doppler. The additional delay of 10 km is induced through transmission in optical fibers of the corresponding length, after signal conversion from RF to optical. It aims at shifting the target echo away from the blind area to avoid simultaneous transmission and reception. The additional Doppler, corresponding to a virtual celerity of the target, is produced through a signal phase increment activated at each detection of pulse falling edge. The purpose of this operation is to keep the target response distinguishable from the environmental clutter which is concentrated around the 0 Doppler. The special interest of the target simulator configuration with respect to the closed-loop is the given possibility to cover the impact of the radiating

elements and the signal propagation.

We give here the different parameters defined for all configurations:

- Bandwidth: $B = 2$ MHz, corresponding to a standard surveillance radar
- Pulse duration: to limit the sidelobes level with CDMA waveforms, the ratio BT_p (*i.e.* the chips number since $\Delta_t = 1/B$) should be high enough. We choose $BT_p = 100$, and so $T_p = 50$ µs
- Number of recurrences: $N_p = 100$
- Number of waveforms generated per family: one waveform per transmitter, *i.e.* $M = 12$
- Waveform families: we generate the waveform families defined and simulated in section 2.2.2, *i.e.* a circulating chirp, a FDMA family, and Gold phase codes family
- Transmission mode: sequential[1], since Hycam could manage 3 simultaneous up-links in its version at the time of the thesis work

It is reminded that the extended description of the signal processing – data acquisition and radar digital processing – is given in appendix A.

Besides, we would like to mention that we have also generated other phase codes family (random binary code, Alltop codes, chaotic code) and a circulating code family. Since we have found these waveforms were less relevant in the current context than the three ones above, they are not studied in details in this thesis, only their ambiguity functions are exhibited in appendix B.

5.3 Identification of the Main Imperfections

Typical radar hardware imperfections have been presented in section 4.2.1. Nevertheless, preponderant phenomena have been noted either during the experiments or

[1] In a sequential mode, each waveform is individually generated, radiated by the corresponding transmitter, then captured and processed in the reception front-end. Then, all sequences have to be combined during the off-line processing to recover the full MIMO capacity. This mode is considered to be equivalent to a simultaneous MIMO transmission since all effects add up in both cases. Even the coupling antenna phenomenon is preserved in sequential transmission since a transmitting antenna diffuses on the adjacent antennas, even if these ones are not fed.

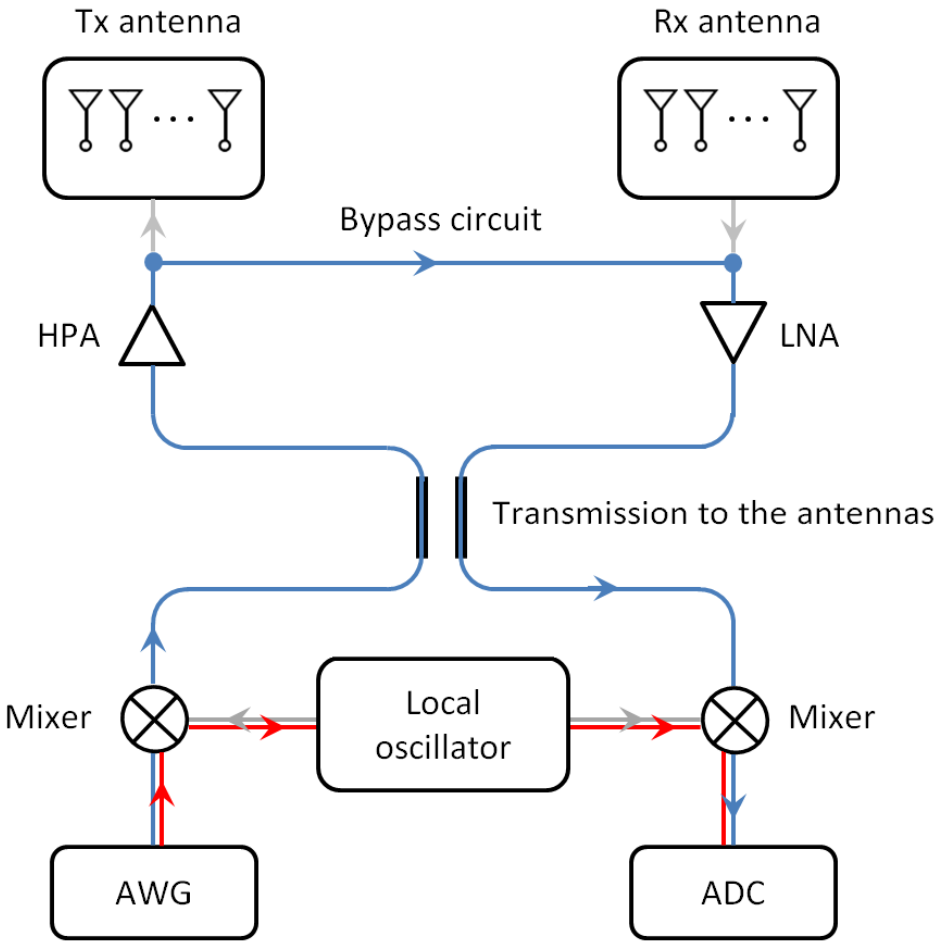

Figure 5.2: Simplified block-diagram of the Hycam testbed with the two closed-loops: the experimental closed-loop in blue and the unexpected closed-loop due to lack of isolation of the mixers in red.

based on the analysis of the resulting ambiguity functions. In this section, we identify the strongest distortions the experimental signals were likely to be subject to.

5.3.1 Imperfect Mixer Isolation

In the radar chain, a local oscillator provides a sine signal for both frequency up-conversion and down-conversion in up-link and down-link, respectively. The frequency conversion is provided by mixers with in theory two signal inputs and one output which is the product of both inputs. In the closed-loop configuration, we have noticed that, in addition to the experimental closed-loop, there was one shorter –

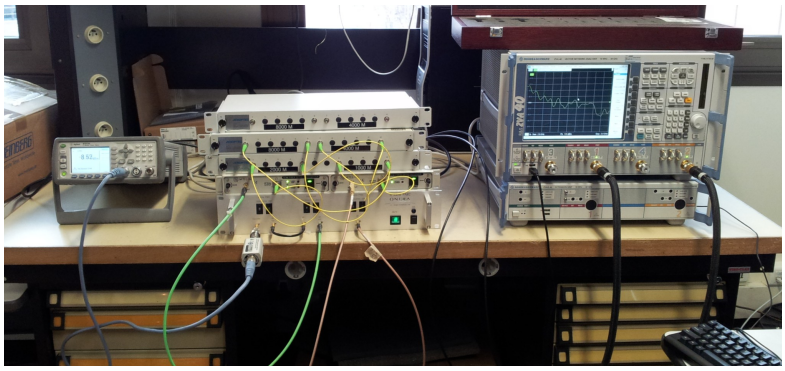

(a) Testbed: VNA on the right, delay line system on the left.

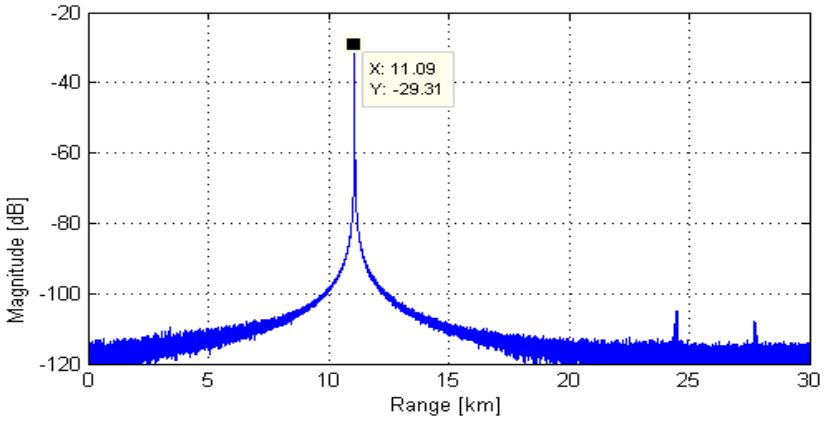

(b) Resulting transfer function, in time domain.

Figure 5.3: Determination of the transfer function of the delay line.

unwanted – closed-loop which is due to a lack of isolation of the carrier frequency mixer. These two closed-loops are represented in fig. 5.2. Therefore, two echoes are expected to be detected at short range (order magnitude of the hundred of meters) and angle of 0 degree. Finally, this effect, which is an imperfection by nature, is actually an interesting opportunity for us to acquire real data that contain two echoes (*i.e.* two targets, equivalently) at short distance. Besides, note that the imperfect mixer isolation is of no impact in a normal use case since the signal is not acquired during pulse transmission but only between two successive pulses.

5.3.2 Truncation of Signal of Interest

In the configuration of the transmission to the target simulator, it has been noticed on some resulting ambiguity functions that an artifact (residual sidelobes) comes

up, moreover only on one side of the range axis. The absence of symmetry in the ambiguity function has given the idea that it is probably a phenomenon which occurs at a specific range section, at several kilometers from the target. It has been first deduced that it is unlikely to be due to multipath because multipath effects are usually limited to a range of hundreds of meters. Our hypothesis was that this issue was coming from imperfections of the optic delay line of the target simulator. This line is actually made of several lines of different lengths connected together and we were expecting a problem in the material or reflections at connections.

In order to analyze the delay line, we have decided to measure the transfer function of the radar calibrator system. We have used a Vector Network Analyzer (VNA) which scans the whole operating bandwidth. The installation is exhibited on fig. 5.3a. After inverse Fourier transform, we could obtain the transfer function in time domain given in fig. 5.3b. It has been determined that the line length corresponds to the time of the transmitted signal to travel to a target in free space at 11 km, whereas it was expected to be 15 km. After investigations, it came out that there was an issue in the design of the line. Finally, since the window of signal acquisition was starting at 15 km and the delay line was shorter than expected, we could determined that 900 m (*i.e.* around 10 %) of the signal re-transmitted by the target was truncated during the acquisitions with the target simulator. Nevertheless, we take this effect as a consequence of a phenomenon that can possibly occur in an operational scenario (target hide out, destructive interference, etc.).

5.3.3 Lack of Phase Alignment

During the experiments in both closed-loop and target simulator configurations, the transmitters were working sequentially, *i.e.* one after the other. One unique AWG was used to generate the waveform of each transmitter one after the other. The waveforms are generated at an intermediate frequency and then up-converted to the carrier frequency by the mixer. Since there is no synchronization between the mixer and the AWG, it results in a random initial phase for each transmitted waveform. It corresponds thus to a lack of alignment of the phase of the transmitters that can lead to a “chaotic" combination of the waveforms at DBF stage, as described in section 4.2.1. In this situation, we can apply the calibration method introduced in section 4.3.3 in order to correct the phase offset of each transmitted signal. Nevertheless, instead of a scene of clutter, there is here only one preponderant target (with a certain speed in

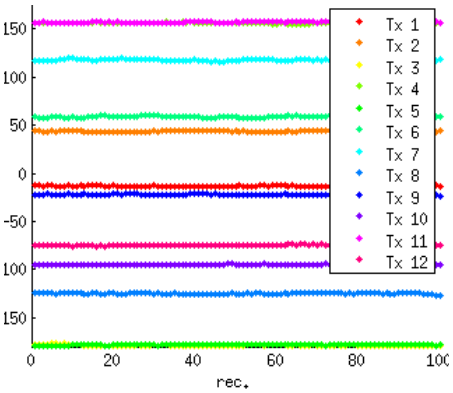

(a) Before calibration – Estimated phase offsets (deg.).

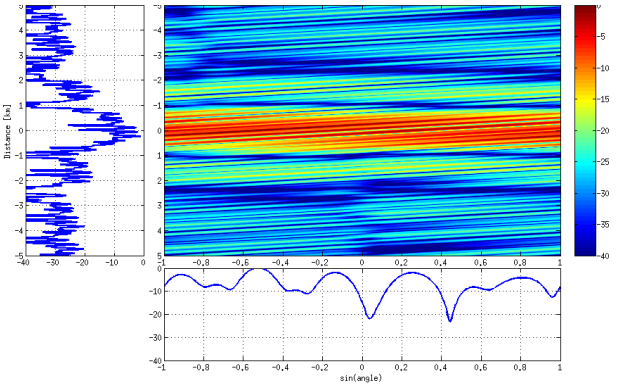

(b) Before calibration – Resulting ambiguity function.

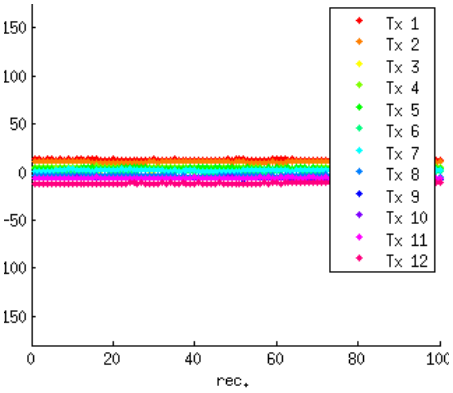

(c) After 1st iteration – Estimated Tx phases.

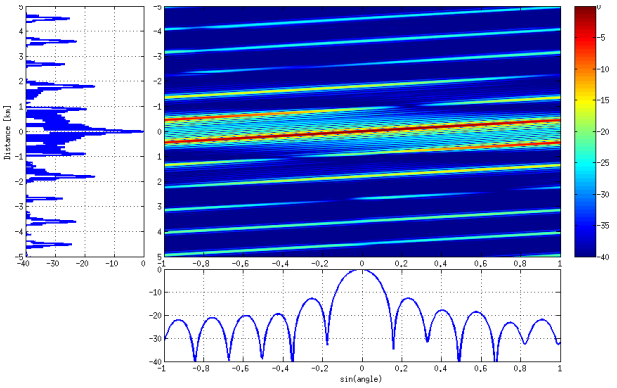

(d) After 1st iteration – Resulting ambiguity function.

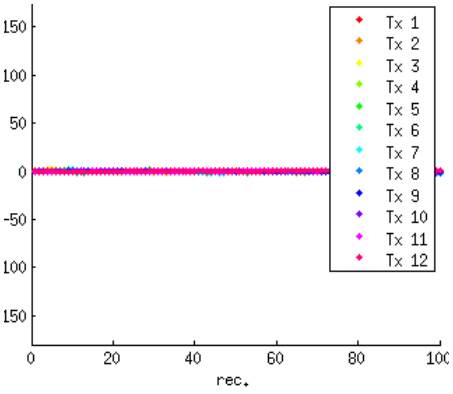

(e) After 2nd iteration – Estimated Tx phases.

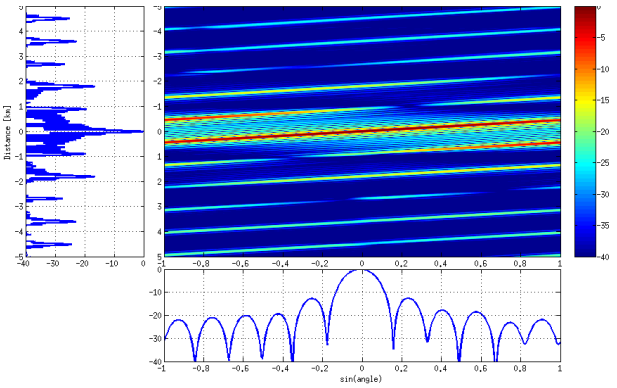

(f) After 2nd iteration – Resulting ambiguity function.

Figure 5.4: Iterative process for the Tx phase offset calibration.

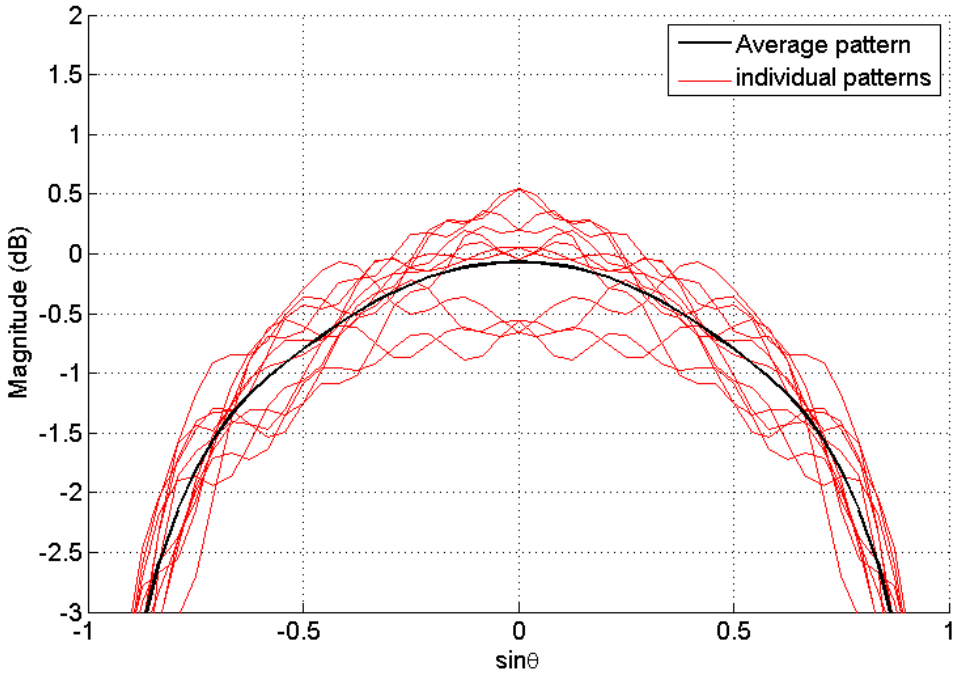

Figure 5.5: Resulting radiation gain for each antenna element for the transmission of Gold phase codes.

the configuration of target simulator). Therefore, in order to increase the precision of the calibration, we have to run the calibration process several times until getting a focused ambiguity function. The successive steps of the calibration are exhibited in fig. 5.4, with the associated phases and resulting ambiguity functions.

5.3.4 Antenna Mutual Coupling

The issue of antenna mutual coupling has been addressed in section 4.2.1. Moreover, we have also mentioned that the radiating elements of the antennas are 45°-tilted so to reduce the mutual coupling. The objective here is to estimate the impact of the antenna coupling on the radiation gain of the antenna elements, based on the measurements processed at radar calibration phase, in order to determine if it has a major impact in terms of signal distortion.

The S-parameters – or scattering parameters – of the radiating elements of Hycam were specially measured once the radar was built, in order to verify if the design specifications were satisfied. These measurements are actually of special interest here for the derivation of the mutual coupling effect. The S-parameters are directly related

to the Z-parameters [54], so it is possible to deduce the antenna impedance matrix **Z**, whose general expression is:

$$\mathbf{Z} = \begin{bmatrix} Z_A & Z_{12} & Z_{13} & \cdots & Z_{1M} \\ Z_{21} & Z_A & Z_{23} & \cdots & Z_{2M} \\ Z_{31} & Z_{32} & Z_A & & \vdots \\ \vdots & \vdots & & \ddots & \\ Z_{M1} & Z_{M2} & \cdots & & Z_A \end{bmatrix} \tag{5.1}$$

where Z_A represents the impedance of one array element, and Z_{ij} represents the mutual impedance between the array elements i and j. The mutual impedance Z_{ij} is a specific value for each two elements depending on the geometry and material of the whole antenna structure.

When defining **v** and **i** as the vectors for the tension and current of each radiating element, respectively, and Z_T the impedance of the measurement equipment at each element, we can write [55]:

$$\mathbf{v} = (\mathbf{Z} + Z_T\mathbf{I})\,\mathbf{i} \tag{5.2}$$

This expression illustrates the fact that each current of the radiating element induces currents in the neighbor elements through electromagnetic influence.

The coupling matrix **C** is defined as [50]:

$$\mathbf{C} = (Z_A + Z_T)\,(\mathbf{Z} + Z_T\mathbf{I})^{-1} \tag{5.3}$$

leading to the following relation:

$$(Z_A + Z_T)\,\mathbf{i} = \mathbf{C}\mathbf{v} \tag{5.4}$$

Thus, the coupling matrix allows to directly deduce the resulting currents **i** in all radiating elements from the voltage command **v**, which is of special interest since the radiation of an antenna element is directly induced by the current that circulates in it.

With the coupling matrix computed from the measured S-parameters, we could determine the resulting radiation patterns of all antenna elements. The results for the transmission of Gold phase codes are given in fig. 5.5. It can be deduced that the worst-case radiation gain discrepancy is limited to 1 dB. Therefore, the mutual

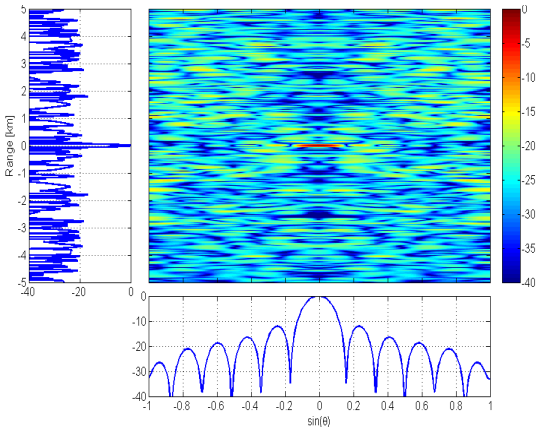

(a) Gold codes – Theory.

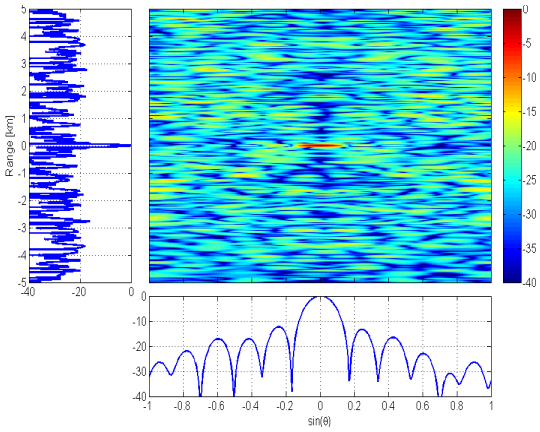

(b) Gold codes – Experiment with Hycam and the target simulator.

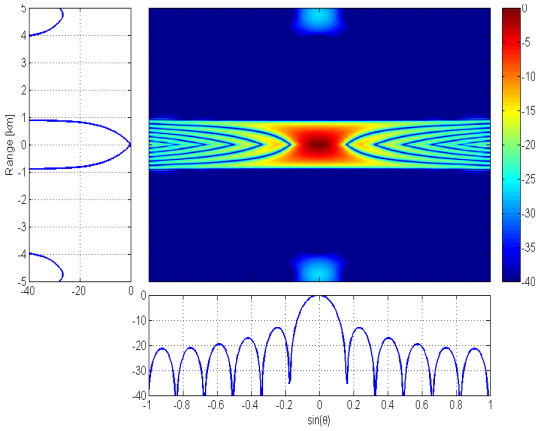

(c) Circulating chirp – Theory.

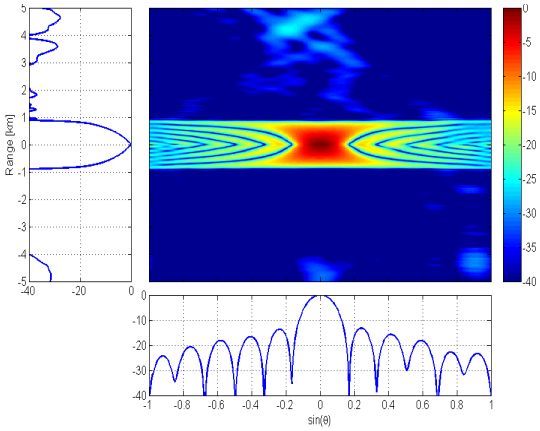

(d) Circulating chirp – Experiment with Hycam and the target simulator.

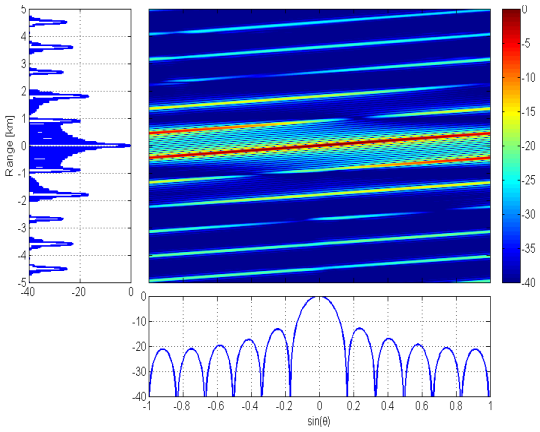

(e) FDMA – Theory.

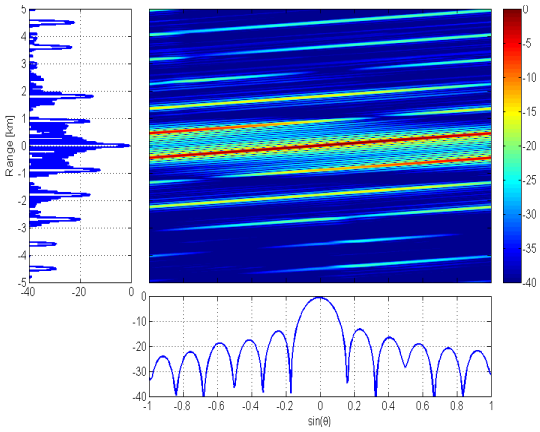

(f) FDMA – Experiment with Hycam and the target simulator.

Figure 5.6: Ambiguity functions (MF output) for different waveform families and acquisition contexts.

coupling with the Hycam radar testbed is estimated to have a limited impact on signal imperfection, especially when compared to the possible impact of the signal truncation issue described previously.

5.4 Analysis Based on MF Outputs

Once the ambiguity functions from all waveform families and in all experimental configurations are processed, we can then extract some relevant insights and comparison based on both visual and quantitative considerations. The elements of comparison are the acquisition contexts (theory vs. experiment in closed-loop vs. experiment with the target simulator) and the transmitted waveform families (Gold codes, circulating chirp, FDMA). Since we specially focus on the characteristics of target response pattern along range and angle dimensions, we will base our analysis on cuts of the ambiguity functions (a 3-dimension data cube, initially) at target Doppler, with plots centered on the target echo.

5.4.1 Qualitative Analysis and Comparison

We have exhibited the resulting ambiguity functions for the 3 representatives types of waveform (CDMA, TDMA, FDMA) in fig. 5.6. On the right, we display the ambiguity functions obtained from the experiment with Hycam facing the target simulator. The ambiguity functions on the left correspond to the theoretical ones and are given for comparison. Here, we do not exhibit the ambiguity functions obtained from the experiment with the radar platform in closed-loop, because differences with the theory cannot be distinguished to the eyes. In a way, this indicates that the internal hardware imperfections of the Hycam platform are limited enough to have imperceptible impacts on the ambiguity functions of all waveforms. Besides, we precise that the ambiguity functions for all generated waveforms and all acquisition configurations (closed-loop configuration included) are displayed in appendix B.

The first visual deduction from the exhibited figures with the target simulator configuration is that the experimental results are quite close to the theoretical ones for all waveform families. Indeed, the shape and level of the main and side lobes of the ambiguity functions look similar between theory and experiment with the target simulator. The signal distortions due to the imperfections of the radar chain are thus deduced to be limited. Nevertheless, an artifact is visible in the upper part of fig. 5.6d.

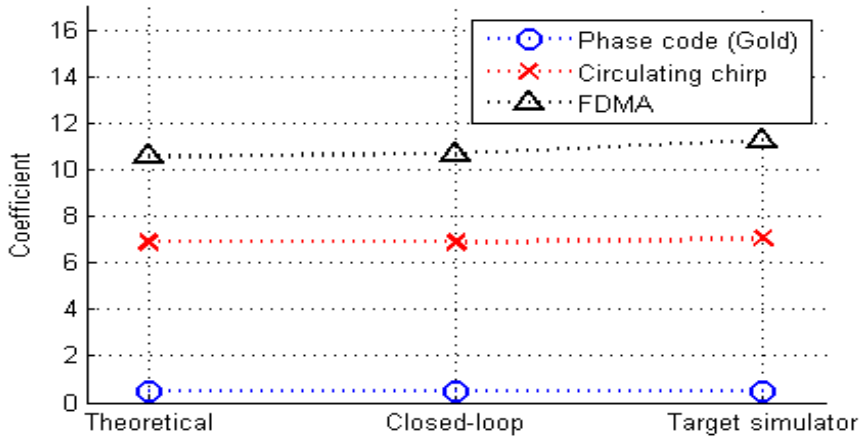

(a) Range resolution.

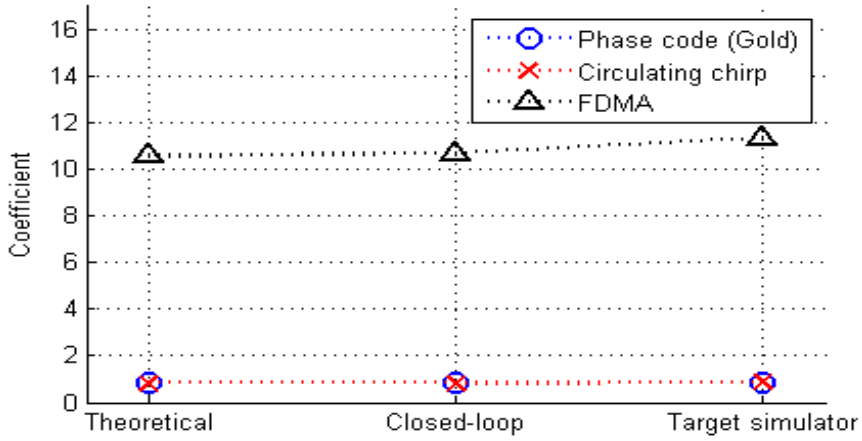

(b) Direction resolution.

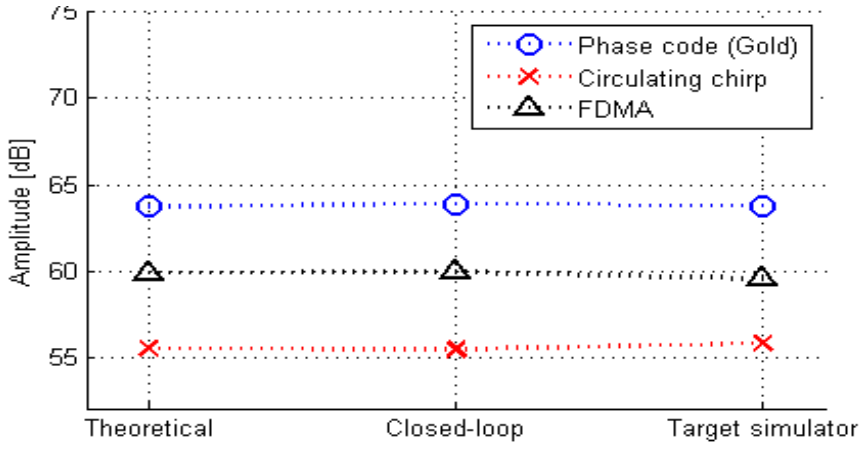

(c) ISLR.

Figure 5.7: Figures of merit for theoretical and experimental configurations and for 3 types of waveforms. Lower values mean better performances in detection.

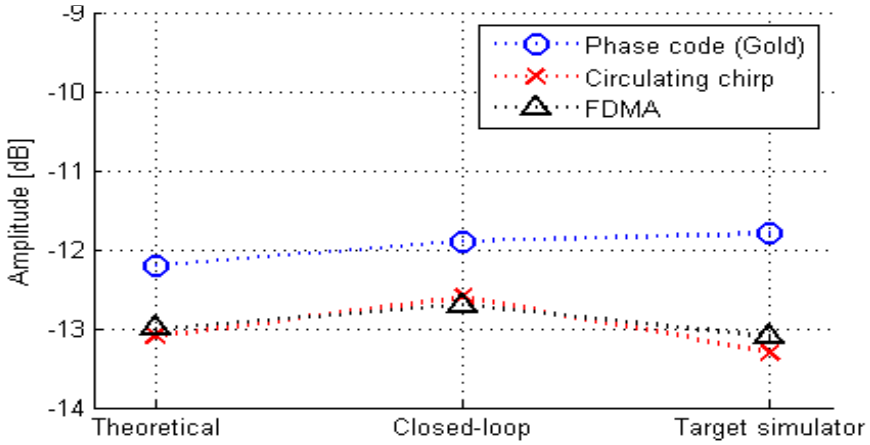

(d) PSLR.

Figure 5.7: *Continued.*

Since this effect is asymmetric and occurs at several kilometers from the target, we analyze it as the probable impact of the truncation of the signal of interest that we have described previously.

5.4.2 Quantitative Comparison

We use here the factors of merit introduced in section 2.2.2 in order to determine the resulting figures of merit for each ambiguity function. It is reminded that these figures are representative of the performances in terms of target angle and range resolutions, and clutter and pointed interference rejections. The computed figures of merit are given in fig. 5.7. Besides, it is reminded that the analysis of the theoretical values and the comparison between waveforms have already been given in section 2.2.2. Concerning the values from the experiments, it can be deduced from the plots that they do not strictly diverge from the theoretical ones, even in the case of the coming up of visible artifacts (of relatively low power though) in the target simulator configuration. More precisely, the performance discrepancies with the theory never exceed 1 for the coefficient of range and direction resolution, and 1 dB for the ISLR and PSLR factors, which is of much lower order of magnitude than the discrepancies between waveform families themselves.

Then, concerning the interpretation of the discrepancies between theory and experiment, it can be said that, when considering the error margin in signal measurement and processing, the encountered fluctuations are too small to give deeper analysis.

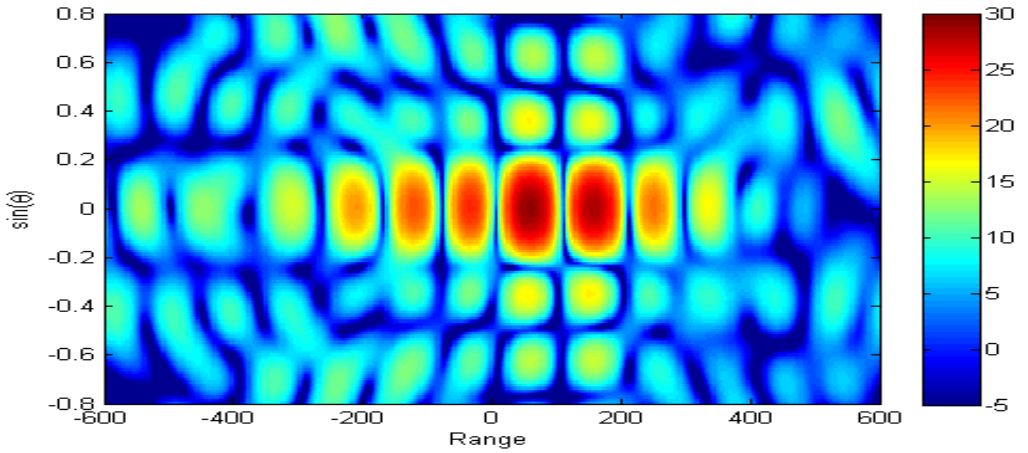

(a) MF output.

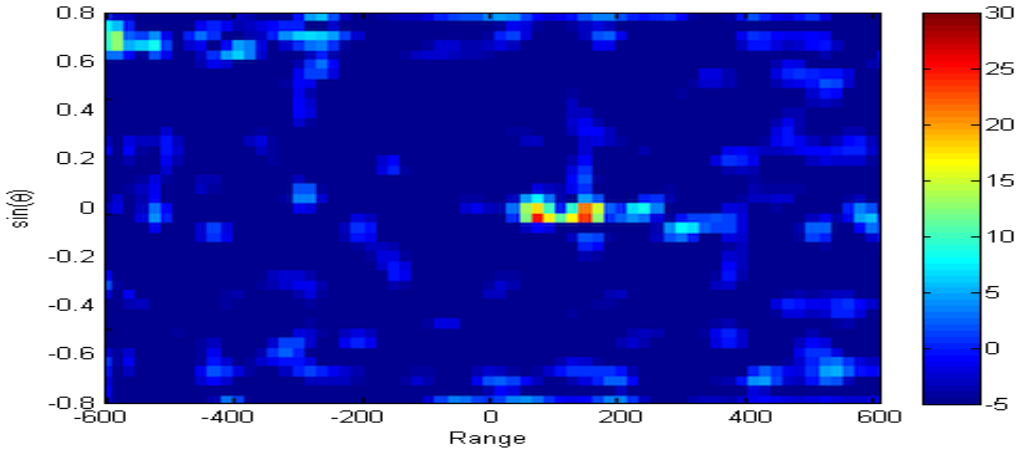

(b) IAA output (iteration 7).

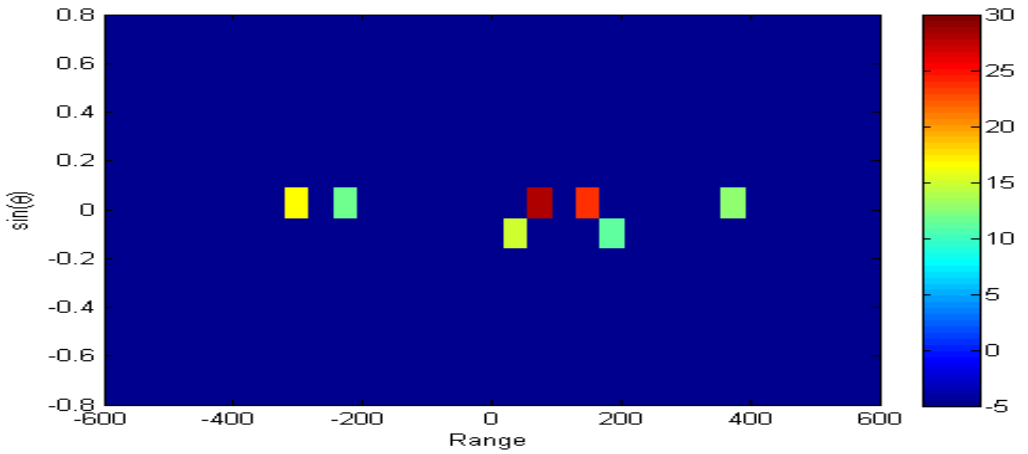

(c) OMP output – classical rejection.

Figure 5.8: Application of the different processing methods on the experimental data (closed-loop configuration). Range resolution cell width = 75 m. Angle resolution cell width = 0.25. Ranges in m.

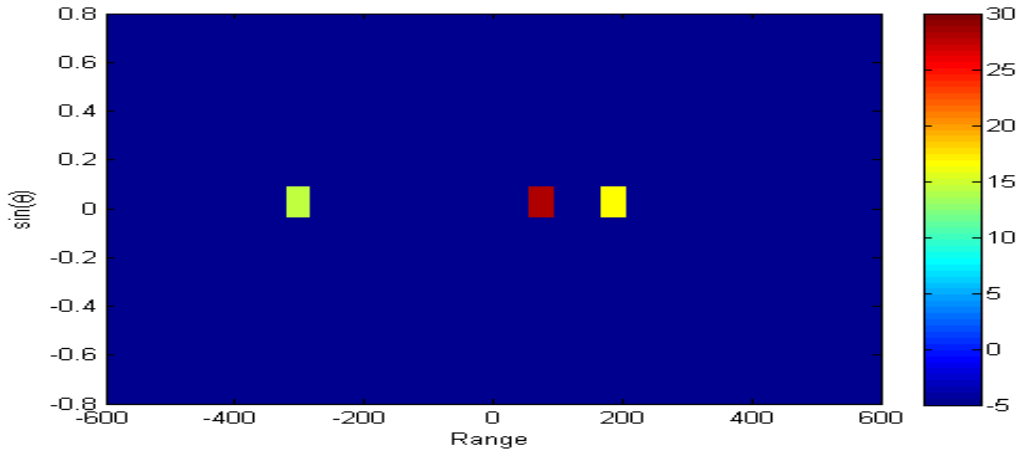

(d) OMP output – extended rejection.

Figure 5.8: *Continued*

5.5 Application of the OMP and IAA on the Experimental Signals

The impact of the imperfections of the real world occurs even if they may not be visible at first sight. Therefore, they may have an impact on detection performance once data-dependent processing schemes are applied, since they are likely to be particularly sensitive to signal model mismatches. Therefore, we will apply the IAA and OMP schemes on the experimental data to exhibit to which extend the final performances are impacted.

We remind that the CDMA have been selected in chapter 2 based on spatial resolution considerations, and then, processing schemes have been introduced in chapter 3 specially to mitigate the residual sidelobes induced by this type of waveforms. In the following, we will apply the IAA and OMP on the experimental data with CDMA waveforms and analyze the results. Note that, even if we have generated and transmitted a family of 12 MIMO waveforms, we will consider only the first 8 waveforms in the processing, due to computational capacity limitation when computing the IAA output.

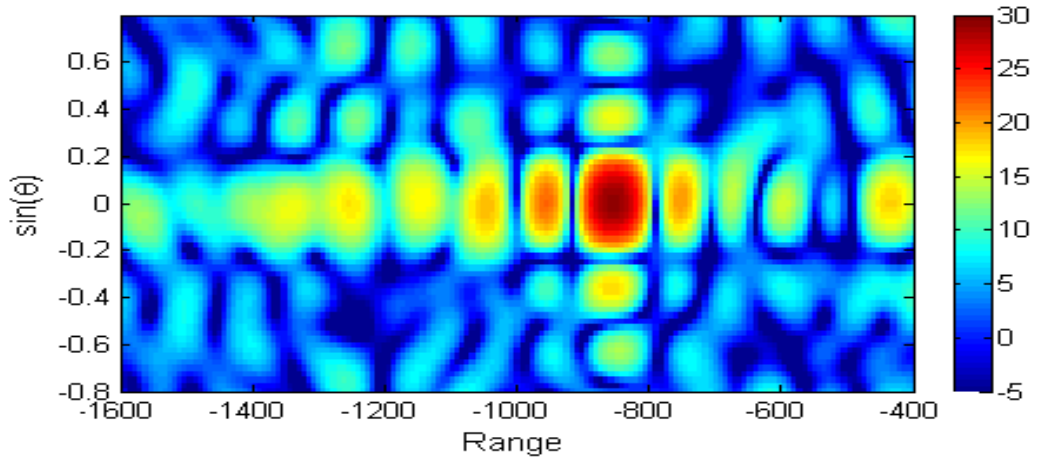

(a) MF output.

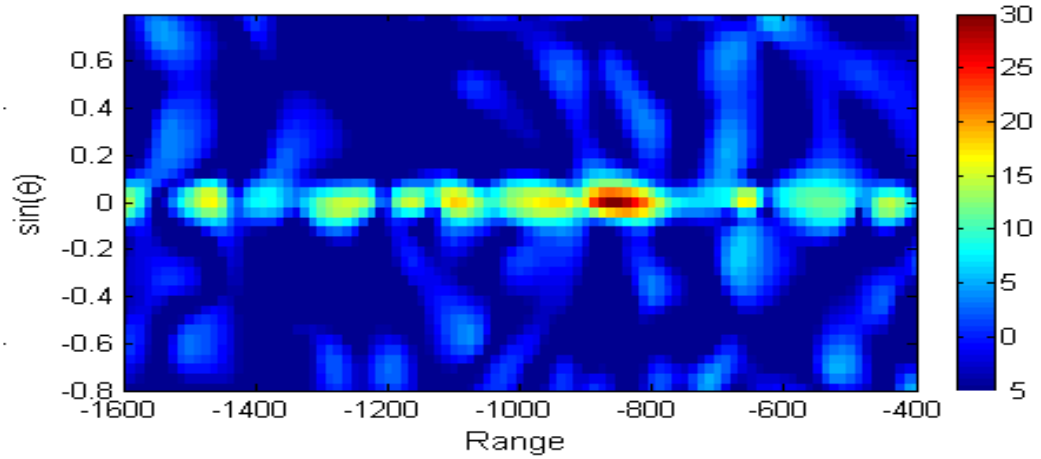

(b) IAA output (iteration 6).

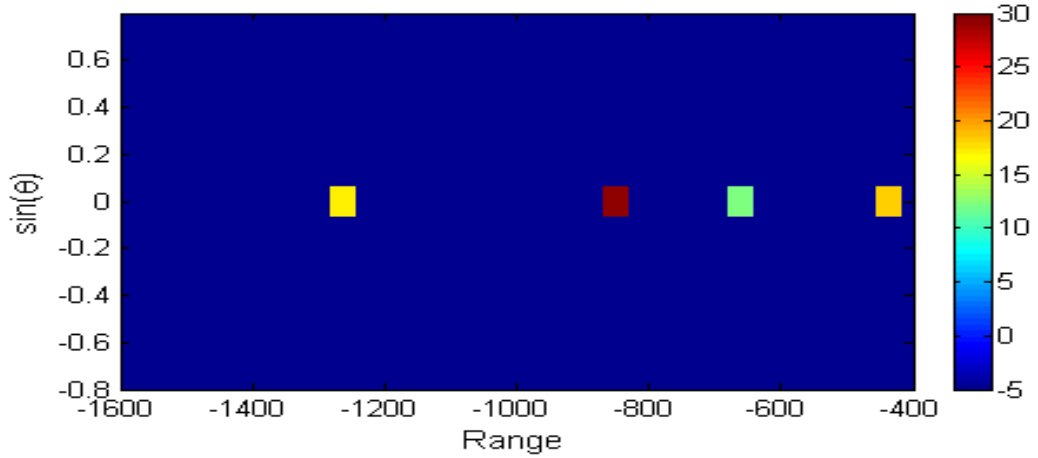

(c) OMP output – extended rejection.

Figure 5.9: Application of the different processing methods on the experimental data (target simulator configuration). Range resolution cell width = 75 m. Angle resolution cell width = 0.25. Ranges in m.

5.5.1 Results From Closed-Loop Experiment

The outputs after application of the different processing methods introduced in this work are exhibited in fig. 5.8 for the experimental data acquired in closed-loop configuration (*i.e.* transmission in the whole radar chain except the antennas). First, fig. 5.8a exhibits the resulting ambiguity function after MF. Two close mainlobes can be noticed, and we can deduce they probably correspond to the two expected “targets" (*i.e.* the two closed-loops identified above). Here, we cannot say if there are other targets in the scene since other potential main lobes cannot be differentiated from the residual sidelobes in the whole range-angle domain.

Now, the IAA output of fig. 5.8b gives two peaks, as expected: one at 140 m corresponding to the experimental radar closed-loop and one at 80 m corresponding most probably to the unwanted shorter closed-loop (due to mixer lack of isolation). Moreover, note that if we set the same detection threshold as for the OMP, *i.e.* at 10 dB above noise level, the IAA will not give additional detection. Here again, these accurate results were at the price of a very long computation (around 20 hours). Moreover, note that both detected targets are at around 75 m distance, *i.e.* one range cell distance.

Then, the results of the application for the OMP with classical rejection are given in fig. 5.8c and they exhibit the two expected targets at similar powers as the IAA did, plus five “ghost" targets above the 10 dB detection threshold. With the proposed extended rejection, the OMP gives the two expected targets plus another one at 14 dB (13 dB below the strongest peak), as visible in fig. 5.8d. We assume that this latter detection is a false alarm due to signal model mismatch since there is no such peak at this position in the IAA output. Besides, note that the right-hand expected target is of lower detected power than with the IAA or with the classical OMP. This can be explained by the fact that right-hand target is at around one range cell distance to the left-hand expected target and so is subject to the “side effect" that occurs with the extended OMP rejection.

5.5.2 Results From Target Simulator Experiment

Now, when applying the different processing methods on the experimental data acquired in target simulator configuration (*i.e.* signal re-transmission with the introduction of delay and Doppler shift), we get the results of fig. 5.9. It can be noticed from fig. 5.9a that the MF output displays one visible main lobe, corresponding to the

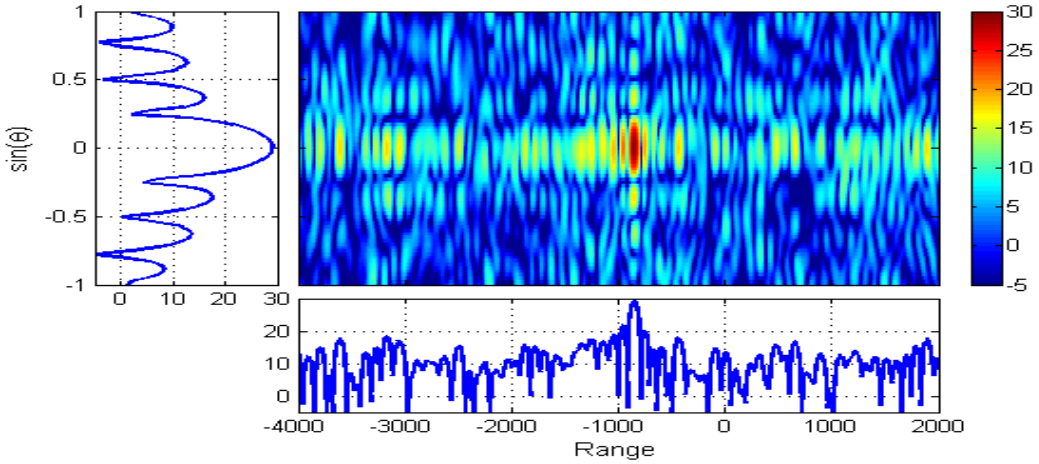

(a) MF.

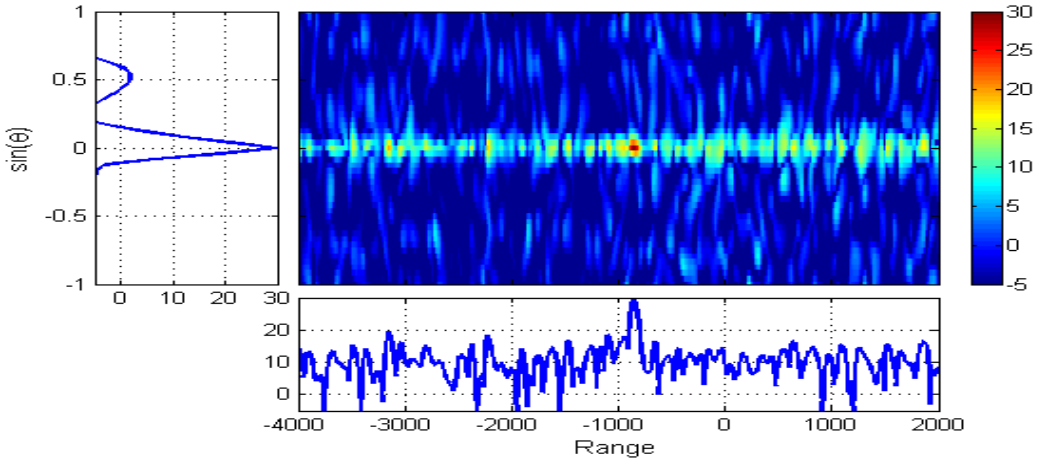

(b) IAA output (iteration 6).

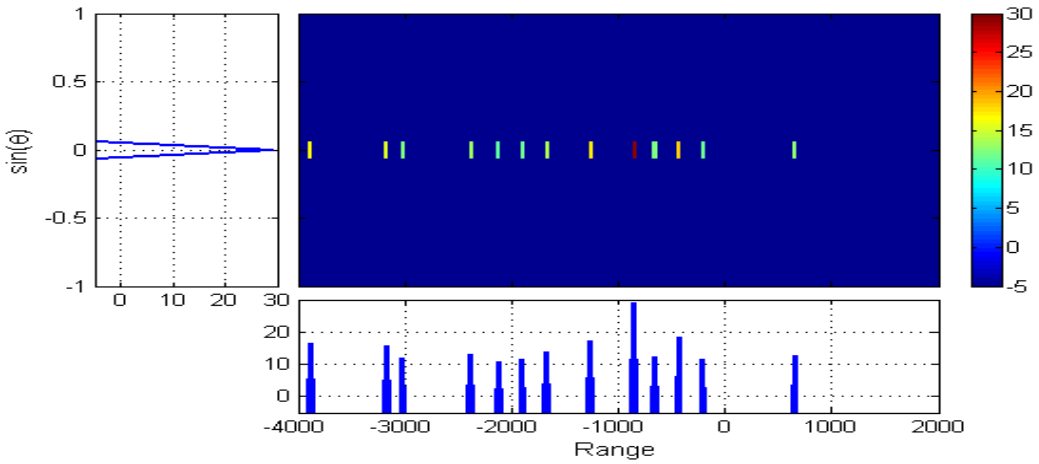

(c) OMP output – extended rejection.

Figure 5.10: Zoom out of plots of fig. 5.9. Cuts at target simulator range and angle are plotted on each side.

target simulator echo. Then, fig. 5.9b depicts the IAA output, where we can observe that the residual sidelobes beyond the target angle are reduced to the level of 0 dB. Nevertheless, some higher sidelobes (up to 19 dB) are visible at target angle along the range axis. The zoom out of fig. 5.10b permits to better visualize the extension of the sidelobes along the range axis. Concerning the OMP output displayed in fig. 5.9c, we can notice the correct estimation of target power, and the coming up of several false alarms. When observing the zoom out of fig. 5.10c, it can be stated that these false alarms are restricted to the target angle and that the strongest one has a power of 18 dB. In this experimental configuration, we remind that the signal of interest was subject to unwanted partial truncation. Therefore, it is difficult to deduce clearly if the unexpected sidelobes giving false alarms are due to the waveform truncation or to another effect (*e.g.* antenna imperfection or propagation issue) having an impact on the signal model.

5.6 Conclusion

The Hycam multifunction radar platform has given us the unique opportunity to acquire MIMO radar signals in real conditions, which constitutes one of the first experiments with such a system. In this way, we have first defined in this chapter the precise contexts of the different experiments. The first one – the closed-loop configuration – was set up specially to confront to the radar internal hardware components. The second one – the RF transmission to a target simulator – was set to confront, in addition, to antenna diffusion and propagation in the real environment. For each of these configurations, we have generated not only CDMA, but also TDMA and FDMA waveforms, in order to give performance comparison in extension.

In addition to the usual unforeseen imperfections, we have identified phenomena that might induce consequent discrepancies with the expected signal to receive. We have described the imperfect mixer isolation impacting the closed-loop configuration, and the signal truncation due to a deficient optical fiber impacting the target simulator configuration.

Once the acquisitions proceeded, we have run the signal processing up to MF and computed the performance figures of merit for all configurations and all waveforms. The comparisons have shown that detection performance with MF was particularly similar between theory and experiments.

Then, since limited model mismatches are nonetheless likely to induce much stronger performance degradation for data-dependent methods, we have applied the IAA and the extended OMP processing schemes on the experimental data. With the data from the closed-loop configuration – subject to marginal model mismatches –, the IAA has provided two accurate echoes, as anticipated, and has mitigated all the residual sidelobes, yet again with computation times that are inadequate for a practical implementation, whereas the extended OMP has given similar results but with one false alarm. This is interpreted as a “residue" of the rejection of a strong target contribution that slightly differs from the modeled one. Now, with the data from the target simulator configuration – subject to more signal distortion –, the IAA and OMP have both mitigated all the sidelobes apart from the range axis at target angle where several sidelobes have remained. Giving a definitive interpretation was premature here since the signal of interest was subject to unexpected truncation, among other discrepancies. This could be further investigated with new experimental acquisitions.

6 Conclusions and Perspectives

6.1 General Conclusion

The numerous advantages of the MIMO radar concept upon today's radar architectures are established. According to many studies, it possibly provides more flexibility for the transmitting beampattern design (including wider scene illumination and longer time on target) and system complexity reduction, through the use of less antennas and the possibility to transfer system control and calibration to the digital domain. This architecture has a strong potential to become the next generation of radar for a large range of applications. But even if a few proofs of concept have been already implemented, the MIMO radar is still at the stage of the theoretical concept and the transposition to the real world is not enacted yet. In particular, the waveform lack of orthogonality and the impact of the hardware imperfections were often not – or partially – tackled in the existing works.

Therefore, it was the ambition of this thesis work to contribute to paving the way to the operational MIMO radar. The objectives were to go beyond the theoretical concept so to allow forward practical implementation. In this way, in its intent of anticipating and compensating the imperfections of the real world, the range of this work goes from MIMO waveform design and processing schemes development to model mismatch analysis and experiment in real conditions.

In this work, we have established and compared the intrinsic properties of each type of MIMO waveform. Based on performance criteria like Cramer-Rao lower bound and figures of merit computed from the ambiguity functions, we have shown that the CDMA waveforms present optimal performance in terms of spatial resolution. Thus,

we have selected the phase codes as relevant MIMO families, to the condition, though, that their “imperfections" can be limited. Indeed, we have shown that the CDMA inevitable lack of orthogonality induces an extensive sidelobe level that is likely to “hide" the secondary targets of the scene. We have explained that the frame of mind of the work would consist in taking on the MIMO waveform intrinsic imperfection and in putting the compensation efforts on the processing on receive. However, the use of CDMA waveforms still allows to proceed, in addition, code sequences design optimization.

We have established that the MF was not designed for mitigating the residual sidelobes and that we had to investigate on data-dependent processing schemes. We have defined the requirements for an operation implementation, in particular in terms of estimation accuracy and sidelobe rejection, computation rapidity, and limitation of training data. In this context, we have explained why many of the techniques of the literature do not satisfy these specific constraints. We have then exhibited that the OMP scheme is one suitable solution with regard to the implementation requirements. Nevertheless this method is subject to strong sensitivity to target localization error, as it could be shown through the introduction of neighbor influence and target grid granularity in simulations. We could solve this issue with the proposition to extend the rejection area within the OMP algorithm. Besides, we have also presented the IAA which has been shown to provide, with only a few training data, results possibly as accurate as Capon, but to the price of a computation time that is not suitable for practical implementation. We have thus proposed to use this scheme as a reference, *e.g.* for making comparison with other methods.

This latter processing scheme analysis had been made with the consideration that the received signals fit the signal model. We have explained that unanticipated signal distortions would induce signal model mismatch that can particularly degrades the detection performance of data-dependent processing. Indeed, the signal of interest would be likely to be partially rejected and artifacts could be induced in the target scene. In this way, we have described the origin of common signal distortions that might occur during signal generation and propagation. Then, we have applied the IAA and OMP methods on simulated signals subject to defective transmitters, and we could show that model mismatches should be anticipated, or even prevented, to avoid strong performance degradation. We have then presented general strategies to this end, based on the representative example of the Hycam radar testbed which is among the very few existing implementations of a MIMO radar. We exhibited that

model mismatches could be prevented at system design stage or anticipated and compensated during system use as illustrated with a proposed method of Tx phase calibration taking advantage of the MIMO flexibility.

In a purpose of making a bridge to the real world up to real implementation, we have set up experiments with the MIMO radar testbed, which is of special interest since they turned out to be among the first substantial experiments to be proceeded in the world. We have defined two distinct experiments in order to confront to the internal radar only (the closed-loop configuration) and to a fully-operational scenario (the target simulator configuration), respectively. We have identified particular unanticipated phenomena during the signal acquisitions: in the first configuration, an imperfect mixer isolation that we actually took as an opportunity for the estimation of two neighbor echoes to detect, and in the second configuration, a truncation of the signal of interest that is more problematic since difficult to isolate from other distortions occurring during signal transmission and propagation. Based on these data, we could exhibit that the signal discrepancies have induced marginal performance impact at the MF output, but stronger performance degradations at the IAA and OMP outputs. More particularly, the second configuration has given many false alarms at target angle that are probably due to the signal truncation, thus stressing the particular sensitivity of such processing schemes to unanticipated model mismatches.

6.2 Way Forward

6.2.1 Performance Improvement of the Proposed Methods

The OMP process is based on an iteration on the targets of the scene, therefore, a consequent drawback of this method is that an imperfect target estimation (*e.g.* an estimated target contribution that does not perfectly match the modeled contribution) can have a harmful impact on the next targets to be detected. This effect is even more significant when it concerns one of the first detected targets which are the ones of stronger power in the scene. We have also cited the “side-effect" of the rejection step of the algorithm that induces the power mitigation of the signal in the resolution cells directly adjacent to the cell of the detected target.

To avoid these issues while benefiting from both the computation rapidity of the OMP and the accuracy of the IAA, we propose to combine both techniques in three steps:

- Proceed the complete OMP scheme
- Compute the covariance matrix from the estimated targets
- Inject this covariance matrix in the IAA process (with a diagonal loading with noise power to avoid bad conditioning).

Therefore, we expect to recover the accuracy of the IAA for the output while greatly reducing the number of iterations needed, and so the computation time.

6.2.2 Model Mismatch Robustification

To complete the present work, new experimental acquisitions can be proceeded in order to investigate further the origins of the false alarms obtained in the target simulator configuration. It could be of particular interest to isolate, when it is possible, the different signal distortions, for example by avoiding the truncation of the signal of interest, or including the antenna coupling in the signal model.

To go further, we propose to better anticipate the possible signal distortions, and then to prevent them to occur, or to include them in the signal model, in a way as a global transfer function that encompasses all the effects that can be measured before the fact. Furthermore, this corresponds to the “MIMO philosophy" which consists in taking on the system imperfections and compensating it through processing after the fact. Nevertheless, as also mentioned in the thesis work, some signal distortions might not be steady or not possible to anticipate, so we propose to develop techniques for enhancing the method robustness with respect to the possible mismatches. These techniques could be inspired by the extension proposed for the OMP rejection where the margin for the “accepted signal" is widen. More generally, it could consist in defining uncertainty areas (in the likelihood sense) around the target estimated “localization" in specific spaces, so to tolerate a specific level of discrepancy with the modeled signal. It could be investigated on how to develop this concept for the consideration of mismatches like antenna amplitude or phase errors and target Doppler.

A Signal Processing Implementation

We present in this appendix how the raw data acquired with Hycam (presented in chap. 4.3.1) are processed, first in real time within the Hycam chain, and then through off-line digital processing. This second operation has been specifically developed in Matlab during the thesis. In order to control and visualize each step, a Graphical User Interface (GUI) has been additionally developed.

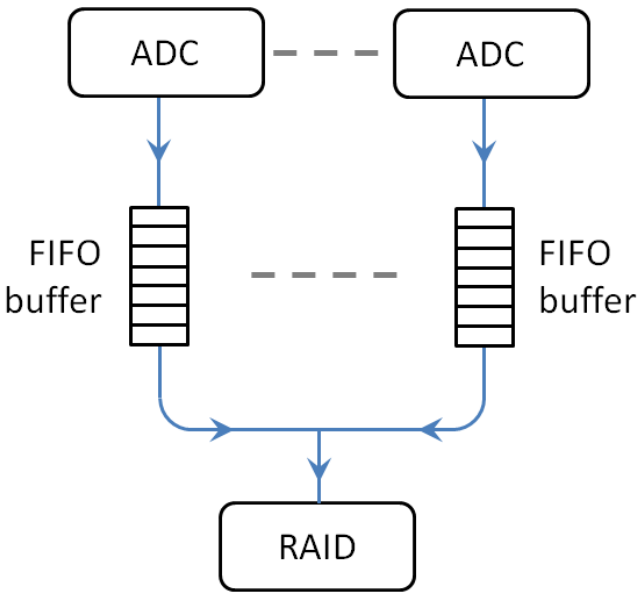

Figure A.1: Illustration of the data saving system. FIFO are buffers of high data rate but limited capacity, whereas the RAID disks are subject to lower data rate but consequent capacity.

A.1 Data Acquisition and Formatting

During the experiments with the Hycam platform, the RF signals captured in the antennas are transmitted to the radar front-end where there are subject to a first processing on the fly: the signals are converted to optical frequencies, transmitted to the optical rotary joint, converted back to RF, down-converted to the intermediate carrier frequency, filtered and finally sampled.

The acquired data are buffered in FIFO (First In, First Out) devices and saved progressively on Redundant Array of Independent Disks (RAID) for offline processing, as illustrated in fig. A.1. The reason for using such a system is the possibility to dispatch the data with redundancy on different disks to reduce the risk of data loss or a faster transfer rate thanks to parallel transfer to different disks simultaneously, as it is the case here. Nevertheless, the capacity of the data link to the RAID devices is limited (such as FIFO capacity of 600 Mo, or rate of the link to the RAID up to 1 Go/s) and thus the experiments have to be “calibrated" in advance so not to overstep these restrictions. Therefore, for some situations, the acquisition had to be limited to one receiver only. Actually it was of no issue for the thesis work since we do not focus on reception beamforming.

The first step to make the signals exploitable with a software like Matlab is to demultiplex them with a script that retrieves the data from the different RAIDS and generates a unique binary file. The second step is the formatting of the data file that is initially a raw concatenation of all experimental signals. In the thesis work, we have presented experiments either in ‘full-MIMO" configuration (in section 4.3.3) or in sequential MIMO configuration (in section 5.2, where each waveform is transmitted one after the other). Therefore, the data formatting operation should be adapted to the MIMO configuration so to retrieve then the sequential signals and add them up in order to recover an equivalent full-MIMO configuration. An algorithm developed on Matlab processes the formatting of the data into separate waveform families, transmitters and recurrences. The data are then ready to be directly exploited as formatted matrix.

A.2 Radar Digital Processing

All the operations of the radar digital processing have been developed on Matlab. Moreover, in order to manage and visualize each step of the whole processing and

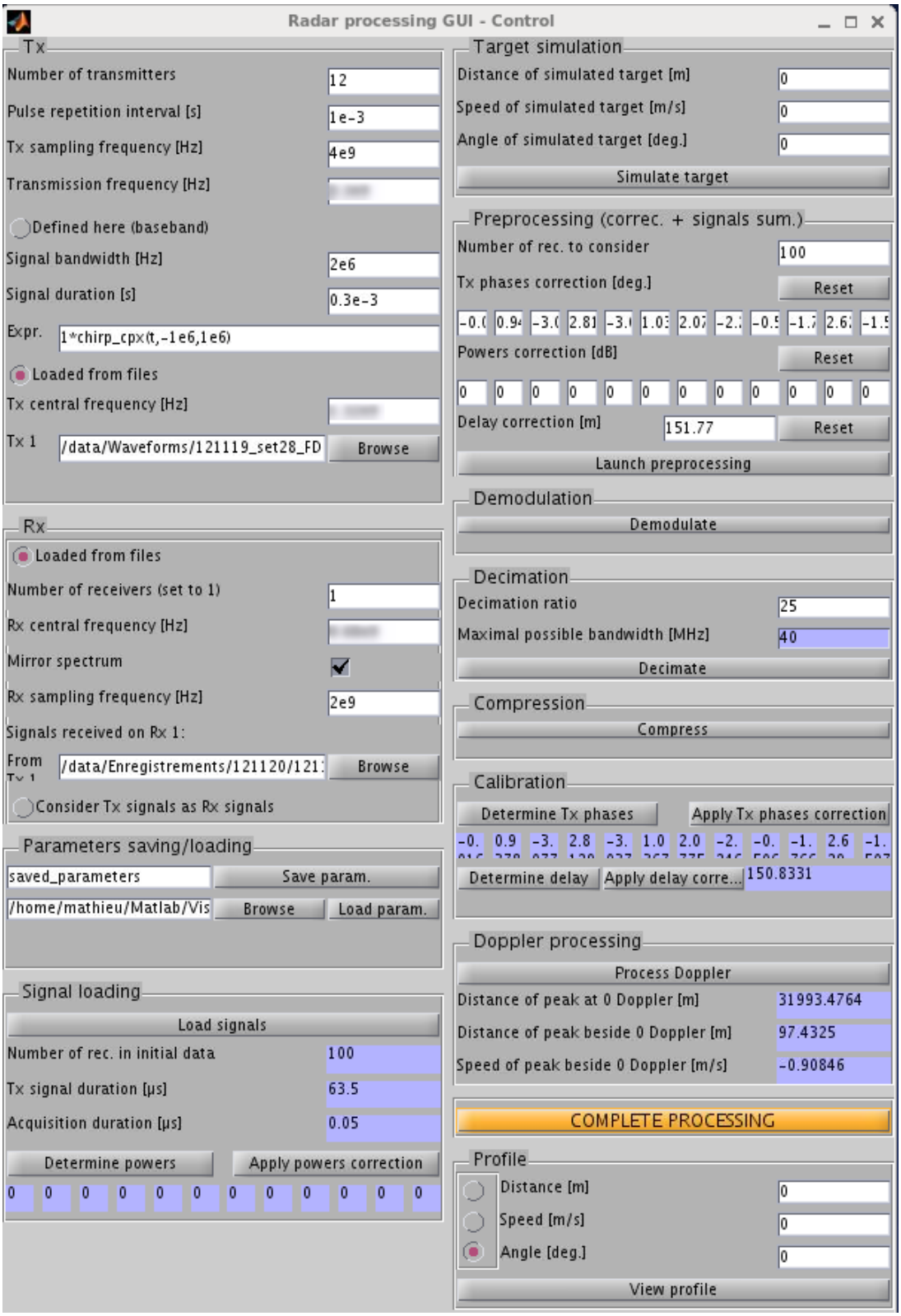

Figure A.2: GUI control panel.

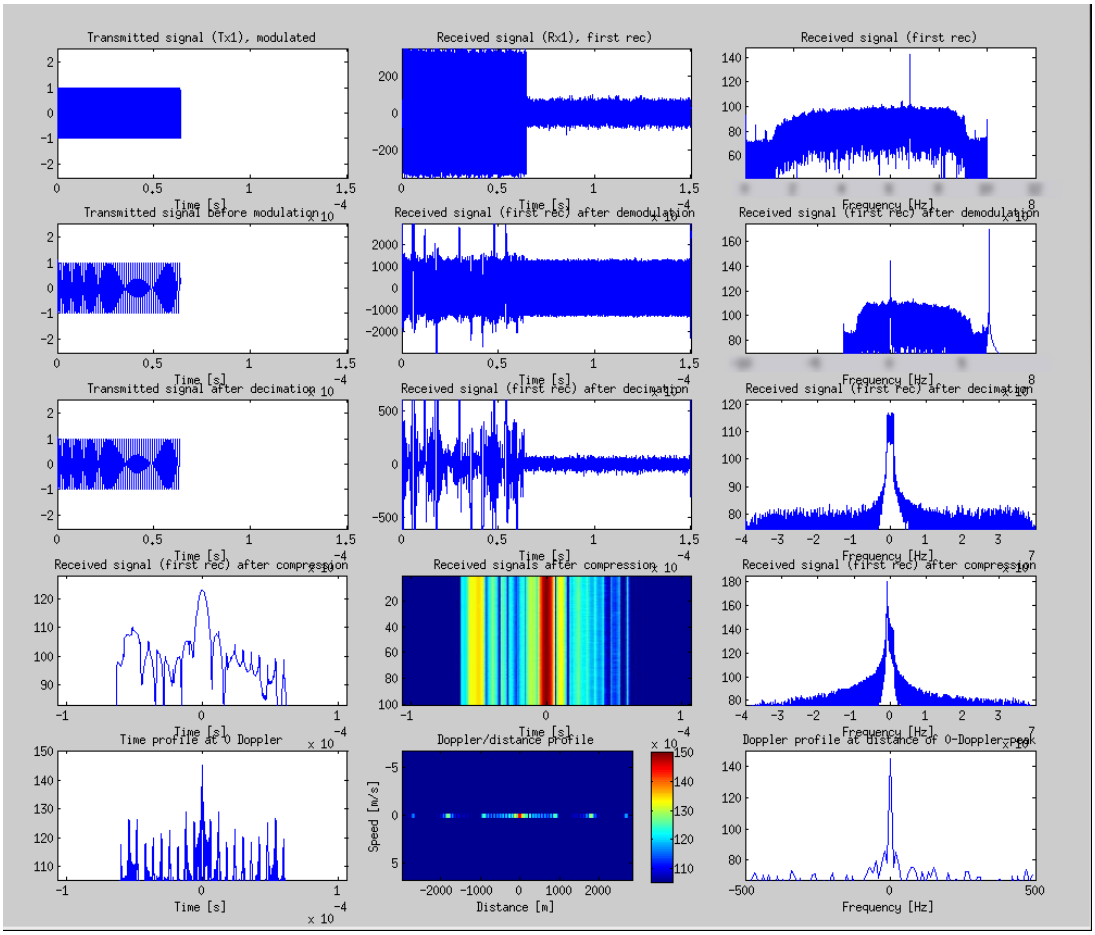

Figure A.3: GUI display panel.

also calibration operations, a GUI has been entirely developed. It is composed of a control panel and a display panel, exhibited in fig. A.2 and A.3, respectively.

Here is an overview of the successive operations of the processing, each one corresponding to a frame of the GUI control panel:

- **Tx:** Definition of the parameters of the transmission and the expressions of all waveforms (usually loaded from the files generated for the experiments).
- **Rx:** Definition of the parameters of the reception and the path to the acquired signals (usually a 3-dimensional data cube). Note that it is also possible to consider the transmitted signals as received ones for the case we want to determine the theoretical ambiguity function.
- **Parameters saving/loading:** A tool to save or load all the entered parameters

and file paths of the panel.

- **Signal loading:** Loading of the signals and extraction of some information in order to control the correct format of the signals.

- **Target simulation:** An option for the case we want to simulate a response from a point target at a specific range/angle/Doppler position. The loaded signals will be adapted the corresponding way.

- **Preprocessing:** An optional step which consists in the correction of the phase offset between transmitters. It is also possible to apply a power correction on the transmitters. In the case of sequential transmission, the signals of each transmitter are finally summed up to recover the full-MIMO configuration.

- **Demodulation:** Demodulation of the signals to baseband, processed in spectral domain.

- **Decimation:** Re-sampling of the signals at a lower frequency, associated with anti-aliasing filtering. The objective is to reduce the size of the data to process, as long as Nyquist condition is fulfilled (an indicator tells the limit decimation ratio).

- **Compression:** MF of the signals with all generated waveforms, one by one. Note that these waveforms have been formerly demodulated and decimated at same frequencies as the signals being processed.

- **Calibration:** The Tx phase offsets can be determined here, *i.e.* once each transmitted signal is separated after the compression step. They can be automatically entered in the preprocessing step to apply the correction and launch again the processing steps (iterative process). In the calibration step, it is also possible to apply a delay correction, for example in the case that the acquisition window does not start at range 0.

- **Tx/Doppler processing:** This step is for the Doppler processing and the Tx beamforming. After this step, we eventually get the ambiguity function in range/angle/Doppler dimensions which can be directly exploited.

- **Complete processing:** A possibility to launch all steps (except the optional ones) on the run.

- **Profile:** An option to display a visualization in two dimensions of the ambiguity function at a specific position of the third parameter.

B Ambiguity Functions From Acquisitions

This appendix is an extension of section 5.4.1. We give here all the ambiguity functions (MF outputs) computed from the theoretical and experimental data.

B.1 CDMA Waveforms

B.1.1 Random Binary Codes

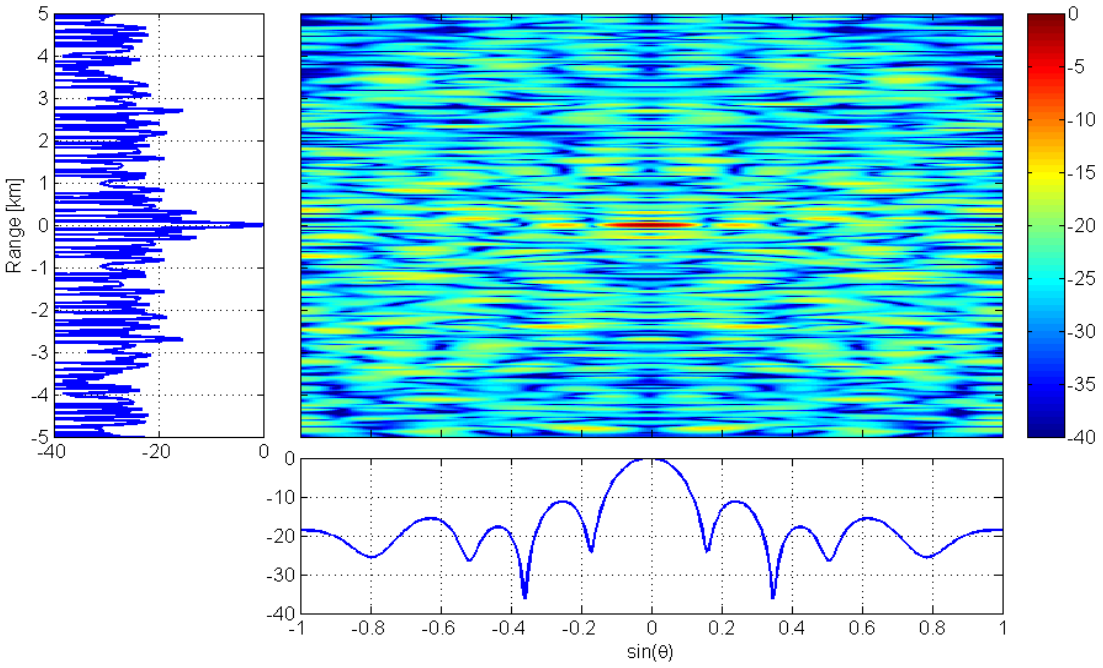

(a) Theoretical data.

Figure B.1: Ambiguity functions (MF output) for a family of random binary phase codes.

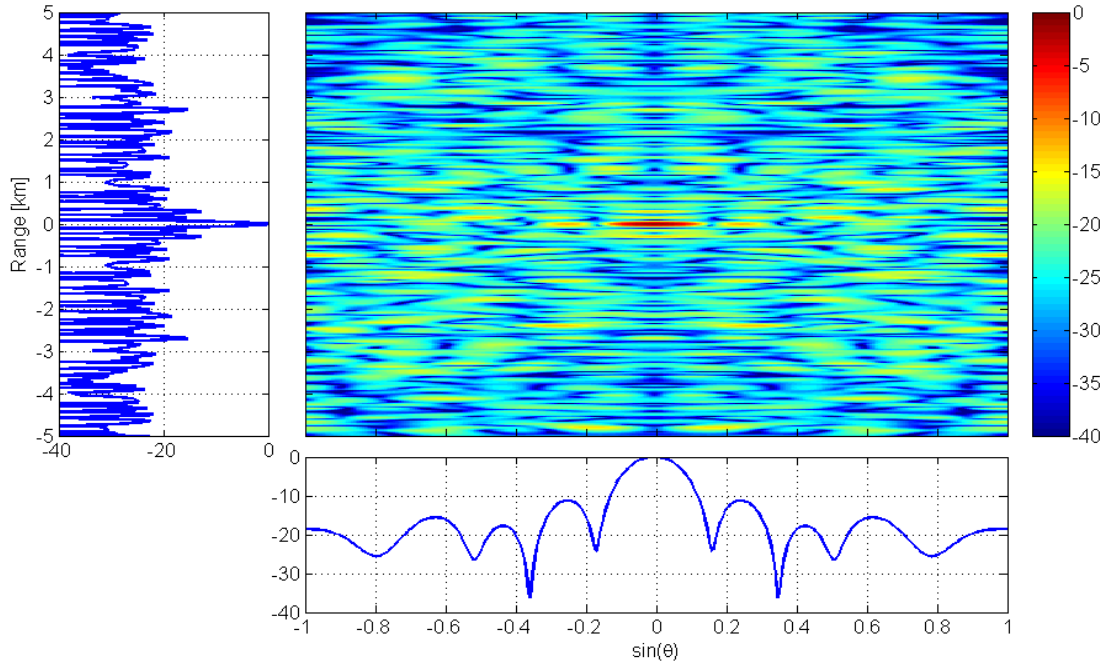

(b) Experimental data – Closed-loop configuration.

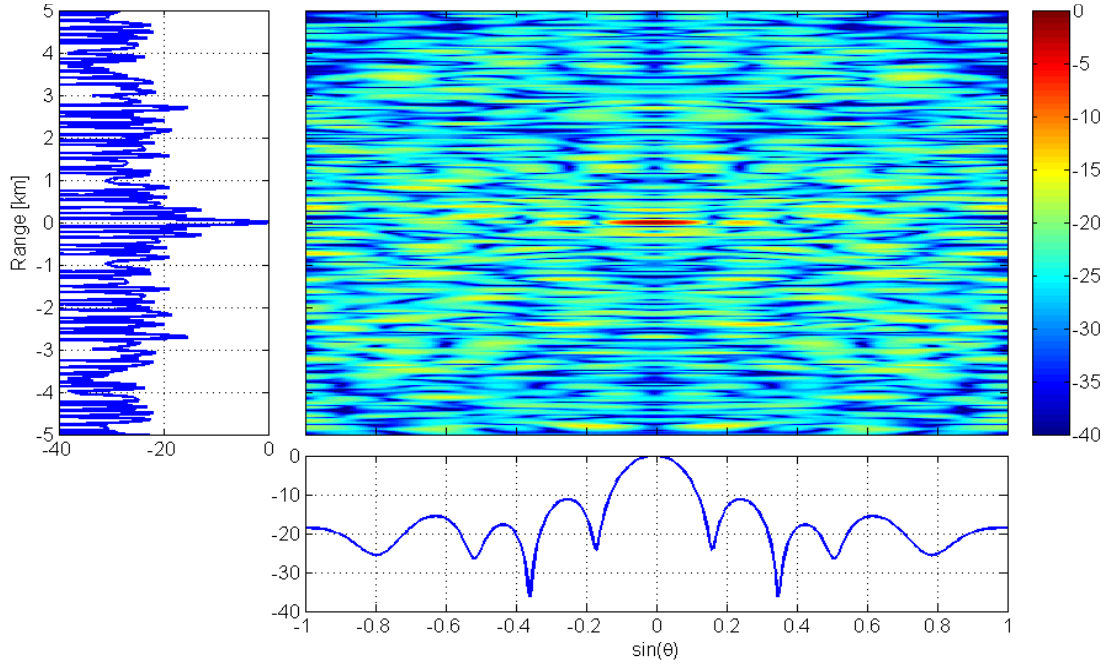

(c) Experimental data – Target simulator configuration.

Figure B.1: *Continued.*

B.1.2 Gold Codes

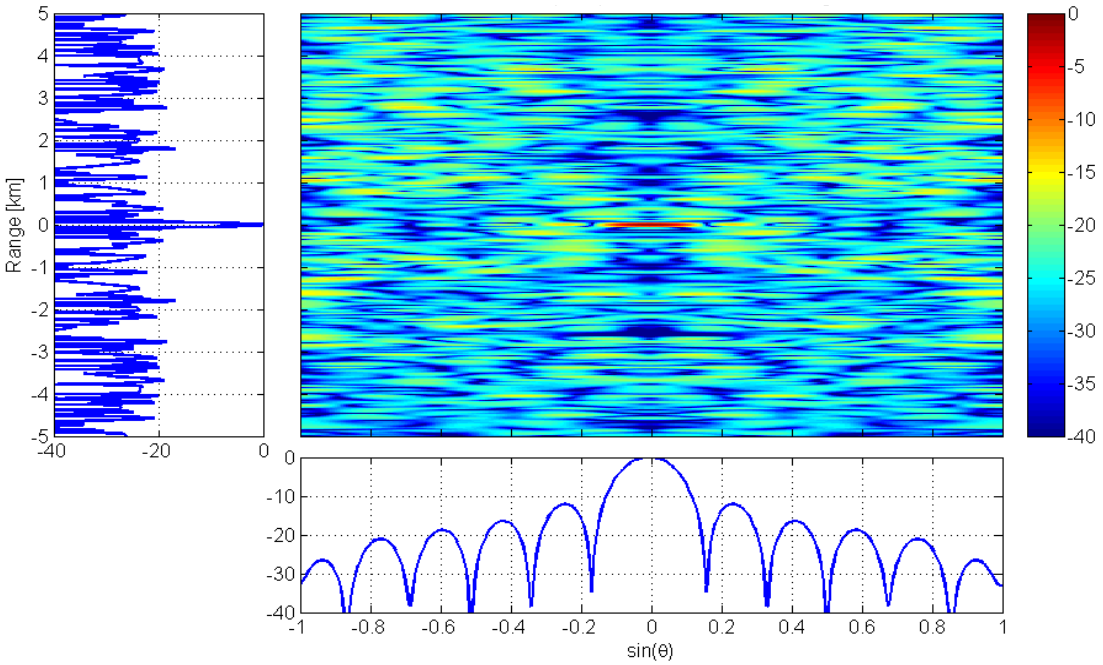

(a) Theoretical data.

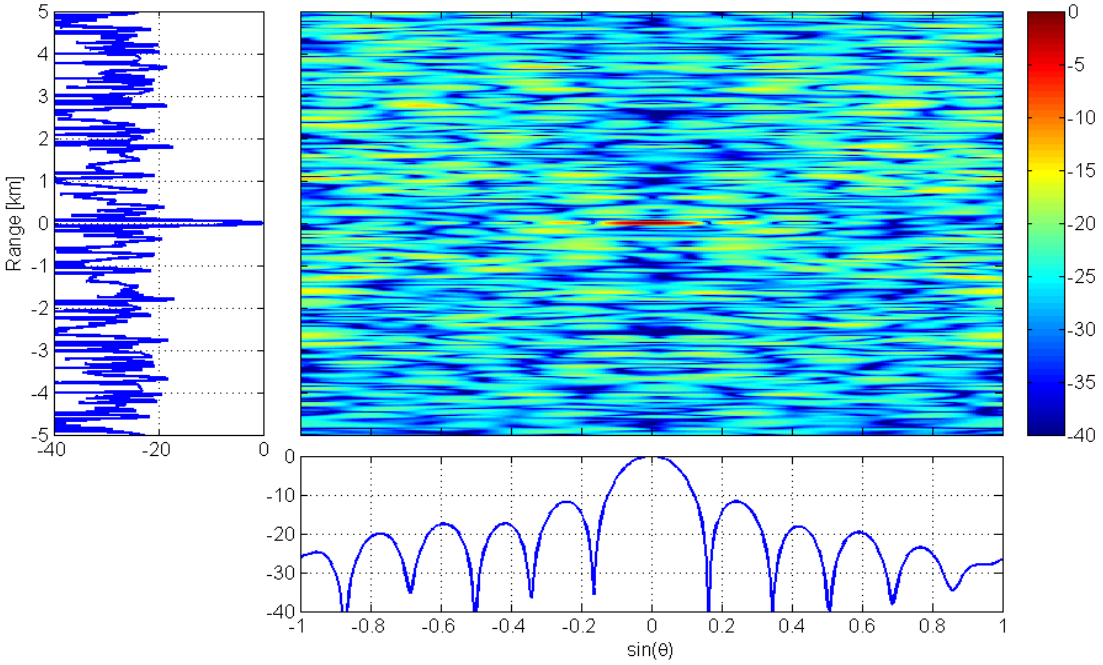

(b) Experimental data – Closed-loop configuration.

Figure B.2: Ambiguity functions (MF output) for a family of Gold codes.

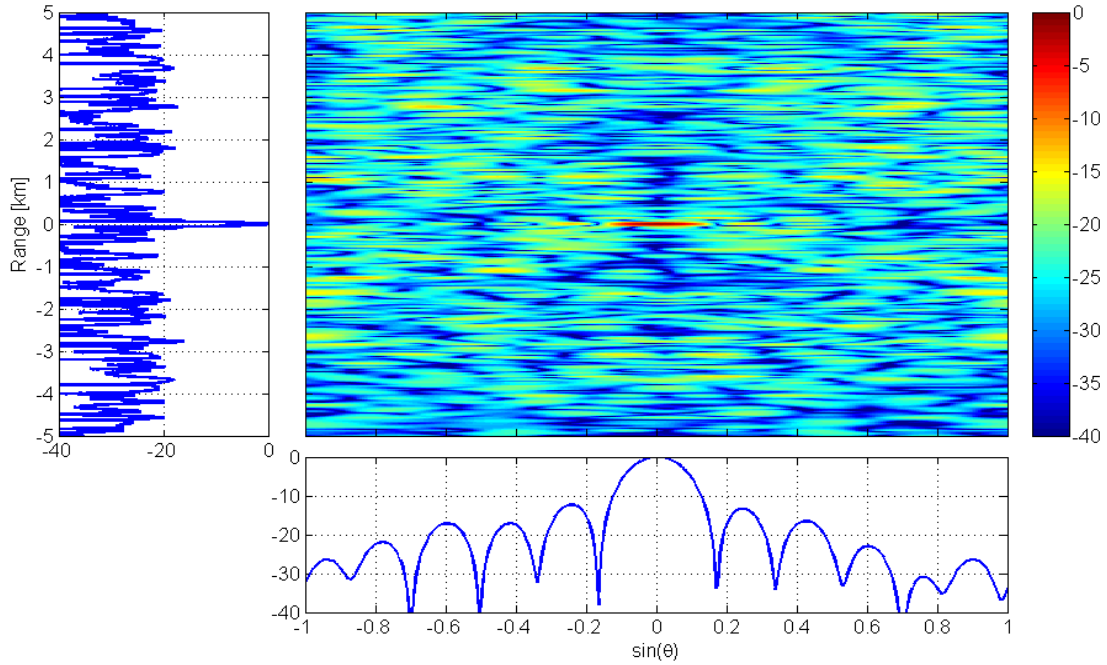

(c) Experimental data – Target simulator configuration.

Figure B.2: *Continued.*

B.1.3 Chaotic Polyphase Codes

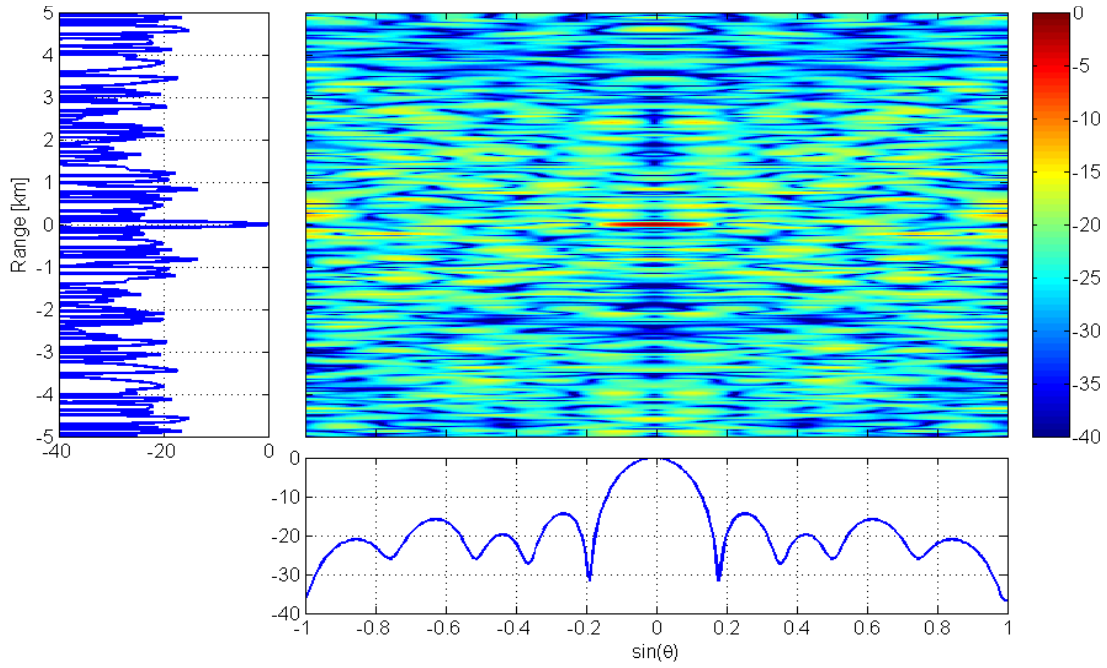

(a) Theoretical data.

Figure B.3: Ambiguity functions (MF output) for a family of chaotic polyphase codes.

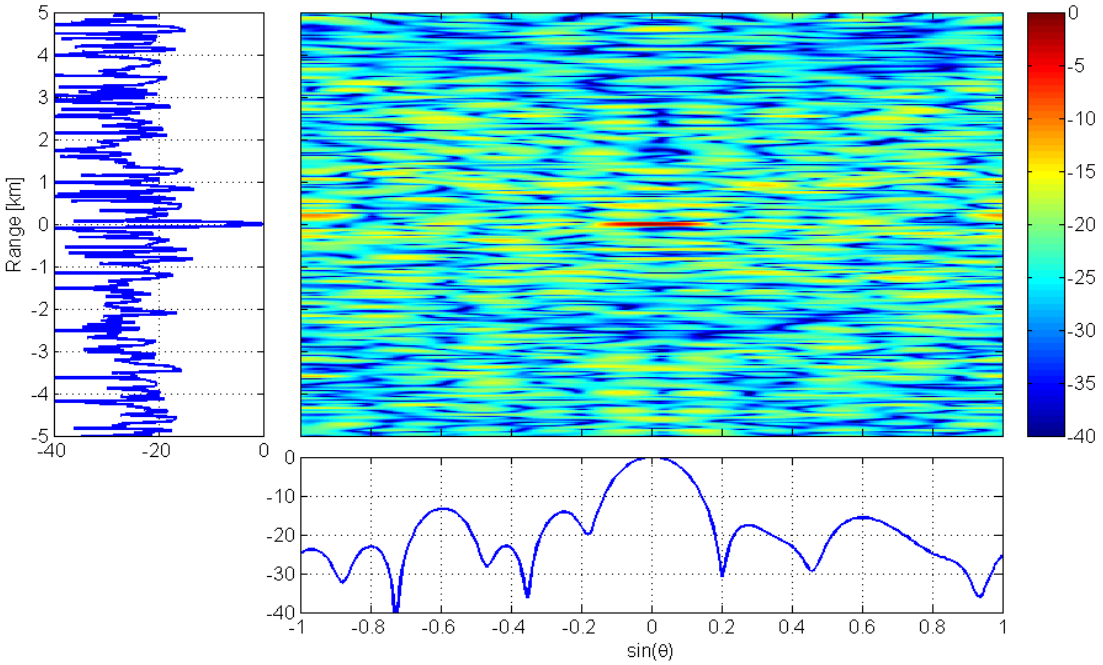

(b) Experimental data – Closed-loop configuration.

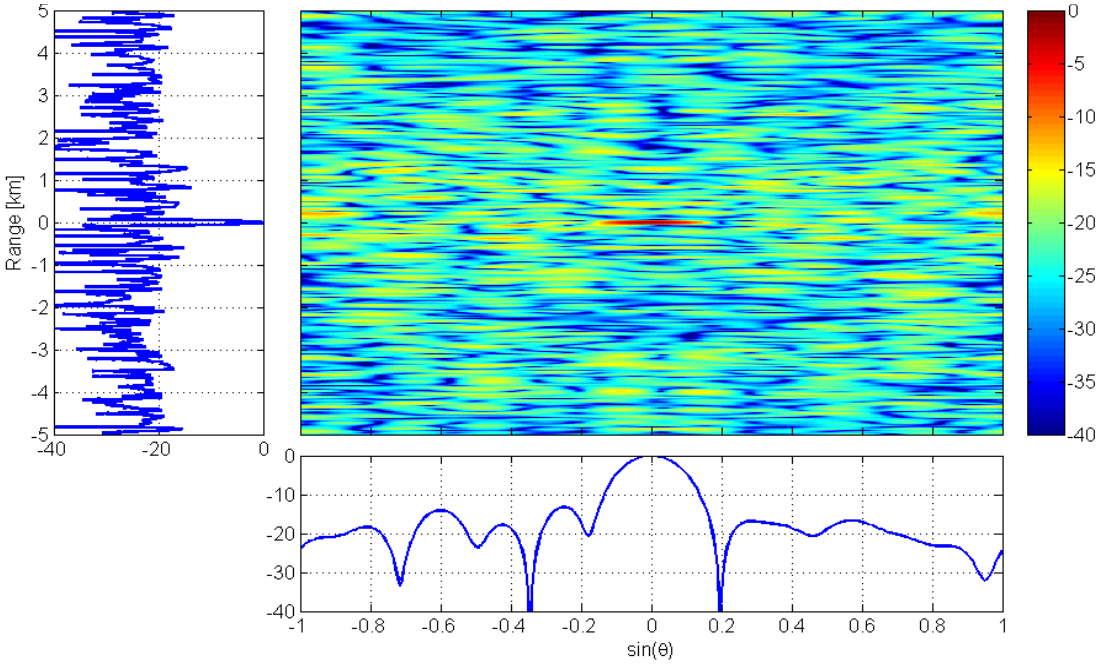

(c) Experimental data – Target simulator configuration.

Figure B.3: *Continued.*

B.2 TDMA Waveforms

B.2.1 Circulating Gold code

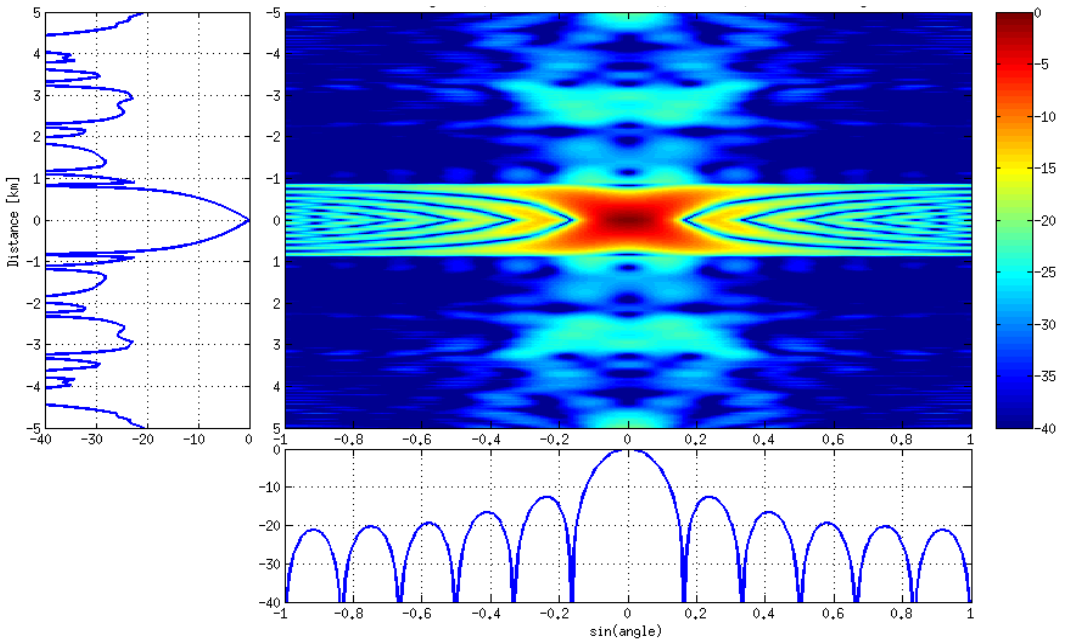

(a) Theoretical data.

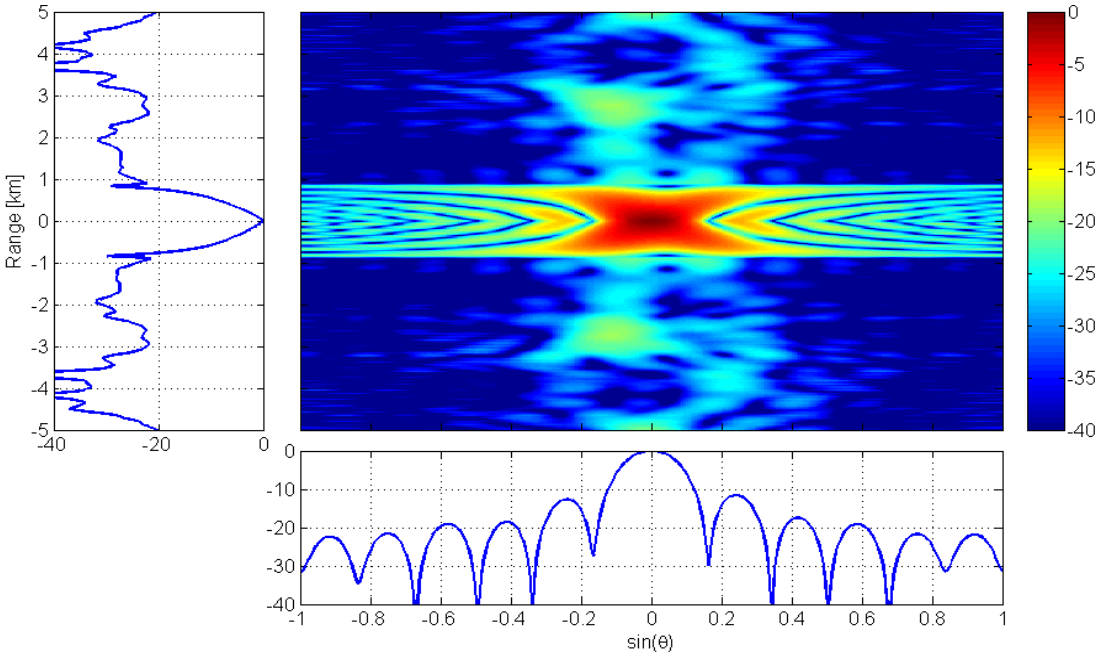

(b) Experimental data – Closed-loop configuration.

Figure B.4: Ambiguity functions (MF output) for a circulating Gold phase code.

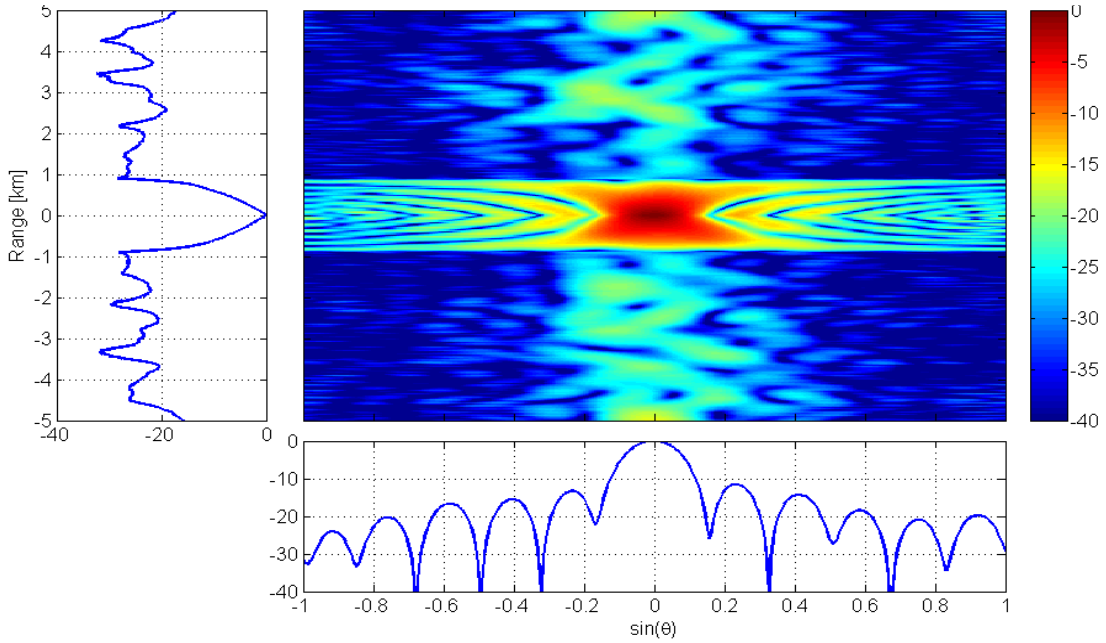

(c) Experimental data – Target simulator configuration.

Figure B.4: *Continued.*

B.2.2 Circulating Gold code – Larger delay between transmitters

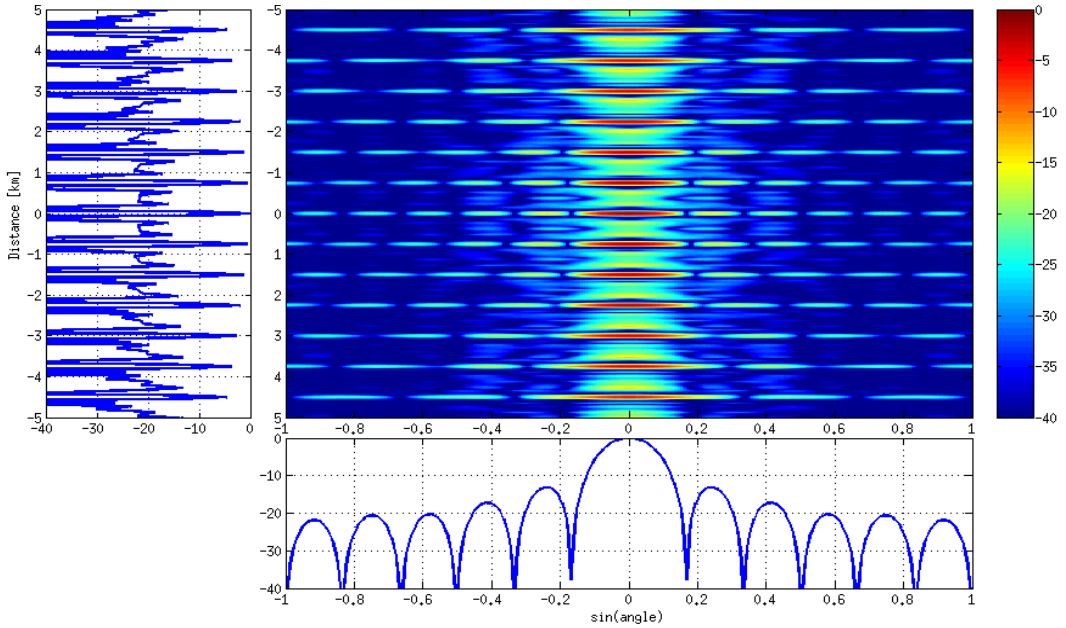

(a) Theoretical data.

Figure B.5: Ambiguity functions (MF output) for a circulating Gold phase code – Ten times larger delay between transmitters.

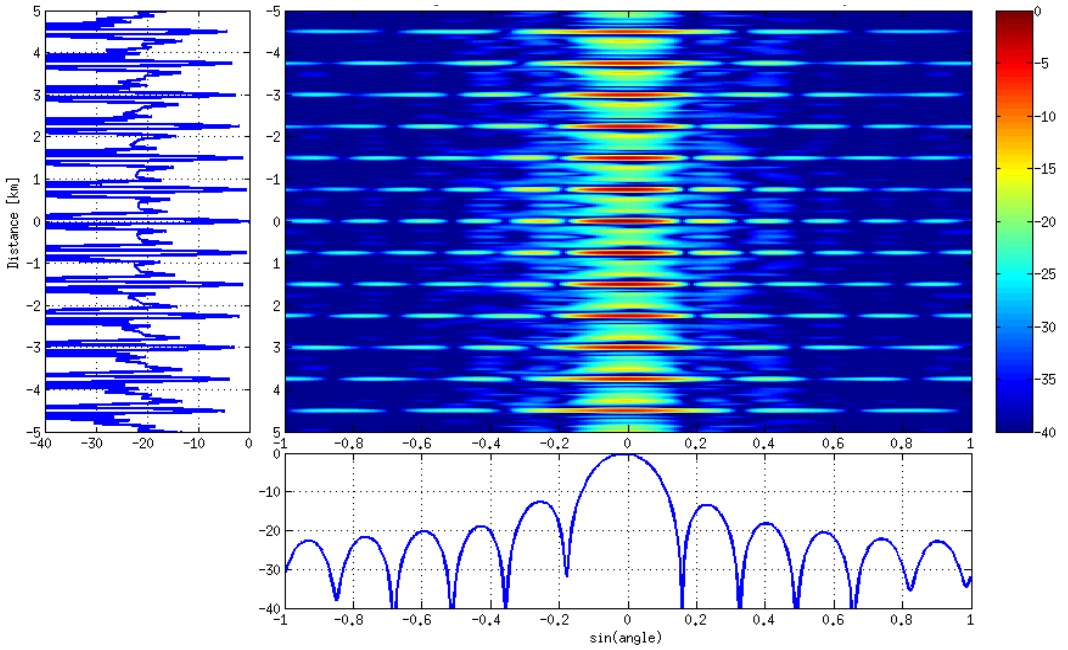

(b) Experimental data – Closed-loop configuration.

Figure B.5: *Continued.*

B.2.3 Circulating chirp

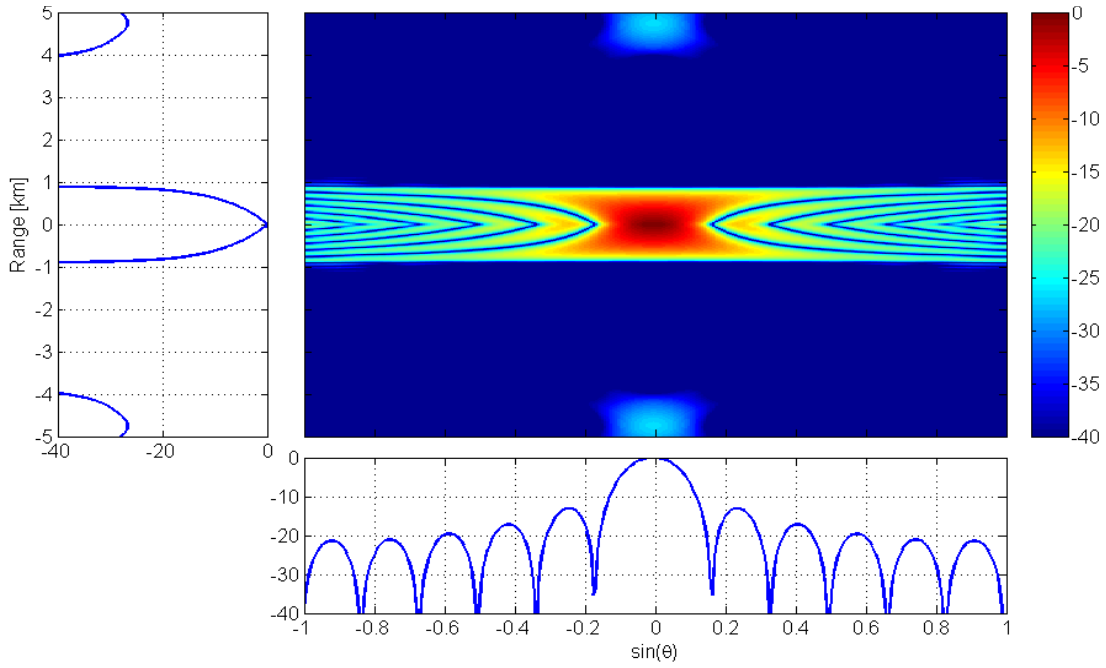

(a) Theoretical data.

Figure B.6: Ambiguity functions (MF output) for a circulating chirp.

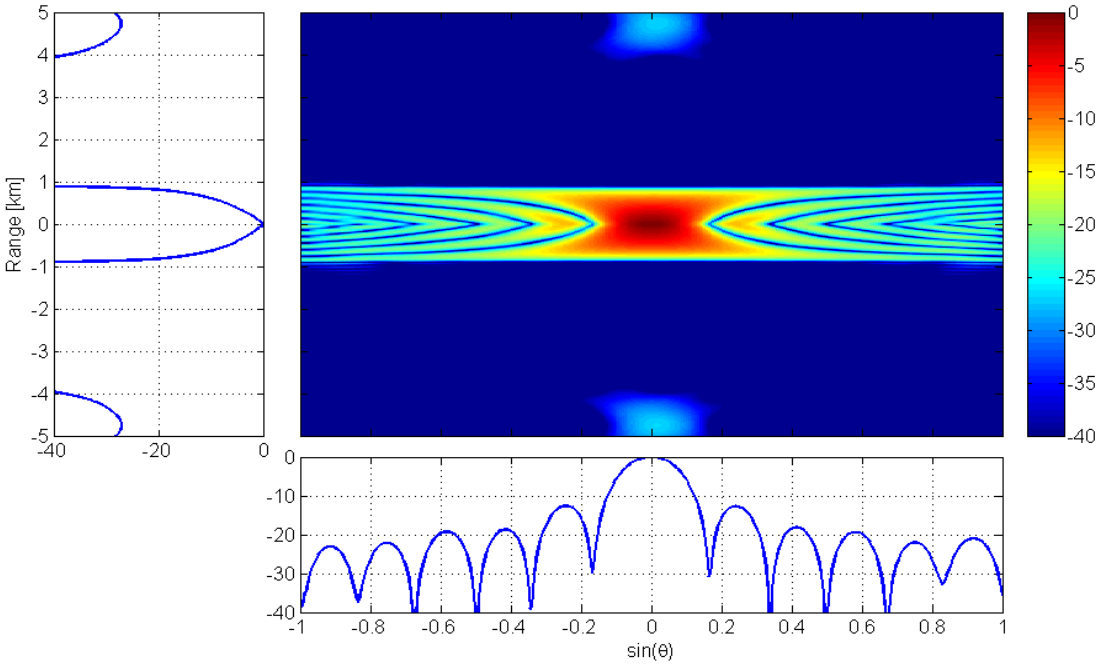

(b) Experimental data – Closed-loop configuration.

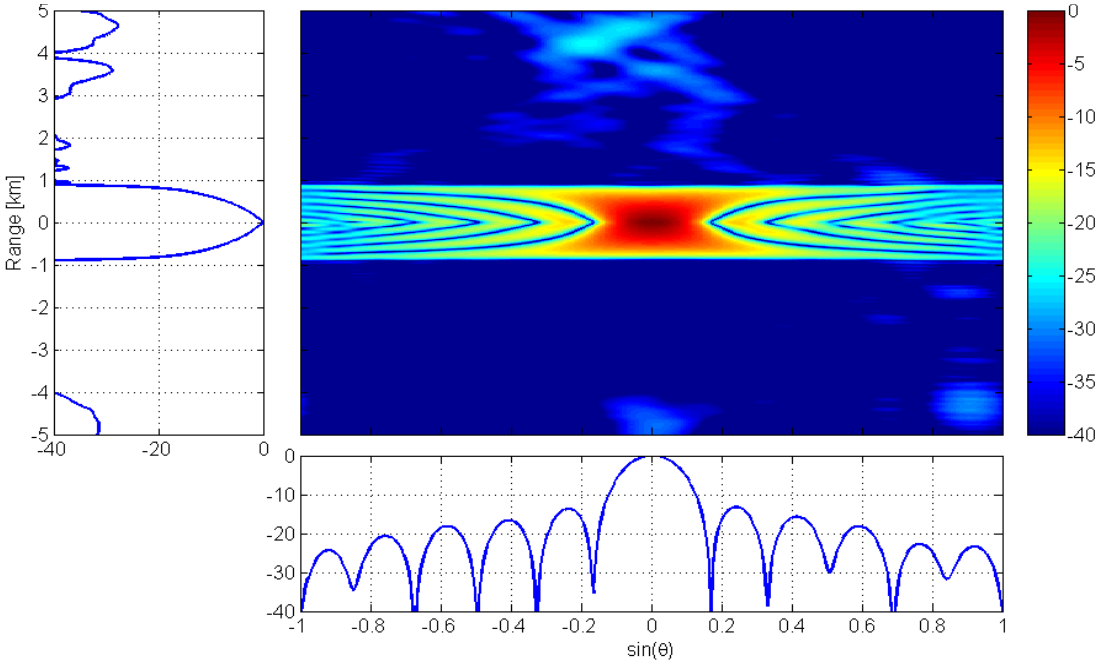

(c) Experimental data – Target simulator configuration.

Figure B.6: *Continued.*

B.2.4 Circulating chirp – Larger delay between transmitters

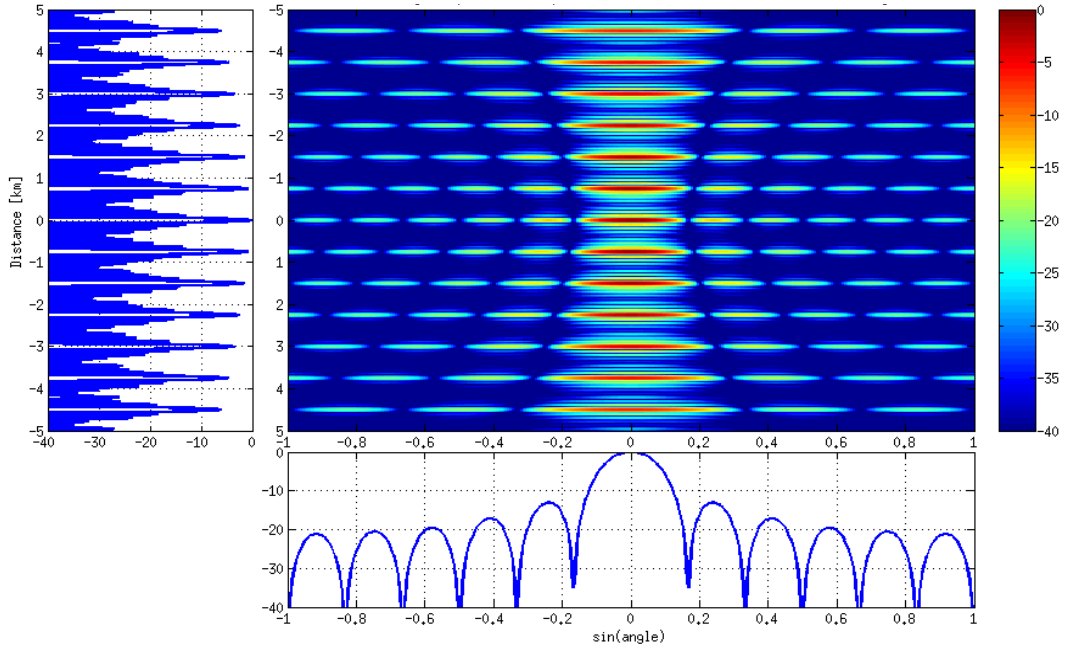

(a) Theoretical data.

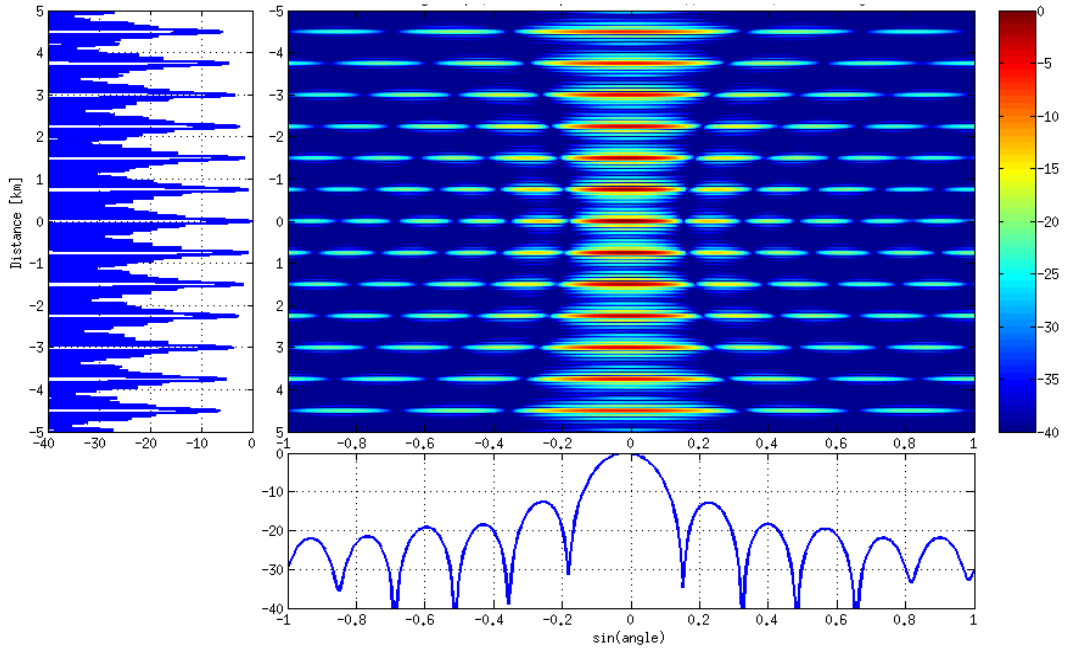

(b) Experimental data – Closed-loop configuration.

Figure B.7: Ambiguity functions (MF output) for a circulating chirp – Ten times larger delay between transmitters.

B.3 FDMA Waveforms

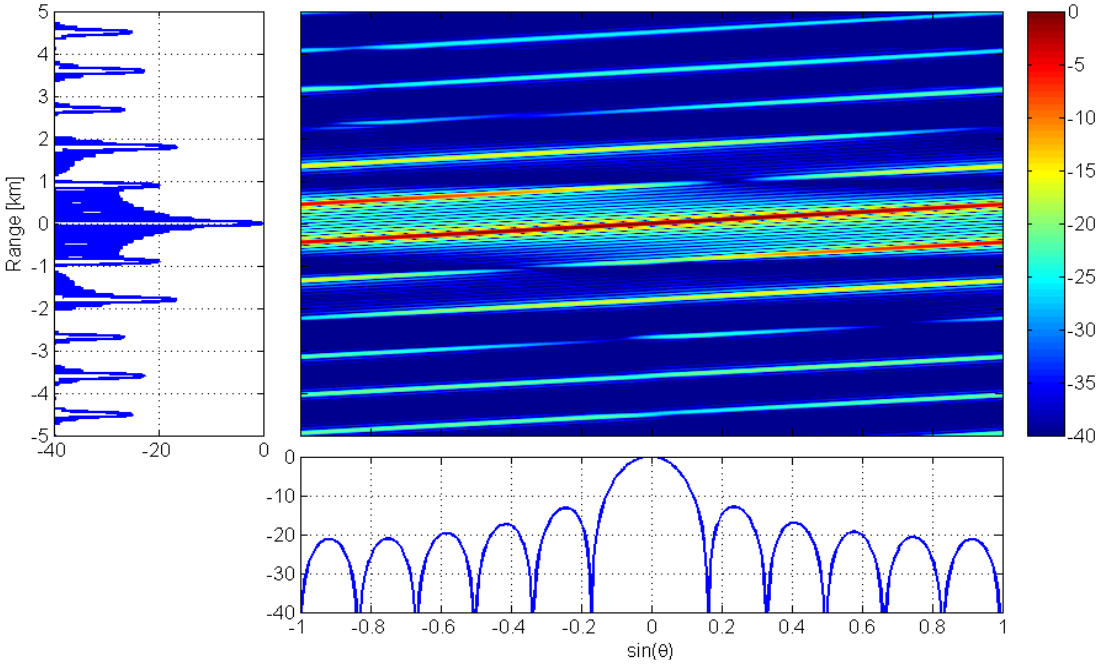

(a) Theoretical data.

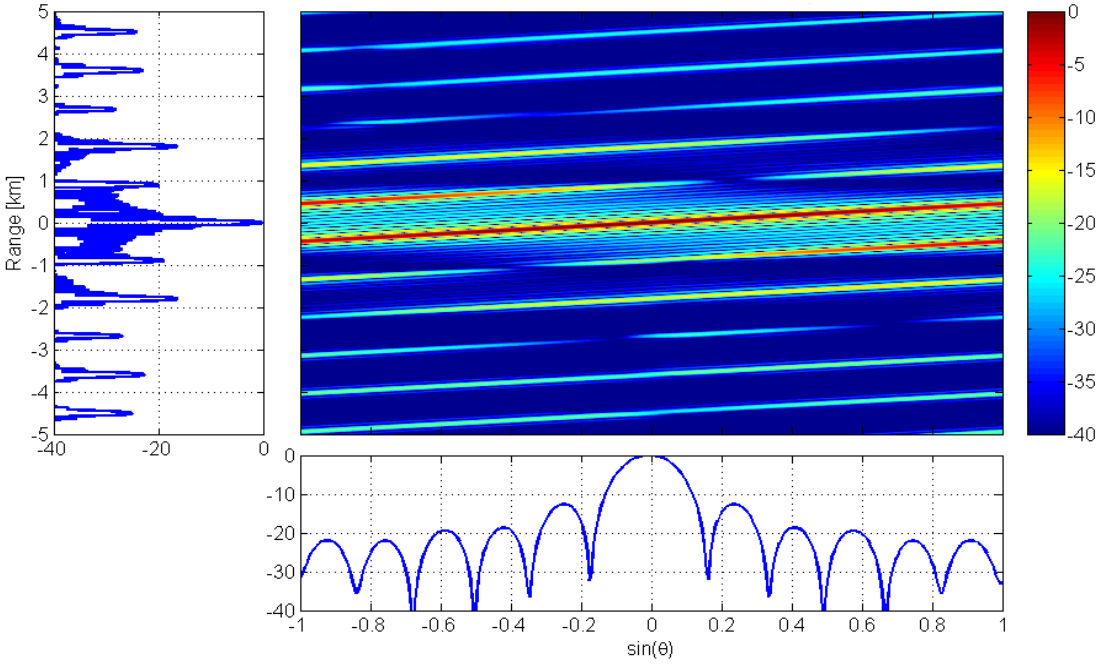

(b) Experimental data – Closed-loop configuration.

Figure B.8: Ambiguity functions (MF output) for a family of FDMA waveforms.

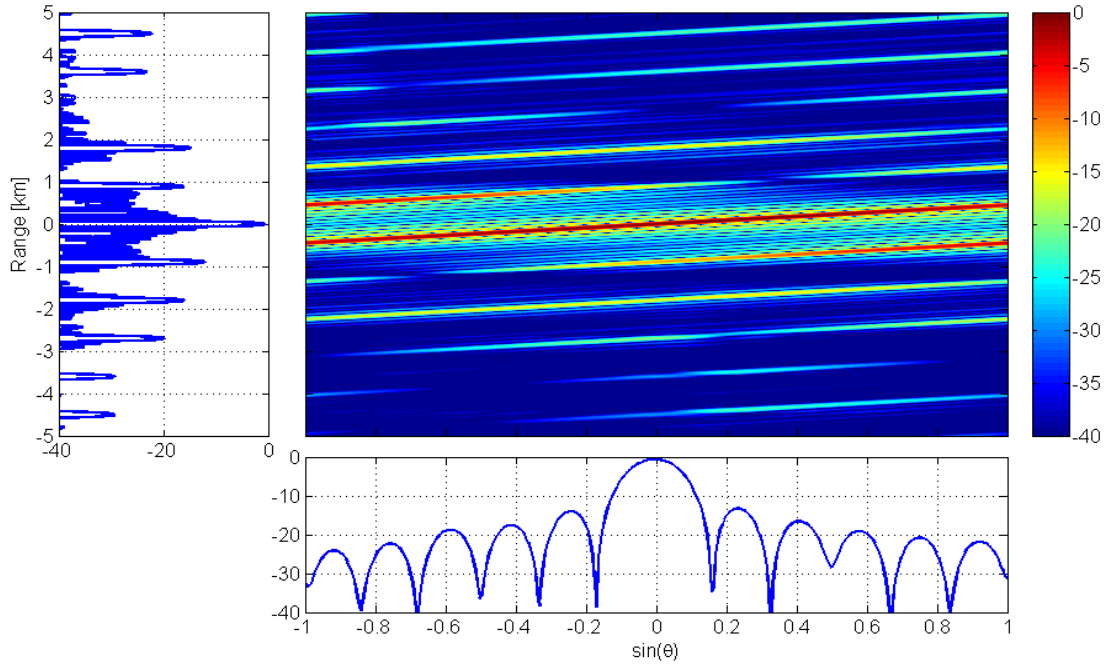

(c) Experimental data – Target simulator configuration.

Figure B.8: *Continued.*

Bibliography

[1] Merrill Ivan Skolnik. *Radar handbook*. McGraw-Hill, 1970.

[2] David K. Barton. *Radar system analysis and modeling*. Artech House, 2004.

[3] Fred E. Nathanson, J. Patrick Reilly, and Marvin N. Cohen. *Radar design principles*, volume 626. McGraw-Hill, New York, 1969.

[4] Harry L Van Trees. Classical detection and estimation theory. In *Detection, estimation, and modulation theory*, pages 19–165. John Wiley & Sons, 2004.

[5] Marc Lesturgie. Some relevant applications of MIMO to radar. In *Radar Symposium (IRS), 2011 Proceedings International*, pages 714–721. IEEE, 2011.

[6] J Dorey and G Garnier. RIAS, synthetic impulse and antenna radar. *ONDE ELECTRIQUE*, 69(6):36–44, 1989.

[7] A-S Luce, Helene Molina, Daniel Muller, and Vincent Thirard. Experimental results on RIAS digital beamforming radar. In *Radar 92. International Conference*, pages 74–77. IET, 1992.

[8] Chen Baixiao, Zhang Shouhong, Wang Yajun, and Wang Jun. Analysis and experimental results on sparse-array synthetic impulse and aperture radar. In *Radar, 2001 CIE International Conference on, Proceedings*, pages 76–80. IEEE, 2001.

[9] Eran Fishler, Alex Haimovich, Rick Blum, Dmitry Chizhik, Len Cimini, and Reinaldo Valenzuela. MIMO radar: an idea whose time has come. In *Radar Conference, 2004. Proceedings of the IEEE*, pages 71–78. IEEE, 2004.

[10] Eran Fishler, Alexander Haimovich, Rick S Blum, Leonard J Cimini, Dmitry Chizhik, and Reinaldo A Valenzuela. Spatial diversity in radars-models and detection performance. *Signal Processing, IEEE Transactions on*, 54(3):823–838, 2006.

[11] DW Bliss and KW Forsythe. Multiple-input multiple-output (MIMO) radar and imaging: degrees of freedom and resolution. In *Signals, Systems and Computers, 2004. Conference Record of the Thirty-Seventh Asilomar Conference on*, volume 1, pages 54–59. IEEE, 2003.

[12] Daniel J Rabideau and Peter Parker. Ubiquitous MIMO multifunction digital array radar. In *Signals, Systems and Computers, 2004. Conference Record of the Thirty-Seventh Asilomar Conference on*, volume 1, pages 1057–1064. IEEE, 2003.

[13] Keith W Forsythe and Daniel W Bliss. MIMO radar: Concepts, performance enhancements, and applications. In Jian Li and Petre Stoica, editors, *MIMO Radar Signal Processing*, pages 65–121. Wiley, 2009.

[14] Chun-Yang Chen and Palghat P Vaidyanathan. MIMO radar space–time adaptive processing using prolate spheroidal wave functions. *Signal Processing, IEEE Transactions on*, 56(2):623–635, 2008.

[15] Vito F Mecca, Dinesh Ramakrishnan, and Jeffrey L Krolik. MIMO radar space-time adaptive processing for multipath clutter mitigation. In *Sensor Array and Multichannel Processing, 2006. Fourth IEEE Workshop on*, pages 249–253. IEEE, 2006.

[16] Jian Li, Petre Stoica, Luzhou Xu, and William Roberts. On parameter identifiability of MIMO radar. *Signal Processing Letters, IEEE,* 14(12):968–971, 2007.

[17] Daniel R Fuhrmann and Geoffrey San Antonio. Transmit beamforming for MIMO radar systems using partial signal correlation. In *Signals, Systems and Computers, 2004. Conference Record of the Thirty-Eighth Asilomar Conference on*, volume 1, pages 295–299. IEEE, 2004.

[18] Petre Stoica, Jian Li, and Yao Xie. On probing signal design for MIMO radar. *Signal Processing, IEEE Transactions on*, 55(8):4151–4161, 2007.

[19] B Boudamouz, P Millot, Ch Pichot, et al. Through the wall radar imaging with mimo beamforming processing-simulation and experimental results. *American Journal of Remote Sensing*, 1(1):7–12, 2013.

[20] Jens Klare and Olaf Saalmann. MIRA-CLE X: A new imaging MIMO-radar for multi-purpose applications. In *Radar Conference (EuRAD), 2010 European*, pages 129–132. IEEE, 2010.

[21] Jian Li and Petre Stoica. MIMO radar – diversity means superiority. In Jian Li and Petre Stoica, editors, *MIMO Radar Signal Processing*, pages 1–64. Wiley, 2009.

[22] M Lesturgie. Improvement of high-frequency surface waves radar performances by use of multiple-input multiple-output configurations. *IET radar, sonar & navigation*, 3(1):49–61, 2009.

[23] Philip Mayne Woodward. Radar ambiguity analysis. Technical report, DTIC Document, 1967.

[24] Geoffrey San Antonio, Daniel R Fuhrmann, and Frank C Robey. MIMO radar ambiguity functions. *Selected Topics in Signal Processing, IEEE Journal of*, 1(1):167–177, 2007.

[25] Olivier Rabaste, Laurent Savy, Mathieu Cattenoz, and Jean-Paul Guyvarch. Signal waveforms and range/angle coupling in coherent colocated MIMO radar. In *Radar (Radar), 2013 International Conference on*, pages 157–162. IEEE, 2013.

[26] Ming Xue, Jian Li, and Peter Stoica. MIMO radar waveform design. In Fulvio Gini, Antonio De Maio, and Lee Patton, editors, *Waveform design and diversity for advanced radar systems*, pages 89–120. IET Press, 2012.

[27] Hongbo Sun, Frédéric Brigui, and Marc Lesturgie. Analysis and comparison of MIMO radar waveforms. In *2014 International Radar Conference*. IEEE, 2014.

[28] RH Barker. Group synchronizing of binary digital systems. *Communication theory*, pages 273–287, 1953.

[29] David Tse and Pramod Viswanath. *Fundamentals of wireless communication*. Cambridge university press, 2005.

[30] Robert Gold. Optimal binary sequences for spread spectrum multiplexing (corresp.). *Information Theory, IEEE Transactions on*, 13(4):619–621, 1967.

[31] Hai Deng. Polyphase code design for orthogonal netted radar systems. *Signal Processing, IEEE Transactions on*, 52(11):3126–3135, 2004.

[32] Hao He, Petre Stoica, and Jian Li. Designing unimodular sequence sets with good correlations—including an application to MIMO radar. *Signal Processing, IEEE Transactions on*, 57(11):4391–4405, 2009.

[33] Bo Liu, Zishu He, Jiankui Zeng, and Benyong Liu. Polyphase orthogonal code design for MIMO radar systems. In *Radar, 2006. CIE'06. International Conference on*, pages 1–4. IEEE, 2006.

[34] Hammad A Khan and David J Edwards. Doppler problems in orthogonal MIMO radars. In *Radar, 2006 IEEE Conference on*, pages 4–pp. IEEE, 2006.

[35] Yang Yang and Rick S Blum. MIMO radar waveform design based on mutual information and minimum mean-square error estimation. *Aerospace and Electronic Systems, IEEE Transactions on*, 43(1):330–343, 2007.

[36] KW Forsythe and DW Bliss. Waveform correlation and optimization issues for MIMO radar. In *Signals, Systems and Computers, 2005. Conference Record of the Thirty-Ninth Asilomar Conference on*, pages 1306–1310. IEEE, 2005.

[37] Geoffrey San Antonio and Daniel R Fuhrmann. Beampattern synthesis for wideband MIMO radar systems. In *Computational Advances in Multi-Sensor Adaptive Processing, 2005 1st IEEE International Workshop on*, pages 105–108. IEEE, 2005.

[38] Tarik Yardibi, Jian Li, Petre Stoica, Ming Xue, and Arthur B Baggeroer. Source localization and sensing: A nonparametric iterative adaptive approach based on weighted least squares. *Aerospace and Electronic Systems, IEEE Transactions on*, 46(1):425–443, 2010.

[39] Laura Anitori, Arian Maleki, Matern Otten, Richard G Baraniuk, and Peter Hoogeboom. Design and analysis of compressed sensing radar detectors. *Signal Processing, IEEE Transactions on*, 61(4):813–827, 2013.

[40] Olivier Rabaste and Laurent Savy. Mismatched filter optimization via quadratic convex programming for radar applications. In *Radar Conference (Radar), 2014 International*, pages 1–6, Oct 2014.

[41] G Babur, P Aubry, and F Le Chevalier. Space-time codes for active antenna systems: Comparative performance analysis. 2013.

[42] Didier Massonnet and Jean-Claude Souyris. From SAR design to image quality. In *Imaging with synthetic aperture radar*, pages 160–162. EPFL Press, 2008.

[43] Jack Capon. High-resolution frequency-wavenumber spectrum analysis. *Proceedings of the IEEE*, 57(8):1408–1418, 1969.

[44] Joseph R Guerci. *Space-time adaptive processing for radar*. Artech House, 2003.

[45] Jean Jacques Fuchs. The generalized likelihood ratio test and the sparse representations approach. In *Image and Signal Processing*, pages 245–253. Springer, 2010.

[46] Shaobing Chen and David Donoho. Basis pursuit. In *Signals, Systems and Computers, 1994. 1994 Conference Record of the Twenty-Eighth Asilomar Conference on*, volume 1, pages 41–44. IEEE, 1994.

[47] Stéphane G Mallat and Zhifeng Zhang. Matching pursuits with time-frequency dictionaries. *Signal Processing, IEEE Transactions on*, 41(12):3397–3415, 1993.

[48] Geoffrey Davis, Stephane Mallat, Zhifeng Zhang, et al. Adaptive time-frequency approximations with matching pursuits. *Wavelets: theory, algorithms, and applications (Taormina, 1993)*, 5:271–293, 1994.

[49] Olivier Rabaste, Laurent Savy, and Guy Desodt. Approximate multitarget matched filter for MIMO radar detection via Orthogonal Matching Pursuit. In *Radar Conference (Radar), 2014 International*. IEEE, Oct 2014.

[50] Thomas Svantesson and Anders Ranheim. Mutual coupling effects on the capacity of multielement antenna systems. In *Acoustics, Speech, and Signal Processing, 2001. Proceedings.(ICASSP'01). 2001 IEEE International Conference on*, volume 4, pages 2485–2488. IEEE, 2001.

[51] David K Barton. Modern radar system analysis. *Norwood, MA, Artech House, 1988, 607 p.*, 1, 1988.

[52] P Brouard, L Constancias, A Brun, S Attia, J Peyret, and P Dreuillet. Hycam: a new S-band surface radar testbed. In *International Radar Conference 2013*. IET, 2013.

[53] John P Stralka, Richard M Thompson, Johnathan Scanlan, and Aaron Jones. MISO radar beamforming demonstration. In *Radar Conference (RADAR), 2011 IEEE*, pages 889–894. IEEE, 2011.

[54] Peter Russer. *Electromagnetics, microwave circuit and antenna design for communications engineering*. Artech House, 2003.

[55] Inder J Gupta and Aharon A Ksienski. Effect of mutual coupling on the performance of adaptive arrays. *Antennas and Propagation, IEEE Transactions on*, 31(5):785–791, 1983.

Publications & Communications

Publication

- **Mathieu Cattenoz**, Sylvie Marcos and Laurent Savy. Extended Orthogonal Matching Pursuit for Robust Localization in MIMO radar. In *IEEE Transactions on Aerospace and Electronic Systems. **Second review in process**.*

International Conferences With Proceedings

- Laurent Constancias, **Mathieu Cattenoz**, Philippe Brouard, and Arnaud Brun. Coherent Collocated MIMO radar demonstration for air defence applications. In *IEEE Radar Conference*, 2013, Ottawa (Canada).

- **Mathieu Cattenoz**, Philippe Brouard, Arnaud Brun, Laurent Constancias, and Laurent Savy. Coherent Collocated MIMO Radar: a Study on Real Data. In *International Radar Symposium*, 2013, Dresden (Germany).

- Olivier Rabaste, Laurent Savy, **Mathieu Cattenoz**, and Jean-Paul Guyvarch. Signal Waveforms and Range/Angle Coupling in Coherent Colocated MIMO Radar. In *International Conference on Radar*, 2013, Adelaide (Australia).

- **Mathieu Cattenoz** and Sylvie Marcos. Adaptive Processing for MIMO Radar Realistic Non Perfectly Orthogonal Waveforms. In *IEEE Radar Conference*, 2014, Cincinnati (USA).

- **Mathieu Cattenoz**, Laurent Savy, and Sylvie Marcos. Adaptive Processing Methods for MIMO Radar Experimental Signals. In *International Radar Conference*, 2014, Lille (France).

- **Mathieu Cattenoz** and Philippe Brouard. An Experimental Demonstration of a

Posteriori Digital Calibration of MIMO Radar System. In *International Radar Conference*, 2014, Lille (France).

Conferences Without Proceedings

- **Mathieu Cattenoz**. Emission colorée pour radar MIMO multifonction. Thales PhDay, 2012, Rungis (France)
- **Mathieu Cattenoz**, Philippe Brouard, Arnaud Brun, Laurent Constancias, and Laurent Savy. The HYCAM Collocated MIMO Radar: Practical Experiments and Performance Analysis. SONDRA Workshop, 2013, La Londe-les-Maures (France)

Intellectual Property

- **Mathieu Cattenoz** and Philippe Brouard. *Enveloppe Soleau*: “Procédé numérique d’étalonnage des phases des voies d’émission d’une antenne réseau radar à capacité MIMO". 2014.
- **Mathieu Cattenoz** and Philippe Brouard. Patent submission: “Procédé numérique d’étalonnage des phases des voies d’émission d’une antenne réseau radar à capacité MIMO". 2015. ***Pending submission***.

Résumé long : Traitements Radar MIMO pour Prévenir et Pallier les Défauts du Monde Réel

We propose here to provide a short version of the thesis in French. The objective is more to give the main results and contributions of the thesis than to go deeply into the analytic derivations.

Contexte et Problématique de la Thèse

La notion de MIMO (multiple-input multiple-output) fait référence à l'utilisation de plusieurs sites d'émission et de réception. Le concept est appliqué initialement dans le domaine des télécommunications. La transposition au domaine du radar est plus récente, les premiers travaux datant de la fin des années 80 [6].

Contrairement aux radars actuels, le radar MIMO permet l'émission de différentes formes d'onde sur chaque élément d'antenne, de façon simultanée, ce que l'on nomme codage spatio-temporel en émission. Un filtre adapté est appliqué en réception pour chaque forme d'onde et la formation de faisceau est ainsi effectuée par le calcul à la réception. On distingue le radar MIMO statistique où les émetteurs sont distants afin de bénéficier de la diversité spatiale, du radar MIMO cohérent où les émetteurs sont disposés sur le même site afin de pouvoir bénéficier de la propriété de convolution des géométries de l'antenne d'émission avec l'antenne de réception, permettant ainsi de mettre en place des antennes lacunaires tout en conservant une directivité forte. La thèse est basée sur ce dernier type de radar MIMO.

Le concept du radar MIMO est prometteur vis-à-vis des nombreux avantages qu'il

apporte par rapport aux architectures radars actuelles [14] [15] [17] [18] : flexibilité pour la formation de faisceau à l'émission – large illumination de la scène tout en récupérant une résolution fine après traitement – et réduction de la complexité des systèmes, via la réduction du nombre d'antennes et la possibilité de transférer des fonctions de contrôle et d'étalonnage du système dans le domaine numérique.

Nous décrivons ensuite le concept de fonction d'ambiguïté en sortie de filtre adapté qui représente l'énergie équivalente rayonnée dans le domaine distance/Doppler/angle et permet ainsi de représenter les capacités de détection du système. L'écriture des expressions analytiques permet de mettre en évidence les trois étapes du traitement MIMO : application du filtre adapté (y compris le traitement Doppler) correspondant à chaque forme d'onde, formation de faisceau d'émission pour récupérer la directivité d'émission, formation de faisceau de réception. Nous introduisons trois paramètres utilisés dans ce travail : M le nombre d'émetteurs, N_c le nombre de moments élémentaires composant les codes de phase, et K le nombre d'échantillons du signal reçu.

Pour l'implémentation de systèmes MIMO, le choix de la forme d'onde est crucial, dans la mesure où chacune présente des avantages et limites propres en termes d'orthogonalité – c'est à dire la capacité à pouvoir extraire les formes d'onde du signal reçu – et de performance en détection. Un nombre limité de travaux présente et compare les caractéristiques des formes d'onde les plus représentatives [26] :

- **TDMA (Time Division Multiple Access) :** il peut s'agir d'activer les émetteurs les uns après les autres, ou d'émettre simultanément une unique forme d'onde (par exemple un chirp, c'est-à-dire un signal à rampe de fréquence) avec un décalage temporel sur chaque émetteur.
- **FDMA (Frequency Division Multiple Access) :** il s'agit d'émettre sur des supports fréquentiels disjoints
- **CDMA (Code Division Multiple Access) :** il s'agit d'émettre des codes de phase ayant des propriétés de quasi-orthogonalité entre eux. De nombreuses séquences de code existent, et nous allons considérer plus spécialement les codes de Gold [30] qui montrent de bonnes propriétés en termes d'autocorrélation et intercorrélation.
- **DDMA (Doppler Division Multiple Access) :** il s'agit de décaler différemment les fréquences de chaque émetteur d'un pulse à l'autre.

Nous avons évoqué les avantages prometteurs du radar MIMO, cependant, les travaux existants prennent insuffisamment en compte les impacts du manque d'orthogonalité des formes d'onde. Par ailleurs, les effets des défauts matériels sont souvent négligés, alors qu'ils peuvent être potentiellement conséquents. Le radar MIMO reste donc encore aujourd'hui au stade du concept théorique. D'où notre problématique : **comment dépasser les imperfections intrinsèques des formes d'onde MIMO tout en garantissant des contraintes d'implémentation opérationnelle acceptables ?**

Dans ce contexte, nous citons néanmoins quelques tentatives visant à optimiser la conception des formes d'onde afin de respecter certains critères [31] [33] [36], au prix cependant d'une baisse des performances sur d'autres plans ; ainsi que certains travaux visant à définir des traitements optimisés, tels les traitements adaptatifs [21] [11], le Compressed Sensing [39] ou encore le calcul de filtres désadaptés optimisés [40]. Ces travaux ne permettent cependant que d'apporter une réponse partielle à la problématique.

Le travail de thèse consiste donc à mettre en place des traitements adaptés aux signaux MIMO permettant d'anticiper et de compenser les défauts du monde réel. Cela se fera en quatre temps :

- Déterminer la famille de formes d'onde présentant le meilleur potentiel pour l'émission MIMO
- Développer des traitements prenant en compte le modèle de signal pour compenser les défauts de la forme d'onde
- Analyser la sensibilité des traitements vis-à-vis des écarts au modèle et proposer des stratégies de prévention
- Évaluer les traitements sur des signaux MIMO acquis en conditions réelles

Les Codes de Phase Comme Formes d'Onde : Motivations et Défis

Nous souhaitons étudier ici les différents types de formes d'onde afin de montrer que les codes de phase, de façon générale, ont le meilleur potentiel pour être utilisés dans les architectures MIMO, en nous basant sur des critères de performance en détection. Nous allons également étudier leurs limites en termes de lobes secondaires induits.

Nous nous référons en premier lieu aux analyses comparatives fournies par la littérature [27], notamment :

- **TDMA :** bonne orthogonalité mais utilisation sous-optimale des ressources (par exemple puissance d'émission ou résolution distance fortement réduites)
- **FDMA :** bonne orthogonalité mais nombreux lobes secondaires dans le plan distance-Doppler
- **CDMA :** faible niveau de lobes secondaires dans le plan Doppler mais haut niveau de lobes secondaires dans le plan distance-angle
- **DDMA :** bonne orthogonalité mais ambiguïtés Doppler

Nous relevons également des travaux sur la borne de Cramér-Rao des différentes formes d'onde [25]. Cette borne correspond à la borne inférieure pouvant être atteinte par un estimateur, donnant ainsi des informations sur la résolution spatiale intrinsèque. Il est montré que les codes de phase présentent le plus petit contour pour cette borne dans l'espace distance-angle, témoignant ainsi d'une meilleure résolution spatiale.

Pour compléter l'analyse, nous définissons quatre métriques de performance pouvant être calculées à partir de la fonction d'ambiguïté, afin de pouvoir comparer les formes d'onde sur des indicateurs quantitatifs :

- **Résolution en distance :** capacité à localiser une cible sur l'axe de la distance
- **Résolution en angle :** capacité à localiser une cible sur l'axe de l'angle
- **Sensibilité au fouillis :** capacité à éliminer la contribution d'un fouillis homogène sur le plan distance-angle
- **Sensibilité à une cible ponctuelle :** capacité à éliminer les interférences ponctuelles de forte puissance

Ces deux dernières métriques s'inspirent de l'Integrated Side Lobe Ratio (ISLR) et du Peak Side Lobe Ratio (PSLR) utilisées en SAR (Synthetic Aperture Radar) [42].

Nous générons des formes d'onde synthétiques avec notamment les paramètres suivants : 12 émetteurs, bande de fréquence de 2 MHz, pulse de 64 μs, cible ponctuelle

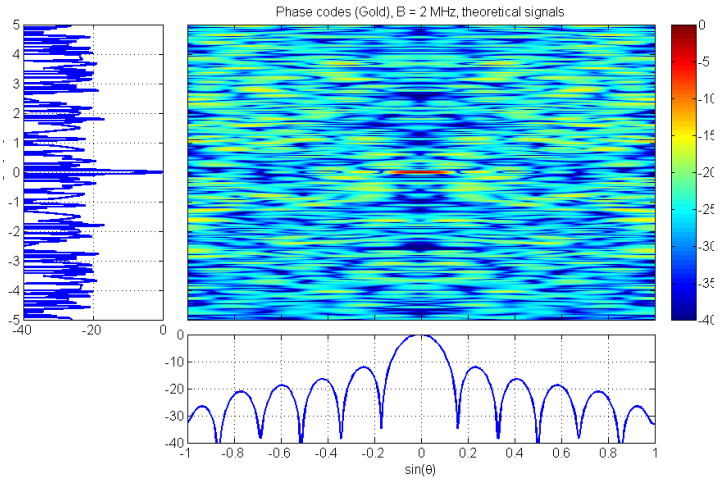

(a) Codes de phase (séquences Gold).

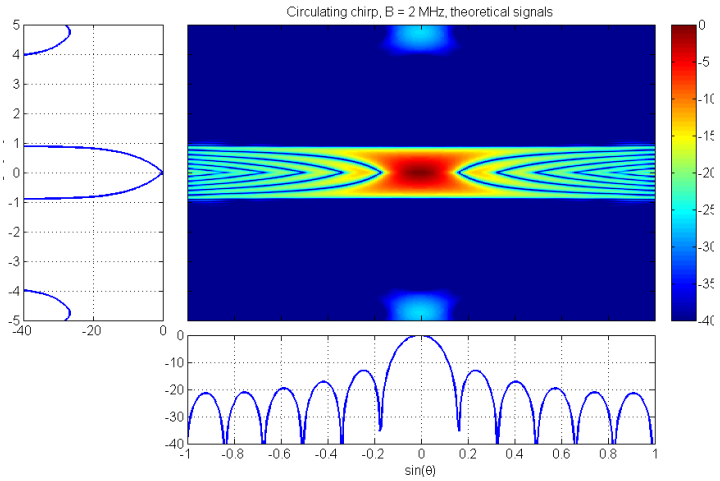

(b) Chirp circulant.

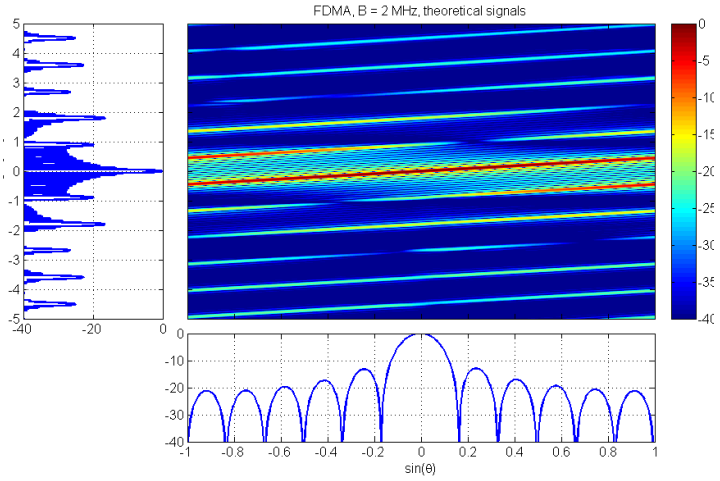

(c) FDMA.

FIGURE C.1 – Fonctions d'ambiguïté (sorties de filtre adapté) pour différentes formes d'onde.

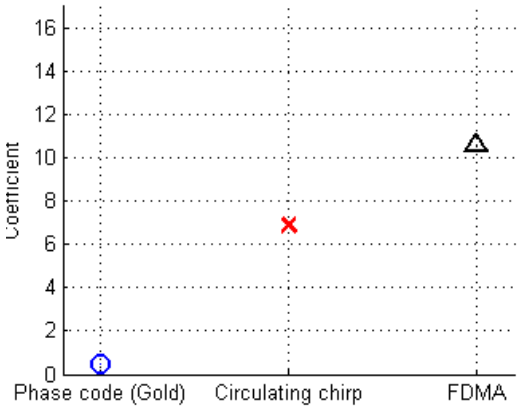

(a) Résolution en distance.

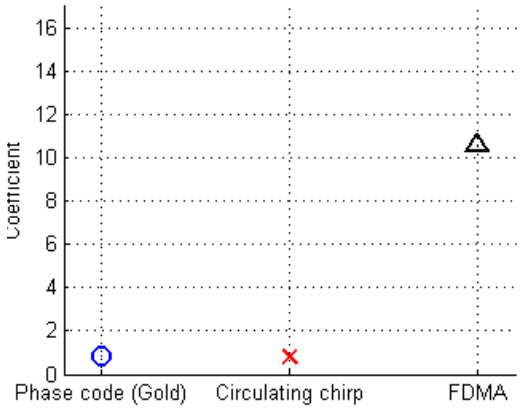

(b) Résolution en angle.

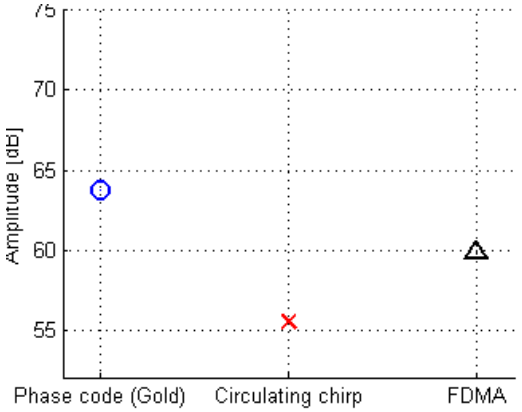

(c) Sensibilité au fouillis.

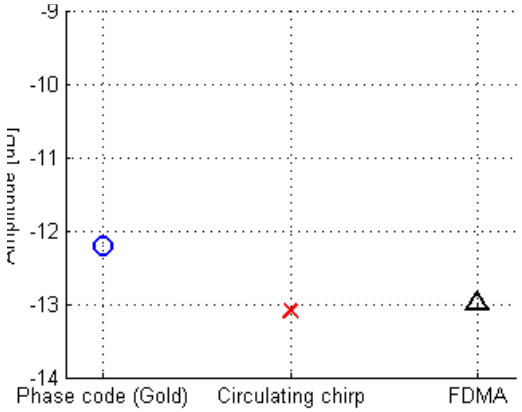

(d) Sensibilité à une cible ponctuelle.

FIGURE C.2 – Métriques de performance pour la quantification des performance en détection des formes d'onde CDMA, TDMA et FDMA. Les faibles valeurs correspondent aux meilleures performances.

placée à l'origine. Nous traitons ensuite les données jusqu'au filtre adapté (fig. C.1), ce qui nous permet ensuite de calculer les différentes métriques de performance (fig. C.2). Celles-ci confirment à nouveau le caractère optimal des codes de phase en termes de résolution spatiale, mais met également en avant leur sensibilité forte aux interférences du fait des nombreux lobes secondaires résiduels induits.

Afin d'analyser l'origine des lobes résiduels, nous avons défini un formalisme mathématique pour l'expression des signaux traités. Dans le modèle de signal, nous prenons en compte les propriétés intrinsèques des formes d'onde, et donc les défauts des codes de phase. Nous mettons ainsi en évidence que le "plancher" de lobes résiduels est dû à la somme des autocorrélations et intercorrélations des codes de phase. Nous

montrons ensuite que ce défaut peut avoir plusieurs conséquences néfastes sur les performances en détection, notamment :

- **Désensibilisation vis-à-vis des cibles secondaires :** les lobes secondaires peuvent être au dessus du niveau de bruit et ainsi “cacher" des cibles secondaires qui auraient pu normalement être détectées
- **Perte de puissance :** le lobe principal perd quelques dB en puissance du fait de l’“éparpillement" de l’énergie, ce qui réduit la probabilité de détection
- **Sensibilité au fouillis :** la présence des lobes résiduels induit une sensibilité accrue aux interférences provenant de distances et angles divers.

En considérant que nous puissions supprimer les lobes résiduels qui dégradent fortement les performances en détection, nous pouvons estimer que les codes de phase peuvent être particulièrement adaptés aux émissions MIMO.

Développement de Traitements Supprimant les Lobes Secondaires Résiduels

Nous faisons le constat que le filtre adapté, conçu pour optimiser le rapport signal à bruit, ne permet pas la réduction des lobes résiduels. Nous proposons ici de développer des traitements basés sur un modèle de signal intégrant les propriétés des formes d’onde et notamment leur manque d’orthogonalité. Nous étudions ici différents traitements existants et analysons s’ils peuvent satisfaire les conditions d’emploi en situation réelle.

Nous étudions d’abord les traitements adaptatifs de type Capon, connus pour offrir un bonne résolution spatiale tout en éliminant les lobes secondaires [21]. Nous proposons ici d’adapter le traitement à l’estimation d’un jeu de deux paramètres : la distance et l’angle. Nos simulations montrent qu’il est possible de supprimer l’ensemble des lobes résiduels, cependant cela nécessite au préalable de calculer une matrice de covariance de taille $MN_c \times MN_c$, et dans la plupart des situations opérationnelles, il n’est pas possible de disposer d’assez de récurrences pour estimer correctement cette matrice. Nous avons ensuite l’idée d’appliquer le traitement Capon sur un seul paramètre et d’utiliser l’autre dimension pour fournir des données permettant d’estimer la

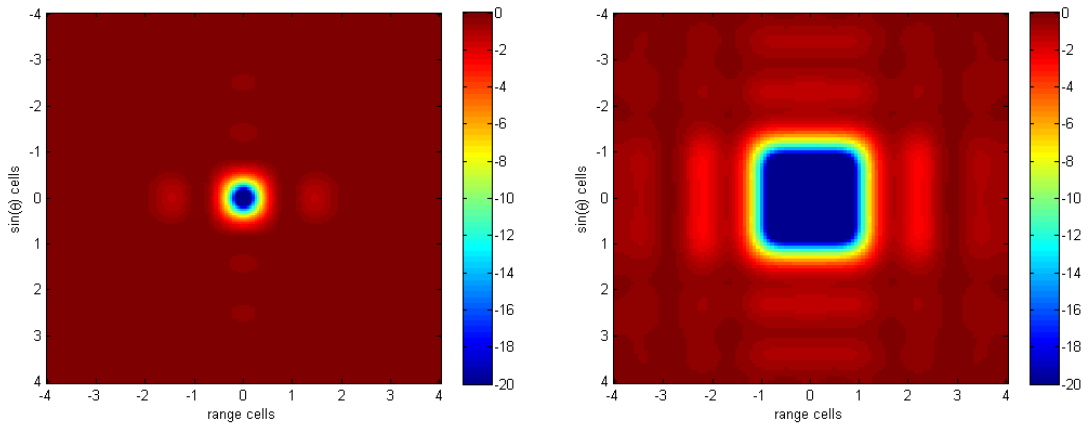

(a) Suppression classique.

(b) Suppression étendue.

FIGURE C.3 – Gain en puissance dans l'espace des paramètres de cible après une itération de l'OMP.

matrice de covariance. Cependant, nos simulations montrent que nous ne disposons pas de suffisamment de degrés de liberté pour obtenir des résultats meilleurs que ceux du filtre adapté. Nous introduisons ensuite le Compressed Sensing qui exploite le caractère "creux" (*sparse*) des signaux reçus. Certains travaux [39] présentent des résultats performants, cependant nous établissons que dans notre contexte, la complexité calculatoire induite n'est pas compatible avec une implémentation opérationnelle.

Nous introduisons ensuite l'Iterative Adaptive Approach (IAA), basé sur les moindres carrés pondérés [38], dont l'intérêt repose sur un précision similaire au Capon tout en ne nécessitant qu'un nombre très limité de données d'apprentissage (moins de 10 typiquement). Cependant, il s'agit d'un processus itératif imposant d'inverser une matrice de taille $MK \times MK$ à chaque étape, ce qui est incompatible avec les capacités calculatoires en conditions réelles. Nous gardons néanmoins cette technique comme une "référence" pour effectuer des comparaisons avec d'autres traitements.

Nous étudions maintenant l'Orthogonal Matching Pursuit (OMP) qui est un algorithme itératif basé sur la décomposition d'un signal en les contributions de plusieurs formes d'onde spécifiques [48]. Chaque itération consiste à déterminer la valeur maximale de la sortie du filtre adapté – correspondant à la cible prépondérante –, et à retirer la contribution de cette cible du signal reçu. La complexité calculatoire est largement réduite, étant donné que la matrice à inverser pour la $k^{\text{ème}}$ cible n'est plus que de taille $k \times k$.

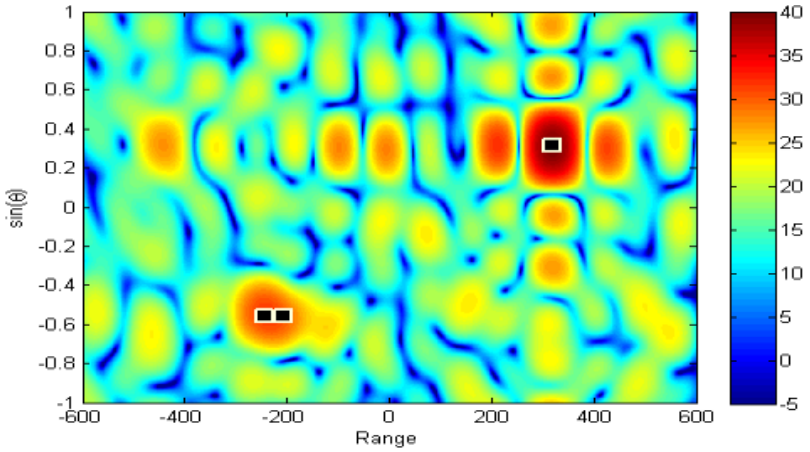

(a) Sortie du filtre adapté. Les cibles sont localisées par les marques noires.

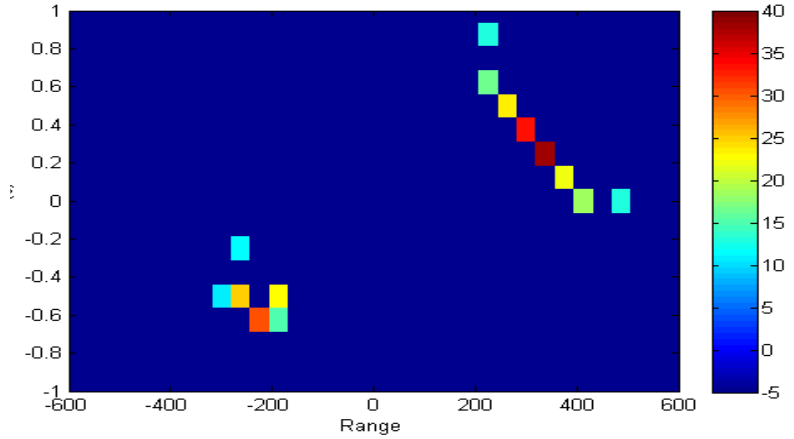

(b) Sortie de l'OMP – suppression classique.

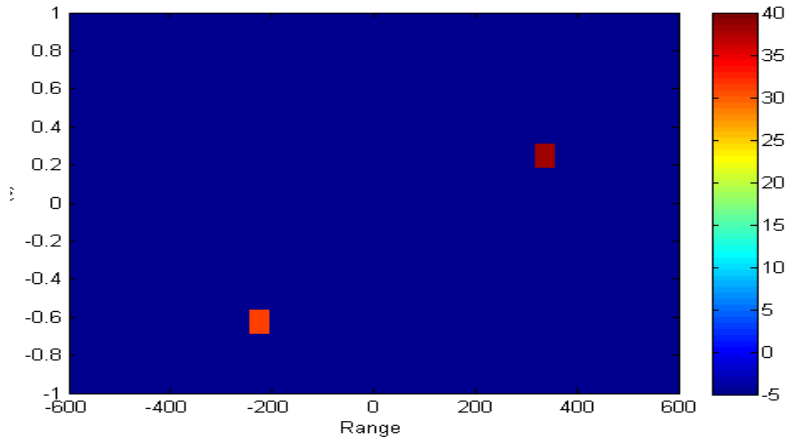

(c) Sortie de l'OMP – suppression étendue.

FIGURE C.4 – Détection de cibles avec le scénario "pernicieux" proposé, issus de codes de phase simulés. Largeur de la cellule de résolution en distance = 75 m. Largeur de la cellule de résolution en angle = 0,25.

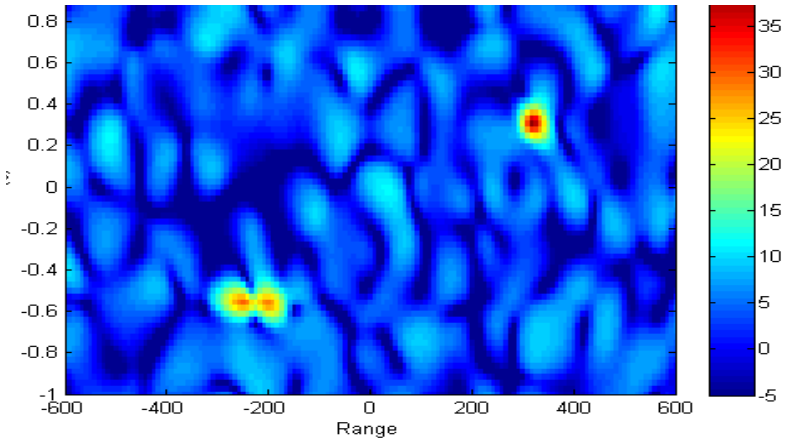

(d) Sortie de l'IAA (itération 11).

FIGURE C.4 – *Suite.*

Cependant, nous avons identifié la sensibilité particulière de l'OMP aux erreurs de localisation des cibles. Ces erreurs peuvent être induites par la "granularité" de la grille de recherche (la position d'une cible est associée au nœud le plus proche) ou par l'influence de deux cibles proches. Nous proposons d'augmenter la robustesse par rapport à ce problème en étendant la zone de rejet à chaque itération. Plus précisément, en plus de la contribution à la position détectée, nous proposons de retirer également les contributions des 8 positions à proximité (à des distances d'une demi-case de résolution). Nous montrons que cela permet de créer un "masque" qui retire toutes les contributions éventuelles sur une zone à peine plus large qu'une case de résolution (fig. C.3). Nous notons néanmoins que le signal distant d'une case de résolution (c'est-à-dire en bordure de masque) subit une perte de puissance de l'ordre de 15 dB.

Afin d'illustrer le gain de robustesse vis-à-vis des erreurs de localisation, nous mettons en place un scénario "pernicieux" constitué de trois cibles non situées sur des nœuds de la grille, la prépondérante étant isolée, et les deux plus faibles étant placées à une demi-case de résolution de distance l'une de l'autre. Ce scénario permet ainsi de générer une des pires situations en termes de création d'erreurs de localisation de cibles. Les résultats (fig. C.4) montrent que l'OMP avec suppression classique est sujet à de nombreuses fausses alarmes alors que l'OMP avec suppression étendue ne présente aucune fausse alarme (les deux cibles proches sont détectées dans la même case distance, ce qui était attendu). Le calcul de la sortie de l'IAA permet, en parallèle, de confirmer que cette technique donne une précision de détection correcte tout en réduisant les lobes résiduels au niveau du bruit.

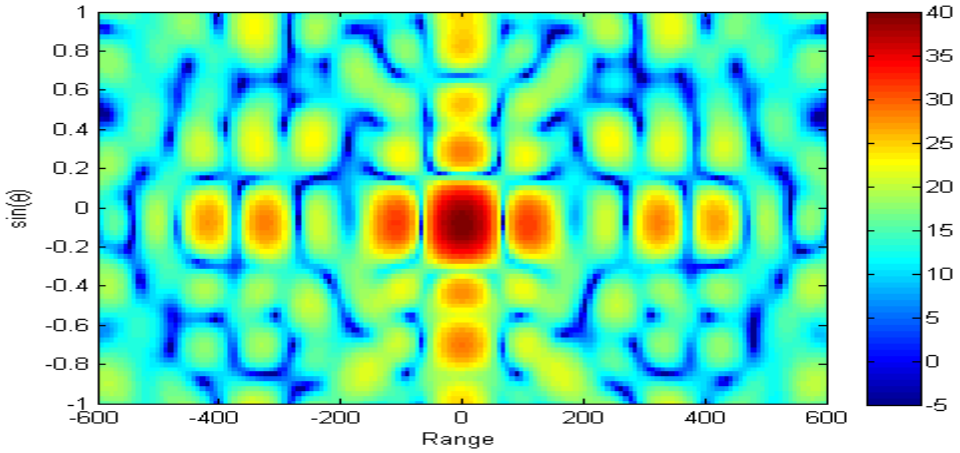

(a) Sortie du filtre adapté.

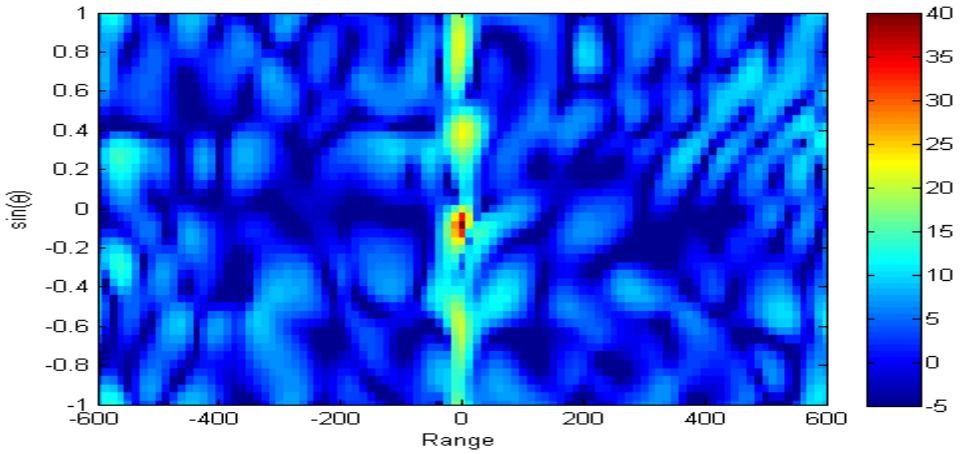

(b) Sortie de l'IAA (itération 10).

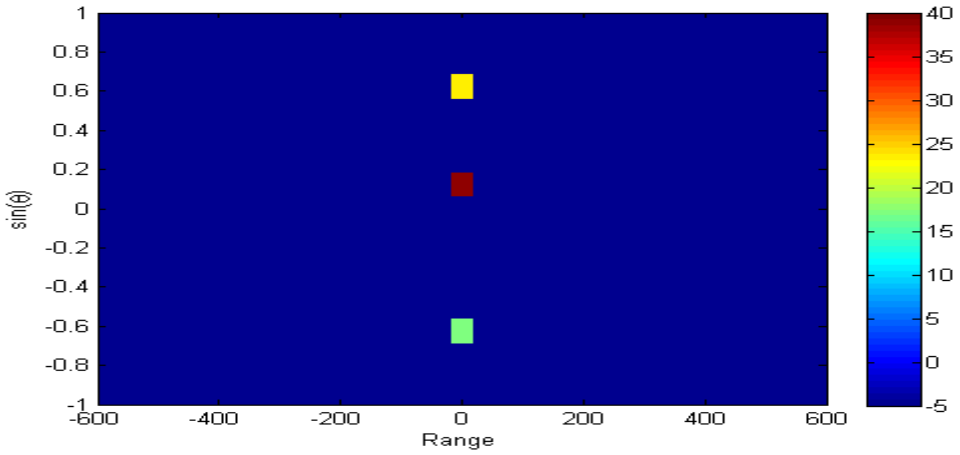

(c) Sortie de l'OMP – suppression étendue.

FIGURE C.5 – Application des différents traitements sur les données issues de codes de phase simulés, avec simulation d'erreurs sur les émetteurs. Largeur de la cellule de résolution en distance = 75 m. Largeur de la cellule de résolution en angle = 0,25.

Écarts au Modèle : Analyse d'Impact et Stratégies de Prévention

Les traitements basés sur un modèle de signal sont connus pour être particulièrement sensibles aux écarts au modèle. C'est pourquoi il est crucial d'étudier les possibles distorsions auxquelles peuvent être soumis les signaux lors de leur génération et propagation, ainsi que les façons d'empêcher les dégradations de performance, que ce soit en éliminant les distorsions ou en les intégrant au modèle de signal.

Dans un premier temps, nous présentons quelques unes des origines des écarts qui ne sont habituellement pas pris en compte dans le modèle de signal :

- **Non linéarités dans la chaîne radar :** certains composants par exemple fonctionnent en dehors des zones linéaires, leur comportement peut également varier en fonction des conditions environnementales
- **Manque d'alignement entre les voies :** il peut arriver que les voies d'émission ne soient pas alignées, du fait de différences de chemin électrique ou d'une mauvaise synchronisation temporelle des générateurs de formes d'onde
- **Couplage mutuel d'antenne :** l'influence électromagnétique entre éléments d'une antenne provoque l'induction de courants dans les éléments voisins
- **Cibles rapides :** nous avions fait l'hypothèse de cibles lentes, ainsi, une cible rapide (à partir de 100 m/s dans notre contexte) serait sujette à une évolution de sa phase durant le pulse dûe au Doppler.

Pour estimer la sensibilité des traitements proposés vis-à-vis des écarts au modèle, nous définissons une simulation avec des émetteurs chacun sujet à des erreurs aléatoires sur la phase et le module (avec des écarts types respectivement de $2\pi/10$ et de 10% du module). Les résultats obtenus (fig. C.5) montrent l'apparition de lobes à distance de la cible de façon équivalente pour l'IAA et l'OMP, certains jusqu'à des puissances de 18 dB en dessous de celle de la cible.

Dans un deuxième temps, avant d'illustrer des stratégies de protection contre les écarts au modèle, nous présentons la plateforme Hycam installée à l'ONERA. Il s'agit d'une plateforme expérimentale multifonction de radar de surface en bande S pouvant générer jusqu'à 12 formes d'onde différentes simultanément, et recevoir sur

FIGURE C.6 – La plateforme Hycam installée à l'ONERA (site de Palaiseau). Le doctorant est donné à titre indicatif.

16 antennes (fig. C.6). Notons à titre d'illustration que lors de la conception de ce système [52], des contraintes ont été imposées sur les éléments rayonnants et les amplificateurs pour prévenir certaines distorsions.

Par ailleurs, nous relevons le fait que le radar MIMO apporte une flexibilité permettant de transférer des fonctions de contrôle et d'étalonnage du système dans le domaine numérique, ouvrant ainsi la voie au radar "tout numérique" et permettant d'alléger les contraintes et ressources nécessaires à la conception.

Nous profitons de cette propriété du radar MIMO pour définir une méthode numérique d'étalonnage des phases des émetteurs "après coup". Il s'agit d'un processus automatique qui, basé sur des signaux d'opportunité, estime le décalage de phase à l'origine de chaque émetteur à partir de chaque forme d'onde extraite du signal reçu, puis qui applique la correction correspondante afin d'aligner chacun des signaux émis. Afin d'illustrer le fonctionnement de cette méthode, nous mettons en place une expérimentation en conditions réelles avec la plateforme Hycam. Nous générons une famille de codes de Gold de 1023 moments transmise sur une bande de fréquence de 20 MHz par trois sous-réseaux d'émission intentionnellement non alignés en phase. Nous faisons une acquisition isotropique du fouillis environnant qui contient nos

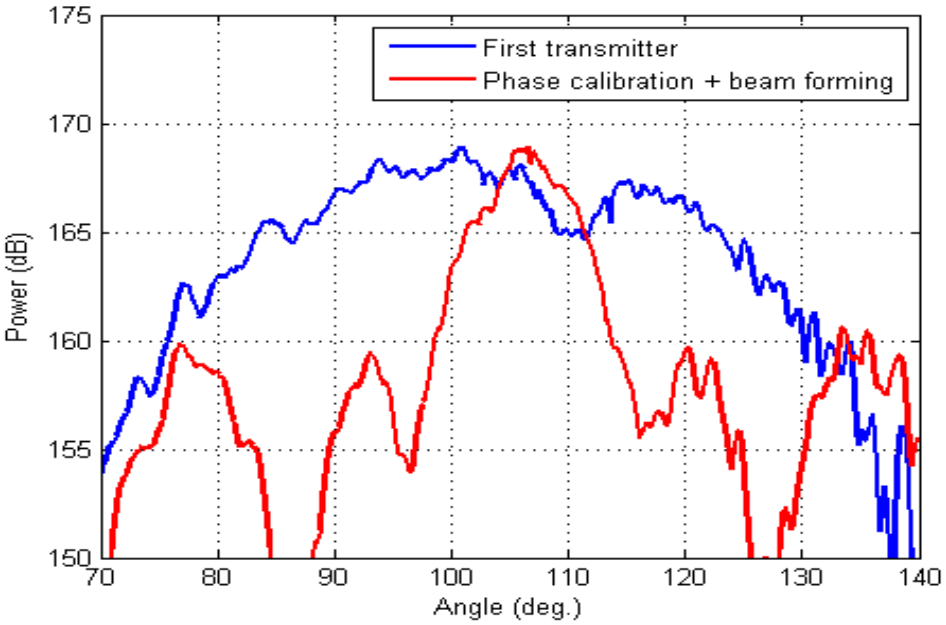

FIGURE C.7 – Effet de la calibration sur des signaux expérimentaux : coupe à distance fixée de la contribution d'un point brillant. En bleu : un seul émetteur. En rouge : après étalonnage des 3 émetteurs et formation de faisceau.

signaux d'opportunité. Nous appliquons ensuite l'ensemble de la chaîne de traitement sur les données obtenues, ainsi que la méthode d'étalonnage numérique. Là où l'absence d'étalonnage aurait donné une figure d'interférence chaotique, nous obtenons ici une focalisation correcte de l'énergie (fig. C.7), ce qui permet ainsi d'apporter une preuve de concept de la possibilité de numériser des fonctions d'ajustement du système d'une architecture MIMO.

Evaluation des Traitements sur les Signaux Expérimentaux

La plateforme MIMO Hycam constitue une opportunité toute particulière pour acquérir des signaux en conditions réelles, d'autant plus que ce genre d'acquisitions est particulièrement rare dans la littérature. Cela nous permet ici de tester en pratique la robustesse des techniques développées aux imperfections du monde réel.

Dans cette optique, nous définissons deux niveaux de configurations expérimentales :

- **Configuration boucle fermée :** le circuit de transmission du radar est rebouclé juste avant les antennes sur le circuit de réception, ce qui permet de ne se confronter qu'aux composants internes.
- **Configuration avec simulateur de cible :** le signal est émis en direction d'un simulateur de cible composé d'un calibrateur actif, de composants électro-optiques et d'antennes directives, permettant ainsi de modifier le signal reçu de façon à simuler une cible à une certaine distance et avec un certain Doppler. Cette configuration plus générale permet de se confronter également à l'émission et la propagation des signaux.

Concernant les paramètres expérimentaux, nous choisissons une bande de fréquence de 2 MHz, une longueur de pulse de 50 µs, 12 formes d'onde générées pour chaque famille considérée, à savoir codes de phase Gold, chirp circulant et FDMA. Par ailleurs, l'émission des formes d'onde s'effectue séquentiellement dans la mesure où Hycam, à cette date, peut gérer jusqu'à 3 voies montantes simultanément. Au cours des acquisitions, plusieurs phénomènes prépondérants non anticipés ont été relevés :

- **Isolation imparfaite du mélangeur :** nous avons relevé que le mélangeur (qui fournit les signaux permettant de monter en fréquence à l'émission et de descendre en fréquence à la réception) n'était pas parfaitement isolé électriquement, ce qui entraîne l'existence d'une deuxième boucle fermée, celle-ci étant plus courte que celle créée intentionnellement. Cela peut cependant être une opportunité d'étude de deux échos proches l'un de l'autre.
- **Troncature du signal d'intérêt :** nous avons remarqué après coup que la fenêtre d'acquisition était décalée par rapport à l'écho reçu, du fait d'une fibre optique défectueuse. Cela s'est traduit par la perte d'environ 10 % du signal d'intérêt.
- **Manque d'alignement des phases :** étant donné l'émission séquentielle des formes d'onde, l'absence de synchronisation induit une phase initiale aléatoire pour chaque émetteur. Cela a cependant été corrigé grâce à la méthode de calibration numérique des phases.
- **Couplage mutuel d'antenne :** afin d'estimer l'impact de ce phénomène, nous avons calculé la matrice de couplage à partir de la matrice des paramètres S (mesurée lors des phases de validation d'Hycam). Nous en avons déduit que l'impact était marginal, en comparaison des autres distorsions existantes.

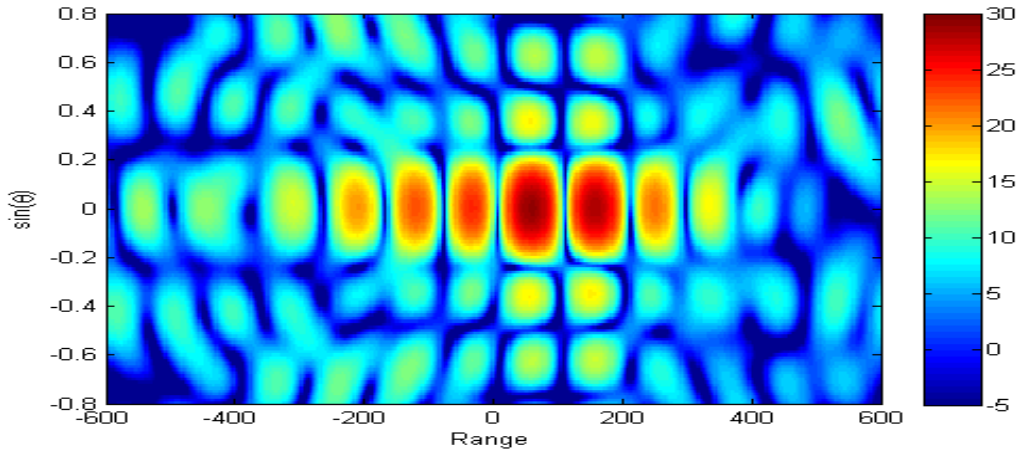

(a) Sortie du filtre adapté.

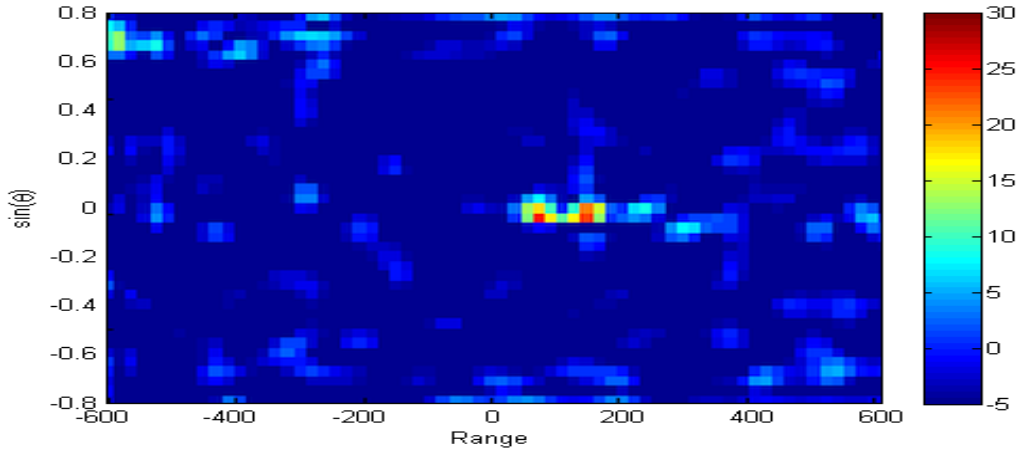

(b) Sortie de l'IAA (itération 7).

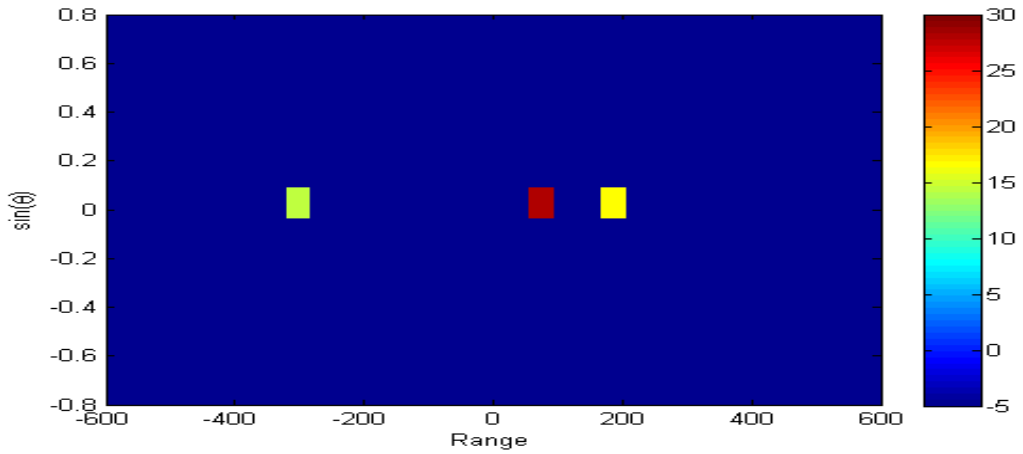

(c) Sortie de l'OMP – suppression étendue.

FIGURE C.8 – Application des différents traitements sur les données expérimentales issues de la configuration boucle fermée. Largeur de la cellule de résolution en distance = 75 m. Largeur de la cellule de résolution en angle = 0,25.

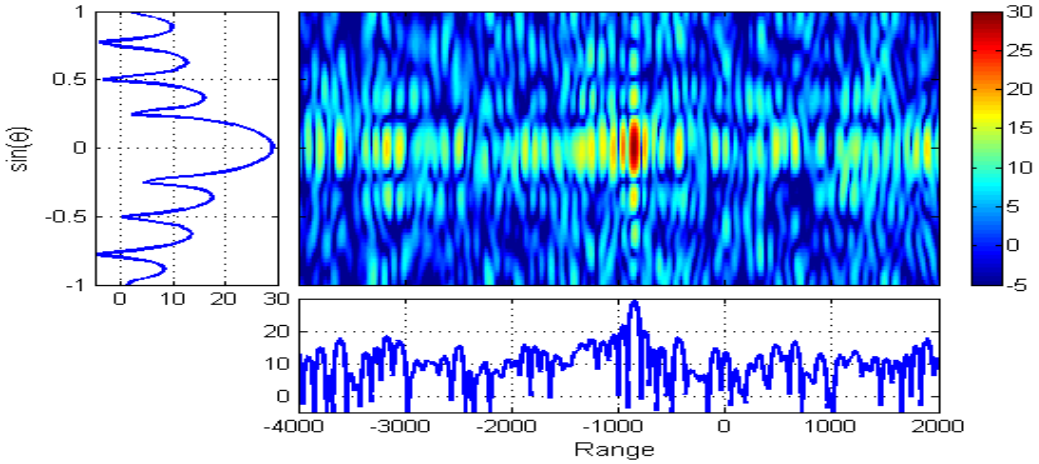

(a) Sortie du filtre adapté.

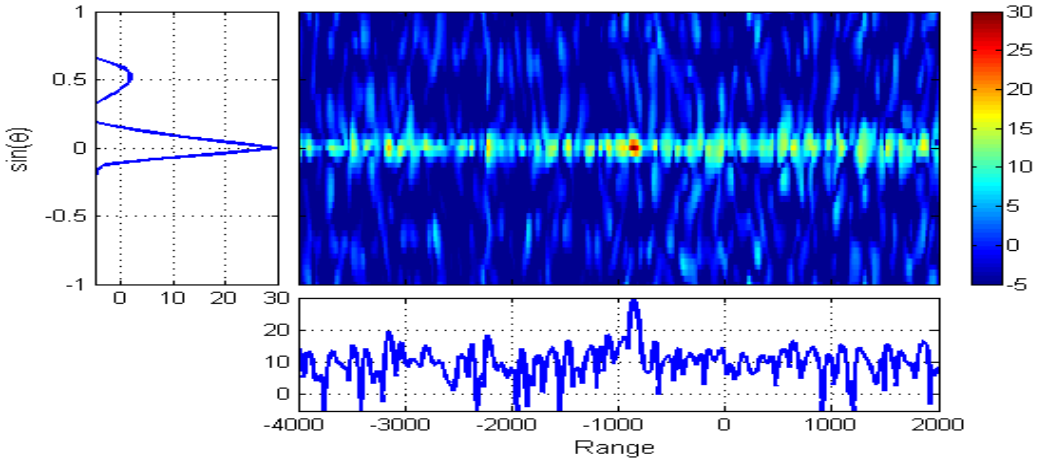

(b) Sortie de l'IAA (itération 6).

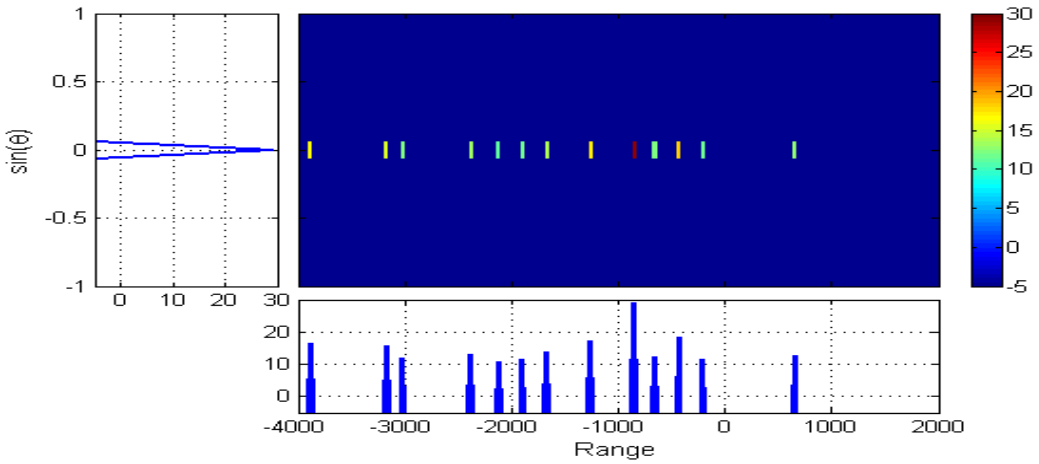

(c) Sortie de l'OMP – suppression étendue.

FIGURE C.9 – Application des différents traitements sur les données expérimentales issues de la configuration avec le simulateur de cible. Largeur de la cellule de résolution en distance = 75 m. Largeur de la cellule de résolution en angle = 0,25.

Par la suite, nous appliquons les métriques de performance en sortie du filtre adapté, ce qui nous permet de relever qu'aucune valeur ne s'écarte particulièrement des valeurs théoriques. Nous en déduisons que l'impact des défauts réels dans les deux configurations expérimentales est marginal en sortie de filtre adapté. Cependant, lorsque nous appliquons ensuite les traitements basés sur un modèle de signal, les dégradations s'avèrent plus conséquentes dans certains cas, même si la grande majorité des lobes secondaires est supprimée. Ainsi, en configuration boucle fermée (fig. C.8), l'OMP permet la détection des deux échos attendus et d'une fausse alarme, là où l'IAA fournit uniquement les deux échos attendus. Dans la configuration avec le simulateur de cible (C.9), les deux traitements fournissent de nombreuses fausses alarmes à l'angle de la cible sur une grande partie de l'axe distance. A ce stade, il est difficile d'isoler précisément le phénomène à l'origine de cette dégradation de performance, néanmoins nous pouvons conclure que l'IAA et l'OMP peuvent être, dans certains cas, beaucoup plus sensibles aux écarts au modèle que le filtre adapté.

Conclusions

Nous avons évoqué les avantages du radar MIMO par rapport aux radars actuels, notamment vis-à-vis de sa flexibilité pour la formation de faisceau à l'émission et les possibilités de réduire la complexité des systèmes. Nous avons également mentionné l'insuffisance de prise en compte dans les travaux actuels des défauts intrinsèques des formes d'onde et des imperfections matérielles. Cela a justifié l'ambition de cette thèse de contribuer à ouvrir la voie vers le radar MIMO opérationnel, en proposant des méthodes d'anticipation et de compensation des défauts du monde réel.

Nous avons ainsi établi, à partir de critères de performance quantitatifs, la résolution spatiale optimale qu'apportent les codes de phase. Ils peuvent ainsi être préconisés pour l'émission MIMO, à la condition que le niveau de lobes secondaires qu'ils induisent soit résolu. Nous avons proposé d'accepter ces défauts et de concentrer les efforts sur le traitement à la réception. Cependant, l'optimisation de séquences de code peut être menée en parallèle.

Nous avons ensuite expliqué pourquoi de nombreuses techniques d'estimation ne peuvent s'appliquer à notre problématique, notamment du fait des contraintes inhérentes à l'implémentation opérationnelle. A l'inverse, nous avons montré que l'OMP est une technique satisfaisante vis-à-vis de ces contraintes. Nous avons cependant

mis en évidence la sensibilité particulière de l'OMP aux erreurs de localisation des cibles. En conséquence, nous avons proposé une extension de l'algorithme résolvant le problème. Nous avons également introduit l'IAA qui fournit une précision toute particulière, néanmoins au prix d'une complexité calculatoire inadéquate.

Par la suite, nous avons décrit des phénomènes issus de la génération et propagation des signaux pouvant induire des distorsions non intégrées au modèle de signal. Au travers de simulations, nous avons montré que cela pouvait dégrader particulièrement les performances en détection de l'IAA et de l'OMP. Ceci nous a amenés à préconiser d'anticiper voire de prévenir l'apparition de ces distorsions. Dans cette optique, après avoir décrit la plateforme MIMO Hycam, nous avons illustré ces concepts au travers d'une méthode numérique d'étalonnage des canaux d'émission.

En dernier point, nous avons proposé de finaliser le pont avec le monde réel en mettant en place des expérimentations MIMO. Nous avons défini deux configurations distinctes, la première focalisée sur la chaîne matérielle interne, et la seconde prenant en compte également l'émission et la propagation. Nous avons montré sur ces acquisitions que des distorsions ayant un impact très limité sur la sortie du filtre adapté peuvent induire de bonnes performances (cas de la première configuration) ou au contraire de fortes dégradations de performance (cas de la deuxième configuration) en sortie de traitements dépendants du modèle de signal, selon que les écarts au modèle soient suffisamment pris en compte ou non dans ce modèle.

Pour terminer, en termes de perspectives par rapport à ce travail de thèse, nous proposons d'élaborer une méthode combinant rapidité de l'OMP et précision de l'IAA en calculant dans un premier temps la sortie de l'OMP afin de déterminer la matrice de covariance qui en résulte, et dans un second temps d'injecter cette matrice dans l'algorithme de l'IAA, afin de réduire fortement le nombre d'itérations nécessaires. Afin d'augmenter la robustesse aux erreurs de modèle, nous proposons la piste d'intégrer un “écart acceptable" sur la détection du signal d'intérêt, dans l'esprit de l'extension de l'OMP proposée qui consiste à considérer également les positions voisines dans un espace spécifique. Cela permettrait ainsi de tolérer une certaine marge d'erreur sur différents paramètres.